

Eruptive history, magma dynamic, and magmatic process of  
effusive-explosive transition at Kelud volcano, Indonesia

インドネシア・ケルード火山における噴出史、噴火ダイナミクスとマグマ過程にお  
ける噴出-爆発の遷移

By

Jananda Nuralam Indriyanto

**Doctoral Thesis**

In partial fulfilment of the requirements for the degree of Doctor of Science

Department of Geosciences, Geotechnology, Material Engineering  
for Resources, Akita University

March 2023

© Jananda Nuralam Indriyanto, 2023

**Major advisor: Prof. Tsukasa Ohba**

All right reserved. This thesis has never been submitted for a degree.

## Abstract

Kelud is considered one of the deadliest volcanoes in Indonesia due to its proximity to three cities in East Java (Malang, Kediri, and Blitar) and violent eruptions over the last century. Regardless of the frequently witnessed eruptions, the volcanic stratigraphy for the historical ages has been poorly understood. This thesis presents first documentation of volcanic stratigraphy for the last 1300 years of activity at Kelud. Componentry and  $^{14}\text{C}$  data are coupled with detailed field observation to develop a comprehensive stratigraphic reconstruction to characterize the main eruption types. The volcanic succession can be subdivided into ten bedsets composed of pyroclastic density current (PDC) and tephra fallout deposits. A total of twelve fallout deposits and ten individual PDC units were identified between  $\sim 1.3$  and 0.1 cal. ka B.P. The fallout layers are thin, derived from short-sustained eruption columns, whereas massive to stratified PDC deposits were originated from low-column collapses. The variable deposit types described in this study suggest that Kelud is capable of producing a wide spectrum of pyroclastic products and its eruptive frequency increases over time (from once  $\sim 100$  years to once  $\sim 10$  years). This first stratigraphic framework, which documents extended records from the oldest witnessed eruption in Kelud (1000 C.E.), sheds new insights into Kelud's activity during historical time.

Transitions between effusive and explosive eruptions of compositionally similar magma are commonly observed at many subduction-related volcanoes worldwide, including Kelud. Various pre- and syn-eruptive aspects, such as degassing pattern, initial volatile and crystal contents, as well as ascent and crystallizations in the conduit, are key processes that produce effusive and explosive styles. This thesis also explores the driving forces behind effusive and explosive activity at Kelud volcano as well as factors that influence the transitions between the two styles. Using the products from effusive (2007/08 dome) and explosive (2014) eruptions as case studies, the thesis integrates volcanological, textural, and petrological data to investigate degassing and crystallization processes during magma ascent. Pre- and syn-eruptive crystallization and degassing processes are examined via whole-rock geochemical analysis, mineral compositions and thermobarometry, quantitative textural analysis of groundmass microlites, and analysis of volatiles in melt inclusions. Both 2007/08 and 2014 eruptions produced basaltic andesite, similar in terms of whole-rock major element compositions. The melt inclusions and groundmasses also show relatively homogenous compositions, ranging from dacite to rhyolite, although the most evolved melt compositions were observed in the 2007/08 glass (75.0–78.8 wt.%  $\text{SiO}_2$ ). Petrographic observation shows that these products share a resemblance in phenocryst and microlite phases, with plagioclase feldspar dominance in both phases, followed by pyroxenes and Fe-Ti oxides. However, the quantitative modal abundance of the analyzed products reveals that dome samples have relatively high phenocryst contents with low vesicularities compared to the explosive products. This evidence suggests that 2007/08

magma has higher initial viscosity during ascent compared to the 2014 eruption.

The magmatic temperatures are estimated to be between  $\sim 1010$  and  $1050$  °C, with a major crystallization zone between  $\sim 5$  and  $20$  km depth. Based on their volatile contents, melt inclusions have re-equilibrated at a depth of  $\sim 4$ – $16$  km during shallower storage or ascent. The 2007/08 melt inclusions have an average  $\text{H}_2\text{O}$  content of  $1.40$  wt.% with a maximum value up to  $3.96$  wt.%, while those from 2014 eruptions have higher  $\text{H}_2\text{O}$  contents (average  $3.91$  wt.%) reaching  $5.89$  wt.%. The  $\text{CO}_2$  concentrations are typically  $< 200$  ppm, but they may reach up to  $\sim 1500$  ppm in some melt inclusions from the 2014 eruption.  $\text{SO}_3$  and F have average values of  $231 (\pm 109)$  and  $508 (\pm 178)$  ppm that show a negative correlation with  $\text{H}_2\text{O}$  contents. Cl displays constant concentrations ( $1877 \pm 331$  ppm) with variable  $\text{H}_2\text{O}$  content, suggesting the presence of exsolve brine phase at shallow depths that “buffered” melt Cl concentrations. The modeled degassing pathway indicates that 2007/08 magma had experienced open-system degassing, whereas 2014 magma was mostly closed-system. The wide variation of  $\text{H}_2\text{O}$  concentrations in melt inclusions, particularly in the 2007/08 dome, suggests that some inclusions have ruptured on longer time scales, allowing  $\text{H}_2\text{O}$  loss via diffusion. This is consistent with the fact that the 2007/08 melt inclusions have experienced a protracted cooling history at low pressure in the dome.

At a shallower level, a two-step crystallization timing was recorded from variations in the microtextural features and chemical compositions of groundmass glass among the 2007/08 and 2014 eruptions. The 2007/08 dome displays microlites with euhedral morphology that were derived from growth-dominated crystallization under slow ascent rates ( $0.001$ – $0.002$   $\text{m s}^{-1}$ ). By contrast, the 2014 microlites have dominant skeletal morphologies derived from fast ascending magma (up to  $18.70$   $\text{m s}^{-1}$ ) under nucleation-dominated crystallization. The calculated growth rates based on feldspar microlites of 2007/08 and 2014 products are within the ranges of  $1.00 \times 10^{-8}$  to  $1.64 \times 10^{-9}$   $\text{mm s}^{-1}$ , suggesting the effusive and explosive eruptions could have similar initial conditions that started crystallizing from the deeper portion of the conduit. However, due to different ascent pathways of the 2007/08 and 2014 magmas, the style of eruptions produced were different. The low ascent rate led the magma to be efficiently outgassed and produced an effusive regime, whereas higher ascent rates allowed the volatiles to be further exsolved simultaneously and increased the effective pressure on magma, producing a more explosive eruption.

This study demonstrates that at Kelud, the conditions of magma storage in the reservoir and crystallization pathways have significance on the final eruption regime. The capacity of Kelud volcano to switch the eruption behavior from dome-forming to explosive behavior with recurrences possibility and little warning time after the initial dome growth should be considered when assessing hazard for future eruption scenarios.

## Chapter contents

<b>Abstract</b> .....	<b>3</b>
<b>Chapter contents</b> .....	<b>5</b>
<b>List of Figures</b> .....	<b>8</b>
<b>List of Table</b> .....	<b>16</b>
<b>Acknowledgement</b> .....	<b>19</b>
<b>Chapter 1 Introduction</b> .....	<b>21</b>
1.1. Lava domes and the eruptive products .....	21
1.2. Explosive eruptions and their products .....	22
1.3. Effusive and explosive transitions .....	23
1.4. Tectonic and geological background .....	25
1.5. Historical eruption of Kelud .....	28
1.6. Rationale and outline of the thesis .....	30
References.....	33
<b>Chapter 2 Eruptive history of the last-1300-years activity of Kelud volcano, Indonesia: Inferences from stratigraphy, chronology, sedimentology, componentry, and geochemistry</b> .....	<b>40</b>
2.1. Introduction .....	40
2.2. Geological framework and previous work .....	41
2.3. Materials and methods.....	45
2.3.1. Field observations .....	45
2.3.2. Radiocarbon dating .....	47
2.3.3. Componentry and chemical analysis.....	47
2.4. Stratigraphy of the deposits .....	48
2.4.1. Margomulyo 1 bed-set.....	49
2.4.2. Margomulyo 2 bed-set.....	60
2.4.3. Mulyorejo bed-set .....	61
2.4.4. Bed-sets Karangrejo Fall1 to Karangrejo Fall5.....	62
2.4.5. Sugihwaras bed-set.....	64

2.4.6.	Bambangan bed-set.....	64
2.5.	Geochemistry.....	68
2.6.	Lithofacies association of the eruptive events.....	70
2.6.1.	Margomulyo 1 .....	71
2.6.2.	Margomulyo 2 bed-set.....	72
2.6.3.	Mulyorejo .....	73
2.6.4.	Karangrejo1 to Karangrejo5.....	74
2.6.5.	Sugihwaras bed-set.....	75
2.6.6.	Bambangan .....	75
2.7.	Eruptive activity and hazard implication.....	77
2.7.1.	Eruptive activity .....	77
2.7.2.	Hazard implications.....	79
2.8.	Summary.....	80
	References.....	82
<b>Chapter 3 An overview of the 2007/08 and 2014 eruptions of Kelud volcano, Indonesia.</b>		<b>91</b>
.....		<b>91</b>
3.1.	The 2007/08 eruption.....	91
3.1.1.	Chronology of the 2007/08 eruption .....	91
3.1.2.	The 2014 eruption .....	94
3.2.	Eruptive products and sample descriptions .....	96
	References.....	98
<b>Chapter 4 Pre-eruptive degassing and crystallization process of the 2007/08 and 2014 eruptions of Kelud volcano, Indonesia.</b>		<b>100</b>
.....		<b>100</b>
4.1.	Introduction .....	100
4.2.	Analytical methods .....	101
4.2.1.	Sample selection and preparation.....	101
4.2.2.	Geochemical analysis.....	105
4.2.3.	Data processing .....	106
4.3.	Results .....	107
4.3.2.	Major element geochemistry .....	107
4.3.3.	Volatile concentrations .....	121

4.4.	Discussion.....	125
4.4.1.	Melt inclusion entrapment and crystallization of clinopyroxene hosts.....	125
4.4.2.	Deep and shallow-level degassing history .....	130
4.5.	Summary and origin of effusive-explosive transition at Kelud.....	133
	References.....	134
<b>Chapter 5 Syn-eruptive degassing and crystallization process of the 2007/08 and 2014 eruptions of Kelud volcano, Indonesia. ....</b>		<b>139</b>
5.1.	Introduction .....	139
5.2.	Analytical methods .....	140
5.2.1.	Sample selection and preparation.....	140
5.2.2.	Geochemical analysis .....	143
5.2.3.	Textural analysis.....	143
5.2.4.	Magma ascent rates .....	145
5.3.	Results .....	146
5.3.1.	Petrographic overview.....	146
5.3.2.	Microlite texture and composition .....	150
5.3.3.	Whole-rock and groundmass composition.....	167
5.3.4.	Quantitative textural analysis of feldspar and pyroxene microlite.....	170
5.3.5.	Microlite size distributions (MSDs).....	180
5.4.	Discussion.....	186
5.4.1.	Magma ascent and decompression rates .....	186
5.4.2.	Variable crystallizations during magma ascent .....	189
5.4.3.	Two-step crystallization timings. ....	195
5.4.4.	Effect of initial crystal content on the crystallization and degassing of ascending magma .....	200
5.4.5.	Controls on the effusive-explosive transition at Kelud.....	201
5.4.6.	Hazard implication .....	204
5.5.	Summary.....	207
	References.....	208

## List of Figures

**Figure 1. 1.** Diagram of relative nucleation and growth rate as a function of undercooling ( $\Delta T$ ) temperature from the experimental result of sample Mon6a (modified from Couch et al., 2003b). There are two possible scenarios of the crystallization process, growth-dominated and nucleation dominated. The dominant regime that occurred during crystallization triggered the two distinguished undercooling events. .... 24

**Figure 1. 2.** Schematic map showing tectonic settings and locations of active volcanic arcs in southern part of SE Asia, including the Indonesia archipelago. A) The volcanoes run continuously along the margin of the Eurasian plate (from Sumatra to Mindanao through East Timor) as the consequences of subducted Indo-Australian and the Philippine sea plate beneath the Eurasian plate. B) Shows the distribution of volcanoes around Eastern part of Java. The volcanoes are distributed into two subdivisions, central and east, marked with a black dashed line representing the East Java micro-continent boundary (Sribudiyani et al., 2003; Subroto et al., 2007). Red box represents the designated research area. The subduction slab profile is exhibited by the gray band, which C) shows an enormous gap of slab fragment underneath East Java (Widiyantoro et al., 2011; modified after Dempsey, 2013). .... 27

**Figure 2. 1.** A) Maps showing the distribution of volcanoes along Sunda arc in eastern Java, Indonesia, including the Kelud volcano. B) The geological map of Kelud volcano (modified after Santosa and Atmawinata, 1992; Zaennudin et al., 1992). The volcano is covered by a volcanic succession of lava, pyroclastic, and lahar deposits. C) Simplified stratigraphic section of the studied area coupled with volcanic activity from identified eruption sets (compiled from Hadikusumo, 1974; Kusumadinata, 1979; Wirakusumah, 1991; Santosa and Atmawinata, 1992; Bourdier et al., 1997; Jeffrey et al., 2013; Goode et al., 2019; Maeno et al., 2019a; and Maeno et al., 2019b). .... 44

**Figure 2. 2.** Correlation of selected ten representative stratigraphic logs combined with lithofacies abbreviation of each bed-set. These sections are illustrated based on the different scale and lateral variations of each eruption unit. The UTM coordinates of stratigraphic log are coupled beneath each observation point. .... 46

**Figure 2. 3.** Generalized composite stratigraphy coupled with the assigned lithofacies abbreviations of Kelud products. Red arrow shows the sampling horizon for age determination. Note different scales of each eruption unit. .... 50

**Figure 2. 4.** Variation of relative component proportions ( $n > 3000$ ) and physical features of tephra from Kelud volcano. Sampling horizons are attached next to stratigraphic positions. m: massive, xs: cross-stratified, s: parallel-stratified, lens: lens, i: inverse grading, n: normal grading, l: lithic, p: pumice, sc: scoria, acc: accretionary lapilli-bearing, B: block/bomb, L:

lapilli, and A: ash. The photographs show examples of volcanic ash observed under binocular and polarizing microscopy. Note that the light blue color is caused by the pigment color..... 54

**Figure 2. 5.** Representative photos and illustrations of Kelud products showing A) strata and the relationship between Margomulyo 1, Margomulyo 2, and Mulyorejo bed-sets occurred in the field. B) to D) showing complex eruption units and facies association composing Margomulyo 1 bed-set. E). Elutriation pipes are visible at the top of the layer 1, which often occurs deforming the overlying beds. The yellow line represents each bed-set boundary, while the black line represents the layer boundary. The white triangles indicate the clast grading of lithic or juvenile clasts from the bottom to top of bed for each assigned lithofacies..... 56

**Figure 2. 6.** SEM back-scattered images of low-crystallinity juvenile fragments from non-accretionary lapilli-bearing ash layers (A–D; M–P) and accretionary lapilli-bearing ash layer (E–H). Pumice of non-accretionary lapilli bearing layers mainly have A) fluidal shape with elongated vesicles and B) thin melt film clasts, although minor C) subangular clasts with thick melt film sometimes observed. D) Show bubble nucleation and coalescence features. Similarly, the accretionary-lapilli bearing layer also preserves various pumice morphology, including E) fluidal-shaped vesicular with thick wall, F) angular shape vesicular clast cut by a planar surface, and fused-shaped clasts. Most of the angular pumice clasts preserve G) abundant spherical vesicle with H) intensive micro-deformation due to high-intensity bubble nucleation. I–K) Present typical round and elongated morphologies of ash aggregate with moss-like surface. L) Closer look at core-type ash aggregates hosting multiple juvenile clasts, crystals, and lithic fragments. M–P) Presents typical high vesicularity and less-deformed scoria clast. Q) Represents blocky morphology of R) typical porphyritic lithic fragment, containing plagioclase and augite phenocrysts, while S) and T) shows typical angular crystals cumulates of plagioclase  $\pm$  augite  $\pm$  Fe-Ti oxide contained as a glomerocryst within pumice clasts. White lines and arrows refer to the area in which the vesicularity and vesicle orientations are contrast..... 59

**Figure 2. 7.** Field photos and illustrations of Kelud products from Mr2 through Su bed-set. A). Showing vertical and lateral variations of tephra deposits can be observed on the field. Most of the deposits are covered by extensive vegetation. B) Detailed section displays the intercalation between the pumice-rich lapilli-ash and organic matter-rich layer of KaF1 through KaF5. C) Facies of macca can be found as multiple layers that differ at type locality (i.e., KLD0102 and ATB-02), hosting D) ash aggregates and often contain fibrous charcoal fragments. E) Displays domination of lapilli-size pumice clasts along lithic fragments hosted in the mLA facies..... 63

**Figure 2. 8.** Representative photos and illustrations of complex succession composing Bambang bed-set. A) Lithofacies association of cross-stratified lapilli and ash, massive lapilli and ash, and massive to stratified accretionary lapilli bearing ash. A deformation (sagging) structure is caused by trajectory block in mLA facies. B) and C) Closer look of intercalation

between xsLA and accA that usually contain ash aggregates and lenses of pumice lapilli and ash..... 67

**Figure 2. 9.** Total alkalis vs. silica (after Le Maitre et al., 2002) of analyzed samples plotted along with previously published data of older dome-forming eruption products of Kelud volcano. Red dashed-oval represents the compositional range of analyzed samples in this study. .... 68

**Figure 2. 10.** Major element variations of the volcanic product from the last-1300-years-activity of Kelud volcano were plotted alongside the published data of Kelud's products in the basis of volatile-free, including from the recent activity (1990 and 2007). .... 69

**Figure 3. 1.** Simplified sketch of the evolution of the 2007/08 eruption. A) Increase in seismic activity and measured CO<sub>2</sub> fluxes denoted the unrest of the volcano prior to the 2007/08 eruption. B) Early stage of lava dome effusion was recorded from a sudden increase in surface temperature and emission of a steam pulse from a fresh protruding dome material in the lake area. C) Lava dome continuously grew until 30 May 2008, with a height reaching ~200 m from the crater surface. Image from GVP (2008) and Hidayati et al. (2009)..... 93

**Figure 3. 2.** Distribution maps of 2014 eruption deposits (after Maeno et al., 2019a; Goode et al., 2019). The inset map shows the location of Kelud volcano, alongside other volcanoes on Java Island, and the distribution of fallout deposits of the 2014 eruption produced during stage II (CPF). .... 95

**Figure 3. 3.** Example and description of juvenile products from the 2007/08 and 2014 eruptions of Kelud..... 97

**Figure 4. 1.** Simplified sketch of the evolution of the 2007/08 lava dome and 2014 explosive eruptions. A) Increase in seismic activity and measured CO<sub>2</sub> fluxes denoted the unrest of the volcano prior to the 2007/08 eruption. B) Early stage of lava dome effusion was recorded from a sudden increase in surface temperature and emission of a steam pulse from a fresh protruding dome material in the lake area. C) Lava dome continuously grew until 30 May 2008, with a height reaching ~200 m from the crater surface. D) Seven years later, the 2007/08 dome was destroyed by an eruption on 13 February 2014 and produced ballistic bombs and PDCs towards the NE flanks of Kelud. E) At 11 PM on the same day, the plinian eruption column was developed and completely destroyed the 2007/08 dome, producing 0.24–0.47 km<sup>3</sup> pumice fallout deposits along the WSW and W directions. F) The marginal column collapse occurred on 14 February, emplacing pumice-rich PDC deposits along the main river flow around Kelud volcano..... 103

**Figure 4. 2.** Stages and distribution maps of 2014 eruption deposits (after Maeno et al., 2019a;

Goode et al., 2019). Roman numerals indicate eruption stages in the center column and distribution map. The inset map shows the location of Kelud volcano, alongside other volcanoes on Java Island, and the distribution of fallout deposits of the 2014 eruption produced during stage II (CPF). Sample localities are marked with red circles. .... 104

**Figure 4. 3.** Typical clinopyroxene phenocrysts used for this study. Clinopyroxene compositions of analyzed samples plotted on quadrilateral (Di-Hd-En-Fs) diagram for A) 2007/08 dome, B) 2014 PDC-1, and C) 2014 CPF are usually augite to diopside (Morimoto, 1989). Plots of  $\text{Al}_2\text{O}_3$  vs. D) wollastonite end-members (mol.%) and E) Mg# of all measured clinopyroxene shows systematic compositional variations between different eruptive products, including phenocrysts from previous study (Jeffrey et al., 2013). .... 110

**Figure 4. 4.** Typical *cpx*-hosted silicate melt inclusions used for this study. A) Raman shift indicates  $\text{H}_2\text{O}$  usually present in the analyzed SMI. B) Although no visible daughter mineral observed, some inclusions may contain nanolite in the glass phase. Total alkalis vs. silica (after Le Maitre et al., 2002) of whole-rock, groundmass glass, and SMI of 2007/08 and 2014 volcanic products plotted along with previously published data of 2007/08 eruption of Kelud (Jeffrey et al., 2013). Yellow circle represents SIMS crater. .... 115

**Figure 4. 5.** Major element variation diagrams of bulk, groundmass glass, and SMI of 2007/08 and 2014 eruptions of Kelud. Melt inclusion compositions are corrected for PEC. All whole-rock, groundmass glass, and SMI values are normalized to 100 wt.% on a basis of volatile-free.  $\text{FeO}^*$  is all iron values reported as  $\text{FeO}$ . .... 121

**Figure 4. 6.**  $\text{CO}_2$  and  $\text{H}_2\text{O}$  contents in melt inclusions measured by SIMS. Isobars curves (*fine black lines*) and vapor isopleths (*grey dashed lines*) are calculated at  $1050^\circ\text{C}$  using the *VolatileCalc 2.0* (Newman and Lowenstern, 2002). Bold solid lines represent closed-system degassing pathway, while blue dashed line for open-system degassing. The grey area is obtained simulating the degassing of the two groups of melt inclusions having the highest  $\text{H}_2\text{O}$  and  $\text{CO}_2$  contents, using closed system condition and initial excess of fluid from 0.5 to 3%. .... 122

**Figure 4. 7.** Volatile contents in SMI and groundmass glass plotted against  $\text{K}_2\text{O}$  as a differentiation indicator. A) Fluorine versus  $\text{K}_2\text{O}$ , B)  $\text{SO}_3$  versus  $\text{K}_2\text{O}$ , and C) Cl vs  $\text{K}_2\text{O}$ . Dashed lines represent detection limit of each measured volatile in groundmass glass using EPMA. .... 124

**Figure 4. 8.** Histograms of pressure at which clinopyroxene hosts were crystallized. A) Calculated using Neave and Putirka (2017) clinopyroxene barometer. B) calculated pressure using B) Equation 32b of Putirka (2008) and C) using Equation 32c of Putirka (2008). Histogram of last re-equilibration pressures based on  $\text{H}_2\text{O}$  and  $\text{CO}_2$  concentrations in 2007/08 and 2014 SMIs computed using *VolatileCalc 2.0* (Newman and Lowenstern, 2002) at  $1050^\circ\text{C}$ .

- ..... 126
- Figure 4. 9.** Plots of water content versus indicators of magmatic differentiation: A) SiO<sub>2</sub> and B) K<sub>2</sub>O. H<sub>2</sub>O has negative correlations with SiO<sub>2</sub> and K<sub>2</sub>O, indicating last equilibrium stage of melt inclusion following vapor-saturated crystallization during decompression. Some inclusions might have experienced ruptured during ascent as suggested from low water contents. .... 129
- Figure 4. 10.** Variations of volatile concentrations against H<sub>2</sub>O content. A) sulfur, B), fluorine, and C) chlorine R represents ratio of Cl and H<sub>2</sub>O for rhyolite melts, whereas D for dacite melts (Webster, 2004). .... 132
- Figure 5. 1.** Simplified sketch of the evolution of the 2007/08 lava dome and 2014 explosive eruptions. A) Increase in seismic activity and measured CO<sub>2</sub> fluxes denoted the unrest of the volcano prior to the 2007/08 eruption. B) Early stage of lava dome effusion was recorded from a sudden increase in surface temperature and emission of a steam pulse from a fresh protruding dome material in the lake area. C) Lava dome continuously grew until 30 May 2008, with a height reaching ~200 m from the crater surface. D) Seven years later, the 2007/08 dome was destroyed by an eruption on 13 February 2014 and produced ballistic bombs and PDCs towards the NE flanks of Kelud. E) At 11 PM on the same day, the plinian eruption column was developed and completely destroyed the 2007/08 dome, producing 0.24–0.47 km<sup>3</sup> pumice fallout deposits along the WSW and W directions. F) The marginal column collapse occurred on 14 February, emplacing pumice-rich PDC deposits along the main river flow around Kelud volcano. .... 141
- Figure 5. 2.** Stages and distribution maps of 2014 eruption deposits (after Maeno et al., 2019a; Goode et al., 2019). Roman numerals indicate eruption stages in the center column and distribution map. The inset map shows the location of Kelud volcano, alongside other volcanoes on Java Island, and the distribution of fallout deposits of the 2014 eruption produced during stage II (CPF). Sample localities are marked with red circles. .... 142
- Figure 5. 3.** Plot of vesicularity as a function of total phenocryst content showing the difference between effusive and explosive eruption products. The distribution of modal proportion is displayed in volume percent (vol.%) by counting >1000 points for the selected clast types from the studied eruption products. Error bars representing (2σ) were obtained by applying the method of Van der Plas and Tobi (1965). .... 148
- Figure 5. 4.** Mineral assemblages contained in groundmass of 2007/08 and 2014 eruptions of Kelud. The groundmass mostly consists of plagioclase feldspar, pyroxene, and Fe-Ti oxide microlites, with occasional observed nanolite phase. .... 149

- Figure 5. 5.** Variation of microlite morphologies per size interval linked with eruption type and stages. .... 153
- Figure 5. 6.** Textures and zonation of feldspar microlites observed in the 2007/08 and 2014 products, including descriptions and interpretative sketches: oscillatory zoning with a) resorbed core or b) euhedral core and euhedral to subhedral overgrowth rim; normal zoning with distinct compositional variation between c) euhedral or d) resorbed core and growing rim; e) oscillatory zoning with resorbed core, where the overgrowth rim has skeletal morphology; and f) hollow texture highlighting a remnant core of skeletal crystallization. All elemental images use distribution of calcium in the analyzed feldspar microlites. Note different scales of each crystal. .... 154
- Figure 5. 7.** Feldspar microlite compositions of analyzed samples plotted on ternary (An-Ab-Or) diagram show (upper) the general distribution of all microlite compositions from different eruption events and (lower) the microlite composition plotted separately for each defined clast type. .... 158
- Figure 5. 8.** Textures and zonation of pyroxene microlites observed in the 2007/08 and 2014 products, including descriptions and interpretative sketches: a) normal zoning sharp boundary between Fe-poor euhedral core and Fe-rich overgrowth rim; b) oscillatory zoning that show successive growth of Fe-poor and Fe-rich rims over the resorbed core; c) sector zoning in basal cut as hourglass sector around an unzoned core and often appear with thin Ca-rich bands due to local partitioning effect of feldspar crystallization; d) resorbed core and skeletal overgrowth with thin Ca-rich band; and e) hollow texture highlighting a normal zoning from the remnant core of euhedral/hopper crystallization. The elemental images mostly use distribution of calcium and iron to distinguish textural variation in the analyzed pyroxene microlites. Note different scales of each acquired crystal. .... 162
- Figure 5. 9.** Pyroxene microlite compositions of analyzed samples plotted on quadrilateral (Di-Hd-En-Fs) diagram show the discrimination of pyroxene species in A) 2007/08 lava dome, B) 2014 PDC-1, and C) 2014 CPF (Morimoto, 1989). .... 163
- Figure 5. 10.** A) Total alkalis vs. silica (after Le Maitre et al., 2002) of whole-rock and groundmass glass of 2007/08 and 2014 volcanic products plotted along with previously published data of 2007/08 eruption of Kelud. B) Zoomed-in plot of whole-rock composition data. All data recalculated to 100% on a basis of volatile-free. .... 168
- Figure 5. 11.** Major element variation diagrams of bulk and groundmass glass of 2007/08 and 2014 eruptions of Kelud. All whole-rock and groundmass glass values are normalized to 100 wt.% on a basis of volatile-free. FeO\* is all iron values reported as FeO. .... 170

**Figure 5. 12.** Plot of microlite aspect ratios (Short axis over Intermediate axis ( $S/I$ ) vs Short axis over Long axis ( $S/L$ )) for (upper) plagioclase feldspar microlites and (lower) pyroxene microlites. The feldspar and pyroxene microlites share similar aspect ratios and have wide ranges of crystal habits, covering rectangular prism, acicular, and tabular..... 171

**Figure 5. 13.** Variation in 2D and 3D textural parameters of 2007/08 and 2014 products. Areal number density of feldspar microlite ( $N_A$ ,  $\text{mm}^{-2}$ ) plotted against A) feldspar microlite crystallinity ( $\phi$ ), together with products from other dome-forming eruption of Merapi volcano, Indonesia (Hammer, 2000; Preece et al., 2013), B) feldspar microlite mean crystal area in  $\mu\text{m}^{-2}$ , and C) short/intermediate axis ratio ( $S/I$ ). D) Feldspar microlite mean crystal area ( $\mu\text{m}^{-2}$ ) vs.  $S/L$ . Volumetric number density of feldspar microlite (MND,  $\text{m}^{-3}$ ) plotted against E) feldspar microlite crystallinity ( $\phi$ ) and F) characteristic length of feldspar microlite in  $\mu\text{m}$ . Curves on plots B) represent isocrystallinity curves (in percentage values) calculated using a simple model of circular crystal sections at a particular  $N_A$  and crystal size..... 176

**Figure 5. 14.** Variation in 2D and 3D textural parameters of 2007/08 and 2014 products. Areal number density of pyroxene microlite ( $N_A$ ,  $\text{mm}^{-2}$ ) plotted against A) pyroxene microlite crystallinity ( $\phi$ ), B) pyroxene microlite mean crystal area in  $\mu\text{m}^{-2}$ , and C) short/intermediate axis ratio ( $S/I$ ). D) Pyroxene microlite mean crystal area ( $\mu\text{m}^{-2}$ ) vs.  $S/L$ . Volumetric number density of pyroxene microlite (MND,  $\text{m}^{-3}$ ) plotted against E) pyroxene microlite crystallinity ( $\phi$ ) and F) characteristic length of pyroxene microlite in  $\mu\text{m}$ . Curves on plots B) represent isocrystallinity curves (in percentage values) calculated using a simple model of circular crystal sections at a particular  $N_A$  and crystal size..... 177

**Figure 5. 15.** BND and MND relationship for A) feldspar microlite and B) pyroxene microlites in the 2014 eruption's products. .... 179

**Figure 5. 16.** Microlite size distributions (MSDs) of feldspar (A–C) and pyroxene (D–F) microlites from different eruption event and stages plotted in binary population density ( $\text{mm}^{-4}$ ) vs. crystal size (mm). The linier best-fit slopes and intercepts of each MSD are reported in Tables 5.5 and 5.6. Envelopes around the distribution points represent the  $1\sigma$  standard deviation acquired from CSDcorrections v1.61 of Higgins (2000; 2006). .... 185

**Figure 5. 17.** Magma ascent rates and decompression rates calculated using MND water exsolution rate mater for plagioclase feldspars and pyroxenes. Ascent and decompression rates obtained from feldspar and pyroxenes are systematically similar, although pyroxenes have slightly higher values (less than one order)..... 187

**Figure 5. 18.** Variation of groundmass glass compositions of 2007/08 and 2014 products plotted against total groundmass crystallinity that includes all microlite mineral phases present (feldspars, pyroxenes, and Fe-Ti oxides). .... 192

**Figure 5. 19.** Variation of microlite morphologies linked with crystallization time and decompression rate for every eruption types and stages. The variation of feldspar and pyroxene morphologies for every eruption type and stage. The shapes characterization based on the experimental result of Lofgren (1974), Couch et al., (2003a; 2003b), and Shea & Hammer (2013) through observing the size and abundance of feldspar and pyroxene microlite contained in the samples. .... 193

**Figure 5. 20.** Schematic illustrations showing the relationship between feldspar microlite crystallization and water saturation timing that produced studied volcanic products. Left graphs illustrate the water solubility in silicate melt (dashed lines) and effects of decompression during ascent on evolution of water content in magma (solid color lines). (Right graphs) feldspar microlite compositions coupled with morphological variations per size interval plotted in the feldspar ternary (An-Ab-Or) diagram display the compositionally differ towards different eruptive stages. Curves are generated using SOLVCALC (Wen and Nekvasil, 1994), representing isothermal sections of the dry ternary solvus at 400, 600, 800 and 1000 °C..... 199

**Figure 5. 21.** Schematic illustrations of magma dynamics during ascent for A) 2007/08 dome-forming eruption, B) onset of 2014 eruption, C) climactic plinian event in 2014 eruption... 203

**Figure 5. 22.** A) Plot of  $\log(\text{MND})$  vs  $\text{SiO}_2$  concentration. MND data were compiled from previous publications of Redoubt (Wolf and Eichelberger, 1997), Mount St. Helens (Cashman, 1992), Pinatubo (Hammer et al., 1999; Borisova et al., 2005), Izu-Oshima (Toramaru et al., 2008), Unzen (Noguchi et al., 2008), and Merapi (Preece et al., 2013; 2016). B) Plot of  $N_A$  vs  $\phi$  in comparison with other eruptions with various explosivity. .... 206

## List of Table

<b>Table 2. 1</b> Summary of radiocarbon dating results from designated charcoal and carbonized matter.....	47
<b>Table 2. 2.</b> Summary of description and interpretation of common lithofacies of Kelud's volcanic products. Modified from Sulpizio et al. (2007) and Macorps et al. (2018). See the text for detailed explanations. ....	51
<b>Table 2. 3.</b> Classification and description of clast types used for component analysis in this study. ....	55
<b>Table 2. 4.</b> Summary of lithofacies association and interpretation of each eruption episode. m: massive, xs: cross-stratified, s: parallel-stratified, lens: lens, i: inverse grading, n: normal grading, l: lithic, p: pumice, sc: scoria, acc: accretionary lapilli-bearing, B: block/bomb, L: lapilli, and A: ash.....	70
<b>Table 4. 1.</b> Representative clinopyroxene host compositions of products from 2007/08 and 2014 eruptions analyzed using electron microprobe. Stages I and II of the 2014 eruption refer to chronology of Maeno et al. (2019a). FeO*= total iron. LD: lava dome; BP DG: banded pumice dark grey; SB: scoria bomb; TWP: transparent white pumice; TPP: transparent pink pumice.	108
<b>Table 4. 2.</b> Whole-rock major and trace element concentrations of the volcanic products from 2007/08 and 2014 eruptions. Stages I and II of the 2014 eruption refer to chronology of Maeno et al. (2019a). FeO*= total iron. ....	112
<b>Table 4. 3.</b> Representative analyses of melt inclusion compositions from 2007/08 and 2017 eruptions. Stages I and II of the 2014 eruption refer to chronology of Maeno et al. (2019). Lithology types are as follows: lava dome (LD), banded pumice dark grey (BP DG), scoria bomb (SB), transparent white pumice (TWP), and transparent pink pumice (TPP). MI denotes melt inclusion number. PEC denotes degree of post-entrapment <i>crystallization</i> corrected for (%). All major elements (in wt. %) determined by electron microprobe <i>with</i> all values are shown after PEC correction. P <sub>2</sub> O <sub>5</sub> <sup>b</sup> and H <sub>2</sub> O in wt. % and CO <sub>2</sub> , SO <sub>3</sub> , F, and Cl in ppm were measured by ion microprobe. ....	116
<b>Table 4. 4.</b> Representative groundmass and interstitial glass compositions of the volcanic products from 2007/08 and 2014 eruptions analyzed using electron microprobe. Stages I and II of the 2014 eruption refer to chronology of Maeno et al. (2019). FeO*= total iron. LD (GM): lava dome groundmass; LD (IG): lava dome interstitial glass; BP W: banded pumice white part; BP LG: banded pumice light grey; BP DG: banded pumice dark grey; SB: scoria bomb; NTWP: non-transparent white pumice; TWP: transparent white pumice; TPP: transparent pink pumice;	

TGP: transparent grey pumice; and S: scoria..... 118

**Table 5. 1.** Representative feldspar microlite composition of products from 2007/08 and 2014 eruptions analyzed using electron microprobe. FeO\*= total iron LD: lava dome; BP W: banded pumice white part; BP LG: banded pumice light grey; BP DG: banded pumice dark grey; SB: scoria bomb; NTWP: non-transparent white pumice; TWP: transparent white pumice; TPP: transparent pink pumice; TGP: transparent grey pumice; and S: scoria..... 155

**Table 5. 2.** Representative pyroxene microlite composition of products from 2007/08 and 2014 eruptions analyzed using electron microprobe. FeO\*= total iron. LD: lava dome; BP W: banded pumice white part; BP LG: banded pumice light grey; BP DG: banded pumice dark grey; SB: scoria bomb; NTWP: non-transparent white pumice; TWP: transparent white pumice; TPP: transparent pink pumice; TGP: transparent grey pumice; and S: scoria. .... 164

**Table 5. 3.** Summary of quantitative textural analysis of feldspar microlite. Lithology types are LD: lava dome; BP W: banded pumice white part; BP LG: banded pumice light grey; BP DG: banded pumice dark grey; SB: scoria bomb; NTWP: non-transparent white pumice; TWP: transparent white pumice; TPP: transparent pink pumice; TGP: transparent grey pumice; and S: scoria. .... 172

**Table 5. 4.** Summary of quantitative textural analysis of pyroxene microlite. Lithology types are LD: lava dome; BP W: banded pumice white part; BP LG: banded pumice light grey; BP DG: banded pumice dark grey; SB: scoria bomb; NTWP: non-transparent white pumice; TWP: transparent white pumice; TPP: transparent pink pumice; TGP: transparent grey pumice; and S: scoria. .... 173

**Table 5. 5.** Summary of MSD results and calculated growth rates (G) and nucleation rates (J) for feldspar microlites. Lithology types are LD: lava dome; BP W: banded pumice white part; BP LG: banded pumice light grey; BP DG: banded pumice dark grey; SB: scoria bomb; NTWP: non-transparent white pumice; TWP: transparent white pumice; TPP: transparent pink pumice; TGP: transparent grey pumice; and S: scoria. .... 181

**Table 5. 6.** Summary of MSD results and calculated growth rates (G) and nucleation rates (J) for pyroxene microlites. Lithology types are LD: lava dome; BP W: banded pumice white part; BP LG: banded pumice light grey; BP DG: banded pumice dark grey; SB: scoria bomb; NTWP: non-transparent white pumice; TWP: transparent white pumice; TPP: transparent pink pumice; TGP: transparent grey pumice; and S: scoria. .... 183

**Table 5. 7.** Summary of input parameters and results for magma ascent and decompression rates calculated using Toramaru et al. (2008). Lithology types are LD: lava dome; BP W: banded pumice white part; BP LG: banded pumice light grey; BP DG: banded pumice dark grey; SB:

scoria bomb; NTWP: non-transparent white pumice; TWP: transparent white pumice; TPP: transparent pink pumice; TGP: transparent grey pumice; and S: scoria. .... 188

## Acknowledgement

I would first and foremost like to express my gratitude to my major advisor Prof. Tsukasa Ohba. I am grateful to you for giving me the opportunity to be one of your students. I appreciate all of the intellectual insight, advice, constructive feedbacks, and continuous supports over the course of the last few years.

I am indebted to the many people I've been lucky enough to learn from and collaborate with in this project. I am especially grateful to Astiti Anggorowati for providing Kelud's samples. I really appreciate your kindness during this pandemic time in which I couldn't conduct any fieldwork to Indonesia. Dr. Takashi Hoshide is acknowledged for supporting information and discussion during my manuscript writing. Prof. Andrea Agangi is acknowledged for comprehensive discussion during manuscript writing and data discussion. Dr. Mirzam Abdurrachman is thanked for motivations throughout my study. I am grateful to Dr. Genji Saito for assistance during FTIR analysis, guidance in studying melt inclusions, and his kind support during my trip to Geological Survey of Japan. Dr. Keiko Matsumoto is thanked for assisting the Raman analysis and her kind insight about melt inclusion. Dr. Yuusuke Minami is also thanked for becoming host researcher during my trip to GSJ, life advice, and good humor. I could not say anything but thank you. I am also thankful to Dr. Kenji Shimizu for the ion probe, sample preparations, and for discussions about the melt inclusions data. Thank you so much for your warm welcome at Kochi Core Center, and always answering my questions all the time. I am also grateful for Dr. Takayuki Ushikubo for his kindness preparing out SIMS machine every time I conducted the analysis, thanks for the life advice and continuous support after leaving the KCC.

I am grateful to Ms. Yumi Hayakawa for patient technical assistance ordering a lot of lab supplies for my research purposes. All member of Petrology and Volcanology group for their continuous supports through ups and downs: Muhammad Andriansyah Gurusinga, Muhammad

Arfah, Masamichi Ikeda, Akira Chiba, Hirata Aoi, Nobuhiro Koizumi, Wildan Nur Hamzah, and Rinaldi Ikram. All Indonesian residence in Akita: Meriyani Rika, Sugiyati Kamada, Ani Komatsu, Dewi Koseki, Raden Eliani, Nana Sugawara, and all their families in here are thanked for their supports during my doctoral study in Akita University. Their meals during every gathering we had, were always delicious and decent. All members of Indonesian student association of Akita University: Nanda Ajeng Nurwantari, Muhammad Arfah, Cendi Diar Permata Dana, Alfath Salni, Enrico Gilrandy Wahyu Suharjo, Fadlin, Muhammad Andriansyah Gurusinga, Muhammad Sulzuhair, Rahman Ardhiansyah, Renaldi Suhendra, Reza Al Furqon, Rinaldi Ikram, and Wildan Nur Hamzah. Thank you for accepting me for who I am and keeping me mentally motivated to go all this through. To my late-night working buddies: Jonathan Tandang Macuroy, Enrico Gilrandy Wahyu Suharjo, and Masaya Koseki, thanks, guys for being there every time I was in university. You guys are a good buddies. To my office mates (S-201 squad), you have made the past few years such a friendly, fun and productive place to work: Ly, Kazuki, June, Jane, Abir, Bui, and Paolo, thank you!. All the people whom I cannot say your names one-by-one, thank you.

Special thanks to my parents: Indriyanto and Eny Joharaeni; my brothers: Nurani Hardikananda Indriyanto, Jananda Forestrika Indriyanto, and Syaif Al Islam Indriyanto for your unconditional love and continuous supports through everything. I dedicate this writing for all of you. To Adi Sulaksono, Mega Pasa, Rika Meriyani, and Sugiyati Kamada, thank you for always providing ears for my stories. You guys are the best!

Last but not least, I acknowledge Leading Program of Akita University for providing the funding the research and Monbukagakusho (MEXT) for granting me the scholarship.

## Chapter 1

### Introduction

This thesis presents an investigation of Kelud's eruptive history during the last 1300 years, the magma dynamics of effusive and explosive activity at Kelud, and the factors contributing to the transitions between these contrasting eruptive styles from compositionally similar magma.

Specifically using the 2007/08 and 2014 eruptions as case studies, this thesis combines textural and petrological observations with volcanological records in order to evaluate processes involved in magma storage and during ascent for generating the variable eruption styles at Kelud. To evaluate the pre- and syn-eruptive processes that responsible for the development of each eruption style and its variation, this study focuses the observation on the chemical variation of whole rock, melt inclusions, and groundmass glass, coupled with quantitative textural analysis of groundmass microlite contained in each volcanic product.

#### **1.1. Lava domes and the eruptive products**

Dome-forming (effusive) eruptions are commonly observed at silicic volcanoes worldwide, in which the viscous magma extrudes and rapidly cools onto the surface (Fink and Anderson, 2000). Lava domes have various types, dimensions, and morphologies according to the formation processes, cooling history, and yield strengths of lava during the extrusions. Their diameters vary from a few meters to several kilometers, with heights reaching over one kilometer (Siebert et al., 2011; Ashwell et al., 2018). Although most of the dome-forming eruptions are considered less hazardous (VEI 1–2), they may pose a significant threat due to their unpredictable growth nature. For example, as the dome grew bigger, it may reach certain instability points and collapse to generate high-concentration pyroclastic density currents (PDCs), blowing down nearby infrastructure. Alternatively, the effusive activity may also acts

as a ‘cap rock’ that initiate pressure accumulations, increasing the probability to produce higher explosive activity following the lava dome growth. Variations in extrusion rates and transitions into a more explosive behavior (or *vice versa*) have been frequently observed at several volcanoes around the world, such as Mount St. Helens (United States), Unzen (Japan), Pinatubo (Philippines), Merapi (Indonesia), Soufrière Hills (Montserrat), and Lascar (Chile). Understanding the processes responsible for the development of this activity is necessary for assessing the volcanic hazard posed by the volcanoes with such eruption behavior.

## 1.2. Explosive eruptions and their products

The explosive eruption has become the most spectacular display in nature and provides a wide range of eruption styles and regimes (Cioni et al., 2000; Branney and Kokelaar, 2002). In most cases, the explosive eruption is generated by intermediate to silicic magmas and is often associated with pyroclastic density currents (PDCs) along the deposition of tephra fallout originating from magmatic or phreatomagmatic eruption (Branney and Kokelaar, 2002; Ohba et al., 2012). The PDCs result from the mixture of vapor phases and volcanic fragments as a heterogeneous material that flows because of their relative density (Carey, 1991; Branney and Kokelaar, 2002; Sulpizio et al., 2014; Jordan et al., 2018). They may contain multiple fragments in the form of pumice and scoria flows deriving from the collapse of plinian eruption columns (Charbonnier and Gertisser, 2008; Goode et al., 2019) or block and ash flows as the response to the disruption and collapse of the lava fronts or the solidified lava dome (Branney and Kokelaar, 2002; Charbonnier and Gertisser, 2011; Ashwell et al., 2018; Macorps et al., 2018). The generation of pyroclastic deposits, including the emplacement process, has been studied during the last few decades (e.g., Sulpizio and Dellino, 2008). Most studies revealed an understanding of architectural elements of the deposits, including the flow rheology for recognizing the flow behavior in pyroclastic deposition (Patra et al., 2005; Doyle et al., 2010; Sulpizio et al., 2014, Zrelak et al., 2020). These studies also contributed a generalized model of

the eruption dynamics, such as erupted volume and eruption column height calculation models. Several methods have been developed to identify the eruption behavior based on the observation of the physical characteristics and textural variations of the volcanic products (e.g., Toramaru et al., 2008; Preece et al., 2016; Murch and Cole, 2019), which are essential for understanding the eruption dynamics in terms of volcanic hazard assessment.

### **1.3. Effusive to explosive transitions**

Previous studies suggested that the variation in eruptive styles from effusive (i.e., dome-forming) to explosive (i.e., plinian type) was promoted by the different original volatile concentrations in the magma body (i.e., stratification of volatile components) (e.g., Eichelberger and Westrich, 1981). Later research demonstrated that various degrees of gas loss from distinct degassing patterns (open vs. closed) during ascent significantly affect the eruption style produced and their transitions (e.g., Preece et al., 2016; Murch and Cole, 2019; Bernard and de Maisonneuve, 2020). In open-system degassing, the volatile components are exsolved and outgassed from the melt via permeable flow through the conduit or conduit walls (Cassidy et al., 2018; Murch and Cole, 2019). Consequently, the resulting residual melt will have depleted volatile components, which will further produce effusive eruptions. By contrast, in a closed-system degassing, the exsolved volatiles are ensnared as bubble phases in the magma rather than outgassed because of an equilibrium state. Therefore, closed-system degassing promotes higher impermeable vesicularity and higher pore pressure for generating explosive eruptions. The rate of magma ascent has a significant effect on the extent of degassing, as a rapid ascent prevents volatiles from being outgassed from the system, thereby increasing the probability of producing explosive eruptions. (Toramaru et al., 2008; Preece et al., 2016). The rate of magma ascent is highly determined by a complex interplay that includes magma properties, crystal cargo geometry, reservoir pressure, magmatic influx, and conduit geometry (Toramaru et al., 2008; Cassidy et al., 2018).

Comparatively, little attention has been paid to the transitions between eruptive styles in most natural and experimental studies of these two distinct eruption styles (Preece et al., 2016; Cassidy et al., 2018). Previous models indicate that degassing and crystallization at shallower levels can affect critical points in producing an eruption by inducing rheological changes in magma (e.g., Cassidy et al., 2018). Minor changes in volatile content and crystallization regime will lead to substantial changes in discharge rates and eruption behaviors (Cassidy et al., 2018). For example, degassing during ascent increases the crystallization rate of magma and further increases the relative viscosity of magma to produce dome-forming eruptions (e.g., Bernard and de Maisonneuve, 2020). Moreover, adiabatic decompression affects magma crystallization during ascent (e.g., Cashman and Blundy, 2000). Since the solubility of volatile components such as H<sub>2</sub>O is pressure-dependent (e.g., Moore et al., 1995), the depressurization of a melt occurs as the volatile components are exsolved during ascent. This causes a significant increase in undercooling temperature (here in refers to as  $\Delta T$ , different in liquidus temperature and actual magmatic temperature) and ultimately promotes the crystallization of anhydrous minerals, especially plagioclase feldspar (e.g., Couch et al., 2003a; 2003b). Later, the  $\Delta T$  will govern the nucleation and growth of groundmass microlites at the shallower levels due to decompression during magma ascent (Fig.1.1).

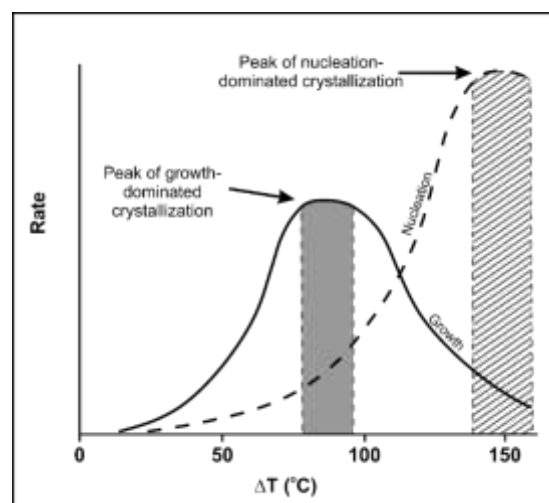


**Figure 1. 1.** Diagram of relative nucleation and growth rate as a function of undercooling ( $\Delta T$ ) temperature from the experimental result of sample Mon6a (modified from Couch et al., 2003b).

There are two possible scenarios of the crystallization process, growth-dominated and nucleation dominated. The dominant regime that occurred during crystallization triggered the two distinguished undercooling events.

#### **1.4. Tectonic and geological background**

The volcanism of Indonesia is associated with some distinct subduction zones, including the Sunda, Banda, Sangihe, and Halmahera arcs (Fig. 1.2). Kelud is part of the Sunda arc that covers the area between the Andaman Islands north of Sumatra and Flores south of Sumatra. The Sunda arc is well known as one of the biggest volcanic chains in the world. It is located at the western to southern margin of the Sunda shelf as the consequence of the continuous subduction of Indo-Australian plate beneath the Eurasian plate at a rate of ~50 to 80 mm/year (Fig 1.2A). The Sunda arc is a part of the Eurasian plate and is believed to be the continental core of SE Asia (Hamilton, 1979). The Sunda arc has been developed since early Mesozoic through the amalgamation of continental blocks (Hall, 2002). Due to different propagation angles, the subduction slab beneath the Indonesian archipelago has different configurations (Hall, 2002). According to Hamilton (1979), the age of the subducting slab decreases across the arc following the west-east direction with the compositional and thickness variation of the overriding plate. Beneath Sumatra, the subduction slab is oblique, whereas steepened subduction slab (to ~ 60°) occurs beneath Java (Whitford, 1975; Curray, 1989; Widiantoro et al., 2011).

The petrology and geochemistry of Pleistocene to modern volcanic products (i.e., lava and intrusion) along the Sunda volcanic arc have been investigated in detail since the late 1970s (Whitford, 1979; Gasparon et al., 1994; Kadarsetia, 2016). According to the previous studies, the Sunda arc consists of basaltic-andesites to andesites that have high-K calc-alkaline to arc-tholeiite affinities (e.g., Stolz et al., 1988; Varekamp et al., 1989). The average silica content is ~55 wt. %, with most of the volcanic rocks have undergone complex differentiation processes (i.e., assimilation and magma mixing) compared to other magmatism from other volcanic arcs or orogenic settings (Whitford 1975). The chemical variation of volcanic rocks along the Sunda

arc is interpreted as the result of melting from different sources (i.e., sedimentary, mantle material) beneath the Eurasian plate (Whitford et al., 1977, 1979, 1981; Whitford & Jezek, 1979; 1982; Whitford, 1975). Across-arc Hf and Nd isotope ratios reveal that the subducted sources are heterogenous, including various sediments that may contribute to the down-going plate along Java (Handley, 2006; Handley et al., 2011). Moreover, along-arc geochemical investigation suggests a significant variations in lithospheric and crustal thickness in western and eastern Java, as indicated by the progressive increase in Sr isotope ratios from West and Central Java towards East Java (Whitford et al., 1979; Handley, 2006; Dempsey, 2013). It also implies that the eastern part of Sunda volcanic arc was contaminated by a more 'continental' component compared to the western part (i.e., East Java micro-continent; Sribudiyani et al., 2003; Dempsey, 2013).

East Java covers a wide area of nine active volcanoes, which showed activity during the last 10.000 years to be developed. In general, the volcanoes in East Java are divided into three groups, front-arc, rear-arc, and back-arc volcanic chain (Fig 1.2B and C). The front-arc volcanic chain consists of Wilis, Kelud, and Semeru, whereas Arjuno-Welirang, Bromo-Tengger, Lamongan, Argopuro, Raung, and Ijen a rear-arc volcanic chain with the Ringgit-Besar volcanic complex lies as part of a back-arc volcanic chain. The front-arc volcano, especially Kelud, had shown activity that primarily produced volcanic products with 52 to 58 wt.% of SiO<sub>2</sub> (Kadarsetia, 2016).

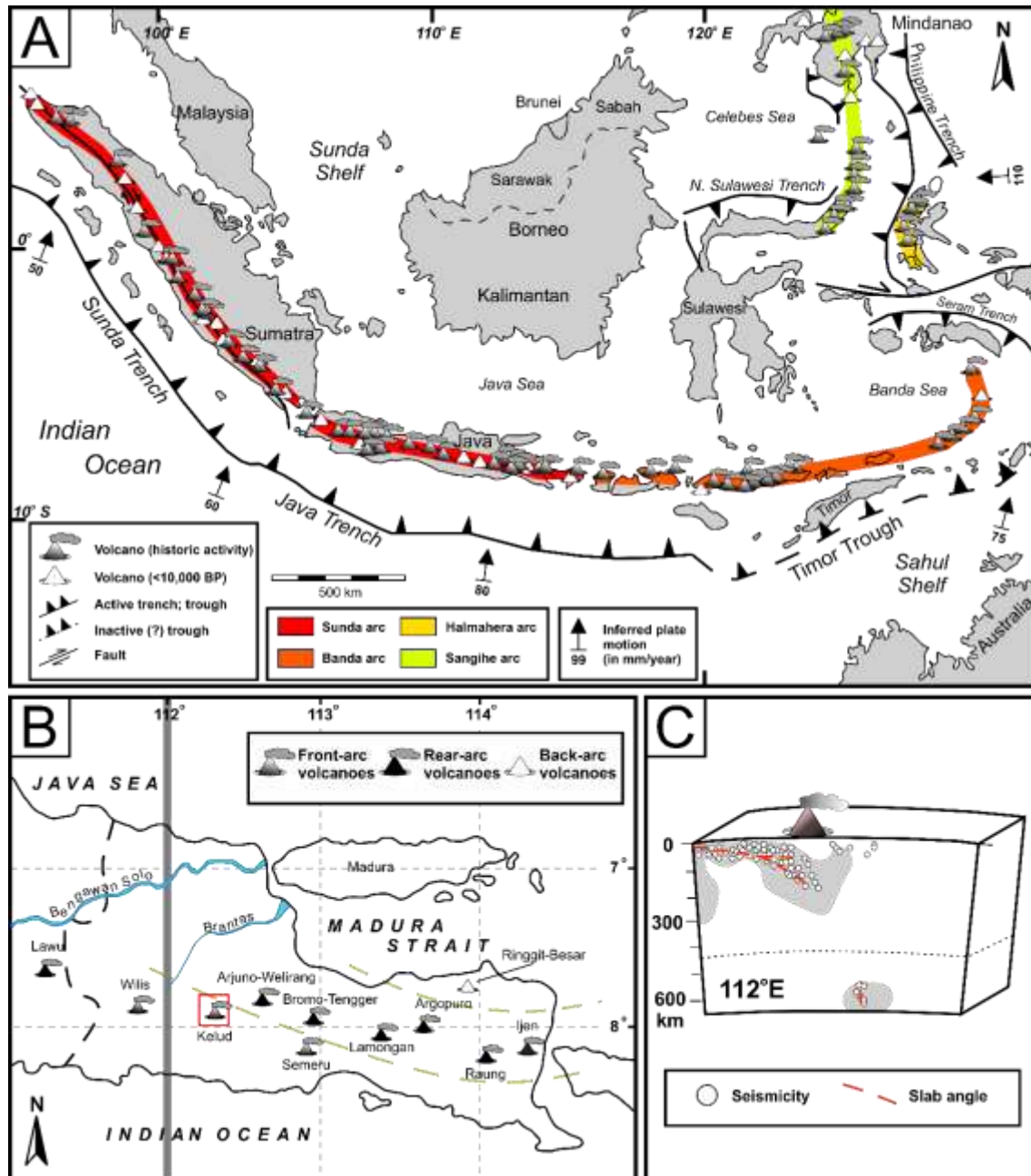


**Figure 1. 2.** Schematic map showing tectonic settings and locations of active volcanic arcs in southern part of SE Asia, including the Indonesia archipelago. A) The volcanoes run continuously along the margin of the Eurasian plate (from Sumatra to Mindanao through East Timor) as the consequences of subducted Indo-Australian and the Philippine sea plate beneath the Eurasian plate. B) Shows the distribution of volcanoes around Eastern part of Java. The volcanoes are distributed into two subdivisions, central and east, marked with a black dashed line representing the East Java micro-continent boundary (Sribudiyani et al., 2003; Subroto et al., 2007). Red box represents the designated research area. The subduction slab profile is exhibited by a gray band which C) shows an enormous gap of slab fragment underneath East Java (Widiyantoro et al., 2011; modified after Dempsey, 2013).

### 1.5. Historical eruption of Kelud

The first historical records of Kelud and its activity were done in the 18th Century by the Dutch during the 17<sup>th</sup>–19<sup>th</sup> century colonialization (Kusumadinata, 1979; Wirakusumah, 1991). They revealed that the historical eruptive behavior of Kelud typically consists of VEI 1-4 eruptions generating PDCs from vulcanian eruptions or collapse of lava domes. Other types of deposits have been identified at Kelud and classified according to dominant component lithology, including (i) scoria-rich pyroclastic flow deposits and (ii) pumice-rich PDC deposits (Wirakusumah, 1991; Bourdier et al., 1997; Maeno et al., 2019a).

It has been noted that there was a shift in the style of activity from the 20th century (Kusumadinata, 1979; Wirakusumah, 1991). The following are brief descriptions of notable eruptions that occurred in the 20<sup>th</sup> century:

**1901:** The eruption of Mount Kelud occurred at midnight between May 22 and 23, 1901. The first eruption occurred around 00.00–01.00. For two hours, the eruption activity increased, and at 03.00, the main eruption occurred. Thick eruption smoke rose from Kelud crater, followed by the onset of lapilli rain around Kelud. The subsequent occurrence was a shower of hot ash. At 3.30 a.m., hot ash began to fall in Kediri, and sulfur could be smelled everywhere. According to information, the Kelud crater lake water was boiling approximately 12 days before the eruption. Approximately 0.2 km<sup>3</sup> of solid material was ejected during the eruption. The death toll is high, but information regarding the number is unclear.

**1919:** The eruption of 1919 was the biggest catastrophe in the 20<sup>th</sup> century. The eruption occurred between 19 and 20 May 1919 at 01:05 WIB. Moments later, the pyroclast began to fall from the sky, causing the majority of house roofs to be destroyed. The wind primarily dispersed ash precipitation to the east. Approximately 0.2 km<sup>3</sup> of volcanic materials were deposited during the 1919 eruption. Before the eruption, the crater lake contained 0.04 m<sup>3</sup> of water; during the eruption, this volume of water was drastically reduced following the emplacement of primary lahar along the main river through the city of Blitar. The flow speed

of the lahar was estimated at around 18 m/s, with a maximum distance reaching 37.5 km from the eruption vent.

**1951:** On 31 August 1951, the eruption occurred. At 06:15 WIB, thick white smoke emanated from Kelud's summit. Fifteen minutes later, the thick black smoke was observed rising from the Kelud crater, leaning towards the southwestern direction reaching Bandung with estimated material ejected around  $0.2 \text{ km}^3$ . The syn-eruptive lahar was observed at a maximum distance of ~12 km from the eruption vent. Total casualties were estimated at >160 people, with seven dying from the eruption and 157 injured. Around 320 hectares of plantation and forestry areas were damaged.

**1966:** After the 1951 eruption, the new crater was formed 79 meters below the previous crater. This decrease in the bottom of the crater caused the volume of lake water to reach about 21.6 million  $\text{m}^3$  before the 1966 eruption. This volume is much larger than the volume of water before the 1951 eruption, which was only  $1.8 \times 10^{-3} \text{ km}^3$ . The eruption occurred on 26 April 1966 at 20.15, triggering the lahar emplacement along K. Badak, K. White, K. Ngobo, K. Konto, and K. Semut. The total casualties were estimated at around 210 people in the Jatilengger and Atas Kedawung areas. This eruption produced tephra of about  $0.09 \text{ km}^3$ . Fifteen minutes prior to the eruption, an earthquake was recorded by seismographs at the Margomulyo Post. The color of the lake water before the eruption also changed from dark green to yellowish green.

**1990:** The eruption occurred consecutively on 10 February 1990 from 11.41 to 12.21 WIB. The initial stage of the eruption was phreatomagmatic that produced a thin ash distribution around the summit, while the subsequent eruption was larger with sand, lapilli, and stone-throwing spread over a radius of  $3.5 \text{ km}^2$  (Bourdier et al., 1997). Following the onset eruption, the co-PDC ash clouds associated with the plinian eruption were emplaced along the valley in the southwest direction as far as 5 km distance from the crater, producing tephra deposits with  $\sim 0.13 \text{ km}^3$  that covered an area of  $1700 \text{ km}^2$ . Around 500 houses and 50 school buildings were damaged, and a total of 32 human casualties were recorded (Jeffrey et al., 2013).

## 1.6. Rationale and outline of the thesis

Recently, the Kelud volcano has become the most active and dangerous volcano in Java because it lies over the boundary of the densely populated cities, such as Malang, Kediri, and Blitar. There have been more than 30 eruptions during the historical record. Many previous works mostly provided the records as brief documentation or local narrations (e.g., [Kimerling, 1920](#); [Hadikusumo, 1973](#)). It is recorded that since 1500 AD, the eruption of Kelud volcano (predominantly by magmatic Plinian) has caused around 15,000 fatalities. About 5000 of the total number of victims were caused during an explosive pyroclastic eruption that triggered the lahar deposit emplacement in February 1990 ([Sudradjat, 1991](#)). After 17 years of dormancy, a new lava dome emerged from the eruption center, replacing the crater lake ([Hidayati et al., 2009](#)). More recent study from Hadikusumo (1973) and Kusumadinata (1979) recorded that most casualties were caused by eruptions preceded by lava dome formation. The 1951 and 2014 eruptions are good examples of explosive plinian types following the dome-forming eruptions. Detailed stratigraphy of the 2014 eruption confirmed that the eruption occurred after lava domes developed over several years ([Maeno et al., 2019a](#); [Maeno et al., 2019b](#); [Goode et al., 2018](#)). Nevertheless, the detailed documentation of products older than historical records (see chapter 2) is still inadequate.

Textural and petrological approaches were motivated by the limited documentation of the eruption products. The magmatic eruption, especially the plinian eruption, has a high magnitude and discharged volume that can cover a wide area. However, the mechanisms behind such eruptions are still debatable among world researchers (e.g., [Melnik and Sparks, 1999](#); [Toramaru et al., 2008](#)). Their volcanic products can be used to better understand the kinetics behind decompression-induced crystallization and devolatilization ([Couch et al., 2003a, 2003b](#), [Suzuki et al., 2018](#)). Furthermore, the chemical and textural observation can provide a generalized idea about the triggers behind the transition of eruption style from compositionally similar magma (e.g., [Preece et al., 2016](#); [Bernard and de Maisonneuve, 2020](#)). In this thesis, textural and

petrological approaches were examined from the most recent volcanic products (2007/08 and 2014 eruptions) to better understand the magma plumbing system and conduit dynamic beneath Kelud volcano. Petrological and textural analyses of well-constrained samples coupled with volcanological and geophysical data were used to evaluate various pre- and syn-eruptive processes (i.e., magma storage and ascent conditions) responsible for such transition. The 2007/08 dome samples compared to explosive 2014 products are specifically used as a comparison in understanding the crystallization and degassing processes involved prior to and within dome-forming and plinian eruptions. This thesis is presented as follows:

**Chapter 1:** Introduction. This chapter presents the introduction, geological background of the Sunda arc, brief information on East Java volcanism, project motivation and objectives, and the thesis outline.

**Chapter 2:** Eruptive history of the last-1300-years activity of Kelud volcano, Indonesia: Inferences from stratigraphy, chronology, sedimentology, componentry, and geochemistry. This chapter investigates the eruptive products that Kelud produced during the historical time using field- and component- approaches. This chapter is based on the following paper published in Journal of Volcanology and Geothermal Research: Indriyanto, J. N., Ohba, T., Hoshide, T., & Angkasa, S. S., 2023. Eruptive history of the last-1300-years activity of Kelud volcano, Indonesia: Inferences from stratigraphy, chronology, sedimentology, componentry, and geochemistry. Journal of Volcanology and Geothermal Research, 433 (November 2022), 107723. <https://doi.org/10.1016/j.jvolgeores.2022.107723>

**Chapter 3:** An overview of the 2007/08 and 2014 eruptions of Kelud volcano, Indonesia. This chapter provides detailed background information on the 2007/08 and 2014 eruptions, including monitoring and chronology data, description of the deposits, and componentry data used for chapters 4 and 5.

**Chapter 4:** Pre-eruptive degassing and crystallization process of the 2007/08 and 2014 eruptions of Kelud volcano, Indonesia. This chapter investigates degassing and crystallization

processes that occurred prior to both 2007/08 and 2014 eruptions, using major elements and volatile components in silicate melt inclusions. Magma storage and degassing patterns are gained from geothermobarometry of the melt inclusions and the host clinopyroxene phenocrysts.

**Chapter 5:** Syn-eruptive degassing and crystallization process of the 2007/08 and 2014 eruptions of Kelud volcano, Indonesia. This chapter examines short timescale variations of shallow magma ascent and conduit processes during effusive and explosive eruptions using quantitative microlite textural analysis and petrological data of the 2007/08 and 2014 products. In this chapter, the kinetics of eruption based on detailed mineralogical, geochemical, and quantitative textural aspects are also exclusively deliberated.

## References

- Ashwell P.A., Kennedy B.M., Edwards M., Cole J.W., 2018. Characteristics and consequences of lava dome collapse at Ruawahia, Taupo Volcanic Zone, New Zealand. *Bull. Volcanol.* 80 (5), 43. <https://doi.org/10.1007/s00445-018-1217-1>
- Bernard, O., & Bouvet de Maisonneuve, C., 2020. Controls on eruption style at Rabaul, Papua New Guinea – Insights from microlites, porosity and permeability measurements. *J. Volcanol. Geotherm. Res.* 406. <https://doi.org/10.1016/j.jvolgeores.2020.107068>
- Bourdier, J. L., Pratomio, I., Thouret, J.-C., Boudon, G., Vincent, P.M. 1997. Observations, stratigraphy and eruptive processes of the 1990 eruption of Kelut volcano, Indonesia. *J. Volcanol. Geotherm. Res.* 79, 181–203. [https://doi.org/10.1016/S0377-0273\(97\)00031-](https://doi.org/10.1016/S0377-0273(97)00031-)
- Branney, M. J. & Kokelaar, P. 2002. Pyroclastic Density Currents and the Sedimentation of Ignimbrites. Geological Society, London, *Memoirs*, 27: pp143
- Cashman, K. V., Blundy, J.D., 2000. Degassing and crystallization of ascending andesite and dacite. *Phil. Trans. Roy. Soc. Lon. A* 358, 1487-1513. <https://doi.org/10.1098/rsta.2000.0600>
- Cassidy, M., Manga, M., Cashman, K., Bachman, O., 2018. Controls on explosive-effusive volcanic eruption styles. *Nat. Commun.* 9, 2839. <https://doi.org/10.1038/s41467-018-05293-3>
- Charbonnier, S.J., Gertisser, R., 2008. Field observations and surface characteristics of pristine block-and-ash flow deposits from the 2006 eruption of Merapi volcano, Java, Indonesia. *J. Volcanol. Geotherm. Res.* 177, 971-982.
- Charbonnier, S.J., Gertisser, R., 2011. Deposit architecture and dynamics of the 2006 block-and-ash flow of Merapi Volcano, Java, Indonesia. *Sedimentology* 58, 1573–1612. <https://doi.org/10.1111/j.1365-3091.2011.01226.x>
- Carey, S.N., 1991. Transport and deposition of tephra by pyroclastic flows and surges. In: Fisher RV, Smith R (ed) *Sedimentation in volcanic setting*. SEMP Special Publication,

45, 3959

- Caudron, C., Mazot, A., Bernard, A., 2012. Carbon dioxide dynamics in Kelut volcanic lake. *J. Geophys. Res.* 117:B05102. <https://doi.org/10.1029/2011JB008806>
- Cassidy, M., Manga, M., Cashman, K., Bachmann, O., 2018. Controls on explosive-effusive volcanic eruption styles. In *Nat. Commun.* (Vol. 9, Issue 1). Nature Publishing Group. <https://doi.org/10.1038/s41467-018-05293-3>
- Cioni, R., Marianelli, P., Santacroce, R., Shrana, A., 2000. Plinian and Sub-plinian eruptions. In *Sirgudsson, H., Houghton, B., Rymer, H., McNutt, S., Stix, J., (Eds) Encyclopedia of Volcanoes: Academic Press: pp.477-494.*
- Couch, S., Sparks, R.S.J., Carroll, M.R., 2003a. The kinetics of degassing-induced crystallization at Soufrière Hills volcano, Montserrat. *J. Petrol.* 44, 1477–1502. <https://doi.org/10.1093/petrology/44.8.1477>
- Couch, S., Harford, C.L., Sparks, R.S.J., Carroll, M.R., 2003b. Experimental constraints on the conditions of formation of highly calcic plagioclase microlites at the Soufrière Hills volcano, Montserrat. *J. Petrol.* 44, 1455–1475. <https://doi.org/10.1093/petrology/44.8.1455>
- Curry, J., R. 1989. The Sunda Arc: a model for oblique plate convergence. *Netherlands Journal of Sea Research*, 24, 131 - 140.
- Dempsey, S., R., 2013. Geochemistry of volcanic rocks from the Sunda Arc, Durham theses, Durham University. Available at Durham E-Theses Online: <http://etheses.dur.ac.uk/6948/>
- Eichelberger, J.C., Carrigan, C.R., Westrich, H.R., Price, R.H., 1986. Non-explosive silicic volcanism. *Nature* 323, 598-602.
- Fink, J.H., Anderson, S.W., 2000. Lava domes and coulees. In: *Sirgudsson, H., Houghton, B., McNutt, S.R., Rymer, H., Stix, J. (Eds.) Encyclopedic of Volcanoes. Academic Press. pp 307-319.*

- Gasparon, M., Hilton, D.R. & Varne, R. 1994. Crustal contamination processes traced by helium isotopes: examples from the Sunda arc, Indonesia. *Earth and Planetary Science Letters*, 126, 15-22.
- Global Volcanism Program, 2008. Report on Kelud (Indonesia) (Wunderman, R., ed.). Bulletin of the Global Volcanism Network, 33:3. Smithsonian Institution. <https://doi.org/10.5479/si.GVP.BGVN200803-263280>
- Goode, L.R., Handley, H. K., Cronin, S. J, Abdurrachman, M., 2019. Insights into eruption dynamics from the 2014 pyroclastic deposits of Kelut volcano, Java, Indonesia, and implications for future hazards. *J. Volcanol. Geotherm. Res.* 382, 6-23. <https://doi.org/10.1016/j.jvolgeores.2018.02.005>
- Jeffery, A.J., Gertisser, R., Troll, V.R. et al., 2013. The pre-eruptive magma plumbing system of the 2007–2008 dome-forming eruption of Kelut volcano, East Java, Indonesia. *Contrib. Mineral. and Petrol.* 166, 275–308. <https://doi.org/10.1007/s00410-013-0875->
- Jordan, N.J., Rotolo, S.G., Williams, R., Speranza, F., McIntosh, W.C., Branney, M.J., Scaillet, S., 2018. Explosive eruptive history of Pantelleria, Italy: Repeated caldera collapse and ignimbrite emplacement at a peralkaline volcano. *J. Volcanol. Geotherm. Res.* 349, 47–73. <https://doi.org/10.1016/j.jvolgeores.2017.09.013>
- Hall, R., 2002. Cenozoic geological and plate tectonic evolution of SE Asia and the SW Pacific: computer-based reconstructions, model and animations. *Journal of Asian Earth Science.* 20, 353–431.
- Hamilton, W., 1979. Tectonics of the Indonesian region. U.S. Geological Survey Professional Paper 1078, 1-345.
- Handley, H.K., 2006. Geochemical and Sr-Nd-Hf-O isotopic constraints on volcanic petrogenesis at the Sunda arc Indonesia. Ph.D. Thesis. Durham University.
- Handley, H.K., Turner, S., Macpherson, C.G., Gertisser, R., Davidson, J.P., 2011. Hf-Nd isotope and trace element constraints on subduction inputs at island arcs: limitations of

- Hf anomalies as sediment input indicators. *Earth and Planetary Science Letters* 304, 212-223.
- Hidayati, S., Kristianto, Basuki, A., Mulyana, I., 2009. A new lava dome emerged from crater lake of Kelud volcano, East Java, Indonesia. *Jurnal Geologi Indonesia* 4 (4), 229–238. <http://dx.doi.org/10.17014/ijog.vol4no4.20091>.
- Hidayati, S., Triastuty, H., Mulyana, I., Adi, S., Ishihara, K., Basuki, A., Kuswandarto, H., Priyanto, B., Solikhin, A., 2019. Differences in the seismicity preceding the 2007 and 2014 eruptions of Kelud volcano, Indonesia. *J. Volcanol. Geotherm. Res.* 382, 50–67. <https://doi.org/10.1016/j.jvolgeores.2018.10.017>
- Kadarsetia, E., 2016. Petrogenesis batuan Gunungapi Kelud, Jawa Timur. Pusat Vulkanologi dan Mitigasi Bencana Geologi (CVGHM): In Indonesian.
- Le Maitre, R.W., Streckeisen, A., Zanettin, B., La Bas, M.J., Bonin, B., Bateman, P., Bellieni, G., Dudek, A., Efremova, J., Keller, J., Lameyre, J., Sabine, P.A., Schmidt, R., Sørensen, H., Woolley, A.R., 2002. *Igneous Rocks. A classification and Glossary of Terms. Recommendations of the International Union of Geological Sciences subcommission on the systematics of igneous rocks.* Cambridge University Press, Cambridge, 252 pp.
- Macorps E., Charbonnier S.J., Varley N.R., Capra L., Atlas Z., Cabré J., 2018. Stratigraphy, sedimentology and inferred flow dynamics from the July 2015 block-and-ash flow deposits at Volcán de Colima, Mexico. *J. Volcanol Geotherm. Res.* 349, 99–116. <https://doi.org/10.1016/j.jvolgeores.2017.09.025>
- Maeno, F., Nakada, S., Yoshimoto, M., Shimano, T., Hokanishi, N., Zaenuddin, A., Iguchi, M., 2019a. A sequence of a plinian eruption preceded by dome destruction at Kelud volcano, Indonesia, on 13 February, 2014, revealed from tephra fallout and pyroclastic density current deposits. *J. Volcanol. Geotherm. Res.* 382, 24–41. <https://doi.org/10.1016/j.jvolgeores.2017.03.002>
- Maeno, F., Nakada, S., Yoshimoto, M., Shimano, T., Hokanishi, N., Zaenuddin, A., Iguchi, M.,

- 2019b. Eruption pattern and a long-term magma discharge rate over the past 100 years at Kelud volcano, Indonesia. *J. Disaster. Res.* 14 (1), 27–39. <https://doi.org/10.20965/jdr.2019.p0027>
- Matsumoto, K., & Geshi, N., 2021. Shallow crystallization of eruptive magma inferred from volcanic ash microtextures: a case study of the 2018 eruption of Shinmoedake volcano, Japan. *Bull Volcanol*, 83(5). <https://doi.org/10.1007/s00445-021-01451-6>
- Moore, G., Vennemann, T., Carmichael, I.S.E., 1995. Solubility of water in magmas to 2 kbar. *Geology*, 23 (12), 1099–1102. [https://doi.org/10.1130/0091-7613\(1995\)023<1099:SOWIMT>2.3.CO;2](https://doi.org/10.1130/0091-7613(1995)023<1099:SOWIMT>2.3.CO;2)
- Murch, A.P. and Cole, P.D., 2019. Using microlites to gain insights into ascent conditions of differing styles of volcanism at Soufrière Hills Volcano, J. *Volcanol. Geotherm. Res.* 384, 221–231. <https://doi.org/10.1016/j.jvolgeores.2019.07.022>
- Ohba, T., Hayashi, S., Ban, M., Kondo, A., Kuzumaki, T., Suzuki, S., Furuki, K., 2012. Eruptive History at Chokai Volcano during the Last 4000 Years: Implication from Ash Layers Preserved in Peat Soil. *Bull. Soc. Japan*, 57, 65-76 (in Japanese, with English abstract) [https://doi.org/10.18940/kazan.57.2\\_65](https://doi.org/10.18940/kazan.57.2_65)
- Preece, K., Barclay, J., Gertisser, R., Herd, R. A., 2013. Textural and micro-petrological variations in the eruptive products of the 2006 dome-forming eruption of Merapi volcano, Indonesia: Implications for sub-surface processes. *J. Volcanol. Geotherm. Res.* 261, 98–120. <https://doi.org/10.1016/j.jvolgeores.2013.02.006>
- Preece, K., Gertisser, R., Barclay, J., Charbonnier, S.J., Komorowski, J.-C., Herd, R.A., 2016. Transitions between explosive and effusive phases during the cataclysmic 2010 eruption of Merapi volcano, Java, Indonesia. *Bull. Volcanol.* 78, 54. <https://doi.org/10.1007/s00445-016-1046-z>
- Siebert, L., Simkin, T., Kimberly, P., 2011. *Volcanoes of the world*, 3rd edn. University of California Press, Los Angeles, p 551

- Sribudiyani, S., Muchsin, N., Ryacudu, R., Kunto, T., Astono, P., Prasetya, I., Sapiee, B., Asikin, S., Harsolumakso, A.H., Yulianto, I., 2003. The Collision of the East Java Microplate and Its Implication for Hydrocarbon Occurrences in the East Java Basin. January. IPA Proceedings (03) G-085. <https://doi.org/10.29118/ipa.1530.03.g.085>
- Stolz, A. J., Varne, R., Wheller, G. E., Feden, J. D., Abbott, M. J., 1988. The geochemistry and petrogenesis of K-rich alkaline volcanics from the Batu tara volcano, estern Sunda arc. *Contributions to Mineralogy and Petrology*: 98, 374-389.
- Sudradjat, A. (1991). A Preliminary Account of the 1990 Eruption of the Kelut Volcano. In A. Sudradjat (Ed.), *The Dynamics of Indonesian Volcanoes* (pp. 447-462). Handover: Padjadjaran University, Bandung, Indonesia.
- Sulpizio, R., Dellino, P., Doronzo D.M., Sarocchi, D., 2014. Pyrocalstic density currents: state of the art and perspective. *J. Volcanol. Geotherm. Res.* 283, 36-65. <http://dx.doi.org/10.1016/j.jvolgeores.2014.06.014>
- Surono, 2007, Pusat Vulkanologi Dan Mitigasi Bencana Geologi, Pos Pengamatan Gunungapi Kelut (Hasil evaluasi tingkat kegiatan G. Kelut): Departemen Energi Dan Sumber Daya Mineral, Republik Indonesia, Badan Geologi, Nomor, 112/GK/X/2007, 30 Oktober 2007. In Indonesian.
- Suzuki, Y., Maeno, F., Nagai, M., Shibutani, H., Shimizu, S., Nakada, S., 2018. Conduit process during climatic phase of Shinmoe-dake 2011 eruption (japan: Insight into intermittent explosive activity and transition in eruption style of andesitic magma: *J. Volcanol. Geotherm. Res.* 358, 87-104. <https://doi.org/10.1016/j.jvolgeores.2018.02.008>
- Toramaru, A., Noguchi, S., Oyoshihara, S., Tsune, A., 2008. MND (microlite number density) water exsolution rate meter. *J. Volcanol. Geotherm. Res.* 175(1-2), 156-167. <https://doi.org/10.1016/j.jvolgeores.2008.03.035>
- Van der Plas, L., Tobi, A.C., 1965. A chart for judging the reliability of point counting results. *Am. J. Sci.* 263, 87-90. <https://doi.org/10.2475/ajs.263.1.87>.

- Varekamp, J. C., van Bergen, M. J. Vroon, P. Z., Poorter, R. P. E., Wirakusumah, A. D., Erfan, R., Suharyono, K., Sriwana, T., 1989. Volcanism and tectonics in the eastern Sunda Arc, Indonesia. *Netherlands Journal of Sea Research*: 24, 303-312.
- Widiyantoro, S., Pesicek, J. D., & Thurber, C. H. (2011). Subducting slab structure below the eastern Sunda arc inferred from non-linear seismic tomographic imaging. *Geological Society, London, Special Publications*. DOI: 10.1144/SP355.7
- Whitford, D.J., 1975. Strontium isotopic studies of the volcanic rocks of the Sunda arc, Indonesia, and their petrogenetic implications. *Geochim, cosmochim. Acta* 39: 1287-1302.
- Whitford, D.J. & Jezek, P.A., 1979. Origin of the late Cenozoic lavas from the Banda arc, Indonesia: Trace element and Sr isotope evidence. *Contributions to Mineralogy and Petrology*: 68: 141-150.
- Whitford, D.J. & Jezek, P.A., 1982. Isotopic constraints on the role of subducted sialic material in Indonesian island arc magmatism. *Geological Society of America Bulletin*: 93: 504-513.
- Whitford, D.J., Compston, C., Nicholls, I.A., Abbott, M. J., 1977. Geochemistry of late Cenozoic lavas from eastern Indonesia: the role of subducted sediments in petrogenesis. *Geology* 5: 571-575.
- Whitford, D.J., Nicholls, I. A., Taylor, S. R., 1979. Spatial variations in the geochemistry of Quaternary lavas across the Sunda arc in Java and Bali. *Contributions to Mineralogy and Petrology*: 70, 341-356.
- Zrelak, P.J., Pollock, N.M., Brand, B.D., Sarocchi, D., Hawkins, T., 2020. Decoding pyroclastic density current flow direction and shear conditions in the flow boundary zone via particle-fabric analysis. *J. Volcanol. Geotherm. Res.* 402. <https://doi.org/10.1016/j.jvolgeores.2020.106978>

## Chapter 2

# Eruptive history of the last-1300-years activity of Kelud volcano, Indonesia: Inferences from stratigraphy, chronology, sedimentology, componentry, and geochemistry

### 2.1. Introduction

Reconstructing the eruptive history is a critical step for assessing the potential hazard of volcanoes. Once determined, the eruptive history can provide valuable information to constrain the volcanic hazard of future eruptions (e.g., [Brown and Branney, 2004](#); [Platz et al., 2007](#); [Prambada et al., 2016](#)). The reconstruction of eruptive history requires an understanding of the characteristics of eruption products in a robust stratigraphic framework to reconstruct the evolution of eruption styles of an active volcano (e.g., [Cronin et al., 2013](#); [Dávila-Harris et al., 2013](#); [Prambada et al., 2016](#); [Jordan et al., 2018](#); [Harijoko et al., 2021](#)). In this context, observing the successive sets of volcanic products in a comprehensive stratigraphic order can provide a record on the evolution of eruptive activity, especially when a volcano has undergone various eruptions intercalated by repose periods (e.g., [Abdurachman et al., 2000](#); [Gertisser et al., 2012](#); [Pistolesi et al., 2015](#); [Patrick et al., 2020](#)). Such information is necessary for reconsidering volcanic hazards and risk management of future eruption scenarios and cannot be acquired solely from time-limited historical records.

Kelud is considered one of the deadliest volcanoes in Indonesia due to the frequent eruptions (once every ~10 years) and its proximity to densely populated areas ([Bourdier et al., 1997](#); [Jeffery et al., 2013](#); [Goode et al., 2019](#)). The historical records of Kelud show variable eruptions since 1000 C.E., with frequently occurring explosive eruptions over the last century ([Kusumadinata, 1979](#); [Santosa and Atmawinata, 1992](#); [Goode et al., 2019](#); [Hidayati et al., 2009](#); [Maeno et al., 2019b](#)). However, in most cases, the records remain fragmentary and are limited

only to brief documentation of the eruption types based on local narrative records (i.e., explosive or non-explosive; [Hadikusumo, 1974](#); [Kusumadinata, 1979](#)). Although the eruptive history of Kelud has been studied over the last 30 years, the previous research predominantly focused the observations on the most recent eruptions (i.e., 1990, 2007-2008, and 2014; [Bourdier et al., 1997](#); [Thouret et al., 1998](#); [Hidayati et al., 2009](#); [Jeffery et al., 2013](#); [Goode et al., 2019](#); [Hidayati et al., 2019](#); [Maeno et al., 2019a](#)). The lack of detailed information on historical eruptions, such as stratigraphy, eruption type, and the emplacement processes of the deposits, especially pre-1900 C.E., makes the hazard assessment at Kelud poorly constrained. This study aims to reconstruct the eruptive history of Kelud volcano and to investigate the temporal variation of eruptive style and frequency that have occurred in the past millennium. In this contribution, I present the first detailed stratigraphical records combined with sedimentological, geochronological, geochemical, and componentry results of the volcanic products from the last 1300 years of activity of Kelud. In particular, I hope this work will provide insight for further hazard assessment at Kelud volcano.

## **2.2. Geological framework and previous work**

The Kelud volcano is a hinge-like stratovolcano with a crater lake manifestation located in East Java, Indonesia (Fig. 2.1). With a height of 1,731 m.a.s.l. (meter above sea level), it has developed above the Kawi-Butak Formation ([Hadikusumo, 1974](#); [Santosa and Atmawinata, 1992](#)). The succession of Kelud is mainly composed of basaltic-andesite to andesite products ( $\text{SiO}_2$  ranges from 53 to 57 wt.%) with calc-alkaline affinity, typical of subduction-related stratovolcanoes ([Bourdier et al., 1997](#); [van Bergen et al., 2000](#); [Jeffery et al., 2013](#), [Kadarsetia, 2016](#)). The activity of Kelud began in the Middle Pleistocene and has been subdivided into two main groups: 1) Old Kelut Group; and 2) Kelut Group ([Wirakusumah, 1991](#); [Santosa and Atmawinata, 1992](#)). The Old-Kelut Group (<238 ka) comprises basaltic to andesitic lavas and pyroclastic deposits (dominated mainly by ignimbrite) that are widely distributed on the

northwest-southeast flank. This group includes the parasitic activity from Kramasan (99 k.a.) and Umbuk (39 k.a.) cones that produced lava flows and pyroclastic flows (Santosa and Atmawinata, 1992; Zaennudin et al., 1992). The oldest volcanic product that can still be observed is the remnant of lava domes in the crater area (i.e., Lirang, Kelud, and Sumbing; Fig. 2.1), which indicates the clockwise shifts of the eruption center during the evolution of Kelud volcano (Wirakusumah, 1991; Santosa and Atmawinata, 1992; Kadarsetia, 2016; Goode et al., 2019).

The activity related to the Kelut Group started in the Holocene and continues to this day, consisting of the Badak I, Badak II, and Kelud Formations (Wirakusumah, 1991). These units resulted from activity that produced pyroclastic density currents (PDCs) and lava dome. In most cases, the PDC deposits were emplaced along the main rivers on the western flanks, such as Konto, Ngobo, and Sumberagung (Fig. 2.1B; Hadikusumo, 1974; Bourdier et al., 1997). According to Wirakusumah (1991) and Zaennudin et al. (1992), the youngest activity of Kelud volcano that produced the Kelud Formation was estimated to have occurred since 4 ka and includes the products from historical eruptions.

The most recent historical activity of Kelud (Fig. 2.1C) denotes variable volcano explosivity indexes with transitions from VEI 4-scale Plinian eruptions (1901, 1919, 1951, 1966, 1990, and 2014) to smaller-scale lava dome growth (Goode et al., 2019; Hidayati et al., 2019; Maeno et al., 2019a;). These eruptions often produced devastating lahars, which have caused the highest number of fatalities according to local Kelud historical records (Thouret et al., 1998; Manville, 2015; Hidayati et al., 2019). A pyroclastic eruption in 1919, for instance, caused about 5000 casualties after the eruption triggered the emplacement of lahar deposits (Sudradjat, 1991). Similar cases also occurred in 1951, 1966, and 1990, causing a total of 250 casualties (e.g., Kusumadinata, 1979; Thouret et al., 1998). The activity continued in 2007 when a new lava dome emerged that caused a temperature increase and shrinkage of the crater lake (Hidayati et al., 2009; Jeffrey et al., 2013). The latest eruption occurred seven years later in early 2014, and

was initiated by the destruction of the 2007–2008 dome, followed by the generation of a climatic Plinian column reaching the stratosphere (GVP, 2014; Goode et al., 2019; Hidayati et al., 2019; Maeno et al., 2019a).

Despite the extensive observations of the witnessed eruptions, the stratigraphic records on Kelud Formation, especially older than 1000 C.E., are entirely unknown. To fill this gap, this chapter focuses on the late-Holocene activity of Kelud, extending stratigraphic records of the Kelud Formation through 1300 years ago.

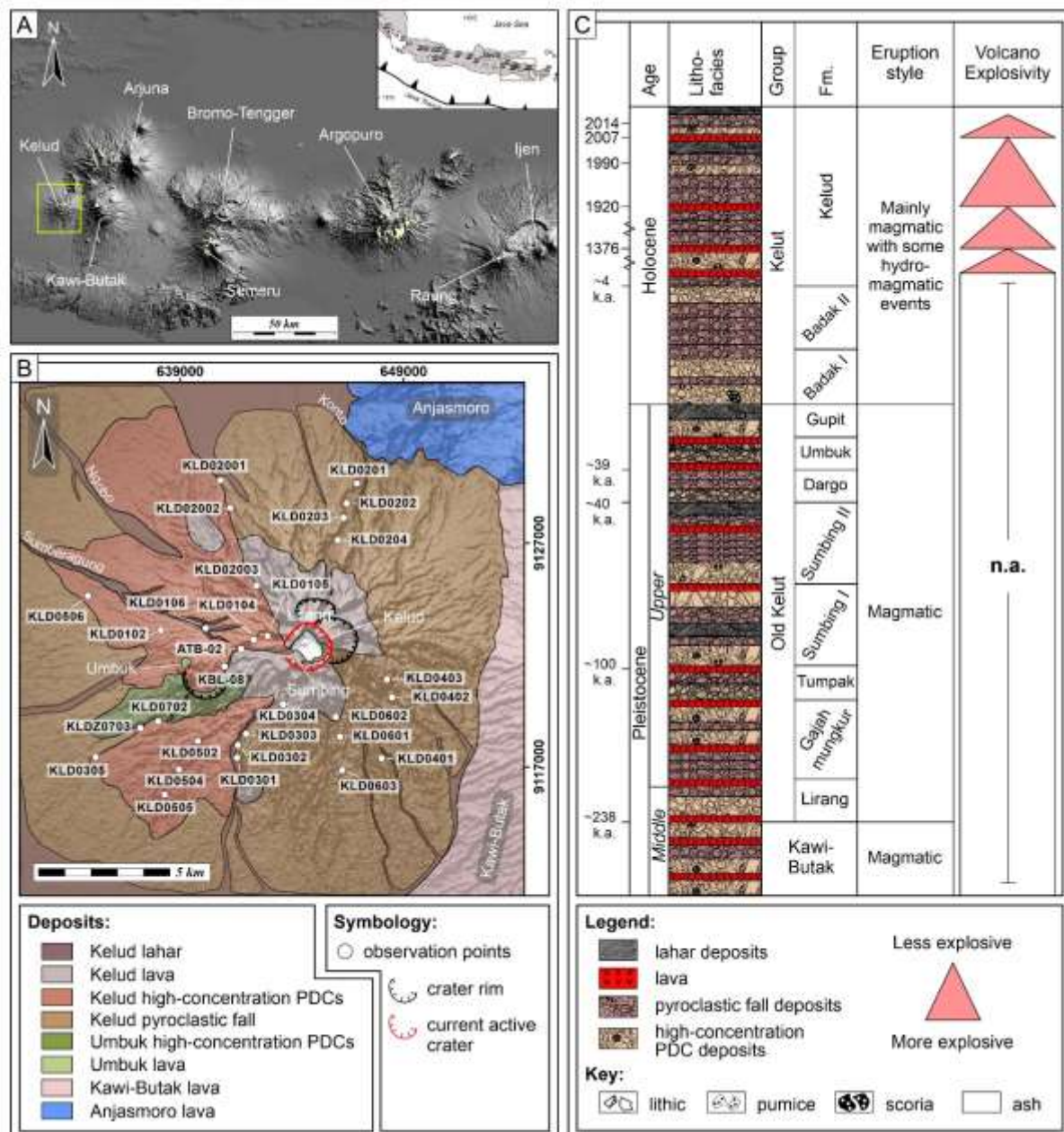


**Figure 2. 1.** A) Maps showing the distribution of volcanoes along Sunda arc in eastern Java, Indonesia, including the Kelud volcano. B) The geological map of Kelud volcano (modified after Santosa and Atmawinata, 1992; Zaennudin et al., 1992). The volcano is covered by a volcanic succession of lava, pyroclastic, and lahar deposits. C) Simplified stratigraphic section of the studied area coupled with volcanic activity from identified eruption sets (compiled from Hadikusumo, 1974; Kusumadinata, 1979; Wirakusumah, 1991; Santosa and Atmawinata, 1992; Bourdier et al., 1997; Jeffrey et al., 2013; Goode et al., 2019; Maeno et al., 2019a; and Maeno et al., 2019b).

## 2.3. Materials and methods

### 2.3.1. Field observations

Volcanic products were observed and logged from accessible exposures at the type locality (Fig. 2.1B). Following the criteria of Fisher and Schmincke (1984), each *bed-set* (informal name for a *Member* in a defined *Formation*; Lucchi, 2013) is separated according to the presence of organic-matter-rich layer or variation in primary bedforms and sedimentary discontinuities (i.e., erosion surfaces), which suggest a quiescent time of eruptive activity. The lithofacies were then classified following the non-genetic and non-stratigraphic schemes used by Sulpizio et al. (2007) and Macorps et al. (2018) based on visual inspection of primary sedimentary structures, grain-size range, and textures of the volcanic products (e.g., White and Houghton, 2006; Table 2). The lithofacies classification is subsequently used to determine an eruption unit composing each *bed-set* representing the emplacement of individual fallout or PDC. Furthermore, the association of single or multiple-eruption units is referred to as an eruption episode.

The distributions of PDC deposits are firmly controlled by the topography of the volcanic edifice. They are mainly concentrated on the western flank of Kelud, where the opening of the horseshoe-shaped crater occurs. Ten key sections (ATB-02, KBL-08, KLD0102, KLD0104, KLD0105, KLD0106, KLD0402, KLD0502, KLDZ0703, and KLD0702) were used to correlate different volcanic products and to reconstruct the representative stratigraphic section (Fig. 2.2). The maximum pumice clast size (MP) and maximum lithic clast size (ML) represent the average diameter of the 20 largest measured juvenile clasts (pumice and scoria clasts) and lithic clasts, respectively (e.g., Bonadonna et al., 2013; Jordan et al., 2018). The observation points are presented in UTM coordinates adapting WGS Datum 1984 southern hemisphere.

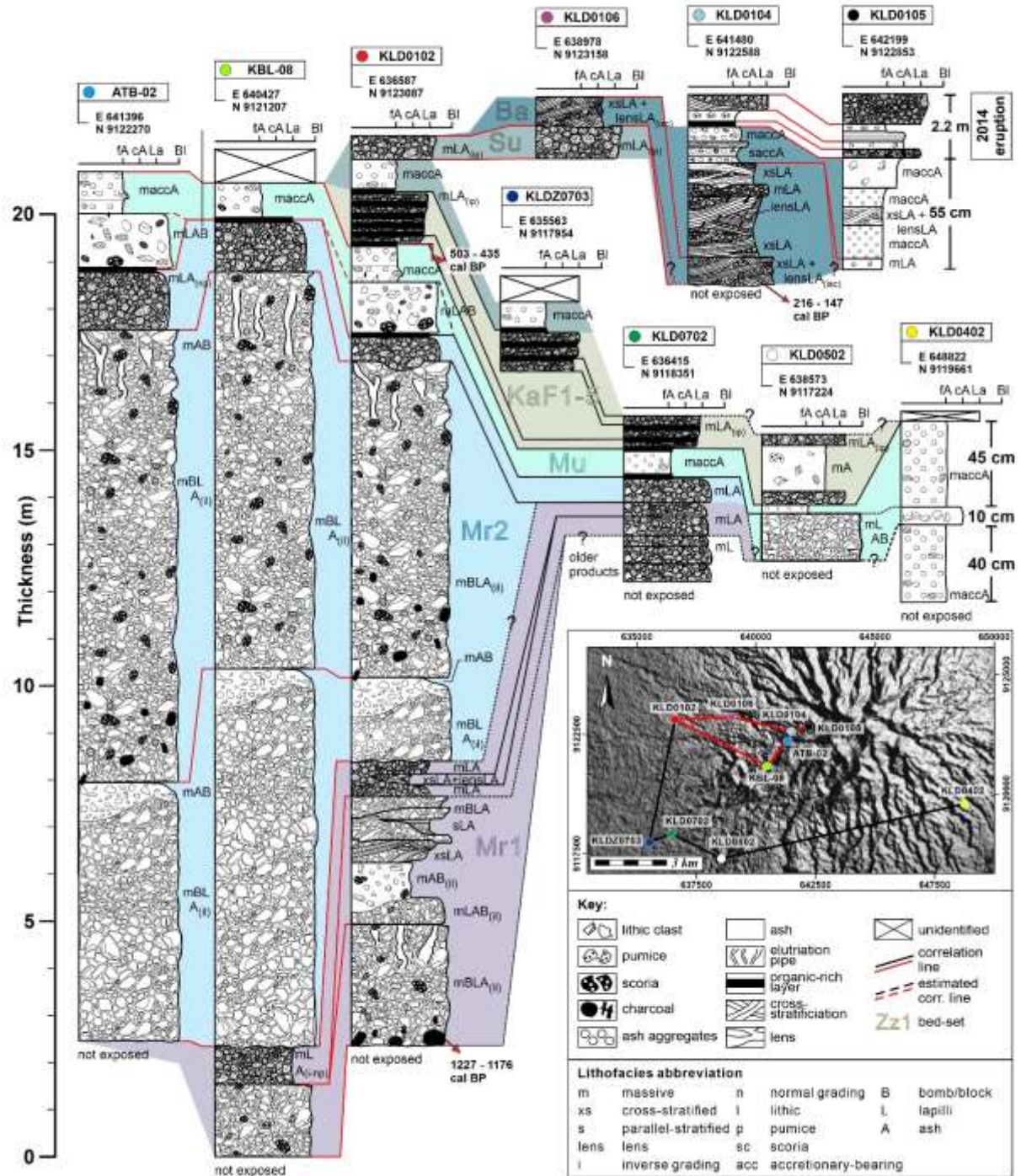


**Figure 2.** Correlation of selected ten representative stratigraphic logs combined with lithofacies abbreviation of each bed-set. These sections are illustrated based on the different scale and lateral variations of each eruption unit. The UTM coordinates of stratigraphic log are coupled beneath each observation point.

### 2.3.2. Radiocarbon dating

Three charcoals and carbonized organic matter clasts were collected for radiocarbon age determination. The measurement of  $^{14}\text{C}$  concentration was carried out at the High-sensitive Accelerator Mass Spectrometry Center of Yamagata University, Japan, preceded by Acid-Alkali-Acid (AAA) treatment. The sterilized samples were then converted into graphite from  $\text{CO}_2$  using catalysis. The carbon isotopic ratio  $\delta^{13}\text{C}$  (‰) was used for correcting the isotope fractionation to acquire  $^{14}\text{C}$  ages. The  $^{14}\text{C}$  ages were calibrated using OxCal v4.4.4 software (Ramsey, 2017) by applying the IntCal20 (Reimer, 2020) atmospheric curve dataset (Table 2.1).

**Table 2. 1** Summary of radiocarbon dating results from designated charcoal and carbonized matter.

Relative age (Bedset-Layer)	Sample ID	Organic matter type	$\delta^{13}\text{C}$ (‰)	Radioactive carbon age (yr BP $\pm 1\sigma$ )	Cal. $^{14}\text{C}$ age (% probability)	
					1 $\sigma$	2 $\sigma$
Mr1-Layer1	KLD0102.5	Charcoal	-27.17 $\pm$ 0.49	1300 $\pm$ 20	1280 - 1262 cal BP (24.2%)	1288 - 1242 cal BP (44.1%)
					1208 - 1179 cal BP (44.1%)	1227 - 1176 cal BP (51.3%)
KaF1-Layer1	KLD010106	Carbonized matter	-21.54 $\pm$ 0.42	388 $\pm$ 20	496 - 456 cal BP (60.2%)	503 - 435 cal BP (75.5%)
					349 - 340 cal BP (8.0%)	360 - 330 cal BP (20.0%)
Ba-Layer1	KLD0105	Charcoal	-29.32 $\pm$ 0.45	204 $\pm$ 20	292 - 275 cal BP (21.3%)	298 - 266 cal BP (27.9%)
					207 - 200 cal BP (6.2%)	216 - 147 cal BP (58.6%)
					186 - 152 cal BP (40.8%)	22 cal BP (8.9%)

### 2.3.3. Componentry and chemical analysis

Componentry and chemical analysis were conducted using several instruments at the Faculty of International Resource Sciences, Akita University, Japan. For ash componentry, a total of 27 samples from selected horizons were sieved with 1 phi interval (from -1 to 4) and then dried overnight at 60°C after being cleaned and purified using an ultrasonic cleaner. The component analysis for fraction of  $-1 < \phi < 2$  was performed under a binocular microscope, while the

fraction of  $2 < \phi < 4$  was carried out on polished thin sections under transmitted light and electron microscopes. The volcanic products were classified into several types based on their surface and physical appearance (e.g., color and texture; Macorps et al., 2018). The componentry was quantified by point counting, with a minimum of 500 grains counted for each fraction (i.e., Macorps et al., 2018; Heinrich et al., 2020). The morphological and textural observations were conducted using a JEOL JSM-IT300LV scanning electron microscope (SEM) operated at 15 kV accelerating voltage and 2.2 nA beam current. Whole-rock compositions were acquired from multiple juvenile lapilli of 25 selected horizons. The major element concentrations were measured using a Rigaku ZSX Primus II X-ray fluorescence (XRF) spectrometer.

#### **2.4. Stratigraphy of the deposits**

Volcanic products of the last 1300 years are well-preserved in a 32-m-thick composite stratigraphic section that is subdivided into 10 bed-sets based on their stratigraphic position (Fig. 2.3). I identified four main components within each bed-set (see Table 2.3 for the detailed description of each clast subdivision): (i) subrounded dark brown to yellow-colored, dense to highly vesicular fresh volcanic glasses are considered as juvenile fragments derived from the erupting magma; (ii) lithic fragments, which are angular, dense to slightly vesicular volcanic clasts are identified as fragments derived from erosion of previously existing dome or lava plug by their oxidized or hydrothermally altered appearances; (iii) free crystals derived from volcanic fragments of type (i) or (ii); and (iv) accessory clasts, consisting of rounded or elongated moss-like aggregates of type (i), (ii), or (iii). The proportion of each component for every studied sample is presented in Fig. 2.4.

The following sections describe each bed-set based on the stratigraphic order, covering the sedimentological characteristics, clast componentry, and the assigned lithofacies classifications (Table 2.2). Unless specified below, each studied bed-set contains juvenile components;

vesicular fluidal clasts, blocky clasts with thick melt film, and blocky vesicular clasts with concave edges (Table 2.3; Figs. 2.6A–H and N–P). On the other hand, the lithic fragments in the bed sets are blocky clasts with stepped surfaces (Table 3; Figs. 6Q and R).

#### 2.4.1. Margomulyo 1 bed-set

The Margomulyo 1 bed-set (Mr1) is the oldest bed-set observed in this study, with unknown basal contact due to the limited exposure of the outcrop (Figs. 2.2 and 2.3). The Mr1 consists of four layers with distinct sharp contacts in between and are distributed mainly to the west of the study area (Figs. 2.2 and 2.5). Layers 1–3 commonly fill the topographic lows, whereas layer 4 occurs mantling the paleo-topography. Layer 1 is the thickest and coarsest grained in the Mr1 bed-set. The thickness varies from >3.1 m to >1.5 m at 3 km (KBL-08) towards 6 km (KLD0102; Figs. 2.2 and 2.4), with a maximum outreach of ~10 km away from the eruption vent. Layer 1 comprises a massive, inverse-graded, poorly to moderately sorted, grey to reddish-grey lithic breccia, with a fine lapilli and coarse ash matrix (mBLA(il) lithofacies; Figs. 2.5B–C; Table 2.2). The fragments are angular to subrounded blocks and lapilli of dense lithics with minor subangular pumice and scoria clasts, while the matrix (~35 vol.%) comprises fine lapilli to coarse ash of angular lithic, pumice, scoria, and crystals. Elutriation pipes (~12–22 cm width) are visible at the top of the deposit, which often deform the overlying beds (Fig. 2.5E). Radiocarbon dating of ~22-cm-long charcoal within layer 1 yielded an age of 1.3–1.1 cal. ka B.P. (Table 2.1).

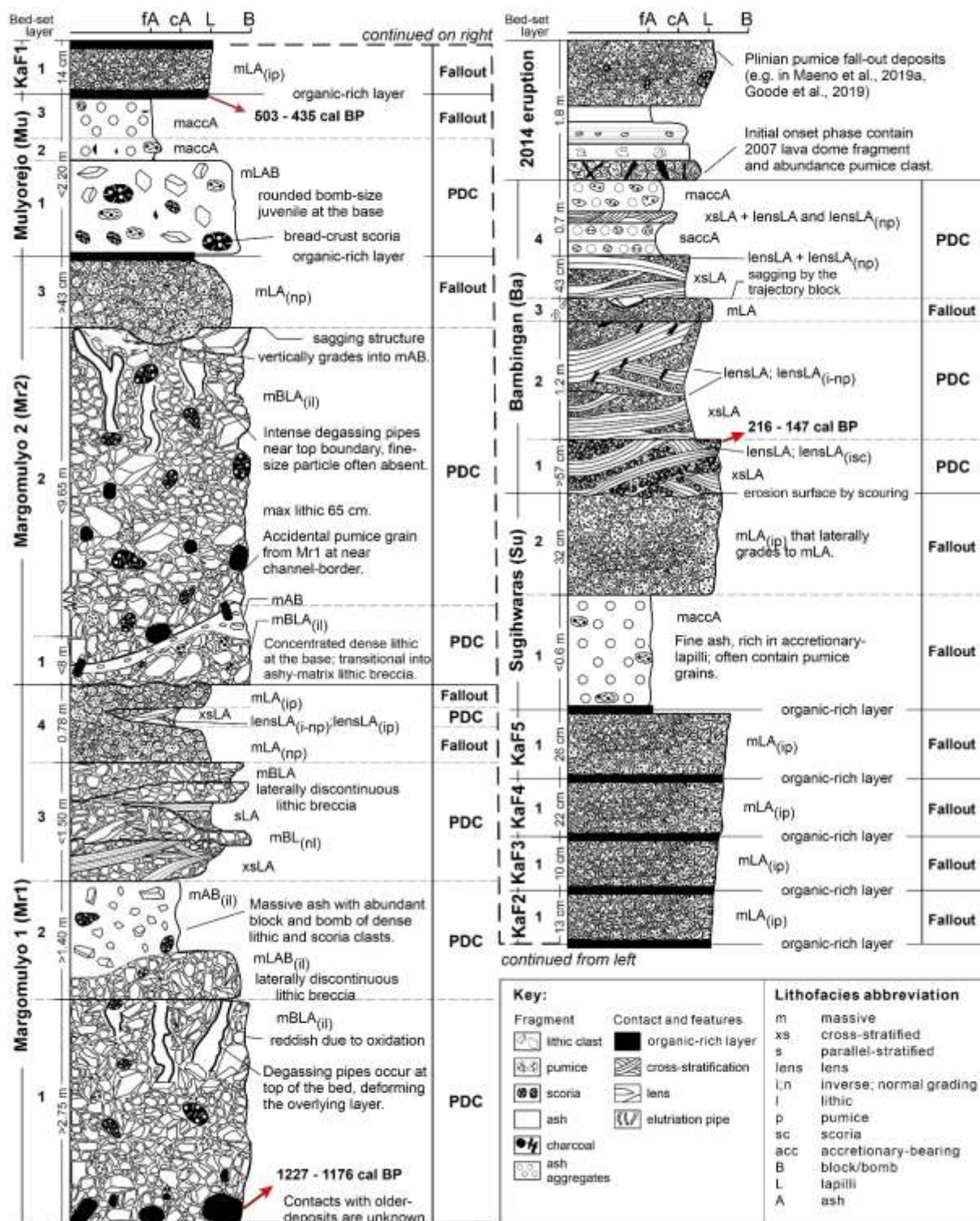


Figure 2. 3. Generalized composite stratigraphy coupled with the assigned lithofacies abbreviations of Kelud products. Red arrow shows the sampling horizon for age determination. Note different scales of each eruption unit.

**Table 2. 2.** Summary of description and interpretation of common lithofacies of Kelud's volcanic products. Modified from Sulpizio et al. (2007) and Macorps et al. (2018). See the text for detailed explanations.

Lithofacies	Description	Interpretation	Corresponding figure
<i>Massive lithofacies</i>			
mBLA <sub>(il)</sub> , mBLA <sub>(nl)</sub> , mBL <sub>(nl)</sub> , mLAB <sub>(il)</sub> .	Massive block, lapilli and ash with inverse grading of lithic clasts (mBLA <sub>(il)</sub> ), sometimes with normal grading (mLA <sub>(nl)</sub> ), massive block and lapilli (mBL), and massive lapilli ash with abundant block (mLAB) that sometimes show inverse grading of lithic clasts (mLAB <sub>(il)</sub> ). Generally filling topographic lows, very thick beds, massive, and moderate to poor sorting. They have variable proportions of subrounded pumice lapilli with subordinate scoria and lithic lapilli in a glassy and crystal-rich matrix. mBL <sub>(nl)</sub> may grade laterally into mBLA <sub>(nl)</sub> . Clasts are dominated by lithic (ML=65 cm) and vesicular juvenile fragments (MP=28 cm) with abundant charcoal fragments.	The general massive and poorly sorted appearance indicates the progressive aggradation of a high-concentration current at a granular-flow boundary zone. The inverse grading of lithic blocks indicates particle segregation of the largest clast due to kinetic sieving and kinematic squeezing in flow-boundary zones. Various clast components represent the mixture of multi-component of the high concentration current that may be derived from erosion of a conduit wall or removal of dome material from vulcanian explosions or substrate-scoured during transportation.	Figs. 2.2, 2.3, and 2.5A–E.
mAB, mAB <sub>(il)</sub>	Massive ash with significant block (mAB), sometimes with inverse grading of lithic clasts (mAB <sub>(il)</sub> ). Some vertically grading from mBLA <sub>(il)</sub> or mLAB <sub>(il)</sub> . Massive, medium to thin bed, poorly sorted, and matrix-supported of coarse to fine ash. Clasts are angular dense lithic (ML=14 cm) and scoria (MP=21 cm). Vertically and laterally graded from mBLA <sub>(il)</sub> and mLAB <sub>(il)</sub> lithofacies.	Fine ash is deposited by gentle settling from the ash cloud. Fine clast could also be elutriated from the high-concentration basal current within fluid escaped-dominated flow boundary zone.	Figs. 2.2, 2.3, and 2.5A–C
mA, mLA, mLA <sub>(np)</sub> , mLA <sub>(ip)</sub>	Massive ash (mA), massive lapilli and ash (mLA), sometimes with normal grading (mLA <sub>(np)</sub> ) or inverse grading of pumice clasts mLA <sub>(ip)</sub> . Generally mantling the topography, thin to medium beds with massive, clast-supported, and well-sorted features. The mLA facies has variable proportions of subrounded pumice lapilli	Well sorted and framework-supported pumice lapilli resulted from the direct fallout from an umbrella cloud. Generally thin to medium bed thicknesses and lack of accidental clasts indicates a short-lived explosion and a stable vent system with less erosion or widening features.	Figs. 2.2, 2.5A–E, 2.7A,B,E, and 2.8A.

	with subordinate scoria (MP=2.4 to 6.2 cm) and lithic lapilli (ML=1.4 to 5.1 cm) in a glassy and crystal-rich matrix. Along the distance, mLA may laterally grade into mA.		
maccA	Massive, accretionary-lapilli-bearing ash. Mantling bed of massive and poorly sorted fine ash with accretionary lapilli. Can be found mantling the topography or filling the topographic low; ash aggregates, subrounded vesicular juvenile (pumice and scoria; MP=5.1 cm), and lithic (ML=4.5 cm) are evenly distributed within the beds.	Well-sorted nature indicates ash deposition directly from the umbrella cloud or lofted ash of diluted density current. Accretionary lapilli could indicate ash aggregation driven by electrostatic force or water droplets during the deposition.	Figs. 2.2, 2.3, 2.5A, 2.7A, C–D, and 2.8B.

*Stratified lithofacies*

xsLA	Cross-stratified lapilli and ash. Cm-thick low angle cross-stratification of lapilli and ash. The clast proportion varies from lithic-rich, pumice-rich, or scoria-rich, with a significant proportion of crystal ash. Maximum clast diameters are 1.7 cm and 3.8 cm for lithic and pumice, respectively.	Good sorting and cross-stratification indicate the deposits from a diluted PDC within the traction-dominated flow boundary zone; produced by current unsteadiness that records multiple truncations with the suspension and traction dominated the grain-by-grain deposition.	Figs. 2.2, 2.3, 2.5B, D, and 2.8A–C.
sLA	Stratified lapilli and ash (sLA). Generally show poor sorting of lapilli and ash deposit. Laterally grades from mBL <sub>(nl)</sub> and the stratification can be observed at a certain distance. Dominated by lithic clasts (ML=6 cm) with subordinate vesicular juvenile (MP=4.5 cm) and crystals.	The parallel stratification reflects the unsteady deposition of diluted PDC in the localized traction-dominated flow boundary zone.	Fig. 2.5C
saccA	Stratified, accretionary-lapilli-bearing ash; occurs as stacked successions of centimeters-thick and poorly sorted beds with variable thicknesses at the outcrop scale. Juvenile (MP=3.2 cm), lithic (ML=1.5 cm), and crystal clasts have almost similar proportions.	Gentle settling accumulation of ash from the phoenix cloud that accompanied the lowermost part of the PDCs. Similar to the maccA, accretionary lapilli could indicate fine ash aggregation driven by electrostatic force or water droplets during the deposition.	Figs. 2.3, 2.8A–B

*Lenticular lithofacies*

lensLA, lensLA <sub>(ip)</sub> , lensLA <sub>(i-np)</sub> , lensLA <sub>(isc)</sub> .	Lens of lapilli and ash (lensLA). Lenses of coarse lapilli and ash; coarse lapilli usually mark out the inverse (lensLA <sub>(ip)</sub> ) or inverse to normal grading of pumice	The discrete accumulation of clasts in the form of lenses is affected by continuous changes in the current condition at a flow boundary zone, resulting in	Figs. 2.5B, D and 2.8A–C.
---------------------------------------------------------------------------------------	----------------------------------------------------------------------------------------------------------------------------------------------------------------------------------	------------------------------------------------------------------------------------------------------------------------------------------------------------	---------------------------

	clast (lensLA <sub>(i-np)</sub> ) or inverse grading of scoria clast (lensLA <sub>(isc)</sub> ). Cm-thick, well-sorted, and clast-supported lenses.	the clast entrapment and particle segregation of diluted density currents.	
--	-----------------------------------------------------------------------------------------------------------------------------------------------------	----------------------------------------------------------------------------	--

*Composite lithofacies*

xsLA + lensLA	An alternation of cross-stratified lapilli and ash (xsLA) with lens of lapilli (lensLA). Lenticular of inverse to normal-graded, well-sorted lapilli and ash deposits separated by cm-thick, stratified fine lapilli to ash beds. Clasts are dominated by lithic-rich, pumice-rich or scoria-rich with abundant free crystals.	The alternation of cross-stratified lapilli and ash with vertically graded lenses of lapilli and ash indicates accumulation from multiple pulses developed within the traction-dominated flow boundary zone. The lens facies record grain-by-grain deposition of the basal part of each pulse, while stratified facies indicate a more dilute part of the uppermost current.	Fig. 2.5B, D, and 2.8A–C
---------------	--------------------------------------------------------------------------------------------------------------------------------------------------------------------------------------------------------------------------------------------------------------------------------------------------------------------------------	------------------------------------------------------------------------------------------------------------------------------------------------------------------------------------------------------------------------------------------------------------------------------------------------------------------------------------------------------------------------------	--------------------------

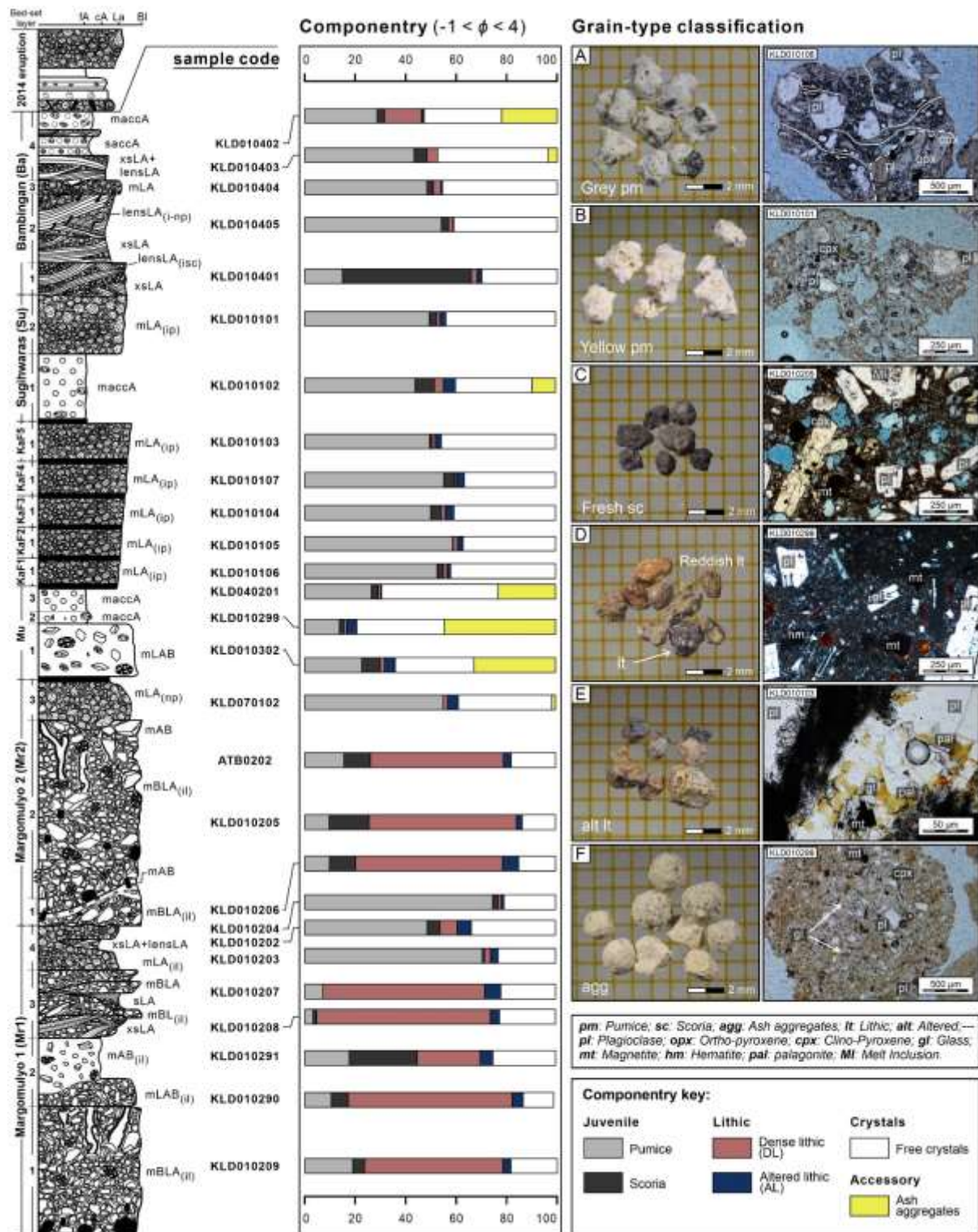


**Figure 2. 4.** Variation of relative component proportions ( $n > 3000$ ) and physical features of tephra from Kelud volcano. Sampling horizons are attached next to stratigraphic positions. m: massive, xs: cross-stratified, s: parallel-stratified, lens: lens, i: inverse grading, n: normal grading, l: lithic, p: pumice, sc: scoria, acc: accretionary lapilli-bearing, B: block/bomb, L: lapilli, and A: ash. The photographs show examples of volcanic ash observed under binocular and polarizing microscopy. Note that the light blue color is caused by the pigment color.

**Table 2. 3.** Classification and description of clast types used for component analysis in this study.

Type	Clast	Description	Morphology	Corresponding figures
Juvenile	Pumice	Translucent, glossy, fresh vesicular volcanic glass with a rough to moderately smooth surface. The clasts have two distinct appearances: grey pumice and yellow pumice. The phenocrysts consist of plagioclase, pyroxene, and glomerocrysts of plagioclase + pyroxene + Fe-Ti oxide.	Vesicular fluidal-shaped, vesicular angular-shaped, and poorly vesiculated fused-shaped clasts.	Figs. 2.4A–B and 2.6A–H
	Scoria	Dark brown vesicular to dense spheroidal fragments with a vitreous luster. Showing similar mineralogy to the pumice clasts.	Funnel-shaped, subrounded with moss-like texture cut by planar surface, and vesicular with concave edges.	Figs. 2.4C and 2.6M–P.
Lithic	Dense lithic	Sub-aphyric to aphyric, angular, dense, coherent fragments. Two types of dense lithic: dark grey lithic and reddish grey lithic. Porphyritic textures with plagioclase, clinopyroxene, and minor orthopyroxene. Reddish grey lithics exhibit brown to red staining due to the abundance of hematite.	Blocky with stepped fracture.	Figs. 2.4D and 2.6Q–R.
	Altered lithic	Brown to yellow, angular, dense volcanic fragments with a pervasive alteration. Display palagonitization of groundmass glass, indicating alteration caused by water.	Blocky with stepped fracture.	Fig. 2.4E.
Crystals	Free crystals	Millimetric to sub-millimetric isolated minerals of plagioclase, pyroxene, and <i>glomerocryst</i> of plagioclase ± clinopyroxene ± Fe-Ti oxide.	Blocky.	Figs. 2.6S–T
Accessory	Ash aggregates	Yellow with a dull luster, consisting of multiple fragments of fine ash particles. The ash aggregates are core-type and host lithics, pumice clasts, crystals, and glass shards.	Rounded or elongated moss-like.	Figs. 2.4F and 6I–L

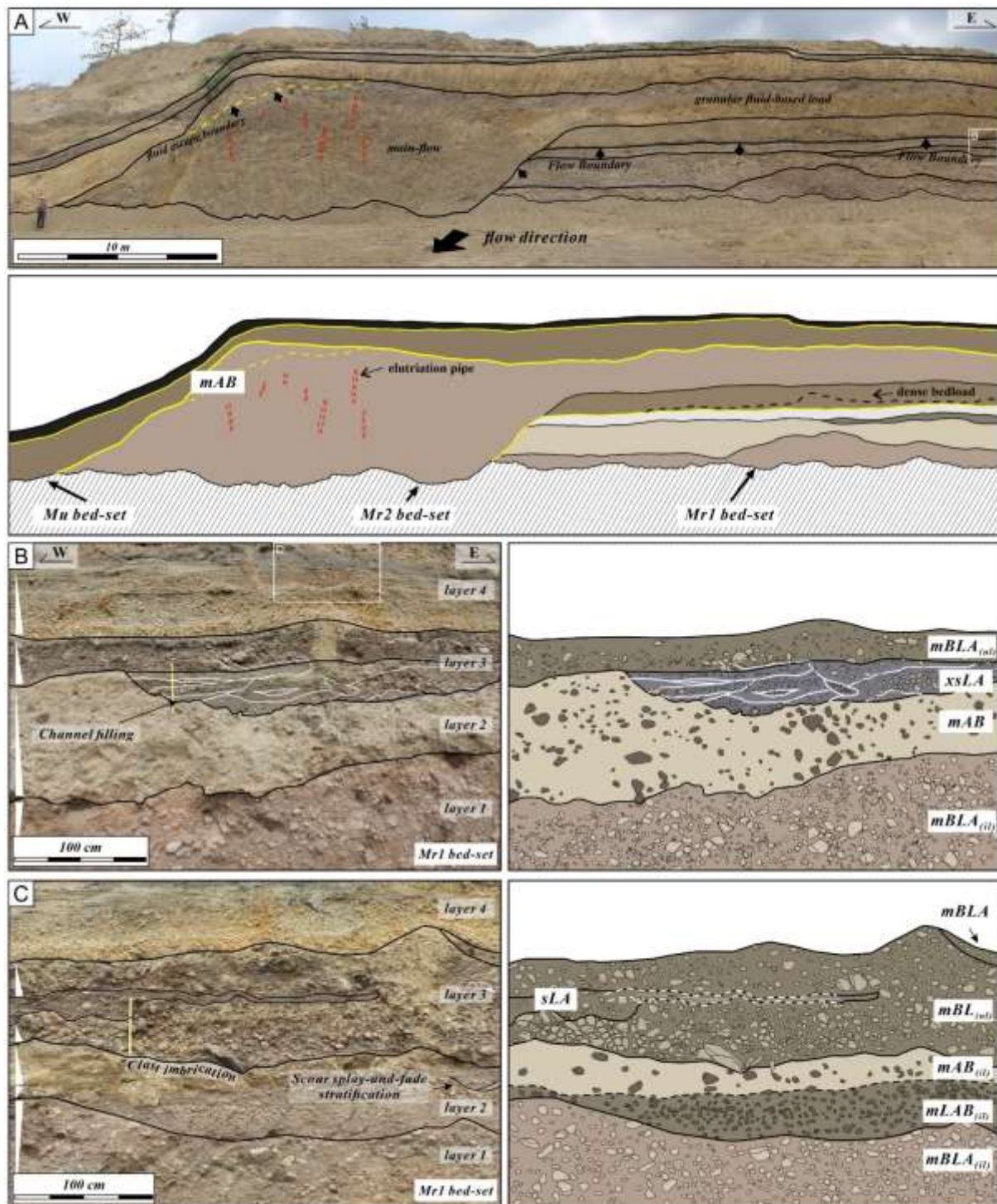


**Figure 2. 5.** Representative photos and illustrations of Kelud products showing A) strata and the relationship between Margomulyo 1, Margomulyo 2, and Mulyorejo bed-sets occurred in the field. B) to D) showing complex eruption units and facies association composing Margomulyo 1 bed-set. E). Elutriation pipes are visible at the top of the layer 1, which often occurs deforming the overlying beds. The yellow line represents each bed-set boundary, while the black line represents the layer boundary. The white triangles indicate the clast grading of lithic or juvenile clasts from the bottom to top of bed for each assigned lithofacies.

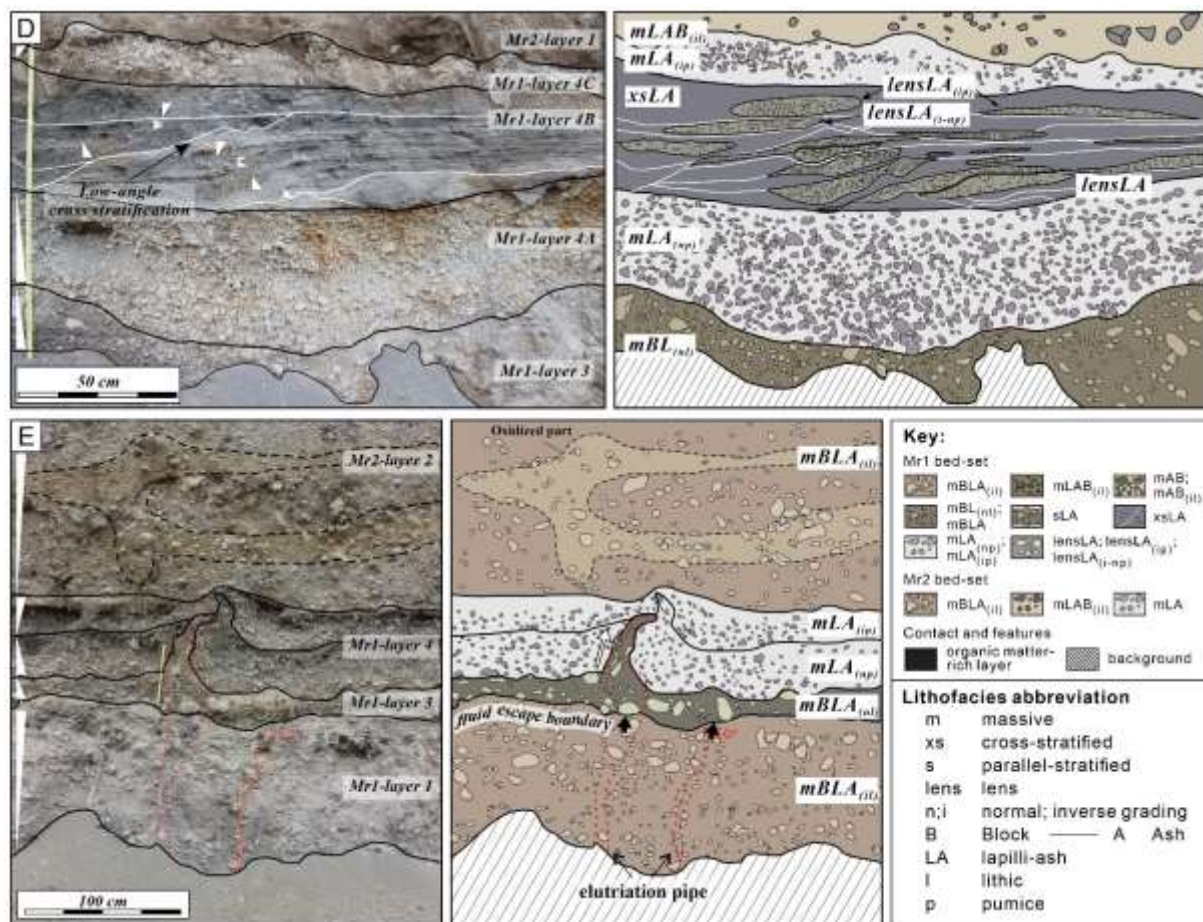


Figure 2. 5. (continued).

Layers 2 and 3 are up to 1.5 m thick beds, which are best seen at the Margomulyo section, 6 km away from the eruption vent (KLD0102; Figs 2.2 and 2.5B–C). Layer 2 consists of massive, grey, inverse-graded, moderate to well-sorted lithic lapilli and block, with a fine ash matrix (mLAB<sub>(il)</sub>) that vertically grades to massive, well-sorted ash with abundant blocks, which locally shows a scour splay-and-fade stratification and normal grading of lithic clasts (mAB and mAB<sub>(nl)</sub>) lithofacies; Figs. 2.5B–C). The fragments are composed of subangular to subrounded lithic, pumice, and scoria clasts with angular lithic, scoria, crystals, and minor pumice fine ash matrix (~15–20 vol.%). Layer 3 comprises massive to stratified, grey, normal-graded, clast-supported, poorly to moderately sorted lithic breccia, with a fine lapilli and coarse ash matrix (mBLA<sub>(nl)</sub>) and sLA lithofacies; Figs 2.5B–C; Table 2.2) that lies over a cross-stratified, well-sorted lapilli and ash bed (xsLA lithofacies; Figs 2.5B; Table 2.2). At the base,

layer 3 shows an imbrication of dense lithics (up to 39 cm in diameter; mBL<sub>(nl)</sub> lithofacies) that gradually becomes scattered toward the upper part. Laterally, layer 3 grades to massive breccia with abundant ash (mBLA lithofacies; Fig. 5C; Table 2.2), consisting of lithic and subordinate pumice clasts within a lithic- and crystal-rich ash matrix.

Layer 4 comprises three sub-layers that consist of up to 78-cm-thick mantling beds of two massive, normal- to inverse-graded, well-sorted, and clast-supported lapilli and ash deposits (mLA<sub>(np)</sub> and mLA<sub>(ip)</sub> lithofacies; Table 2.2), which are separated by cross-stratified, clast-supported, moderate to well-sorted lapilli and ash deposit (millimeter to centimeter strata; bed 4B, xsLA+lensLA lithofacies; Figs. 2.5C–D). Beds 4A and 4C have fragments of pumice, scoria, and lithic lapilli within crystal-rich ash matrices (~10–15 vol.%). In contrast, layer 4B is dominated by fine lapilli and ash of pumice, crystals, and subordinate lithic fragments.

Ash componentry of layers 1 to 3 predominantly consists of lithic clasts (52–72 vol.%) with subordinate juvenile and crystals (Fig. 2.4). The clast contents show a similar proportion through the stratigraphic position, as observed in lithofacies mBLA<sub>(il)</sub>, mLAB<sub>(il)</sub>, xsLA, and sLA. In mAB lithofacies, however, a decrease in lithic is observed along with an increase in juvenile and crystal contents. Ash componentry of layer 4 shows a distinct proportion compared to layers 1 to 3, with juvenile clasts as the most abundant component, followed by subordinate lithics and crystals (Fig. 2.4). The relative abundance of the three components does not vary significantly among the mLA lithofacies and with the distance. However, the xsLA has slightly higher lithic and crystal components compared to mLA lithofacies.

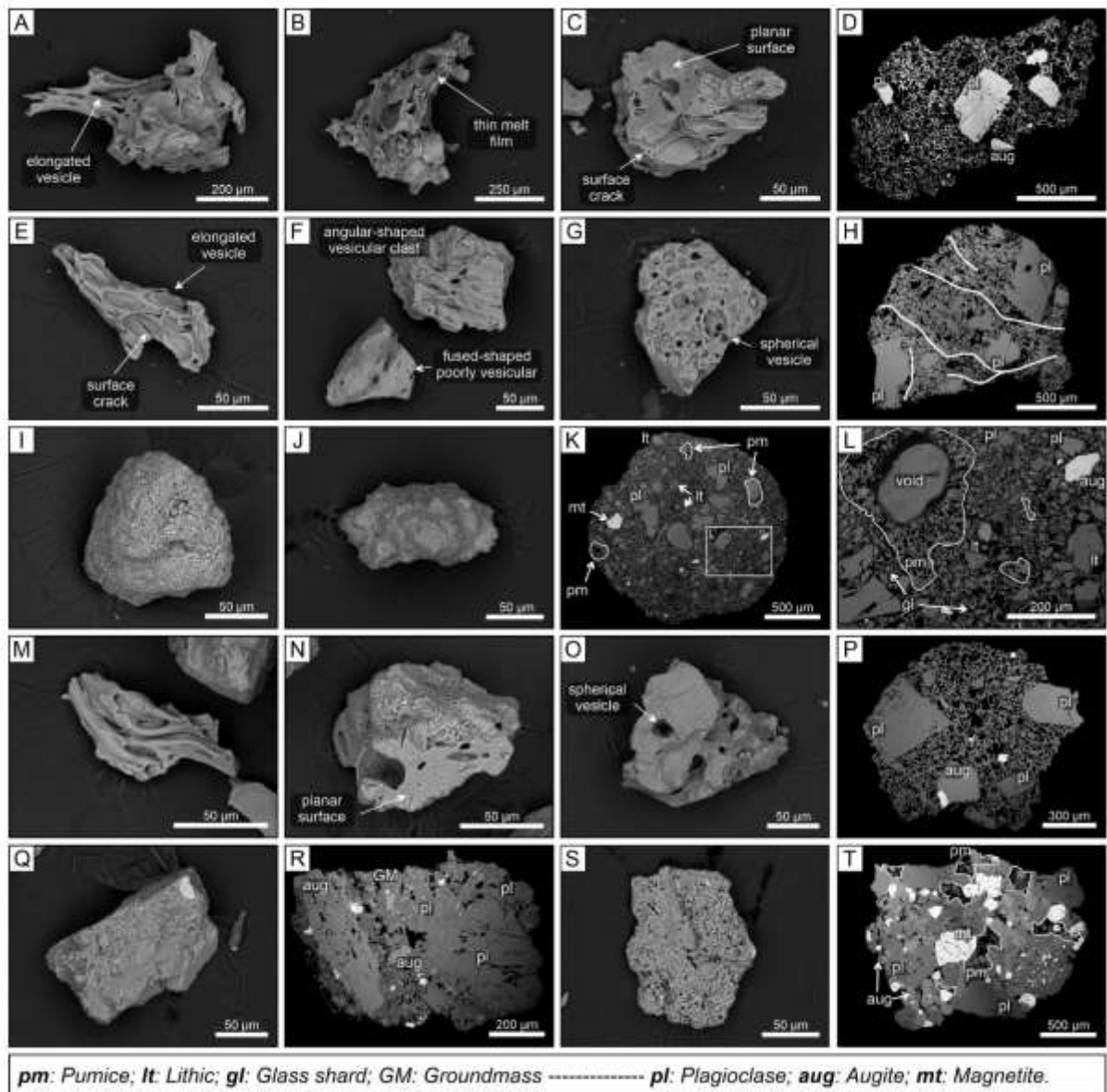


**Figure 2. 6.** SEM back-scattered images of low-crystallinity juvenile fragments from non-accretionary lapilli-bearing ash layers (A–D; M–P) and accretionary lapilli-bearing ash layer (E–H). Pumice of non-accretionary lapilli bearing layers mainly have A) fluidal shape with elongated vesicles and B) thin melt film clasts, although minor C) subangular clasts with thick melt film sometimes observed. D) Show bubble nucleation and coalescence features. Similarly, the accretionary-lapilli bearing layer also preserves various pumice morphology, including E) fluidal-shaped vesicular with thick wall, F) angular shape vesicular clast cut by a planar surface, and fused-shaped clasts. Most of the angular pumice clasts preserve G) abundant spherical vesicle with H) intensive micro-deformation due to high-intensity bubble nucleation. I–K) Present typical round and elongated morphologies of ash aggregate with moss-like surface. L) Closer look at core-type ash aggregates hosting multiple juvenile clasts, crystals, and lithic fragments. M–P) Presents typical high vesicularity and less-deformed scoria clast. Q) Represents blocky morphology of R) typical porphyritic lithic fragment, containing plagioclase

and augite phenocrysts, while S) and T) shows typical angular crystals cumulates of plagioclase  $\pm$  augite  $\pm$  Fe-Ti oxide contained as a glomerocryst within pumice clasts. White lines and arrows refer to the area in which the vesicularity and vesicle orientations are contrast.

#### 2.4.2. Margomulyo 2 bed-set

The Margomulyo2 bed-set (Mr2) contains the thickest and coarsest pyroclastic deposits studied in this work. The Mr2 consists of three layers that are exposed in sections along the western flank of the volcano, which lies with an erosive basal contact over pumice deposits of the Mr1 bed-set (Figs. 2.2 and 2.4A). Layers 1 and 2 commonly fill the topographic lows, whereas layer 3 shows mantle bedding structure (Figs. 2.3 and 2.4). Layers 1 and 2 have variable thicknesses of  $>7.5$  m at 3 km (KBL-08) that decrease to 1.7 to 7 m thick towards 6 km (KLD0102; Figs. 2.2 and 2.4), with a maximum outreach  $\sim 13$  km away from the eruption vent. Both layers 1 and 2 comprise a massive, inverse-graded, poorly to moderately sorted, grey to reddish-grey lithic breccia, with a fine lapilli and ash matrix (mBLA<sub>(il)</sub>) that vertically grades to massive ash with abundant block fragments (mAB lithofacies; Figs. 2.2 and 2.4A; Table 2.2). The fragments are angular to subrounded blocks and lapilli of dense lithic with minor subangular pumice and scoria clasts, while the matrix contains angular lithic, pumice, scoria, and crystals fine lapilli to coarse ash ( $\sim 20$ – $25$  vol.%). Elutriation pipes ( $\sim 15$ – $20$  cm width) are visible in the upper part of layer 2 (Fig. 2.4A).

Layer 3 has a sharp basal contact and locally shows sagging structures containing a higher concentration of large clasts (9 cm average, up to 14 cm), where it overlies layer 2 (Fig. 2.3). Layer 3 is up to 52-cm-thick at southwest exposures (i.e., KBL08 and KLD0102; Fig. 2.2) and comprises a massive, normal-graded, well-sorted, and clast-supported bed of mostly crystal-rich pumice lapilli and ash (mLA<sub>(np)</sub> lithofacies; Table 2.2). The fragments are typically vesicular juveniles (pumice and scoria) and lithic lapilli, while the matrix ( $\sim 10$ – $15$  vol.%) consists of pumice, lithic, and crystals ash.

Ash componentry of the Mr2 bed-set is predominantly composed of lithic clasts (52–72 vol.%)

with subordinate juveniles and crystals (Figs. 2.4). The clast contents show a similar proportion through the stratigraphic position, as observed in mLAB<sub>(il)</sub> lithofacies of layers 1 and 2, although the juvenile and crystal components slightly increase in mAB lithofacies. Layer 3 shows a distinct proportion compared to other layers, with juvenile (56 vol.%) and crystal (38 vol.%) clasts as the most abundant component, followed by subordinate lithics (Fig. 2.4).

#### 2.4.3. Mulyorejo bed-set

The Mulyorejo bed-set (Mu) lies over a ~20-cm-thick organic-matter-rich layer developed on top of the Mr2 bed-set (Figs. 2.3 and 2.4). It consists of three layers with distinct sharp contacts in between and is exposed in sections along the northwest-southeast flank (Fig. 2.2). Layer 1 is a 0.8–1-m-thick bed and can be found filling the topographic depressions on stations of KLD0102 and KLD0502. It consists of a massive, moderately to poorly sorted yellow lapilli and ash deposit with abundant bombs (mLAB lithofacies; Figs. 2.4A and 2.6C; Table 2.2). The fragments are composed of subrounded juveniles and lithic lapilli, whereas the matrix comprises crystal and juvenile-rich fine ash (~65 vol.%). Layer 1 also exhibits breadcrust scoria clasts near the base, reaching 30 cm in diameter. Laterally, layer 1 grades to massive ash along the east direction, 4.5 km from the vent (Fig. 2.2).

Layers 2 and 3 are 0.2–0.4-m-thick mantling beds that can be observed up to ~8 km away from the eruption vent (KLD0702; Fig. 2.2). They consist of massive, poorly sorted yellow accretionary-lapilli-bearing ash (maccA lithofacies; Figs. 2.4A, 2.6A, and C–D; Table 2.2), containing fibrous charcoal fragments, pumice lapilli, and abundant multi-component ash aggregates of pumice clasts, lithics, and crystals (Fig. 2.7D). Lithic fragments are rare, but they occur as angular non-vesicular basalt. The matrix of layers 2 and 3 are dominated by crystal and juvenile-rich fine ash (~80 vol.%).

Ash componentry of Mu bed-set predominantly consists of juvenile clasts (18–28 vol.%) and isolated crystals (30–45 vol.%) with subordinate lithic clasts (Fig. 2.4). The juvenile and crystal

contents increase towards the stratigraphic position, coupled with a decrease in lithic. The thin bed of maccA lithofacies (layer 2), particularly, has significantly lower juvenile components than other layers.

#### 2.4.4. Bed-sets Karangrejo Fall1 to Karangrejo Fall5

Five bed-sets, KaF1 to KaF5, are separated by an intervening ~4 to 22-cm-thick black, well-sorted, organic-matter-rich layers with diffuse contacts (Figs. 2.3 and 2.6A–B). Each bed-set consists of a very thin (14–22 cm thick) mantling bed of massive, well-sorted lapilli and ash deposit (mLA<sub>(ip)</sub>) that laterally grades to massive ash along the distance (mA lithofacies; Figs. 2.5A–C; Table 2.2). The fragments are dominated by subrounded pumice lapilli (~85–90 vol.%) with subordinate scoria and lithic lapilli bounded in pumice and crystal-rich coarse to fine ash matrices. Ash componentry of mLA lithofacies of KaF1 through KaF5 show a similar clast proportion through the stratigraphic position and predominantly consist of juvenile clasts (44–58 vol.%) and crystals (33–42 vol.%) with subordinate lithic clasts (Fig. 2.4).

Carbon dating of carbonized organic matter in the KaF1 bed-set yielded an age of 0.5–0.4 cal. ka B.P. (Table 2.1), which approximately correlates with the deposits described by Wirakusumah (1991) at Ngobo and Sumberagung Stream (Fig. 2.1).

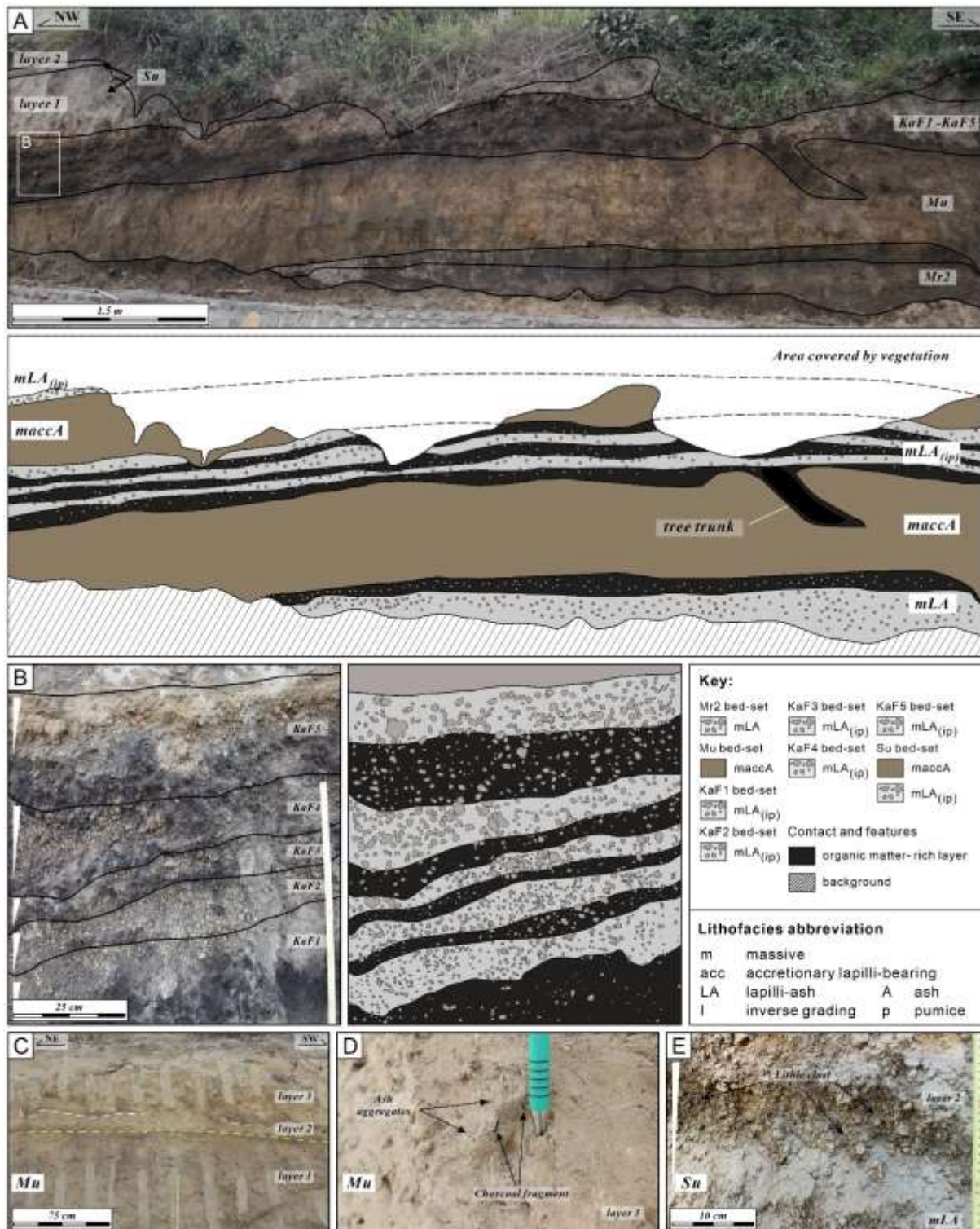


**Figure 2. 7.** Field photos and illustrations of Kelud products from Mr2 through Su bed-set. A). Showing vertical and lateral variations of tephra deposits can be observed on the field. Most of the deposits are covered by extensive vegetation. B) Detailed section displays the intercalation between the pumice-rich lapilli-ash and organic matter-rich layer of KaF1 through KaF5. C) Facies of maccA can be found as multiple layers that differ at type locality (i.e., KLD0102 and ATB-02), hosting D) ash aggregates and often contain fibrous charcoal fragments. E) Displays domination of lapilli-size pumice clasts along lithic fragments hosted in the mLA facies.

#### 2.4.5. Sugihwaras bed-set

The Sugihwaras bed-set (Su) lies with a sharp contact over ~8-cm-thick paleosol developed above the KaF5 bed-set (Figs. 3 and 7A). It consists of two layers that mantle the topography and are mainly exposed on the west to southwest flanks of the volcano (Fig. 2.2). Layer 1 is a 0.4 to 0.6-m-thick bed and cropped out mostly on the southwestern flanks of the studied area. It consists of massive, poorly sorted yellow accretionary-lapilli-bearing ash (maccA lithofacies; Figs. 2.3 and 2.7A; Table 2.2), containing juvenile (pumice and scoria) lapilli and abundant multi-component ash aggregates of pumice clasts, lithics, and crystals in a crystal and juvenile-rich fine ash matrix (~85 vol.%).

Layer 2 comprises a 0.3 m-thick massive, inverse-graded, well-sorted, and clast-supported bed of yellow lapilli and ash (mLA<sub>(np)</sub> lithofacies; Table 2.2). The fragments are typically vesicular juveniles (pumice and scoria) and lithic lapilli bounded in juveniles and crystals ash matrix (~15–20 vol.%).

Ash componentry of Su bed-set predominantly consists of juvenile clasts (52–57 vol.%) and isolated crystals (23–42 vol.%) with subordinate lithics (Fig. 2.4). The relative abundance of the three components does not vary significantly among the maccA and mLA lithofacies, although accessory ash aggregates occur in maccA lithofacies (12 vol.%). Juvenile ash particles exhibit variable morphologies, including vesicular fluidal-shaped clasts (Fig. 2.6E), subrounded clast with moss-like texture cut by planar surface (Fig. 2.6N), and subservient vesicular blocky clasts (Fig. 2.6G).

#### 2.4.6. Bambang bed-set

The Bambang bed-set (Ba) lies with an erosional contact over pumice deposit of Su bed-set and is best seen at the KLD0104 section, 2 km away from the eruption vent (Fig. 2.2). At its maximum thickness, the Ba bed-set comprises four layers with distinct sharp contacts in between. Layers 1, 2, and 4 commonly fill the topographic lows, whereas layer 3 shows typical

mantle bedding.

Layers 1 and 2 are the thickest and coarsest grain in the Ba bed-set. With a maximum outreach of ~4 km, layers 1 and 2 comprise stacked successions of 1.7-m-thick cross-stratified, clast-supported, moderate to well-sorted lapilli and ash deposits (xsLA lithofacies; Figs. 2.8A; Table 2). Each bed mostly shows normal grading, preserving lapilli and ash concentration zones in the form of lenses (lensLA lithofacies; Table 2.2). The lenses are 6 cm thick on average and primarily clast-supported, inversely graded, and consisting of pumice- and scoria-rich lapilli and ash. Radiocarbon analysis of a charcoal fragment of layer 1 yielded a  $^{14}\text{C}$  age of 0.2–0.1 cal. ka B.P. (Table 2.1).

Layer 3 lies with a sharp contact and locally shows block-sag over layer 2 (Fig. 2.8). It consists of a 20-cm-thick mantling bed of massive, well-sorted lapilli and ash deposit (mLA lithofacies; Table 2). The fragments are dominated by pumice lapilli with subordinate scoria, and lithic lapilli bounded in pumice and crystal-rich coarse to fine ash matrix (~45–55 vol.%).

Layer 4 comprises four sub-layers that consist of up to 1.1-m-thick stacked, repetitive successions of cross-stratified, clast-supported, moderately to well-sorted lapilli and ash deposits (bed 4A and 4C; xsLA+lensLA lithofacies) and stratified to massive, moderately to poorly-sorted accretionary-lapilli-bearing ash deposit (bed 4B and D; saccA and maccA lithofacies; Figs. 2.2 and 2.8A–C). The fragments are pumice, scoria, lithic lapilli, and accessory ash aggregates bounded in pumice, lithic, and crystals ash matrix (~70–80 vol.%).

Ash componentry of Ba bed-set predominantly consists of juvenile clasts (52–57 vol.%) and isolated crystals (23–42 vol.%) with subordinate lithic components (Fig. 2.4). The ash aggregates are present only in layer 4, corresponding to finer-grained lithofacies (xsLA and saccA). The relative abundance of the juvenile, lithic, and crystal components does not vary significantly among the massive, stratified, and lenticular lithofacies; however, it shows a general decrease in juvenile contents coupled with an increase in crystal and lithic contents. The juvenile clasts mainly consist of pumice, although the xsLA lithofacies of layer 1 contains

abundant scoria clasts as the dominant juvenile component. The juvenile morphology displays distinct appearances compared to the other bed-sets, which are dominated by fused-shaped, poorly vesicular clasts (Fig. 2.6F) and blocky clasts with thick bubble walls (Fig. 2.6G).

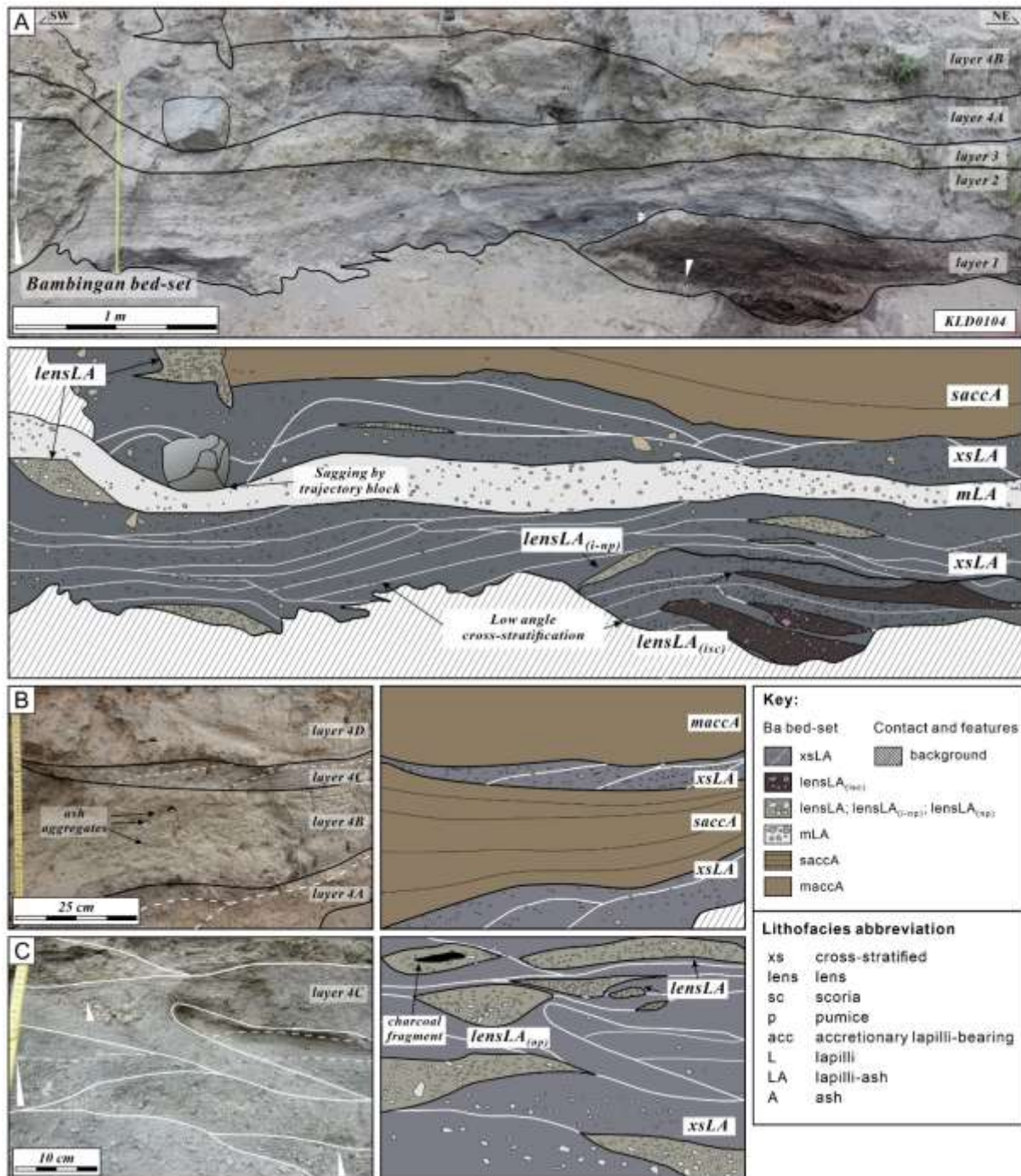


**Figure 2. 8.** Representative photos and illustrations of complex succession composing Bambangian bed-set. A) Lithofacies association of cross-stratified lapilli and ash, massive lapilli and ash, and massive to stratified accretionary lapilli bearing ash. A deformation (sagging) structure is caused by trajectory block in mLA facies. B) and C) Closer look of intercalation between xsLA and accA that usually contain ash aggregates and lenses of pumice lapilli and ash.

## 2.5. Geochemistry

The bulk compositions of the juvenile volcanic products are plotted on variation diagrams with the published data of Kelud volcanic products for the classification (Figs. 2.9 and 2.10). The  $\text{SiO}_2$  varies between 52.0 to 54.9 wt.%, with total alkalis from 2.9 to 3.5 wt.%. They plot in a narrow compositional range and typically Low-K to Medium-K calc-alkaline (Fig. 2.10), basaltic-andesite in the scheme of Le Maitre et al. (2002). They also share similarities to the products formed by other eruptions, including the most recent eruptions (e.g., 1990 and 2007; Bourdier et al., 1997; van Bergen et al., 2000; Dempsey, 2013; Jeffrey et al., 2013; Kadarsetia, 2016). The  $\text{Na}_2\text{O}$  and  $\text{K}_2\text{O}$  positively correlate with the increasing  $\text{SiO}_2$ , whereas  $\text{Fe}_2\text{O}_3^*$ ,  $\text{MgO}$ , and  $\text{CaO}$  display a negative correlation. Similarly, the  $\text{TiO}_2$  negatively correlates with silica, although the data display relatively uniform values ( $\sim 0.6$  wt.%). The  $\text{Al}_2\text{O}_3$  and  $\text{P}_2\text{O}_5$  data show no systematic correlation with the silica concentrations.

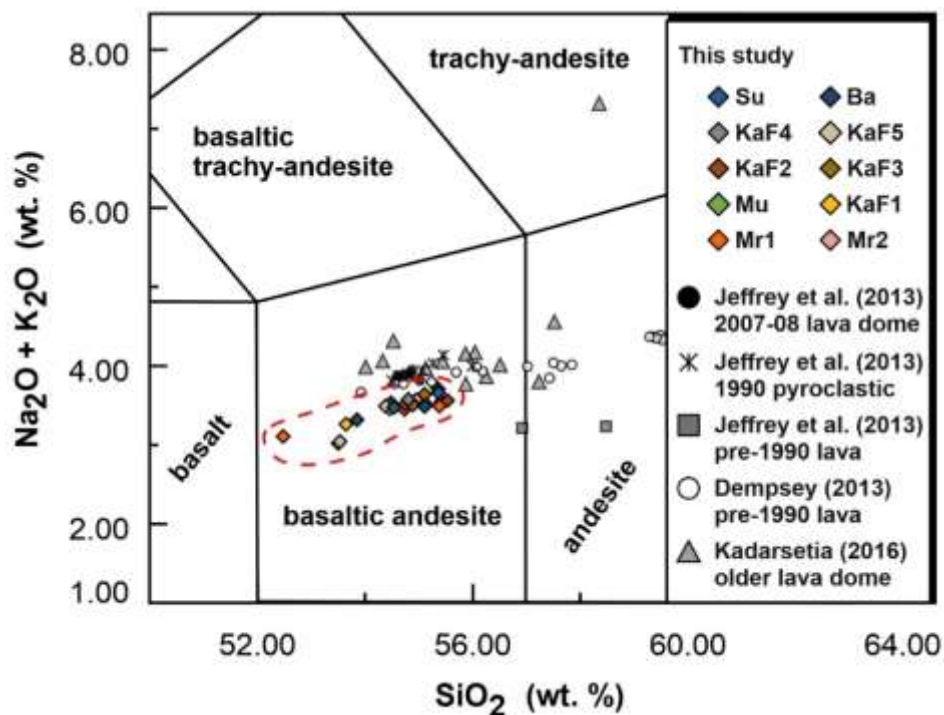


**Figure 2. 9.** Total alkalis vs. silica (after Le Maitre et al., 2002) of analyzed samples plotted along with previously published data of older dome-forming eruption products of Kelud volcano. Red dashed-oval represents the compositional range of analyzed samples in this study.

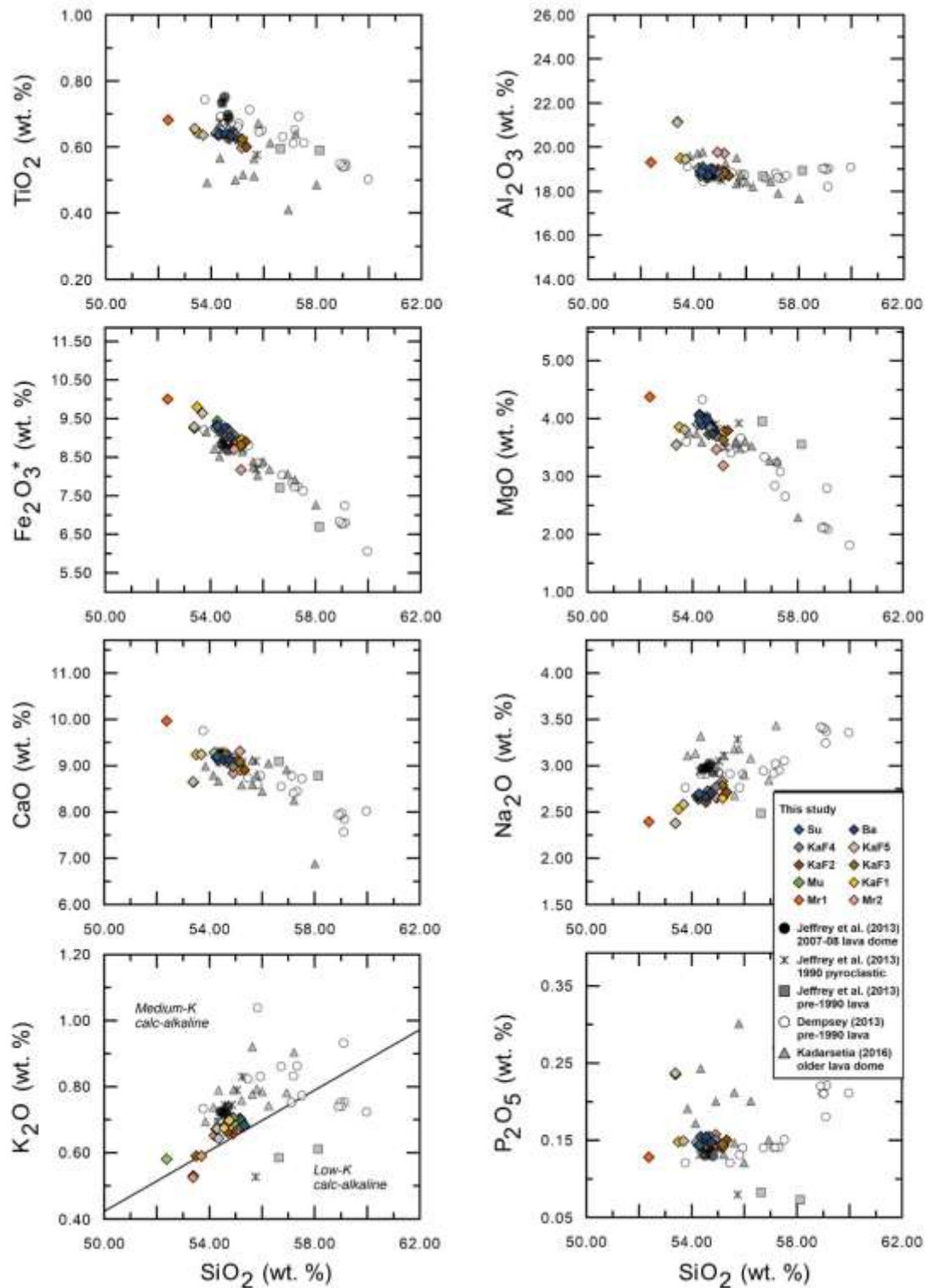


**Figure 2. 10.** Major element variations of the volcanic product from the last-1300-years-activity of Kelud volcano were plotted alongside the published data of Kelud's products in the basis of volatile-free, including from the recent activity (1990 and 2007).

## 2.6. Lithofacies association of the eruptive events

I identified ten bed-sets containing various lithofacies associations (Fig. 2.3, Table 2.4). The lithofacies association for each defined bed-set represents an eruption event that occurred during a specific episode. The correlation between the stratigraphic positions, chronological constrain from radiocarbon dating, physical appearances and structures of the deposits, and emplacement mechanisms of the different eruption episodes. With this information, I present eruption chronology of Kelud volcano for the last 1300 years.

**Table 2. 4.** Summary of lithofacies association and interpretation of each eruption episode. m: massive, xs: cross-stratified, s: parallel-stratified, lens: lens, i: inverse grading, n: normal grading, l: lithic, p: pumice, sc: scoria, acc: accretionary lapilli-bearing, B: block/bomb, L: lapilli, and A: ash.

Bed-set	Lithofacies association	Interpretation
Mr1	mBLA <sub>(il)</sub> + mLAB <sub>(il)</sub> + mAB <sub>(il)</sub> , xsLA + mBL <sub>(nl)</sub> + sLA + mBLA, and mLA <sub>(np)</sub> + xsLA + lensLA <sub>(i-np)</sub> + mLA <sub>(ip)</sub> .	Multi-phase dome destructions that transported as highly energetic PDCs and deposited abundant large dense lithic clasts. Pyroclastic fountaining occurred at the early stage of this episode, producing a massive PDC. The late-stage is noted by the deposition of more diluted PDCs that preserved lithic-rich stratified beds, followed by the deposition of pumice fallout layers. The eruption intensity gradually became smaller, reflected by the instability in the vent area that generated the alternation of mLA with xsLA + lensLA facies.
Mr2	mBLA <sub>(il)</sub> + mAB, and mLA <sub>(np)</sub> .	Similar to Mr1; Successive deposition of PDCs and a fallout layer. The PDCs were derived from disruption of dome/lava plug and granularly transported to sustain massive beds.
Mu	mLAB and maccA	Emplacement of high concentration PDC followed by the deposition of ash fallout from the umbrella cloud.
KaF1	mLA <sub>(ip)</sub>	Fallout products; the eruptions were short-lived and relatively steady. The eruption occurred after a long interlude between each other.
KaF2	mLA <sub>(ip)</sub>	
KaF3	mLA <sub>(ip)</sub>	
KaF4	mLA <sub>(ip)</sub>	
KaF5	mLA <sub>(ip)</sub>	
Su	maccA and mLA <sub>(ip)</sub>	Multiple stages of fallout depositions. The initial stage is noted by an accretionary lapilli-bearing layer that contains abundant juvenile fragments; the maccA facies is interpreted as a vent clearing event before the simultaneous deposition of mLA <sub>(ip)</sub> facies.
Ba	xsLA+lensLA <sub>(isc)</sub> , lensLA <sub>(i-np)</sub> , mLA, and xsLA + lensLA + saccA+ maccA.	Multiple deposition of diluted PDCs and fallout deposits. Onset eruption (xsLA + lesLA facies) originated from an unsteady eruption column followed by deposition a fallout layer (mLA) and generation of diluted PDCs that formed xsLA + lensLA + saccA+ maccA facies association.

### 2.6.1. Margomulyo 1 episode

Mr1 consists of high-concentration PDC deposits, dilute PDCs, and tephra fallout layers interstratified with dilute PDC deposits that were deposited successively. In general, the PDCs of Mr1 have the characteristics of high-concentration density currents based on their general nature of poorly to moderately sorted beds that fill in the topographic lows (Branney and Kokelaar, 2002; Carn et al., 2004; Saucedo et al., 2004; Charbonnier and Gertisser, 2011; Ashwell et al., 2018). The abundant dense lithic components found in layers 1 to 3 (up to 72 vol.%; Fig. 2.4) indicate were produced from erosion or disruption of a previously existing lava dome/plug (e.g., Gertisser et al., 2012; Capra et al., 2015; Macorps et al., 2018). Two PDCs emplacement events were identified from a gradual transition of the lithofacies from massive lithic breccia to thinner and stratified lithic breccia representing multiple stages of lava plug/dome disruption (Figs. 2.2 and 2.3; Table 2.3). Carbon dating of charcoal fragments in layer 1 (mBLA<sub>(il)</sub>) reveals that the Mr1 episode began around 1.3 to 1.1 cal. ka B.P.

At the early stage of PDC deposition (layers 1 and 2; Fig. 2.3), stepwise aggradation of two pulses is identified from the repetitive emplacement of PDC deposits originating from a single main flow (Branney and Kokelaar, 2002; Sulpizio et al., 2014). Clast segregation occurred through kinematic sieving or kinematic squeezing in the PDC body, resulting in the inverse grading of lithic clasts in lithofacies mBLA<sub>(il)</sub>, mLAB<sub>(il)</sub>, and mAB<sub>(il)</sub> (Le Roux, 2003; Saucedo et al., 2004). The poor sorting and massive appearance at the base of this current are consistent with the behavior of high-concentration PDC from a granular-flow regime when the density currents were emplaced (Branney and Kokelaar, 2002; Macorps et al., 2018). However, the presence of fines-dominated bed (mAB lithofacies) that vertically grade from mLAB<sub>(il)</sub> (Fig. 2.5C) implies the progressive change from a granular flow-dominated to a fluid escape-dominated flow boundary zone within the pyroclastic flow (Branney and Kokelaar, 2002; Sulpizio et al., 2014). Additionally, the reddish-grey coloration observed in the upper part of these deposits suggests thermal oxidation towards the surface may have occurred during PDCs

deposition. The presence of elutriation pipes that indicates fluid release confirms the rise of fluid through the deposit, causing rapid thermal oxidation of iron within the deposit (Fisher and Schmincke, 1984; Romero et al., 2017).

The late-stage PDC deposition is identified as diluted PDC deposits from progressive currents from lithic-rich cross-stratified to imbricated and parallel-stratified lithofacies that contain various juvenile and non-juvenile clasts (layer 3; Fig. 2.3 and 2.4). Although most of the deposits show granular flow characteristics, the poor sorting and an imbrication feature of lithic-rich lenses lithofacies (xsLA) indicate that particle segregation and clasts entrapment were dominated by traction and suspension in the tractional-dominated flow boundary zone (Branney and Kokelaar, 2002; Pedrazzi et al., 2013; Sulpizio et al., 2014; Jordan et al., 2018).

The Mr1 episode ended with the deposition of fallout layers interstratified with diluted PDC deposits (layer 4; Fig. 2.5D). The abundant proportion of juvenile components in layer 4 suggests predominantly freshly extruded magma contributions that formed the fallouts and diluted PDC deposits (Sulpizio et al., 2014; Capra et al., 2015; Jordan et al., 2018; Macorps et al., 2018). Since most of the fall layers are thin and contain blocky crystalline ash components (Fig. 2.6Q and S), they were probably generated from a short-lived vulcanian eruption. During the formation of this eruption plume, partial erosion occurred on the conduit wall, as reflected by the significant lithic components (>15 vol.%) in dilute PDC layers (Fig. 2.4). The partial erosion may cause instability in the vent, triggering the marginal column collapse and resulting in the lateral variation of  $mLA_{(n-ip)}$  lithofacies in KLD0702 to  $mLA_{(np)}$  and  $mLA_{(ip)}$  with intercalation of xsLA+lensLA lithofacies observed in KLD0102 (Figs. 2.2 and 2.5D).

### 2.6.2. Margomulyo 2 episode

Similar to Margomulyo1, the eruptive episode of Margomulyo2 began with the generation of high-concentration PDCs, followed by the deposition of a well-sorted fallout layer. Dome/lava plug destructions were recognized at the early stage of the Margomulyo2 episode from two

PDC deposits (layers 1 and 2) emplaced as channel fillings (Figs. 2.4 and 2.5A). Although most deposits show granular flow characteristics, the poor sorting and lithofacies variation grades laterally and vertically from mBLA<sub>(il)</sub> to mAB indicate transitions to a fluid-escaped dominated flow boundary zone towards the upper part of density currents. Stepwise aggradation of two pulses from the main density current is identified from the repetitive emplacement of PDC deposits originating from a single main flow (Branney and Kokelaar, 2002; Sulpizio et al., 2014). These particular portions of PDCs, which show inverse grading of lithics, also suggest that kinematic sieving and squeezing affected the clast segregation in the flow-boundary zone when the basal parts were granularly transported (Le Roux, 2003; Saucedo et al., 2004; Sulpizio et al., 2007; 2014). Furthermore, the presence of elutriation pipes and reddish-grey coloration observed in the upper part of these deposits suggests rapid thermal oxidation through the fluid release during PDCs depositions (Fisher and Schmincke, 1984; Romero et al., 2017; Macorp et al., 2018; Maeno et al., 2019a).

The eruptive episode of Margomulyo2 ended with fallout deposition from a vulcanian eruption, similar to Margomulyo1.

### 2.6.3. Mulyorejo episode

Mulyorejo bed-set comprises lithofacies association of mLAB and maccA (Figs. 2.3; Table 2.4). Based on the poor sorting and massive nature of the deposits, mLAB and maccA lithofacies of layers 1 and 2 are interpreted as PDC deposits (Fisher and Schmincke, 1984; Branney and Kokelaar, 2002; Jordan et al., 2018). In contrast, maccA lithofacies of layer 3 is interpreted as a fallout deposit based on clast-supported beds that mantle the topography (Figs. 2.2 and 2.3). The presence of accretionary lapilli in maccA lithofacies indicates aggregation of fine ash during the fall (e.g., Costa et al., 2010; Brown et al., 2010).

The eruptive episode of Mulyorejo began with the emplacement of PDC deposits (layers 1 and 2), followed by fallout deposition (layer 2.3). The presence of maccA above mLAB lithofacies

indicates ash settling from the phoenix cloud that accompanied the emplacement of lower part of the PDC while it was granularly transported (Branney and Kokelaar, 2002; Sulpizio et al., 2007). The presence of breadcrust scoria in mLAB lithofacies suggests that the large bombs could be deposited from the same PDC body or the bombs were trajected near the vent and transported together with the density current (Graettinger and Valentine, 2017). Considering the low lithic-to-juvenile ratio (Figs. 2.4) and the occurrences of vesicular clast with fluidal shape as the dominant juvenile morphology (Fig. 2.6E), it is likely that the fine ash layers of Mu bed-set were not related to phreatomagmatism. Instead, they were probably derived from the magmatic origin under humid atmospheric conditions (e.g., White and Valentine, 2016). The presence of core-type ash aggregates (Fig. 2.6K and L) as an accessory component of these deposits suggests that the fragmentation happened in a relatively short period, such that the fine fraction pumice acted as a core and grew during the settling (Schumacher and Schmincke, 1991; Brown et al., 2010).

#### 2.6.4. Karangrejo1 to Karangrejo5 episodes

Each episode of Karangrejo eruptions (KaF1–KaF5) is interpreted as a single fallout deposition directly from the eruption column based on their well-sorted, clast-supported, and laterally continuous beds (e.g., Branney and Kokelaar, 2002; Jordan et al., 2018). The earliest episode occurred in 0.5 to 0.4 cal. ka B.P. and deposited mLA lithofacies of KaF1, followed by episodes that produced mLA lithofacies of KaF2 through KaF5. The presence of organic-matter-rich layers that bound each bed-set suggests a long interval between each eruptive episode during which the vegetation grew. The fall layers were generated from steady eruption columns, reflected by nearly no fluctuations in sorting and clast size (Pistolesi et al., 2015; Jordan et al., 2018). However, the occurrence of fine ash that inversely grade upwards to coarse lapilli suggests an increase in intensity towards the late stage of each episode (mLA<sub>(ip)</sub>; e.g., Goode et al., 2019). The relatively thin layers (< 30 cm at the proximal area) and lack of accidental clasts

(Fig. 2.4) suggest that these deposits were derived from short-lived mild eruptions with less erosion of previously existing volcanic products (Dávila-Harris et al., 2013; Pistolesi et al., 2015; Jordan et al., 2018).

#### 2.6.5. Sugihwaras episode

The Sugihwaras episode consists of a series of fallout depositions initiated by an accretionary lapilli-bearing fine ash layer (maccA lithofacies) followed by subsequent deposition of a massive lapilli and ash layer (mLA lithofacies; Fig. 2.3; Table 2.4). The sharp contact between these layers recorded a brief cessation in pyroclastic deposition with no erosion or soil formation (Fig. 2.6A). As reflected in the lack of vertical variation in sorting and clast size, these layers were most likely emplaced from steady eruptive columns. Their similarity in component proportions and major element compositions (Figs. 2.4 and 2.9) implies that these eruptions were probably derived from the same magmatic body (Prambada et al., 2016; Harijoko et al., 2021). However, due to a higher degree of fragmentation, the accretionary lapilli-bearing layer preserves more abundant fine-fraction clasts than the lapilli and ash deposit (Figs. 2.3, 2.7, and 2.8). Moreover, the ash aggregates in maccA lithofacies (layer 1; Figs. 2.6I–L) could indicate an aggregation of fine ash driven by electrostatic force or humid atmospheric conditions during the clast deposition (e.g., Costa et al., 2010; Brown et al., 2010).

#### 2.6.6. Bambang episode

Eruption episode of Bambang occurred on 0.2–0.1 cal. ka B.P. It consists of multiple depositions of dilute PDCs associated with tephra fallout (Fig. 2.3). The remarkable sagging structures and ash aggregates indicate wet emplacement conditions (Sulpizio et al., 2007; Brown et al., 2010; Jordan et al., 2018; Zrelak et al., 2020). In particular, the alternation of stratified and lenticular lithofacies suggests current unsteadiness that records multiple truncations with the suspension and traction dominated the grain-by-grain deposition in the

traction-dominated flow boundary zone (Branney and Kokelaar, 2002; Saucedo et al., 2004; Pedrazzi et al., 2013; Jordan et al., 2018; Zrelak et al., 2020).

Eruptive activity started with an explosive eruption that produced a dilute PDC (represented by layer 1), followed by the deposition of fallout-associated PDC layers originating from the collapse of an eruption column (layers 2 to 4; Fig. 2.3). During this stage, the intermittent pulse was controlled by topography as the currents were turbulently moved along the slope, resulting in the grain-by-grain deposition of the lenticular lithofacies as a basal part of each diluted pulse (Branney and Kokelaar, 2002; Sulpizio et al., 2014). A noticeable scoria component is recorded in layer 1 (~50 wt.%), which then abruptly transitions to pumice-rich towards the overlying layers (Fig. 2.4). The abrupt change could be explained by two possible scenarios: 1) two simultaneously active vents, or 2) a single vent that produced deposits transitioning from scoria to pumice dominant. However, since there is no direct evidence of multiple active vents in the crater area for the last 1000 years, the first scenario is not a plausible mechanism for yielding this transition (Hadikusumo, 1974; Santosa and Atmawinata, 1992; Kadarsetia, 2016). Thus, I infer that scenario two is the most suitable, although the details of how it occurred are still unclear; possible mechanisms may have included different magma sources or heterogeneous degassing within the conduit (e.g., Preece et al., 2016; Cassidy et al., 2018; Latutrie and Ross, 2020).

The activity continued by deposition of the late-stage dilute PDC beds (layer 4) following the deposition of the pumice-fallout layer (layer 3; Fig. 2.6). The sudden increase in lithic components found in layer 4 suggests vent erosion occurred at the end of this eruption episode (Charbonnier and Gertisser, 2011; Pistolesi et al., 2015; Jordan et al., 2018; Ashwell et al., 2018). The massive to stratified, accretionary lapilli-bearing ash (maccA and maccA lithofacies) on top of xsLA (layer 4) implies the gentle settling of particles from the ash cloud that accompanied the moving flow (Sulpizio et al., 2007; Charbonnier and Gertisser, 2011; Dávila-Harris et al., 2013). The abundant fine ash particles and their settling time could have

promoted the ash aggregation driven by electrostatic forces or moisture during the settling (Figs. 2.6K–L; e.g., [Costa et al., 2010](#); [Brown et al., 2010](#)). Furthermore, the occurrences of thin stratified layers and lack of erosional contact indicate that both tractional and direct-fallout mechanisms have coincided during the deposition of these diluted currents. [Sulpizio and Dellino \(2008\)](#) have attributed flow velocity to flow transformation and lithofacies variations of a stratified density current. Similar to the Upper Brown Tuff eruption of Vulcano (e.g., [Lucchi et al., 2022](#)), the high turbulence during deposition may transform a single compound density current into stratified currents by developing separate lobes ([Branney and Kokelaar, 2002](#); [Sulpizio and Dellino, 2008](#)). Here I suggest the maccA and saccA lithofacies produced by lofted fine ash are coeval with the tractional currents that formed the xsLA lithofacies and are genetically related to a single parental density current.

## 2.7. Eruptive activity and hazard implication

### 2.7.1. Eruptive activity

I have identified a total of twelve fallout deposits and ten PDC units formed during ten different eruption episodes in the period between ~1.3 and 0.1 ka (Fig. 2.3). Most hiatus in volcanic activity were interpreted from erosion surfaces and organic matter-rich layers bounding each eruption episode. The oldest eruption of Kelud activity, called Margomulyo1, occurred between 1.3 and 1.1 cal. ka B.P. It consists of a series of vulcanian-type explosions that produced lithic-rich PDCs in-filling the western valleys of Sumberagung Stream. Two eruption columns accompanied by column-collapse PDCs produced thick fallout deposits that dispersed towards the western flank of the volcano. The Margomulyo2 episode occurred after a brief quiescence, during which the fallout layer of Mr1 was eroded following the emplacement of lithic-rich PDC and fallout deposits from the vulcanian-type explosion. The volcano subsequently became dormant for about ~100 years, as indicated by soil development above the deposits (e.g.,

Heinrich et al., 2020). The activity continued in the Mulyorejo episode by emplacing two PDC and one fallout deposits.

The next major eruptions occurred after a dormant period in which ~20 cm of soil developed. Six eruption episodes (Karangrejo1 to Karangrejo5 and Sugihwaras) occurred between 0.5 and 0.2 cal. ka B.P. These episodes produced seven fallout deposits with no activity involving PDC deposition (Fig. 3). The oldest episode, Karangrejo1, can be attributed to the 1481 C.E. eruption since the age overlaps with the one reported by Kusumadinata (1979). At the end of this period, an alternation of ash and pumice fallout layers was deposited during the Sugihwaras episode. Following a brief interval of quiescence, the activity then shifted to predominantly pyroclastic fountaining in the Bambang episode (0.2 to 0.1 cal. ka B.P) that produced three diluted PDC and one fallout deposits.

Despite the newly documented eruption episodes obtained in the present research, the currently available stratigraphy still does not represent all witnessed historical eruptions (i.e., Kusumadinata, 1979; Wirakusumah, 1991). Considering the limited exposures, vegetation cover, or erosion, especially in the proximal area, the correlation for the eruptions younger than 1800 C.E. is not possible at the moment.

Our stratigraphic and chronology data indicate that the eruptive activity of Kelud has a repose period of once every ~100 years. Comparing our results with witnessed historical events (post-1900 C.E.), the eruptive frequency is slightly lower than the frequency recorded from the 20<sup>th</sup>-century eruptions, with ten eruptions occurring over a century (once every ~10 years). This suggests that the eruptive frequency of Kelud has increased over time. The repose ~100 years long seems to be a common case for an active volcano in Indonesia (i.e., Merapi and Slamet; Preece et al., 2016; Harijoko et al., 2021) and other subduction-related volcanoes worldwide (i.e., Puyehue-Cordón Caulle, Chicon, and Sakurajima; Miwa et al., 2013; Pistolesi et al., 2015; Scolamacchia and Capra, 2015; Yamamoto et al., 2018), although I cannot rule out the possibility that I have not found the deposits of other small eruptions. Being constantly active

for the past millennium and having erupted volcanic products with similar chemical signatures (Figs. 2.9) suggest that the magma reservoir beneath Kelud is revitalized by continuous magma injections from a deeper source (Bourdier et al., 1997; Jeffrey et al., 2013; Maeno et al., 2019b). Furthermore, the bulk compositions of the eruptions do not significantly affect the various eruption styles produced, and are similar with Merapi (Preece et al., 2016), Soufrière Hills (Murch and Cole, 2019), Awu (Bani et al., 2020), and Slamet (Harijoko et al., 2021). It seems the processes involving degassing and crystallization at the shallower level may contribute to such variations; though this process needs to be further investigated (e.g., Platz et al., 2007; Miwa et al., 2013; Cassidy et al., 2018; Maeno et al., 2019b; Murch and Cole, 2019).

#### 2.7.2. Hazard implications

The evolution of volcanic activity in the last 1300 years has important implications for the ongoing hazard assessment, particularly in the surrounding area, in which more than 200,000 people are living in the direction of the crater opening. The explosive phases could generate fall deposits covering broad areas with associated high-concentration PDC that can travel >10 km from the eruption vent, blowing down the vegetation and damaging the infrastructures (Figs. 2.1 and 2.2). If erupted on steep terrains (i.e., NE–SW direction of the volcanic vent) or into main rivers (i.e., Sumberagung and Ngobo; Fig. 1), the PDCs could travel further away and reach highly-populated areas, following the scenario of Mulyana et al. (2004), Primulyana et al., (2014), and Maeno et al. (2019a). Considering that ~40% of studied eruptive episodes have produced PDC deposits (Fig. 2.3), the threat of hazardous PDCs should be accounted for when assessing future volcanic hazards around Kelud volcano. Moreover, when a crater lake is present, Kelud tends to produce explosive eruptions associated with diluted PDCs (i.e., Bambang) and syn-eruptive or post-eruptive lahars, as also observed in historical eruptions of Kelud (i.e., 1966 and 1990; Kusumadinata, 1979; Sudradjat, 1991; Thouret et al., 1998), Ruapehu (Manville, 2015), and Taranaki (Torres-Orozco et al., 2017). Similar to the Ijen

(Kusumadinata, 1979; van Bergen, 2000), Chicon (Scolamacchia and Capra, 2015), Sundoro (Prambada et al., 2016), and Azufral (Pardo et al., 2020), such explosive eruptions potentially widen and deepen the crater geometry, increasing the overall water capacity for generating the large-scale hazardous lahars and diluted PDCs.

the threat of devastating PDCs and syn-eruptive or post-eruptive lahars was reduced. The recurrent lava domes/plugs in the past millennia (i.e., Margomulyo1, Margomulyo2, and 2007-2008), along with the remnant of lava dome at the summit (i.e., Lirang and Sumbing), imply that the shallow intrusions and effusive activity can displace the crater lake by gradually replacing it with solidified materials. Accordingly, when the lava dome or plug is formed, the eruptive activity can shift to less hazardous than the explosive phases by reducing the crater potential for accommodating significant lake water, as also observed in Kirishima (Ozawa and Kozono, 2013) and Awu (Bani et al., 2020). However, if an explosive phase occurred following this activity, Kelud can produce high-concentration PDCs (i.e., Mr1 and Mr2) and potentially generate highly explosive pyroclastic fall due to pressure accumulation at shallower conduit, similar to the 2014 eruption Kelud (Goode et al., 2019; Maeno et al., 2019a) and 2011 eruption of Kirishima (Ozawa and Kozono, 2013).

My observations suggest that the condition of the volcanic vent implies a significant contribution to lava-tephra production at Kelud, and thus eruptions with a similar pattern may also occur in the future. This point also emphasizes that Kelud should be considered a high-risk volcano and requires further studies to reconstruct a more sophisticated eruptive history.

## **2.8. Summary**

This study documented the first detailed description of volcanic products from the last 1300 years of activity of Kelud. The following conclusions are reached based on the stratigraphy, geochronology, sedimentology, componentry, and geochemistry of the studied volcanic products.

This work extends the knowledge of historical eruptions on Kelud to  $<1.3$  ka. At least twelve fallout deposits and ten individual PDC units from ten different eruption episodes were identified during the field observation. They can be classified into three types based on their sources and the emplacement processes: 1) highly concentrated PDC deposits associated with lava dome/plug disruption; 2) diluted PDC deposits derived from column collapse; and 3) pyroclastic fallouts deposited by progressive aggradation from the umbrella regions. The high-concentration PDCs were typically produced from a granular-flow regime with kinematic sieving and squeezing affecting the clast segregation. In contrast, the diluted PDCs originated from a tractional-flow regime, with the suspension and traction dominating the grain-by-grain deposition.

The variable eruptive products described in this study suggest that Kelud is capable of producing a wide spectrum of tephra deposits over time. This result is still largely incomplete due to limited exposure of deposits, even in the proximal area. Our stratigraphy and chronology data compared to the witnessed historical eruptions reveal that the Kelud's eruptive frequency increased through time with a shorter repose period (from once / $\sim 100$  years to once/ $\sim 10$  years). Similar magma compositions of the studied volcanic products ( $\text{SiO}_2$  from 52 to 55 wt. %) in comparison with most recent eruptions (i.e., 1990, 2007, and 2014) implies that continuous magma injections have revitalized the magma reservoir beneath Kelud over the last millennium. This first stratigraphy record of the last 1300 years at Kelud highlights the importance of recognizing historical eruptive episodes at any volcano, especially where the historical records are fragmentary and presented only as local narrations. Given the high population density around Kelud, this study can provide critical insight into the future eruption of Kelud in terms of eruption type, scale, and hazard implication. Additionally, the petrological and geochemical studies of Kelud products (including from the most recent activity), combined with geophysical monitoring, are required to give better perspectives on eruption dynamics and the triggering factors at Kelud volcano.

## References

- Abdurachman, E.K., Bourdier, J.-L., Voight, B., 2000. Nuées ardentes of 22 November 1994 at Merapi volcano, Java, Indonesia. *J. Volcanol. Geotherm. Res.* 100, 345-361. [https://doi.org/10.1016/S0377-0273\(00\)00144-X](https://doi.org/10.1016/S0377-0273(00)00144-X)
- Ashwell P.A., Kennedy B.M., Edwards M., Cole J.W., 2018. Characteristics and consequences of lava dome collapse at Ruawahia, Taupo Volcanic Zone, New Zealand. *Bull. Volcanol.* 80 (5), 43. <https://doi.org/10.1007/s00445-018-1217-1>
- Bani, P., Kristianto, Kunrat, S., Syahbana, D. K., 2020. Insights into the recurrent energetic eruptions on Awu, one of the deadliest volcano on earth. *Nat. Hazards Earth Syst. Sci.* 20, 2119–2020. <https://doi.org/10.5194/nhess-20-2119-2020>
- Bourdier, J. L., Pratomo, I., Thouret, J.-C., Boudon, G., Vincent, P.M. 1997. Observations, stratigraphy and eruptive processes of the 1990 eruption of Kelut volcano, Indonesia. *J. Volcanol. Geotherm. Res.* 79, 181–203. [https://doi.org/10.1016/S0377-0273\(97\)00031-0](https://doi.org/10.1016/S0377-0273(97)00031-0)
- Bonadonna, C., Cioni, R., Pistolesi, M., Connor, C., Scollo, S., Pioli, L., Rosi, M., 2013. Determination of the largest clast sizes of tephra deposits for the characterization of explosive eruptions: a study of the IAVCEI commission on tephra hazard modelling. *Bull. Volcanol.* 75, 680. <https://doi.org/10.1007/s00445-012-0680-3>
- Brown, R.J., Branney M.J., 2004. Event stratigraphy of a caldera-forming ignimbrite eruption on Tenerife: the 273 ka Poris Formation. *Bull. Volcanol.* 66, 392–416. <https://doi.org/10.1007/s00445-003-0321-y>
- Brown, R.J., Branney, M.J., Maher, C., Dávila-Harris, P., 2010. Origin of accretionary lapilli within ground-hugging density currents: evidence from pyroclastic couplets on Tenerife. *Geol. Soc. Am. Bull.* 122, 305–320. <https://doi.org/10.1130/B26449.1>
- Calder, E. S., Lavallée, Y., Kendrick, J. E., & Bernstein, M., 2015. Lava Dome Eruptions. In: *The Encyclopedia of Volcanoes*, 343–362. <https://doi.org/10.1016/B978-0-12-385938->

[9.00018-3](#)

- Capra, L., Roverato, M., Groppelli, G., Caballero, L., Sulpizio, R., Norini, G., 2015. Glacier melting during lava dome growth at Nevado de Toluca volcano (Mexico): Evidences of a major threat before main eruptive phases at ice-caped volcanoes. *J. Volcanol. Geotherm. Res.* 294, 1–10. <https://doi.org/10.1016/j.jvolgeores.2015.02.005>
- Cassidy, M., Manga, M., Cashman, K., Bachman, O., 2018. Controls on explosive-effusive volcanic eruption styles. *Nat. Commun.* 9, 2839. <https://doi.org/10.1038/s41467-018-05293-3>
- Carn, S.A., Watts, R.B., Thompson, G., Norton, G.E., 2004. Anatomy of a lava dome collapse: the 20 March 2000 event at Soufrière Hills Volcano, Montserrat. *J. Volcanol. Geotherm. Res.* 131, 241–264. [https://doi.org/10.1016/S0377-0273\(03\)00364-0](https://doi.org/10.1016/S0377-0273(03)00364-0)
- Charbonnier, S.J., Gertisser, R., 2011. Deposit architecture and dynamics of the 2006 block-and-ash flow of Merapi Volcano, Java, Indonesia. *Sedimentology* 58, 1573–1612. <https://doi.org/10.1111/j.1365-3091.2011.01226.x>
- Costa, A., Folch, A., Macedonio, G., 2010. A model for wet aggregation of ash particles in volcanic plumes and clouds: 1. Theoretical formulation. *J. Geophys. Res.* 115, B09201. <https://doi.org/10.1029/2009JB007175>
- Cronin, S.J., Lube, G., Dayudi, D.S., Sumarti, S., Subrandiyo, S., Surono, 2013. Insights into the October–November 2010 Gunung Merapi eruption (Central Java, Indonesia) from the stratigraphy, volume and characteristics of its pyroclastic deposits. *J. Volcanol. Geotherm. Res.* 261, 244–259. <https://doi.org/10.1016/j.jvolgeores.2013.01.005>
- Dávila-Harris, P., Ellis, B.S., Branney, M.J., Carrasco- Núñez, G., 2013. Lithostratigraphic analysis and geochemistry of a vitric spatter-bearing ignimbrite: the Quaternary Adeje Formation, Cañadas volcano, Tenerife. *Bull. Volcanol.* 75, 722–737. <https://doi.org/10.1007/s00445-013-0722-5>
- Dempsey, S., R., 2013. Geochemistry of volcanic rocks from the Sunda Arc, Durham theses,

Durham University. Available at Durham E-Theses Online:  
<http://etheses.dur.ac.uk/6948/>

Fisher, R.V. & Schmincke, H. U. 1984. *Pyroclastic Rocks*. Springer Verlag, Berlin, Heidelberg, 472 pp.

Gertisser, R., Cassidy, N. J., Charbonnier, S. J., Nuzzo, L., & Preece, K., 2012. Overbank block-and-ash flow deposits and the impact of valley-derived, unconfined flows on populated areas at Merapi volcano, Java, Indonesia. *Natural Hazards*, 60(2), 623–648.  
<https://doi.org/10.1007/s11069-011-0044-x>

Goode, L.R., Handley, H. K., Cronin, S. J, Abdurrachman, M., 2019. Insights into eruption dynamics from the 2014 pyroclastic deposits of Kelut volcano, Java, Indonesia, and implications for future hazards. *J. Volcanol. Geotherm. Res.* 382, 6-23.  
<https://doi.org/10.1016/j.jvolgeores.2018.02.005>

Global Volcanism Program (GVP), 2014. Report on Kelut (Indonesia). In: Wunderman, R. (Ed.), *Bulletin of the Global Volcanism Network*. 39. Smithsonian Institution: p. 2. Available at: <https://doi.org/10.5479/si.GVP.BGVN201402-263280>.

Graettinger, A., H., Valentine, G., A., 2017. Evidence for the relative depths and energies of phreatomagmatic explosions recorded in tephra rings. *Bull. Volcanol.* 79, 88.  
<https://doi.org/10.1007/s00445-017-1177-x>

Hadikusumo, 1974. The rise and drop of Mt. Kelut crater bottom after paroxysmal eruptions. *Tectonophysics* 23, 341–347. [https://doi.org/10.1016/0040-1951\(74\)90070-5](https://doi.org/10.1016/0040-1951(74)90070-5)

Harijoko, A., Sari, S.a., Wibowo, H.E., Setiawan, N.I., Muktikanana, M.L.A., 2021. Stratigraphy, chronology, and magma evolution of Holocene volcanic products from Mt. Slamet deposited in the Guci Valley, Central Java, Indonesia. *J. Volcanol Geotherm. Res.* 418. <https://doi.org/10.1016/j.jvolgeores.2021.107341>

Heinrich, M., Cronin, S.J. & Pardo, N., 2020. Understanding multi-vent Plinian eruptions at Mt. Tongariro Volcanic Complex, New Zealand. *Bull. Volcanol.* 82, 30.

<https://doi.org/10.1007/s00445-020-1369-7>

Hidayati, S., Kristianto, Basuki, A., Mulyana, I., 2009. A new lava dome emerged from crater lake of Kelud volcano, East Java, Indonesia. *Jurnal Geologi Indonesia* 4 (4), 229–238.

<http://dx.doi.org/10.17014/ijog.vol4no4.20091>.

Hidayati, S., Triastuty, H., Mulyana, I., Adi, S., Ishihara, K., Basuki, A., Kuswandarto, H., Priyanto, B., Solikhin, A., 2019. Differences in the seismicity preceding the 2007 and 2014 eruptions of Kelud volcano, Indonesia. *J. Volcanol. Geotherm. Res.* 382, 50–67.

<https://doi.org/10.1016/j.jvolgeores.2018.10.017>

Jeffery, A.J., Gertisser, R., Troll, V.R. et al., 2013. The pre-eruptive magma plumbing system of the 2007–2008 dome-forming eruption of Kelut volcano, East Java, Indonesia. *Contrib. Mineral. and Petrol.* 166, 275–308.

Jordan, N.J., Rotolo, S.G., Williams, R., Speranza, F., McIntosh, W.C., Branney, M.J., Scaillet, S., 2018. Explosive eruptive history of Pantelleria, Italy: Repeated caldera collapse and ignimbrite emplacement at a peralkaline volcano. *J. Volcanol. Geotherm. Res.* 349, 47–

73. <https://doi.org/10.1016/j.jvolgeores.2017.09.013>

Kadarsetia, E., 2016. Petrogenesis batuan Gunungapi Kelud, Jawa Timur. Pusat Vulkanologi dan Mitigasi Bencana Geologi (CVGHM): In Indonesian.

Kusumadinata, K., 1979. Catalogue of references on Indonesian volcanoes with eruptions in historical time. *Volcanol. Surv. Indonesia*, pp. 1–820 in Indonesian.

Latutrie, B., Ross, P.S., 2020. Phreatomagmatic vs magmatic eruptive styles in maar-diatremes: a case study at Twin Peaks, Hopi Buttes volcanic field, Navajo Nation, Arizona. *Bull. Volcanol.* 82, 28. <https://doi.org/10.1007/s00445-020-1365-y>

Le Maitre, R.W., Streckeisen, A., Zanettin, B., La Bas, M.J., Bonin, B., Bateman, P., Bellieni, G., Dudek, A., Efremova, J., Keller, J., Lameyre, J., Sabine, P.A., Schmidt, R., Sørensen, H., Woolley, A.R., 2002. *Igneous Rocks. A classification and Glossary of Terms. Recommendations of the International Union of Geological Sciences subcommission*

- on the systematics of igneous rocks. Cambridge University Press, Cambridge, 252 pp.
- Le Roux, J.P., 2003. Can dispersive pressure cause inverse grading in grain flows? Discussion. *J. Sedim. Res.* 73, 333–334. <http://dx.doi.org/10.1306/043002730333>
- Lucchi, F., 2013. Stratigraphic methodology for the geological mapping of volcanic areas: Insights from the aeolian archipelago (southern Italy). *Geological Society Memoir*, 37(1), 37–53. <https://doi.org/10.1144/M37.5>
- Lucchi, F., Sulpizio, R., Meschiari, S., Tranne, C. A., Albert, P. G., Mele, D., & Dellino, P., 2022. Sedimentological analysis of ash-rich pyroclastic density currents, with special emphasis on sin-depositional erosion and clast incorporation: The Brown Tuff eruptions (Vulcano, Italy). *Sedimentary Geology*, 427. <https://doi.org/10.1016/j.sedgeo.2021.106040>
- Macorps E., Charbonnier S.J., Varley N.R., Capra L., Atlas Z., Cabré J., 2018. Stratigraphy, sedimentology and inferred flow dynamics from the July 2015 block-and-ash flow deposits at Volcán de Colima, Mexico. *J. Volcanol Geotherm. Res.* 349, 99–116. <https://doi.org/10.1016/j.jvolgeores.2017.09.025>
- Maeno, F., Nakada, S., Yoshimoto, M., Shimano, T., Hokanishi, N., Zaenuddin, A., Iguchi, M., 2019a. A sequence of a plinian eruption preceded by dome destruction at Kelud volcano, Indonesia, on February 13, 2014, revealed from tephra fallout and pyroclastic density current deposits. *J. Volcanol. Geotherm. Res.* 382, 24–41. <https://doi.org/10.1016/j.jvolgeores.2017.03.002>
- Maeno, F., Nakada, S., Yoshimoto, M., Shimano, T., Hokanishi, N., Zaenuddin, A., Iguchi, M., 2019b. Eruption pattern and a long-term magma discharge rate over the past 100 years at Kelud volcano, Indonesia. *J. Disaster. Res.* 14 (1), 27–39. <https://doi.org/10.20965/jdr.2019.p0027>
- Manville V., 2015. Volcano-Hydrologic hazards from volcanic lakes. In: Rouwet D., Christenson B., Tassi F., Vandemeulebrouck J. (eds) *Volcanic Lakes. Advances in*

- Volcanology. Springer, Berlin, Heidelberg, pp21–71 [https://doi.org/10.1007/978-3-642-36833-2\\_2](https://doi.org/10.1007/978-3-642-36833-2_2)
- Miwa, T., Geshi, N., Shinohara, H., 2013. Temporal variation in volcanic ash texture during a Vulcanian eruption at the Sakurajima volcano, Japan. *J. Volcanol Geotherm. Res.* 260, 80–89. <http://dx.doi.org/10.1016/j.jvolgeores.2013.05.010>
- Mulyana, A.R., Nasution, A., Martono, A., Sumpena, A.D., Purwoto, Santoso, M.S., 2004. Volcanic Hazards Map of Kelud Volcano, East Java Province. Direktorat Vulkanologi dan Mitigasi Bencana Geologi.
- Murch, A.P. and Cole, P.D., 2019. Using microlites to gain insights into ascent conditions of differing styles of volcanism at Soufrière Hills Volcano, J. *Volcanol. Geotherm. Res.* 384, 221–231. <https://doi.org/10.1016/j.jvolgeores.2019.07.022>
- Ozawa, T., Kozono, T., 2013. Temporal variation of the Shinmoe-dake crater in the 2011 eruption revealed by spaceborne SAR observations. *Earth Planet Sp.* 65, 5. <https://doi.org/10.5047/eps.2013.05.004>
- Pardo, N., Avellaneda, J.D., Rausch, J., Jaramillo-Vogel, D., Gutiérrez, M., Foubert, A., 2020. Decrypting silicic magma/plug fragmentation at Azufral crater lake, Northern Andes: insights from fine to extremely fine ash morpho-chemistry. *Bull. Volcanol.* 82, 79. <https://doi.org/10.1007/s00445-020-01418-z>
- Patrick, M.R., Houghton, B.F., Anderson, K.R., Poland, M.P., Montgomery-Brown, E., Johanson, I., Thelen, W., Elias, T., 2020. The cascading origin of the 2018 Kīlauea eruption and implications for future forecasting. *Nat. Commun.* 11, 5646. <https://doi.org/10.1038/s41467-020-19190-1>
- Pedrazzi, D., Martí, J., Geyer, A., 2013. Stratigraphy, sedimentology and eruptive mechanisms in the tuff cone of El Golfo (Lanzarote, Canary Islands). *Bull. Volcanol.* 75, 740. <https://doi.org/10.1007/s00445-013-0740-3>
- Pistolesi, M., Cioni, R., Bonadonna, C., Ekussibdi, M., Bauman, V., Bertagnini, A., Chiari, L.,

- Gonzales, R., Rosi, M., Francalanci, L., 2015. Complex dynamics of small-moderate volcanic events: the example of the 2011 rhyolitic Cordón Caulle eruption, Chile. *Bull. Volcanol.* 77, 3. <https://doi.org/10.1007/s00445-014-0898-3>
- Platz, T., Cronin, S.J., Cashman, K.V., Stewart, R.B., Smith, I.E.M., 2007. Transition from effusive to explosive phases in andesite eruptions — A case-study from the AD1655 eruption of Mt. Taranaki, New Zealand. *J. Volcanol. Geotherm. Res.* 161 (1–2), 15–34. <https://doi.org/10.1016/j.jvolgeores.2006.11.005>
- Prambada, O., Arakawa, Y., Ikehata, K., Furukawa, R., Takada, A., Wibowo, H.E., Nakagawa, M., Kartadinata, M.N., 2016. Eruptive history of Sundoro volcano, Central Java, Indonesia since 34 ka. *Bull. Volcanol.* 78, 81–100. <https://doi.org/10.1007/s00445-016-1079-3>
- Primulyana, S., Hariwaseso, A., Zaenuddin, A., Budianto, A., 2014. Volcanic Hazard Map of Kelud Volcano, East Java Province. Direktorat Vulkanologi dan Mitigasi Bencana Geologi. <https://vsi.esdm.go.id/gallery/picture.php?/29>
- Preece, K., Gertisser, R., Barclay, J., Charbonnier, S.J., Komorowski, J.-C., Herd, R.A., 2016. Transitions between explosive and effusive phases during the cataclysmic 2010 eruption of Merapi volcano, Java, Indonesia. *Bull. Volcanol.* 78, 54. <https://doi.org/10.1007/s00445-016-1046-z>
- Ramsey, C., 2017. Methods for summarizing radiocarbon datasets. *Radiocarbon*, 59 (6), 1809–1833. <https://doi.org/10.1017/RDC.2017.108>
- Reimer, P. J., Austin, W. E. N., Bard, E., Bayliss, A., Blackwell, P. G., Bronk Ramsey, C., Butzin, M., Cheng, H., Edwards, R. L., Friedrich, M., Grootes, P. M., Guilderson, T. P., Hajdas, I., Heaton, T. J., Hogg, A. G., Hughen, K. A., Kromer, B., Manning, S. W., Muscheler, R., ... Talamo, S. (2020). The IntCal20 Northern Hemisphere Radiocarbon Age Calibration Curve (0–55 cal kBP). *Radiocarbon*, 62 (4), 725–757. <https://doi.org/10.1017/RDC.2020.41>

- Romero, J. E., Douillet, G. A., Vargas, S. V., Bustillos, J., Troncoso, L., Alvarado, J. D., Ramón, P., 2017. Dynamics and style transition of a moderate, Vulcanian-driven eruption at Tungurahua (Ecuador) in February 2014: pyroclastic deposits and hazard considerations. *Solid Earth*, 8, 697–719. <https://doi.org/10.5194/se-8-697-2017>
- Santosa. A. and Atmawinata, 1992, Peta geologi lembar kediri, Jawa Timur, Pusat Penelitian dan Pengembangan Geologi (P3G), Bandung. In Indonesian.
- Saucedo, R., Mancías, J.L., Bursik, M., 2004. Pyroclastic flow deposits of the 1991 eruption of Volcán de Colima, Mexico. *Bull. Volcanol.* 66, 291–306. <https://doi.org/10.1007/s00445-003-0311-0>
- Schumacher, R. and Schmincke, H., 1991. Internal structure and occurrence of accretionary lapilli — a case study at Laacher See Volcano. *Bull. Volcanol.* 53, 612–634. <https://doi.org/10.1007/BF00493689>
- Scolamacchia, T., Capra, L., 2015. El Chichón Volcano: Eruptive History. In: Scolamacchia, T., Macías, J. (eds) *Active Volcanoes of Chiapas (Mexico): El Chichón and Tacaná. Active Volcanoes of the World.* Springer, Berlin, Heidelberg. [https://doi.org/10.1007/978-3-642-25890-9\\_3](https://doi.org/10.1007/978-3-642-25890-9_3)
- Sudradjat, A. (1991). A preliminary account of the 1990 eruption of the Kelut volcano. In A. Sudradjat (Ed.), *The Dynamics of Indonesian Volcanoes* (pp. 447-462). Handover: Padjadjaran University, Bandung, Indonesia.
- Sulpizio, R., Mele, D., Dellino, P., La Volpe, L., 2007. Deposits and physical properties of pyroclastic density currents during complex Subplinian eruptions: the AD 472 (Pollena) eruption of Somma-Vesuvius, Italy. *Sedimentology*, 54, 607–635. <https://doi.org/10.1111/j.1365-3091.2006.00852.x>
- Sulpizio, R. and Dellino, P., 2008. Sedimentology, depositional mechanisms and pulsating behaviour of pyroclastic density currents. In: *Caldera Volcanism: Analysis, Modelling and Response. Developments in Volcanology*, Vol. 10, (Eds J. Gottsman and J. Marti),

- 58–96. [https://doi.org/10.1016/S1871-644X\(07\)00002-2](https://doi.org/10.1016/S1871-644X(07)00002-2)
- Sulpizio, R., Dellino, P., Doronzo D.M., Sarocchi, D., 2014. Pyroclastic density currents: state of the art and perspective. *J. Volcanol. Geotherm. Res.* 283, 36–65. <http://dx.doi.org/10.1016/j.jvolgeores.2014.06.014>
- Thouret, J.-C., Abdurachman, K.E., Bourdier, J.-L., Bronto, S., 1998. Origin, characteristics, and behaviour of lahars following the 1990 eruption of Kelud volcano, eastern Java (Indonesia). *Bull. Volcanol.* 59, 460–480. <https://doi.org/10.1007/s004450050204>
- van Bergen, M.J., Bernard, A., Sumarti, S., Sriwana, T., Sitorus, K., 2000. Crater lakes of Java: Dieng, Kelud, Ijen. *Excursion Guidebook—International Association of Volcanology and Chemistry of the Earth’s Interior (IAVCEI) General Assembly, Bali 2000*, p 42.
- White, J.D.L., Houghton, B.F., 2006. Primary volcanoclastic rocks. *Geology* 34, 677–680. <https://doi.org/10.1130/G22346.1>
- White, J.D.L., Valentine, G.A., 2016. Magmatic versus phreatomagmatic fragmentation: absence of evidence is not evidence of absence. *Geosphere* 12, 1478–1488. <https://doi.org/10.1130/GES01337.1>
- Wirakusumah, A.D., 1991. Some studies of volcanology, petrology and structure of Mt. Kelut, east Java, Indonesia (Doctoral dissertation, Victoria University of Wellington).
- Yamamoto, T., Kudo, T., Isizuka, O., 2018. Temporal variations in volumetric magma eruption rates of Quaternary volcanoes in Japan. *Earth Planets Space* 70, 65. <https://doi.org/10.1186/s40623-018-0849-x>
- Zrelak, P.J., Pollock, N.M., Brand, B.D., Sarocchi, D., Hawkins, T., 2020. Decoding pyroclastic density current flow direction and shear conditions in the flow boundary zone via particle-fabric analysis. *J. Volcanol. Geotherm. Res.* 402.
- Zaennudin, A., Dana, I.N., Wahyudin, D., Hadisantono, R.D., 1992. Peta geologi G. Kelut, Jawa Timur. Database of volcanoes in Indonesia. *CVGHM report*.

## Chapter 3

### An overview of the 2007/08 and 2014 eruptions of Kelud volcano, Indonesia.

The 2007/08 eruption is an example of the short-sustained dome-forming activity that has frequently been observed at Kelud over the last century (GVP, 2008; Maeno et al., 2019b). In contrast, the 2014 eruption started with explosions that partially destroyed the 2007/08 dome. These initial explosions were followed by the development of an energetic plinian column in less than one hour, which terminated in the eruption column collapsed (Goode et al., 2019; Hidayati et al., 2019; Maeno et al., 2019a).

Using these two contrasting eruptions as case studies, the driving forces behind variation in eruption styles and their transition at Kelud will be exclusively deliberated. This chapter integrates monitoring reports and previously published documentations to outline the eruptive style, chronology, and deposits produced at every eruption event. These data serve as the foundation for the field sampling strategy and the basis for correlating the petrological and textural data presented in this thesis with the dynamics of each studied eruption.

#### **3.1. The 2007/08 and 2014 eruptions**

##### 3.1.1. Chronology of the 2007/08 eruption

Since the last eruption occurred in 1990, Kelud has been considered dormant. However, in May 2007, the Center of Volcanology and Geological Hazard Mitigation (CVGHM) of Indonesian Ministry identified anomalous CO<sub>2</sub> fluxes (>250 tons/day) in the crater lake column compared to previous years (GVP, 2008; Caudron et al., 2012) (Fig. 3.1A). Four months after that, the total flux of CO<sub>2</sub> had an excess of ~500 tons/day on 11 September, making it the highest CO<sub>2</sub> records by ten times compared to the values observed in 2005 and 2006 (Siebert et al., 2011).

The sudden increases in CO<sub>2</sub> flux had shifted the color of crater lake from green to blueish yellow and had increased its temperature significantly (Surono, 2007). The temperature and chemistry of crater lake continuously changed until October 2007, along with increased seismic activity and deformation. This resulted in the evacuation of ~117,000 individuals within a 10 km radius of the crater, leading to the evacuation of around 117,000 people living in villages within a 10 km radius of the crater (GVP, 2008; Siebert et al., 2011).

On 2–3 November, the seismicity intensified and caused a series of shallow earthquakes and decreased on 4 November 2007 (Hidayati et al., 2009). However, the activity of Kelud significantly increased, denoted by crater lake temperature that reached 50 °C and occasional emissions of steam plumes through ~2 km above the crater surface (Jeffrey et al., 2013). According to GVP (2008), the plumes derived from a fresh black mass of rock that protruded from the crater lake on 4 November (Fig. 3.1B). The dome grew fast and steadily displaced the lake without undergoing violent broad-scale boiling. Steam plumes of various sizes were continuously emitted throughout November; one of the emitted plumes on 11 November had a 3.7 km altitude above the crater surface (Siebert et al., 2011; Caurdon et al., 2012). At this point, the dome had already grown to ~250 m in diameter and was 120 m above lake level. By early December 2007, the dome temperature had reached 210 °C with a lake water temperature of 75 °C (Siebert et al., 2011). The lava dome remained active during the months of November and December 2007, with gradually decreasing seismicity.

The lava dome continuously grew and occasionally emitted steam plumes until May 2008 (Fig. 3.1C). The crater lake had been replaced entirely by the dome materials by 12 May 2008. At the end of May 2008, the lava dome was considered to have stopped growing since there was no sign of further development or seismic activity (GVP, 2008; Jeffrey et al., 2013). The maximum volume of erupted dome material was estimated at  $\sim 3.5 \times 10^{-2} \text{ km}^3$  with a maximum diameter of ~400 m and height of ~260 m by May 2008 (Siebert et al. 2011). No significant activity recorded after May 2008 but occasional diffuse white steams from the dome.

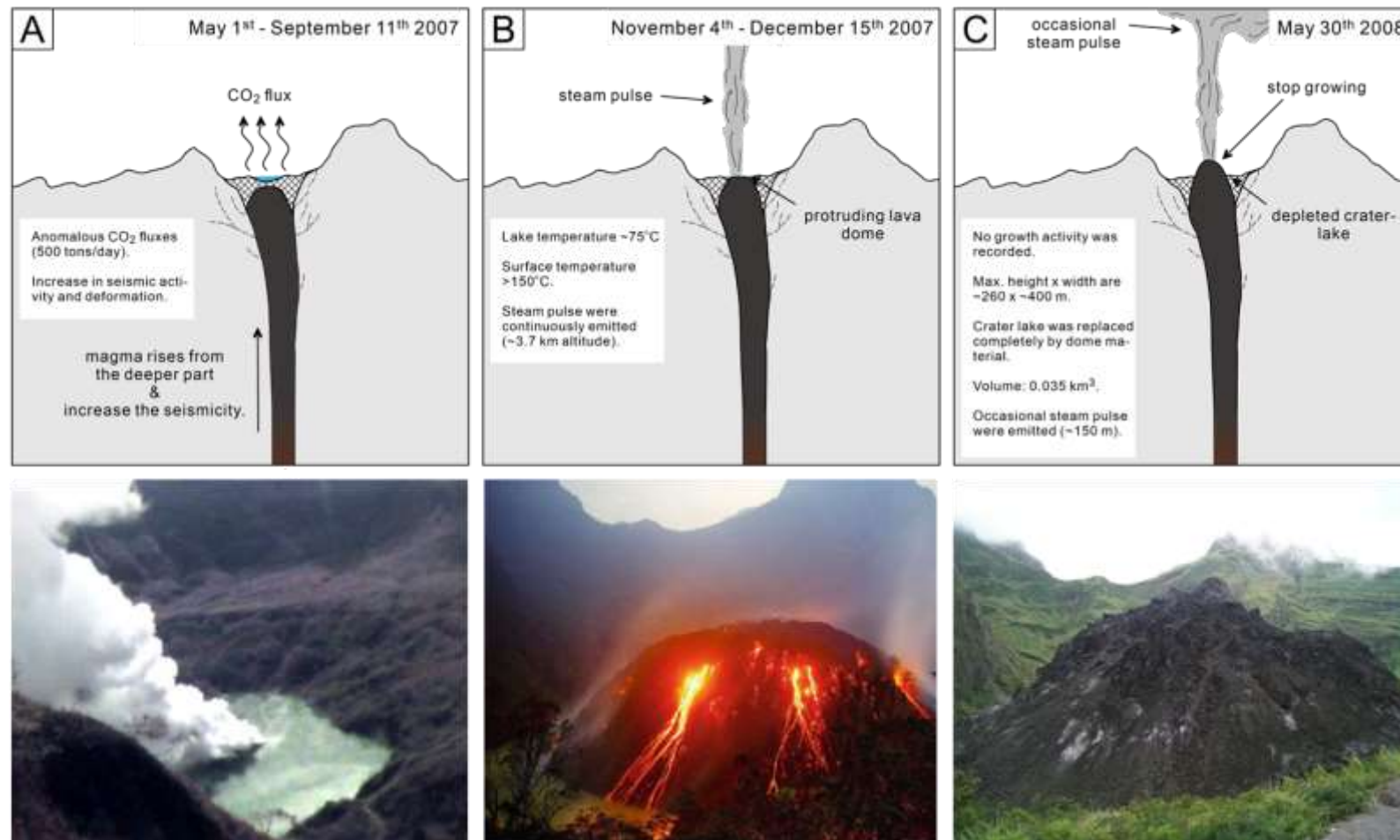


**Figure 3. 1.** Simplified sketch of the evolution of the 2007/08 eruption. A) Increase in seismic activity and measured CO<sub>2</sub> fluxes denoted the unrest of the volcano prior to the 2007/08 eruption. B) Early stage of lava dome effusion was recorded from a sudden increase in surface temperature and emission of a steam pulse from a fresh protruding dome material in the lake area. C) Lava dome continuously grew until 30 May 2008, with a height reaching ~200 m from the crater surface. Image from GVP (2008) and Hidayati et al. (2009).

### 3.1.2. Chronology of the 2014 eruption

The chronology and deposits of the 2014 eruption (Fig. 3.2) have been previously documented in detail (e.g., Goode et al., 2019; Hidayati et al., 2019; Maeno et al., 2019a; 2019b). Maeno et al. (2019a) and Goode et al. (2019) recognized three stages of the 2014 eruption, which will be referred to throughout this following chapter: stage I (13 February 2014), the onset phase and dome disruption explosion; stage II (13–14 February 2014), vent clearing and climactic plinian phase; and stage III (14 February 2014), the collapse of the plinian column. The following will describe the chronology and description of the deposits in detailed.

Stage I is defined as the onset of the eruption and the beginning of the 2014 eruption (Maeno et al., 2019a; 2019b). Badan Nasional Penanggulangan Bencana (BNPB) reported the first eruption occurred at 22:45 local time that produced high-energy PDCs associated with the destruction of the pre-existing lava dome along 6 km towards the northeast direction. Stage II began with a sudden increase in seismic signal at ~23:00 local time (Hidayati et al., 2019; Goode et al., 2019; Maeno et al., 2019a). The stage consisted of a plinian phase that started at ~23:30 and lasted for two hours in total (GVP, 2014). During this time, the dome from 2007–2008 was completely destroyed, and a new 400m-diameter crater was excavated (Fig. 3.2). At 01:12 local time, satellite imagery (CALIPSO) revealed that the eruption plume reached an altitude of 18–19 km. After 23:32 local time, the plume expanded rapidly and reached the stratosphere, with a maximum altitude of 26 km (Fig. 2.2; GVP, 2014; Meano et al., 2019). At 01:30, a decrease in seismic signals triggered the eruption column to be unstable and later collapsed, producing PDCs in Stage (III). On 18 February, post-eruptive lahars were recorded reaching densely populated areas around Kelud (i.e., Kediri, Malang, and Blitar) after heavy rainfall generated lahar emplacements that flooded several main bridges and covered plantations. Following the 18–19 February rainfall, Kelud has become more stable. The evacuation zone was lifted to a 5 km radius from the summit following the lower alert level of Kelud (from 3 to 2) (GVP, 2014). By 20 February, eruption activity continued to decline,

although steam plumes were occasionally observed from the crater area.

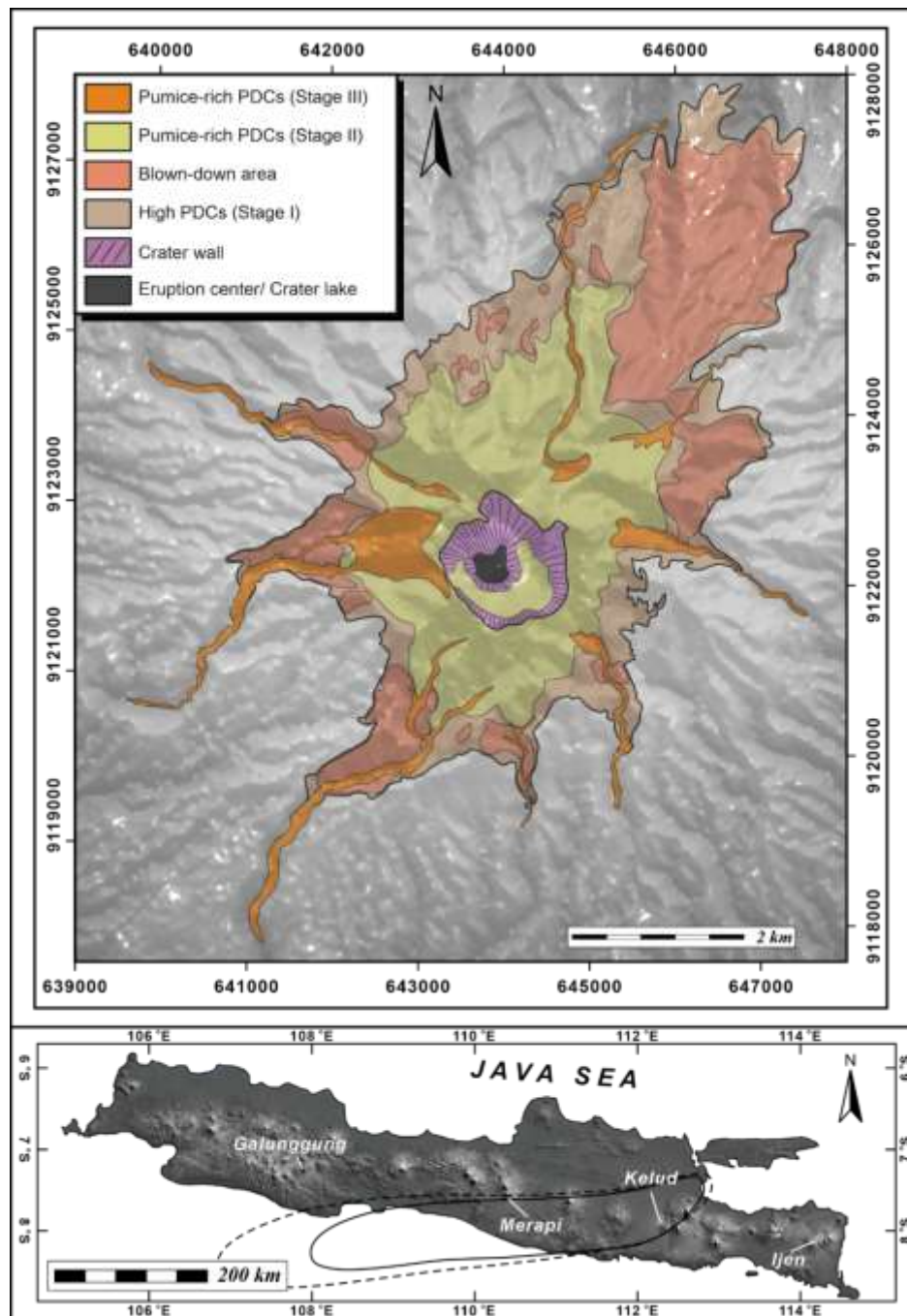


**Figure 3. 2.** Distribution maps of 2014 eruption deposits (after Maeno et al., 2019a; Goode et al., 2019). The inset map shows the location of Kelud volcano, alongside other volcanoes on Java Island, and the distribution of fallout deposits of the 2014 eruption produced during stage II (CPF).

### 3.2. Eruptive products and sample descriptions

The clast componentry of the 2007/08 and 2014 deposits were divided into seven main components based on different visual characteristics (i.e., color and textures). The detailed descriptions of each clast type can be found in Fig. 3.3:

1. Dense dome clast (LD)
2. Transparent white pumice (TWP)
3. Non-transparent white pumice (NTWP)
4. Transparent grey pumice (TGP)
5. Transparent pink pumice (TPP)
6. Banded pumice (BP)
7. Scoria (S)

Type 1 is juvenile, derived from the 2007/08 dome, whereas Types 2 to 7 represent juveniles incorporated into the 2014 deposits. Goode et al. (2019) and Maeno et al. (2019a) reported component proportions in each eruptive stage of 2014, although proportions are relatively similar from Stage I through Stage III. The most abundant clast type in 2014 products is the TWP, with an average content of ~ 50 % by volume, followed by NTWP (10–15 vol.%), TGP (8–14 vol.%), TPP (~8–12 vol.%), and S (8–10 vol.%). Banded pumice clast (BP) was only found within PDC-1 deposits, indicating that the BP clasts were formed during partial dome-disruptions that generated the PDC deposits in Stage I.

Petrographic observation revealed that 2007/08 and 2014 products share similar mineral assemblages. Plagioclase, clinopyroxene, and orthopyroxene appear as dominant phenocrysts and micro-phenocrysts alongside titanomagnetite. Similarly, the groundmass consists of feldspar microlites, clinopyroxene, orthopyroxene, titanomagnetite, and volcanic glass. Apatite is present as an accessory mineral and may occur as a microlite phase together with cristobalite, which infills the vesicles and alters volcanic glass in some dome samples.

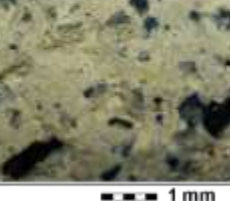
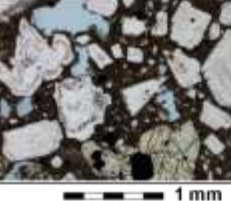
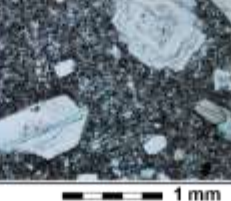
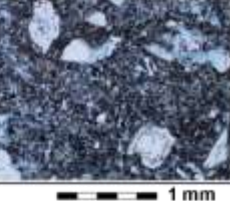
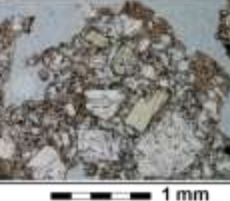
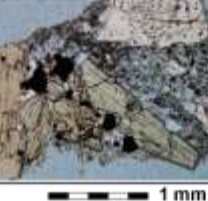
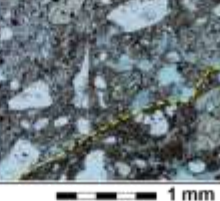
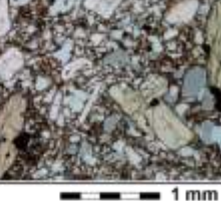
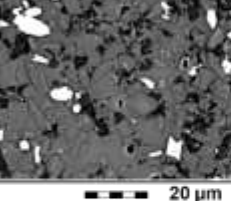
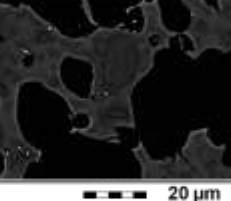
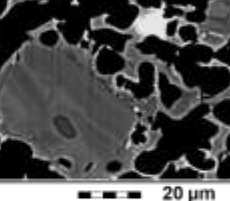
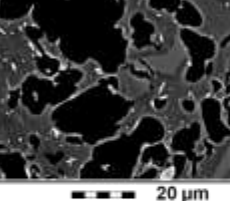
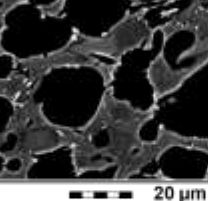
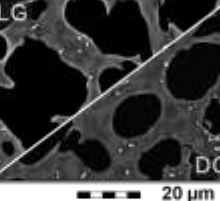
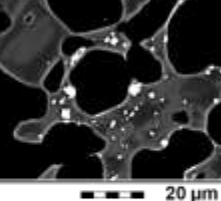
2007-2008 samples	<p>Lava dome (LD)</p>  <p>1 cm</p>	February 2014 samples	<p>Transparent white pumice (TWP)</p>  <p>1 cm</p>	<p>Non-transparent white pumice (NTWP)</p>  <p>1 cm</p>	<p>Transparent grey pumice (TGP)</p>  <p>1 cm</p>	<p>Transparent pink pumice (TPP)</p>  <p>1 cm</p>	<p>Banded pumice (BP)</p>  <p>2 cm</p>	<p>Scoria (S)</p>  <p>5 mm</p>
Binocular observation	 <p>3 mm</p>	Binocular observation	 <p>2 mm</p>	 <p>1 mm</p>	 <p>1 mm</p>	 <p>1 mm</p>	 <p>4 mm</p>	 <p>1 mm</p>
Microscopic observation	 <p>1 mm</p>	Microscopic observation	 <p>1 mm</p>	 <p>1 mm</p>	 <p>1 mm</p>	 <p>1 mm</p>	 <p>1 mm</p>	 <p>1 mm</p>
BSE (1500x)	 <p>20 μm</p>	BSE (1500x)	 <p>20 μm</p>	 <p>20 μm</p>	 <p>20 μm</p>	 <p>20 μm</p>	 <p>20 μm</p>	 <p>20 μm</p>
Description	<ul style="list-style-type: none"> <li>• Black to dark gray consolidated lava.</li> <li>• Massive to scoriaeous.</li> <li>• Vesicle: elongated to irregular.</li> </ul>	Description	<ul style="list-style-type: none"> <li>• White, transparent to translucent, fluidal to spheroidal shape.</li> <li>• Thin melt film.</li> <li>• Vesicle: elongated and spherical.</li> </ul>	<ul style="list-style-type: none"> <li>• White, non-transparent, fluidal to spheroidal shape.</li> <li>• Thin melt film.</li> <li>• Vesicle: elongated and spherical.</li> </ul>	<ul style="list-style-type: none"> <li>• Dark gray, transparent, fluidal to spheroidal shape.</li> <li>• Thin melt film.</li> <li>• Vesicle: elongated and spherical.</li> </ul>	<ul style="list-style-type: none"> <li>• Yellow, transparent to translucent, fluidal to spheroidal shape.</li> <li>• Thin melt film.</li> <li>• Bigger vesicle are dominated by elongated shape, while smaller are spherical.</li> </ul>	<ul style="list-style-type: none"> <li>• Multiple layers from white to dark grey to light grey; transparent to translucent, with fluidal to spheroidal shape.</li> <li>• Vesicle: elongated and spherical.</li> </ul>	<ul style="list-style-type: none"> <li>• Dark grey to dark brown; translucent, with fluidal to spheroidal shape.</li> <li>• Vesicle: mostly spherical with coalescence features.</li> </ul>

Figure 3. 3. Example and description of juvenile products from the 2007/08 and 2014 eruptions of Kelud.

## References

- Caudron, C., Mazot, A., Bernard, A., 2012. Carbon dioxide dynamics in Kelut volcanic lake. *J. Geophys. Res.* 117:B05102. <https://doi.org/10.1029/2011JB008806>
- Jeffery, A.J., Gertisser, R., Troll, V.R. et al., 2013. The pre-eruptive magma plumbing system of the 2007–2008 dome-forming eruption of Kelut volcano, East Java, Indonesia. *Contrib. Mineral. Petrol.* 166, 275–308. <https://doi.org/10.1007/s00410-013-0875-4>
- Global Volcanism Program, 2008. Report on Kelud (Indonesia) (Wunderman, R., ed.). *Bulletin of the Global Volcanism Network*, 33:3. Smithsonian Institution. <https://doi.org/10.5479/si.GVP.BGVN200803-263280>
- Goode, L.R., Handley, H. K., Cronin, S. J, Abdurrachman, M., 2019. Insights into eruption dynamics from the 2014 pyroclastic deposits of Kelut volcano, Java, Indonesia, and implications for future hazards. *J. Volcanol. Geotherm. Res.* 382, 6-23. <https://doi.org/10.1016/j.jvolgeores.2018.02.005>
- Hidayati, S., Kristianto, Basuki, A., Mulyana, I., 2009. A new lava dome emerged from crater lake of Kelud volcano, East Java, Indonesia. *Jurnal Geologi Indonesia* 4 (4), 229–238. <http://dx.doi.org/10.17014/ijog.vol4no4.20091>.
- Hidayati, S., Triastuty, H., Mulyana, I., Adi, S., Ishihara, K., Basuki, A., Kuswandarto, H., Priyanto, B., Solikhin, A., 2019. Differences in the seismicity preceding the 2007 and 2014 eruptions of Kelud volcano, Indonesia. *J. Volcanol. Geotherm. Res.* 382, 50–67. <https://doi.org/10.1016/j.jvolgeores.2018.10.017>
- Maeno, F., Nakada, S., Yoshimoto, M., Shimano, T., Hokanishi, N., Zaenuddin, A., Iguchi, M., 2019a. A sequence of a plinian eruption preceded by dome destruction at Kelud volcano, Indonesia, on 13 February, 2014, revealed from tephra fallout and pyroclastic density current deposits. *J. Volcanol. Geotherm. Res.* 382, 24–41. <https://doi.org/10.1016/j.jvolgeores.2017.03.002>
- Maeno, F., Nakada, S., Yoshimoto, M., Shimano, T., Hokanishi, N., Zaenuddin, A., Iguchi, M.,

2019b. Eruption pattern and a long-term magma discharge rate over the past 100 years at Kelud volcano, Indonesia. *J. Disaster. Res.* 14 (1), 27–39.

<https://doi.org/10.20965/jdr.2019.p0027>

Siebert, L., Simkin, T., Kimberly, P., 2011. *Volcanoes of the world*, 3rd edn. University of California Press, Los Angeles, p 551

Surono, 2007, Pusat Vulkanologi Dan Mitigasi Bencana Geologi, Pos Pengamatan Gunungapi Kelut (Hasil evaluasi tingkat kegiatan G. Kelut): Departemen Energi Dan Sumber Daya Mineral, Republik Indonesia, Badan Geologi, Nomor, 112/GK/X/2007, 30 Oktober 2007. In Indonesian.

## Chapter 4

# Pre-eruptive degassing and crystallization process of the 2007/08 and 2014 eruptions of Kelud volcano, Indonesia.

### 4.1. Introduction

Transitions between effusive and explosive eruptions are frequently observed in arc volcanoes and have been linked to changes in various factors, such as magma composition, volatile content, degassing process, magma recharge, and crystallization during ascent (e.g., Hammer et al., 1999; Jeffrey et al., 2013; Preece et al., 2014; Lormand et al., 2021; Waelkens et al., 2022). Magmatic recharge may affect magma ascent dynamics, influencing the rate of magma ascent and degassing pathways. Previous studies have shown that the style of degassing plays a significant role in governing eruptive behavior (Zurek et al., 2019). During open-system degassing, volatiles are exsolved and outgassed from the melt, leading to effusive eruptive activity (e.g., Noguchi et al., 2008; Toramaru et al., 2008). In closed-system degassing, the exsolved volatiles remain within the system, thus increasing the overpressure to produce explosive eruption (e.g., Preece et al., 2016; Kawaguchi et al., 2021).

Silicate melt inclusions (referred to as SMIs) trapped within phenocrysts offer a valuable geochemical insights for investigating magma sources and magmatic processes, as they can preserve evidence of the pre-eruptive melt that may not be preserved elsewhere. Melt inclusions, for instance, can preserve the composition and dissolved volatile concentrations of a pre-eruptive melt and are commonly utilized to estimate minimum pressures of crystallization and degassing pathways present during crystallization (i.e., Preece et al., 2016; Kawaguchi et al., 2021; Waelkens et al., 2021). However, the interpretation of volatile concentrations in melt inclusions poses challenges due to potential alterations in the initial composition, such as the

development of boundary layer conditions or post-entrapment processes like crystallization and the loss of volatile elements through the crystal lattice or cracks (e.g., Preece et al., 2014; Kawaguchi et al., 2021).

Focusing on the volcanic products from the 2007/08 and 2014 eruptions of Kelud, Indonesia (Fig. 4.1), this chapter presents major elements and volatile components (H<sub>2</sub>O, CO<sub>2</sub>, F, S, and Cl) concentrations in clinopyroxene-hosted melt inclusions gathered from stratigraphically controlled samples of 2007/08 and 2014 eruptions. Additionally, host clinopyroxene crystals, whole-rock, and groundmass glass compositions are presented to supplement the data. Comparison of 2007/08 with 2014 samples elucidates pre-eruptive conditions during the two most recent and contrasting eruption styles of Kelud. The results of this work are beneficial for hazard assessment at Kelud and possibly other volcanoes with similar eruptive behavior worldwide.

## 4.2. Analytical methods

### 4.2.1. Sample selection and preparation

In order to understand the driving force behind the transition between explosive and effusive eruption activity, the volcanic product from 2007 and 2014 eruption of Kelud were examined. Time-controlled samples were collected from both pyroclastic density current and tephra fallout deposits during two episodes of field survey in August 2018 and October 2018 and samples acquired by Astiti Anggorowati in 2017 (personal communication).

Five tephra samples used for silicate melt inclusion (SMI) analysis correspond to the 3 eruptive stages of 2 eruption events: basalt of 2007/08 dome, banded pumice dark grey part (BP DG) and scoria bomb (S) of 2014 PDC-1 (Stage I of Maeno et al., 2019a), as well as transparent pink pumice (TPP) and transparent white pumice of 2014 CPF (Stage II of Maeno et al., 2019a) (Fig. 4.2). Clinopyroxene-hosted SMI were specifically used to obtain information about

volatile characteristics of magma, as well as to avoid the volatile diffusive loss through the lattice during phenocryst growth as observed in some plagioclase phenocrysts with complex zoning (Cassidy et al., 2019). Samples were gently crushed and separated using hand-sieves. Several hundred clinopyroxene crystals were picked by hand under a binocular microscope in the fraction between 0.5 and 1 mm since the clinopyroxene was abundant in this grain size. Each clinopyroxene crystal was then mounted in low viscosity resin and polished by hand down to 0.3  $\mu\text{m}$  using alumina solution until melt inclusions were exposed. Subsequently, clinopyroxene crystals were removed from the resin and mounted together in an indium holder before gold coating for secondary ion mass spectrometry (SIMS).

Additional samples from other eruption stages were also used for whole-rock and groundmass glass analysis (i.e., NTWP and TWP of CPF). Whole-rock compositions of 2007 and 2014 eruption samples were acquired from a fresh fraction of selected samples. Thirty samples were cleaned and purified under wet condition using W-170-ST ultrasonic cleaner, then dried overnight at 60°C before preparing fused glass beads for major and trace element measurements. Loss on ignition (LOI) value was acquired by weighing 3 g of the powdered sample after furnacing at 900 °C for 3 hours.

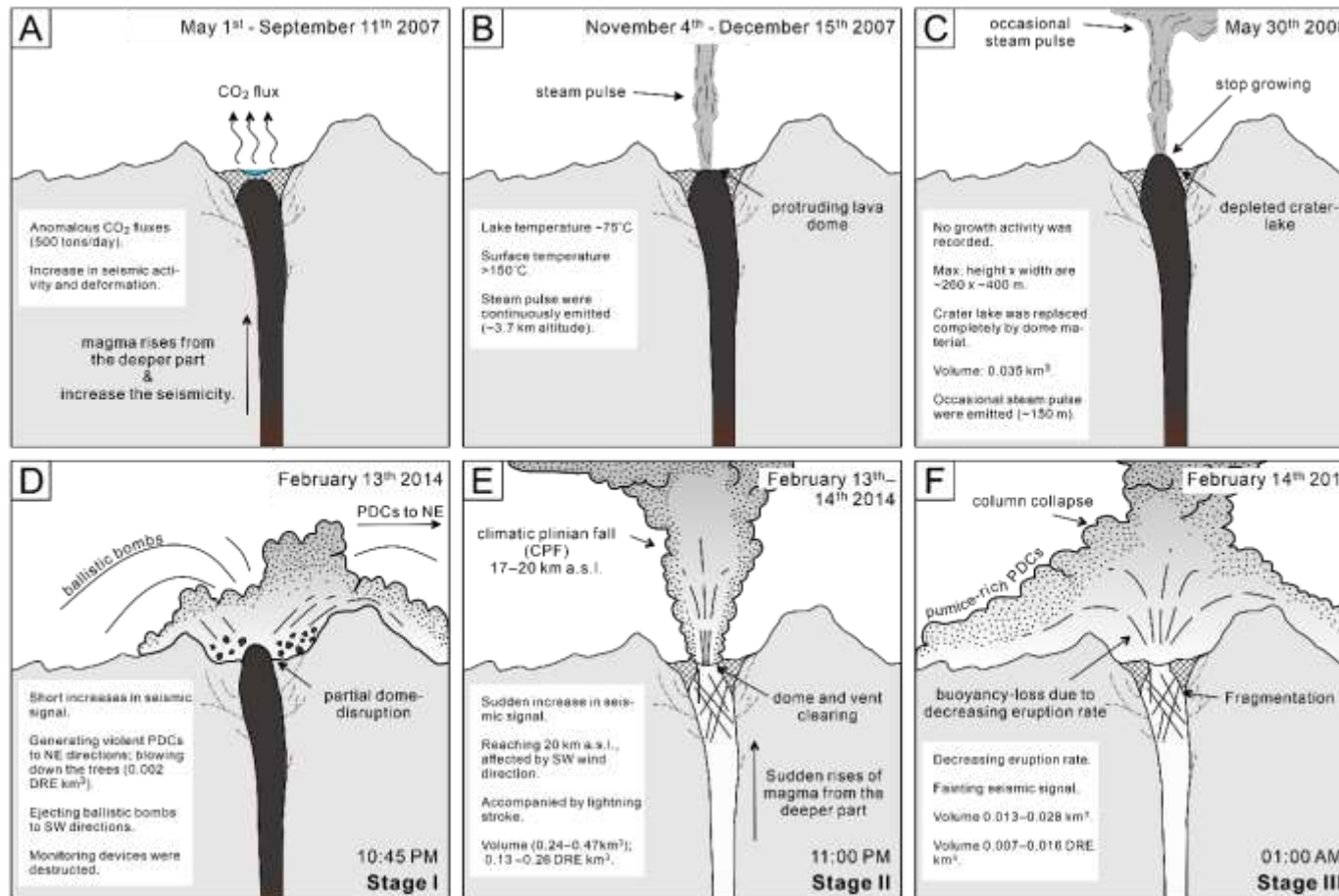


**Figure 4. 1.** Simplified sketch of the evolution of the 2007/08 lava dome and 2014 explosive eruptions. A) Increase in seismic activity and measured CO<sub>2</sub> fluxes denoted the unrest of the volcano prior to the 2007/08 eruption. B) Early stage of lava dome effusion was recorded from a sudden increase in surface temperature and emission of a steam pulse from a fresh protruding dome material in the lake area. C) Lava dome continuously grew until 30 May 2008, with a height reaching ~200 m from the crater surface. D) Seven years later, the 2007/08 dome was destroyed by an eruption on 13 February 2014 and produced ballistic bombs and PDCs towards the NE flanks of Kelud. E) At 11 PM on the same day, the plinian eruption column was developed and completely destroyed the 2007/08 dome, producing 0.24–0.47 km<sup>3</sup> pumice fallout deposits along the WSW and W directions. F) The marginal column collapse occurred on 14 February, emplacing pumice-rich PDC deposits along the main river flow around Kelud volcano.

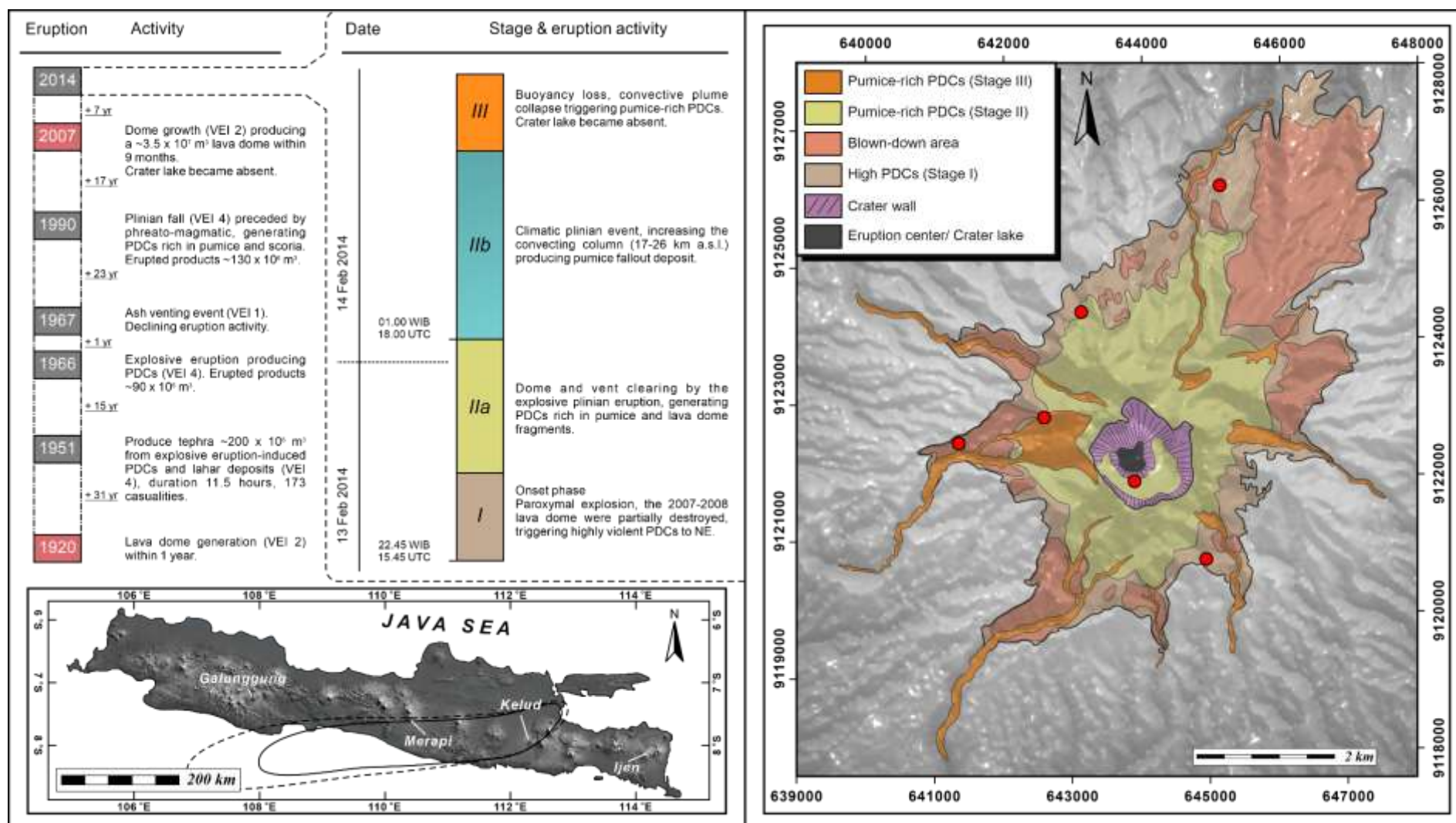


**Figure 4. 2.** Stages and distribution maps of 2014 eruption deposits (after Maeno et al., 2019a; Goode et al., 2019). Roman numerals indicate eruption stages in the center column and distribution map. The inset map shows the location of Kelud volcano, alongside other volcanoes on Java Island, and the distribution of fallout deposits of the 2014 eruption produced during stage II (CPF). Sample localities are marked with red circles.

#### 4.2.2. Geochemical analysis

Whole-rock major and trace elements of 2007 and 2014 eruption samples were measured by X-ray fluorescence (XRF) analysis on flux-fused beads using a Rigaku ZSX Primus II XRF spectrometer at Faculty of International Resource Sciences, Akita University.

Phases contained in melt inclusions were identified using a Raman spectrometer (Renishaw inVia Reflex) attached to a Leica DM2500M microscope with a 100× long working distance lens at the Faculty of International Resource Sciences, Akita University. For this analysis, a 532 nm laser source (Cobolt RL532150) with a laser power of 150 mW and slit size of 1 to 3  $\mu\text{m}$  was utilized. A silicon standard was used to calibrate the spectrometer by counting the spectrum within  $\pm 1 \text{ cm}^{-1}$  of the standard peak at  $520.5 \text{ cm}^{-1}$ . The measured Raman spectra were obtained using simple accumulation with 1s acquisition time. Due to the fluorescence of the epoxy resin filling the mounted grains, a background noise appeared during this analysis. The analyzed points were selected from massive-coherent areas (approximately  $10\mu\text{m}\times 10\mu\text{m}$ ) of melt inclusions to reduce the background. Data were then processed with the Wire 3.4 software package (Renishaw).

Melt inclusions were subsequently analyzed for  $\text{H}_2\text{O}$ ,  $\text{CO}_2$ , F, S, Cl, and  $\text{P}_2\text{O}_5$  concentrations by using a Cameca IMS- 1280HR SIMS at Kochi Institute, JAMSTEC, Japan, following the procedure described by Shimizu et al. (2017). The SIMS analysis was conducted before EPMA analysis to avoid possible carbon contamination from the carbon coating. The acquisition uses a 10-15  $\mu\text{m}$  defocused beam, with a 0.5 primary current, 300 –500 pA, and a 20 keV  $\text{Cs}^+$  ion beam (10 keV at both the ion source and sample surface). Secondary ions were accelerated by a -10 keV electron beam ( $\sim 100 \mu\text{m}$  in diameter) for electrostatic charge compensation, with the field aperture set to  $5 \times 5 \mu\text{m}$  on the sample surface. Negative secondary ions were measured using the peak switching method by an axial electron multiplier (11.9 amu mass position), and the results were based on 10 cycles of measurement with an acquisition time of  $\sim 6$  min for each analysis. The relative analytical uncertainties (2SE%) were frequently checked by measuring

the EPR-G3 in-house basaltic glass standard (Shimizu et al. 2017), yielding values of 0.4, 1.4, 0.7, 0.3, 0.4, and 0.9% for H<sub>2</sub>O, CO<sub>2</sub>, F, Cl, S, and P<sub>2</sub>O<sub>5</sub>, respectively. The measured values for P<sub>2</sub>O<sub>5</sub> are relatively similar between EPMA and SIMS analysis (~80%), so when P<sub>2</sub>O<sub>5</sub> was measured by both methods, SIMS values were used due to lower analytical.

Mineral and glass major elements and volatiles were determined using a JEOL JXA-8230 electron probe microanalyzer (EPMA) at the Faculty of International Resource Sciences, Akita University. Major element and volatiles (S, F, and Cl) in melt inclusions and groundmass glass was analyzed using a 5–10 µm defocused beam, with a 15 kV accelerating voltage and a 6 nA beam current. Peak counting times range from 10 to 20 s for the major elements and 40 to 80 s for the volatiles. Major elements were measured in the clinopyroxene host crystals near each melt inclusion using a focused beam with a 15 kV accelerating voltage, a 20 nA beam current, and applying a beam diameter of 5 µm. Peak counting times per element were set on 10 to 20 s. Natural minerals and synthetic compounds were used as the standard to calibrate the instrument and check the accuracy and precision during element analysis. In order to minimize the alkali migration during acquisition, sodium (*Na*) was always measured first. Detection limits are ~180–250 ppm for major elements, ~35 ppm for Cl, ~70 ppm for S, and ~470 ppm for F. Analytical uncertainties based upon repetitive analysis on natural and synthetic standards were in order of <5 % (relative) for major elements, S, and Cl, and <15 % (relative) for F.

#### 4.2.3. Data processing

All of the major element and volatile data of melt inclusions were corrected to account for the post-entrapment crystallization (PEC) that happened at the interface between melt inclusions and clinopyroxene hosts. Using the reverse fractional crystallization modeling function of the Petrolog3 software (Danyushevsky and Plechov, 2011), the corrections were made by adding 0.1 wt.% of the calculated host clinopyroxene composition that is in equilibrium with the melt inclusion (Nielsen et al., 1988). The calculated degree of PEC is 10%, but typically <8 %.

Corrected volatile concentrations were adjusted, assuming volatiles are incompatible with hosting minerals, and the corrected values are used for the discussion.

### 4.3. Results

#### 4.3.1. Major element geochemistry

##### *Clinopyroxene compositions*

The major element composition of clinopyroxene host crystals was measured and plotted alongside other pyroxene phenocrysts within the same eruptive products from a previous study (Table 4.1 and Fig. 4.3; Jeffrey et al., 2013). Clinopyroxene from the 2007/08 and 2014 samples are generally augite and share compositions, covering a range of  $Wo_{41-46}En_{38-43}Fs_{14-17}$  (Fig. 4.3D). The magnesium number [ $Mg\# = Mg/(Mg + Fe^{2+}) \times 100$  in mole] of the 2007/08 clinopyroxenes ( $Mg\# = 74-80$ ) also overlaps with the 2014 clinopyroxene ranges ( $Mg\# = 73-79$ , Fig. 4.3E). Although the majority of clinopyroxene phenocrysts from the 2007/08 and 2014 samples contain ~1–3 wt.%  $Al_2O_3$ , the 2014 TPP crystals display the largest variation, with values ranging from 1.0 to 5.1 wt.%. These values are similar to the previous analysis of 2007/08 Kelud clinopyroxenes, for which concentrations of 1–5 wt.%  $Al_2O_3$  are reported (Jeffrey et al., 2013). The similarity of clinopyroxene compositions in both 2007/08 and 2014 samples suggests that the analyzed host crystals used for this study are representative of the clinopyroxene population.

**Table 4. 1.** Representative clinopyroxene host compositions of products from 2007/08 and 2014 eruptions analyzed using electron microprobe. Stages I and II of the 2014 eruption refer to chronology of Maeno et al. (2019a). FeO\*= total iron. LD: lava dome; BP DG: banded pumice dark grey; SB: scoria bomb; TWP: transparent white pumice; TPP: transparent pink pumice.

Sample	LD C-4				BP DG				S	
Spot no.	4-3	18-1	4-2	6-1	11-2	17-2	9-1	8-3	18-2	29-1
Eruption	2007/08				2014				2014	
Stage	-	-	-	-	I (PDC-1)				I (PDC-1)	
Mineral	Cpx	Cpx	Cpx	Cpx	Cpx	Cpx	Cpx	Cpx	Cpx	Cpx
Major element (wt.%)										
SiO <sub>2</sub>	52.23	51.43	52.03	51.87	51.42	51.57	51.94	50.63	51.86	51.72
TiO <sub>2</sub>	0.43	0.32	0.39	0.25	0.37	0.43	0.27	0.45	0.32	0.37
Al <sub>2</sub> O <sub>3</sub>	1.90	1.88	1.87	1.25	1.93	1.97	1.50	3.53	1.65	2.10
Cr <sub>2</sub> O <sub>3</sub>	0.07	0.00	0.02	0.00	0.02	0.00	0.06	0.04	0.02	0.00
FeO*	9.76	9.92	9.46	8.92	9.78	9.76	9.31	8.53	9.85	9.55
MnO	0.50	0.53	0.47	0.54	0.52	0.55	0.59	0.37	0.56	0.56
MgO	14.34	14.42	14.86	14.64	13.77	14.34	14.53	14.26	14.23	14.56
CaO	21.00	20.42	20.63	21.65	21.11	20.38	20.98	21.22	20.35	20.26
Na <sub>2</sub> O	0.28	0.27	0.30	0.27	0.27	0.34	0.32	0.28	0.26	0.30
K <sub>2</sub> O	0.00	0.01	0.01	0.01	0.00	0.01	0.00	0.00	0.01	0.01
NiO	0.00	0.00	0.01	0.03	0.00	0.02	0.00	0.02	0.00	0.04
Total	100.51	99.20	100.06	99.43	99.19	99.37	99.49	99.33	99.10	99.46
Structural formula based on O=6 (apfu)										
Si	1.94	1.94	1.94	1.95	1.94	1.94	1.95	1.90	1.96	1.94
Ti	0.01	0.01	0.01	0.01	0.01	0.01	0.01	0.01	0.01	0.01
Al	0.08	0.08	0.08	0.06	0.09	0.09	0.07	0.16	0.07	0.09
Cr	0.00	0.00	0.00	0.00	0.00	0.00	0.00	0.00	0.00	0.00
Fe <sup>3+</sup>	0.04	0.06	0.05	0.07	0.04	0.05	0.06	0.06	0.02	0.04
Fe <sup>2+</sup>	0.27	0.26	0.24	0.21	0.27	0.26	0.24	0.21	0.29	0.26
Mn	0.02	0.02	0.01	0.02	0.02	0.02	0.02	0.01	0.02	0.02
Mg	0.80	0.81	0.83	0.82	0.78	0.80	0.81	0.80	0.80	0.81
Ca	0.84	0.83	0.82	0.87	0.85	0.82	0.84	0.85	0.82	0.81
Na	0.02	0.02	0.02	0.02	0.02	0.02	0.02	0.02	0.02	0.02
K	0.00	0.00	0.00	0.00	0.00	0.00	0.00	0.00	0.00	0.00
Ni	0.00	0.00	0.00	0.00	0.00	0.00	0.00	0.00	0.00	0.00
ΣCation	4.01	4.02	4.02	4.02	4.01	4.02	4.02	4.02	4.01	4.01
XWo	0.43	0.42	0.42	0.44	0.43	0.42	0.42	0.44	0.42	0.42
XEn	0.41	0.41	0.42	0.41	0.41	0.41	0.42	0.41	0.41	0.42
XF <sub>s</sub>	0.16	0.17	0.16	0.15	0.16	0.17	0.16	0.15	0.17	0.16
Total	1.00	1.00	1.00	1.00	1.00	1.00	1.00	1.00	1.00	1.00
Mg#	74.88	76.00	77.40	79.86	74.37	75.68	77.53	79.29	73.63	75.81

**Table 4. 1. (continued).**

Sample	S		TPP				TWP			
	19-1	36-1	7-2	23-1	23-2	29-2	7-2	27-1	6-1	19-1
Spot no.	2014		2014				2014			
Eruption	2014		2014				2014			
Stage	I (PDC-1)		II (CPF)				II (CPF)			
Mineral	Cpx	Cpx	Cpx	Cpx	Cpx	Cpx	Cpx	Cpx	Cpx	Cpx
Major element (wt.%)										
SiO <sub>2</sub>	52.05	51.16	51.97	52.86	52.53	51.37	51.82	52.18	52.30	51.86
TiO <sub>2</sub>	0.36	0.43	0.38	0.27	0.30	0.33	0.29	0.32	0.29	0.34
Al <sub>2</sub> O <sub>3</sub>	1.61	2.54	2.24	1.31	1.27	2.61	1.72	1.50	1.96	1.70
Cr <sub>2</sub> O <sub>3</sub>	0.02	0.00	0.00	0.02	0.00	0.00	0.01	0.00	0.00	0.00
FeO*	9.18	8.70	9.85	8.87	8.95	8.33	9.95	9.24	8.89	8.76
MnO	0.53	0.44	0.54	0.51	0.56	0.35	0.58	0.55	0.40	0.44
MgO	14.68	14.68	14.33	14.59	14.94	14.63	14.45	14.74	14.81	14.84
CaO	20.86	20.94	20.00	21.16	20.99	21.25	19.89	20.33	20.80	20.78
Na <sub>2</sub> O	0.28	0.26	0.31	0.25	0.26	0.25	0.29	0.26	0.23	0.31
K <sub>2</sub> O	0.00	0.00	0.00	0.00	0.00	0.00	0.00	0.00	0.00	0.00
NiO	0.02	0.00	0.00	0.00	0.03	0.03	0.00	0.05	0.00	0.00
Total	99.60	99.16	99.62	99.83	99.82	99.15	98.99	99.17	99.67	99.02
Structural formula based on O=6 (apfu)										
Si	1.95	1.92	1.95	1.97	1.96	1.93	1.95	1.96	1.95	1.95
Ti	0.01	0.01	0.01	0.01	0.01	0.01	0.01	0.01	0.01	0.01
Al	0.07	0.11	0.10	0.06	0.06	0.12	0.08	0.07	0.09	0.08
Cr	0.00	0.00	0.00	0.00	0.00	0.00	0.00	0.00	0.00	0.00
Fe <sup>3+</sup>	0.04	0.06	0.02	0.01	0.04	0.04	0.03	0.02	0.02	0.04
Fe <sup>2+</sup>	0.24	0.22	0.29	0.27	0.24	0.22	0.29	0.27	0.26	0.23
Mn	0.02	0.01	0.02	0.02	0.02	0.01	0.02	0.02	0.01	0.01
Mg	0.82	0.82	0.80	0.81	0.83	0.82	0.81	0.83	0.82	0.83
Ca	0.84	0.84	0.80	0.85	0.84	0.85	0.80	0.82	0.83	0.84
Na	0.02	0.02	0.02	0.02	0.02	0.02	0.02	0.02	0.02	0.02
K	0.00	0.00	0.00	0.00	0.00	0.00	0.00	0.00	0.00	0.00
Ni	0.00	0.00	0.00	0.00	0.00	0.00	0.00	0.00	0.00	0.00
ΣCation	4.01	4.02	4.01	4.00	4.01	4.01	4.01	4.01	4.01	4.01
XWo	0.43	0.43	0.42	0.43	0.43	0.44	0.41	0.42	0.43	0.43
XEn	0.42	0.42	0.41	0.42	0.42	0.42	0.42	0.42	0.42	0.42
XF <sub>s</sub>	0.16	0.15	0.17	0.15	0.15	0.14	0.17	0.16	0.15	0.15
Total	1.00	1.00	1.00	1.00	1.00	1.00	1.00	1.00	1.00	1.00
Mg#	77.00	79.15	73.23	75.03	77.45	79.06	73.96	75.45	76.05	78.26

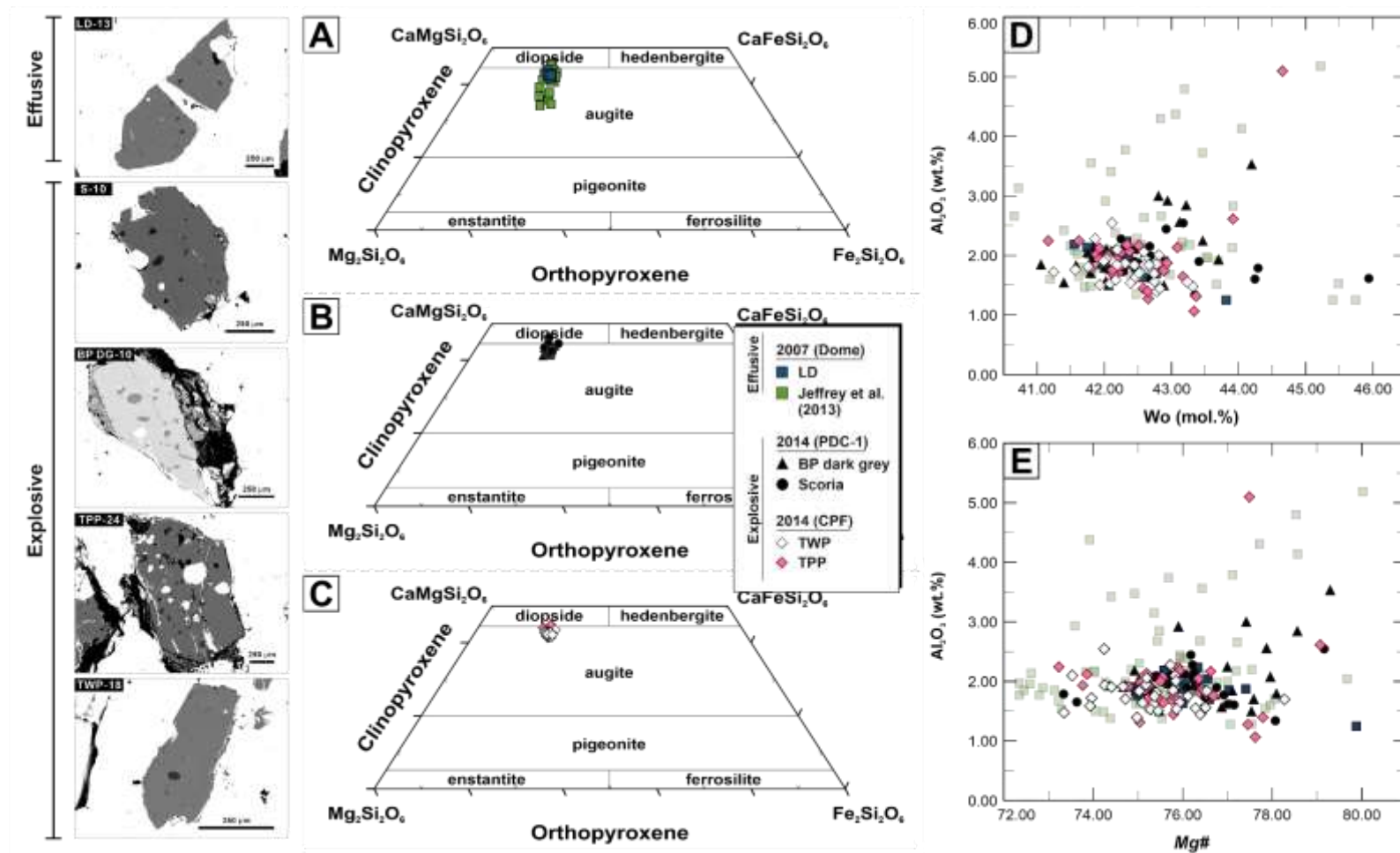


**Figure 4. 3.** Typical clinopyroxene phenocrysts used for this study. Clinopyroxene compositions of analyzed samples plotted on quadrilateral (Di-Hd-En-Fs) diagram for A) 2007/08 dome, B) 2014 PDC-1, and C) 2014 CPF are usually augite to diopside (Morimoto, 1989). Plots of  $\text{Al}_2\text{O}_3$  vs. D) wollastonite end-members (mol.%) and E) Mg# of all measured clinopyroxene shows systematic compositional variations between different eruptive products, including phenocrysts from previous study (Jeffrey et al., 2013).

*SMI, bulk, and groundmass glass compositions*

The bulk-chemical composition of 2007/08 and 2014 products have similar concentrations ( $\text{SiO}_2$  ranges from 54.0 to 55.4 wt.%) and lie within a narrow compositional range of basaltic andesite field in the total alkali vs. silica diagram (Le Maitre et al., 2002) (Fig. 4.4; Table 4.2). A comparison of stratigraphically different lithologies reveals that the 2007/08 dome samples extends to slightly more evolved compositions (54.1–55.4 wt.%  $\text{SiO}_2$ ) than the 2014 products (54.0–55.0 wt.%  $\text{SiO}_2$ ), although the disparities are marginal. A compositional gap of >8 wt.%  $\text{SiO}_2$  is observed between the most evolved whole-rock composition and the least evolved melt inclusions (Fig. 4.4), where the melt inclusions are dacitic to rhyolitic (64.1–74.7 wt.%  $\text{SiO}_2$ ) after PEC correction and normalized to 100 % on a volatile-free basis (Table 4.3). Despite having compositional gap with whole-rock compositions, both 2007/08 and 2014 melt inclusions cover a similar compositional range. Similarly, groundmass glass compositions have compositions of dacite to rhyolite with  $\text{SiO}_2$  ranging from 63.7 to 78.8 wt.% (Table 4.4). The most evolved melt compositions observed in this study come from the 2007/08 domes, which have the  $\text{SiO}_2$  between 75.0 and 78.8 wt.%, while the glass compositions of 2014 products have slightly lower  $\text{SiO}_2$  values ranging from 63.7 to 75.7 wt.%. Furthermore, the major oxides of whole-rock and groundmass are plotted against silica value concerning 100% anhydrous condition (Fig. 4.5). The overall trend of  $\text{K}_2\text{O}$  displays a positive correlation with  $\text{SiO}_2$ , while  $\text{Al}_2\text{O}_3$ ,  $\text{FeO}^*$  (total iron calculated as  $\text{FeO}$ ),  $\text{MgO}$ , and  $\text{CaO}$  correlate negatively with  $\text{SiO}_2$  concentrations.  $\text{TiO}_2$  and  $\text{P}_2\text{O}_5$  show no systematic correlation with the  $\text{SiO}_2$  concentration. The  $\text{Na}_2\text{O}$  trend is inflexed with  $\text{Na}_2\text{O}$  values positively correlate with silica concentrations until ~69 wt.%  $\text{SiO}_2$  before  $\text{Na}_2\text{O}$  begin to decrease with an increase in  $\text{SiO}_2$ .

**Table 4. 2.** Whole-rock major and trace element concentrations of the volcanic products from 2007/08 and 2014 eruptions. Stages I and II of the 2014 eruption refer to chronology of Maeno et al. (2019a). FeO\*= total iron.

Sample	A-2	A-3	B-2	B-5	C-3	C-4	BP W	BP LG
Eruption	2007/08	2007/08	2007/08	2007/08	2007/08	2007/08	2014	2014
Stage	-	-	-	-	-	-	I (PDC-1)	
Major element (wt.%)								
SiO <sub>2</sub>	55.39	54.14	55.43	55.39	54.89	54.56	54.99	54.93
TiO <sub>2</sub>	0.65	0.68	0.64	0.63	0.66	0.66	0.68	0.67
Al <sub>2</sub> O <sub>3</sub>	18.72	18.83	18.71	18.97	18.70	19.02	18.74	18.79
FeO*	8.88	9.39	8.79	8.65	8.99	9.08	9.25	9.01
MnO	0.20	0.21	0.20	0.20	0.21	0.20	0.21	0.21
MgO	3.72	4.04	3.69	3.58	3.83	3.81	3.88	3.80
CaO	8.87	9.38	8.89	8.93	9.08	9.25	8.83	9.13
Na <sub>2</sub> O	2.97	2.77	2.97	2.95	2.83	2.80	2.84	2.85
K <sub>2</sub> O	0.68	0.67	0.71	0.69	0.70	0.67	0.72	0.71
P <sub>2</sub> O <sub>5</sub>	0.15	0.14	0.15	0.15	0.14	0.14	0.15	0.14
Total	100.22	100.25	100.17	100.13	100.04	100.21	100.27	100.23
LOI*	-0.23	0.17	-0.23	-0.03	0.05	-0.11	0.72	0.33
Trace element (ppm)								
V	185	200	173	165	186	179	184	187
Cr	17	18	14	15	16	14	15	15
Sr	591	576	591	597	578	586	574	582
Y	64	65	63	63	62	63	63	63
Zr	47	47	48	47	48	46	47	45
Nb	3	6	9	8	10	5	14	7
Ba	492	441	496	481	442	512	537	491

Sample	BP DG1	BP DG2	TWP1	TWP2	TPP1	TPP2	TGP	SB
Eruption	2014	2014	2014	2014	2014	2014	2014	2014
Stage	I (PDC-1)							
Major element (wt.%)								
SiO <sub>2</sub>	54.01	54.05	54.99	54.67	54.82	54.76	54.56	54.86
TiO <sub>2</sub>	0.69	0.69	0.65	0.66	0.67	0.65	0.67	0.68
Al <sub>2</sub> O <sub>3</sub>	18.94	18.70	18.99	18.90	18.85	18.91	18.82	18.73
FeO*	9.32	9.42	8.69	9.08	9.09	8.86	9.15	9.22
MnO	0.21	0.21	0.20	0.20	0.21	0.20	0.21	0.21
MgO	4.05	4.11	3.64	3.77	3.85	3.69	3.90	3.87
CaO	9.34	9.25	9.12	9.16	9.08	8.99	9.18	8.98
Na <sub>2</sub> O	2.75	2.75	2.86	2.84	2.79	2.80	2.78	2.78
K <sub>2</sub> O	0.66	0.67	0.71	0.70	0.72	0.72	0.68	0.70
P <sub>2</sub> O <sub>5</sub>	0.14	0.15	0.14	0.14	0.15	0.14	0.14	0.14
Total	100.09	100.00	99.988	100.128	100.21	99.72	100.08	100.16
LOI*	-0.07	-0.06	0.02	0.00	0.03	0.05	0.24	0.47

\*LOI: Lost on ignition.

Trace element (ppm)								
V	192	204	178	189	181	184	194	192
Cr	18	22	17	16	14	19	18	17
Sr	579	576	589	588	582	589	581	575
Y	65	65	64	64	63	64	65	62
Zr	45	44	47	45	46	48	46	47
Nb	8	10	7	5	4	6	5	6
Ba	451	496	423	470	452	431	449	504

Sample	NTWP-1	NTWP-2	NTWP-3	NTWP-4	NTWP-5	TWP-1	TWP-2	TWP-3
Eruption Stage	2014	2014	2014	2014	2014	2014	2014	2014
II (CPF)								
Major element (wt.%)								
SiO <sub>2</sub>	54.59	54.58	55.06	54.93	55.01	54.82	54.88	54.64
TiO <sub>2</sub>	0.66	0.66	0.65	0.66	0.66	0.64	0.66	0.65
Al <sub>2</sub> O <sub>3</sub>	18.76	18.74	18.83	18.76	19.00	18.86	18.56	18.60
FeO*	9.05	9.06	8.82	9.04	8.82	8.74	9.07	9.06
MnO	0.20	0.21	0.20	0.20	0.20	0.20	0.21	0.21
MgO	3.96	3.85	3.70	3.85	3.74	3.78	3.92	4.01
CaO	9.19	9.15	8.97	8.87	9.09	9.09	8.96	9.19
Na <sub>2</sub> O	2.75	2.81	2.84	2.85	2.87	2.83	2.81	2.77
K <sub>2</sub> O	0.70	0.70	0.73	0.71	0.71	0.70	0.71	0.68
P <sub>2</sub> O <sub>5</sub>	0.14	0.14	0.14	0.14	0.14	0.14	0.15	0.14
Total	100.00	99.90	99.93	100.03	100.24	99.80	99.93	99.97
LOI*	0.05	0.07	0.05	0.00	0.12	0.16	0.30	0.06
Trace element (ppm)								
V	179	189	171	186	180	177	180	188
Cr	15	16	15	12	18	15	16	16
Sr	580	584	583	580	580	583	566	577
Y	63	63	64	63	63	63	64	62
Zr	45	46	47	48	46	46	47	45
Nb	6	7	6	13	4	6	3	8
Ba	472	476	444	479	444	461	431	413

\*LOI: Lost on ignition.

**Table 4. 2.** (continued).

Sample	TWP-4	TPP-1	TPP-2	TPP-3	TPP-4	S-1
Eruption	2014	2014	2014	2014	2014	2014
Stage						
Major element (wt.%)						
SiO <sub>2</sub>	54.94	55.36	54.69	55.11	54.84	55.01
TiO <sub>2</sub>	0.65	0.64	0.67	0.66	0.67	0.65
Al <sub>2</sub> O <sub>3</sub>	18.85	18.94	18.70	18.60	18.62	18.90
FeO*	8.91	8.66	9.11	9.02	9.20	8.83
MnO	0.21	0.20	0.21	0.21	0.21	0.20
MgO	3.78	3.65	3.91	3.86	3.87	3.71
CaO	9.11	9.02	9.12	8.98	9.03	9.06
Na <sub>2</sub> O	2.88	2.94	2.80	2.87	2.83	2.90
K <sub>2</sub> O	0.71	0.73	0.72	0.71	0.70	0.69
P <sub>2</sub> O <sub>5</sub>	0.15	0.15	0.14	0.15	0.14	0.14
Total	100.18	100.29	100.04	100.16	100.12	100.09
LOI*	0.07	0.04	-0.04	0.07	-0.09	0.05
Trace element (ppm)						
V	179	169	186	179	193	168
Cr	19	15	19	16	16	17
Sr	586	584	577	578	576	587
Y	64	63	64	63	63	63
Zr	47	49	46	47	45	47
Nb	9	8	8	7	4	3
Ba	450	499	436	505	488	492

\*LOI: Lost on ignition.

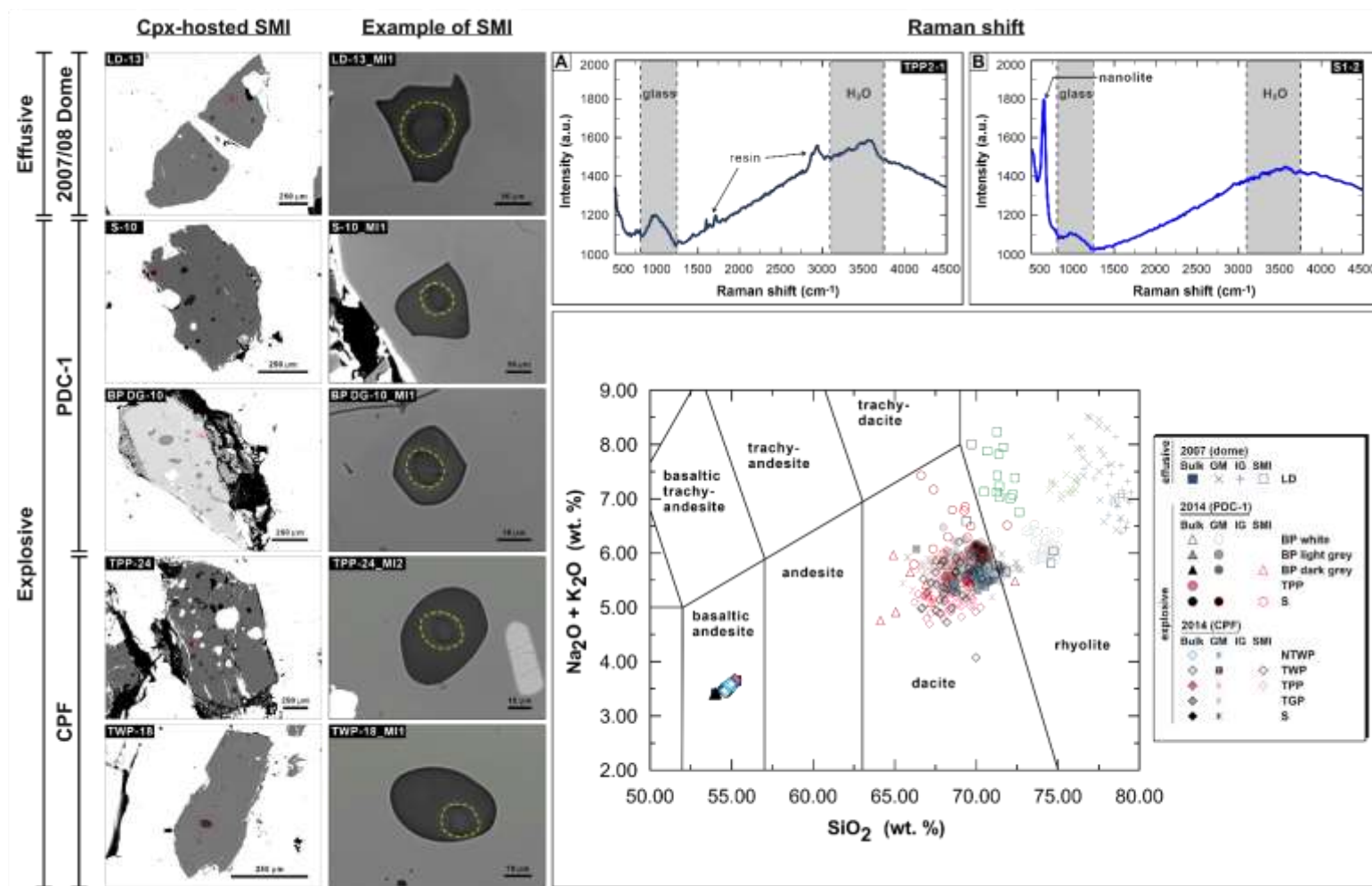


**Figure 4.** Typical *cpx*-hosted silicate melt inclusions used for this study. A) Raman shift indicates H<sub>2</sub>O usually present in the analyzed SMI. B) Although no visible daughter mineral observed, some inclusions may contain nanolite in the glass phase. Total alkalis vs. silica (after [Le Maitre et al., 2002](#)) of whole-rock, groundmass glass, and SMI of 2007/08 and 2014 volcanic products plotted along with previously published data of 2007/08 eruption of Kelud ([Jeffrey et al., 2013](#)). Yellow circle represents SIMS crater.

**Table 4. 3.** Representative analyses of melt inclusion compositions from 2007/08 and 2017 eruptions. Stages I and II of the 2014 eruption refer to chronology of Maeno et al. (2019). Lithology types are as follows: lava dome (LD), banded pumice dark grey (BP DG), scoria bomb (SB), transparent white pumice (TWP), and transparent pink pumice (TPP). MI denotes melt inclusion number. PEC denotes degree of post-entrapment *crystallization* corrected for (%). All major elements (in wt. %) determined by electron microprobe *with* all values are shown after PEC correction.  $P_2O_5^b$  and  $H_2O$  in wt. % and  $CO_2$ ,  $SO_3$ , F, and Cl in ppm were measured by ion microprobe.

Sample	LD C-4			BP DG			SB			TPP			TWP		
MI	25-1	4-2	6-1	8-3	19-3	2-1	7-3	7-2	18-1	16-2	17-2	7-6	28-2	12-3	27-4
Eruption	2007/08			2014			2014			2014			2014		
Stage	-	-	-	I (PDC-1)			I (PDC-1)			II (CPF)			II (CPF)		
Major element (wt.%) <sup>a</sup>															
SiO <sub>2</sub>	65.15	69.00	71.75	60.95	63.89	66.22	66.03	67.76	68.54	63.38	64.01	63.88	63.68	67.08	66.81
TiO <sub>2</sub>	0.37	0.53	0.40	0.37	0.46	0.55	0.60	0.59	0.54	0.39	0.40	0.36	0.60	0.53	0.48
Al <sub>2</sub> O <sub>3</sub>	15.70	14.19	13.69	18.37	17.73	14.23	18.71	16.60	14.90	17.23	17.28	16.13	16.64	15.84	14.70
Cr <sub>2</sub> O <sub>3</sub>	0.00	0.04	0.00	0.00	0.00	0.00	0.00	0.00	0.02	0.01	0.02	0.00	0.02	0.02	0.00
Fe <sub>2</sub> O <sub>3</sub>	0.52	0.43	0.14	0.30	0.16	0.43	0.23	0.34	0.26	0.30	0.28	0.40	0.29	0.40	0.33
FeO	3.33	3.69	1.76	3.22	1.64	3.79	2.28	3.24	2.84	3.18	3.27	3.92	3.20	3.67	3.19
MnO	0.12	0.14	0.04	0.09	0.12	0.13	0.02	0.10	0.06	0.13	0.10	0.12	0.05	0.10	0.07
MgO	1.19	1.50	0.81	1.43	0.56	1.59	0.84	1.20	0.92	1.11	1.17	1.48	1.11	1.29	1.14
CaO	4.89	3.56	2.37	5.57	5.70	3.69	5.06	3.66	0.88	4.90	3.76	4.55	3.80	3.82	3.40
Na <sub>2</sub> O	5.20	4.10	3.16	3.18	3.53	3.85	4.27	4.32	4.39	3.59	3.26	3.50	3.25	4.06	3.75
K <sub>2</sub> O	2.77	1.70	1.83	1.35	1.49	1.73	1.51	1.64	1.82	1.29	1.40	1.54	1.40	1.72	1.69
P <sub>2</sub> O <sub>5</sub>	0.22	0.20	0.09	0.23	0.14	0.22	0.24	0.26	0.18	0.25	0.25	0.28	0.23	0.13	0.16
NiO	0.05	0.00	0.00	0.00	0.00	0.02	0.00	0.00	0.00	0.00	0.00	0.00	0.00	0.03	0.06
Total	99.51	99.07	96.04	95.05	95.40	96.44	99.78	99.70	95.34	95.74	95.21	96.15	94.28	98.68	95.78
P <sub>2</sub> O <sub>5</sub> <sup>b</sup>	0.25	0.20	0.10	0.27	0.16	0.22	0.27	0.26	0.18	0.28	0.28	0.30	0.25	0.14	0.16
PEC <sup>c</sup>	13.31	4.38	0.60	15.36	4.60	3.58	12.65	5.93	0.90	12.03	9.20	8.27	9.21	4.66	5.10

Volatile															
H <sub>2</sub> O <sup>a</sup>	0.54	0.93	3.96	4.95	4.60	3.58	0.22	0.30	4.66	4.26	4.79	3.85	5.72	1.34	4.28
CO <sub>2</sub>	3	112	3	18	261	509	5	8	6	13	397	1570	1773	42	387
SO <sub>3</sub>	192	77	94	550	227	225	362	253	193	292	305	334	409	187	146
F	552	668	378	375	568	488	121	256	624	415	543	552	627	534	589
Cl	1772	1750	2057	1974	2085	2148	1900	1696	1987	2144	2214	2018	1876	1790	1733

<sup>a</sup>All values are shown after PEC corrections.

<sup>b</sup>P<sub>2</sub>O<sub>5</sub> values measured using SIMS.

<sup>c</sup>Post-entrapment crystallization.

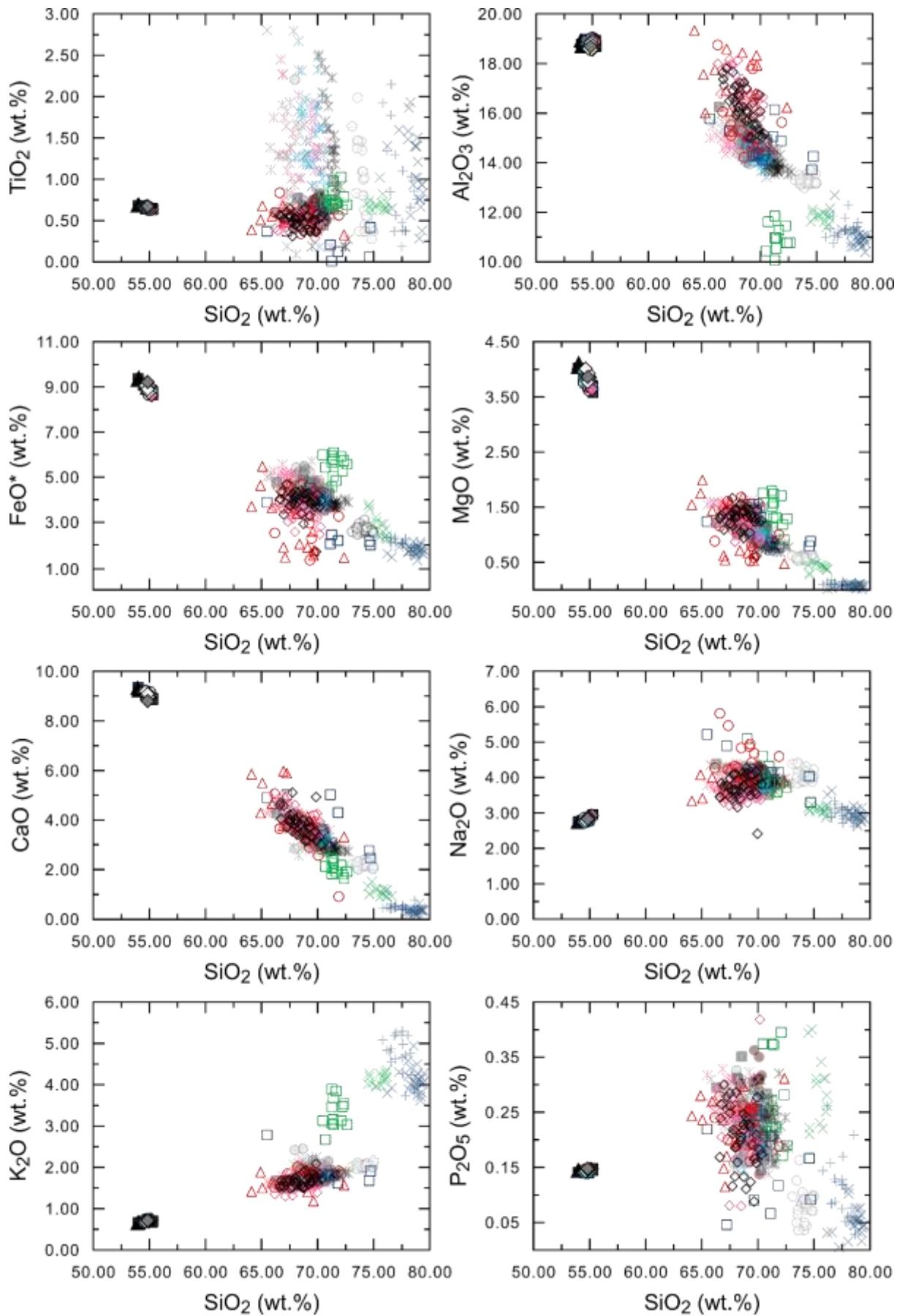
**Table 4. 4.** Representative groundmass and interstitial glass compositions of the volcanic products from 2007/08 and 2014 eruptions analyzed using electron microprobe. Stages I and II of the 2014 eruption refer to chronology of Maeno et al. (2019). FeO\*= total iron. LD (GM): lava dome groundmass; LD (IG): lava dome interstitial glass; BP W: banded pumice white part; BP LG: banded pumice light grey; BP DG: banded pumice dark grey; SB: scoria bomb; NTWP: non-transparent white pumice; TWP: transparent white pumice; TPP: transparent pink pumice; TGP: transparent grey pumice; and S: scoria.

Sample	LD (GM)			LD (IG)				SB			BP W			BP LG		BP DG	
Spot no.	14	2	10	11	12	19	23	15	1	31	26	8	4-2	2-2	6-2	7-5	
Eruption	2007/08			2007/08				2014			2014			2014		2014	
Stage	-			-				I (PDC-1)			I (PDC-1)			I (PDC-1)		I (PDC-1)	
Major element (wt.%)																	
SiO <sub>2</sub>	78.74	78.17	76.82	74.99	76.02	76.57	69.02	69.71	71.24	73.11	73.65	74.25	66.88	69.29	67.77	69.04	
TiO <sub>2</sub>	1.02	1.38	0.28	2.11	1.93	1.29	0.73	0.76	0.55	0.00	0.37	0.45	0.70	0.49	0.62	0.59	
Al <sub>2</sub> O <sub>3</sub>	10.76	11.01	10.74	10.83	11.03	10.96	14.34	14.14	14.38	13.46	13.37	13.42	14.64	14.28	14.11	14.47	
Cr <sub>2</sub> O <sub>3</sub>	0.06	0.01	0.02	0.04	0.02	0.00	0.00	0.00	0.00	0.00	0.00	0.00	0.02	0.07	0.04	0.00	
FeO*	1.29	1.83	1.66	2.02	2.29	2.34	4.71	4.27	4.05	2.72	2.94	2.71	4.80	4.05	5.12	4.77	
MnO	0.05	0.00	0.04	0.05	0.13	0.03	0.17	0.16	0.14	0.12	0.13	0.13	0.20	0.14	0.18	0.24	
MgO	0.06	0.02	0.08	0.09	0.10	0.13	0.84	0.95	1.15	0.51	0.54	0.60	1.41	1.05	1.43	1.27	
CaO	0.18	0.18	0.62	0.43	0.46	0.54	2.95	3.18	3.02	2.26	2.35	2.26	3.56	3.81	3.29	3.26	
Na <sub>2</sub> O	3.11	2.71	2.89	2.81	3.07	3.01	4.04	4.20	4.25	3.96	4.35	4.11	3.99	3.88	3.79	3.89	
K <sub>2</sub> O	4.49	3.85	3.93	4.46	5.10	4.60	1.88	1.79	1.83	2.05	2.04	2.04	1.78	1.58	1.94	2.03	
P <sub>2</sub> O <sub>5</sub>	0.06	0.05	0.06	0.08	0.14	0.09	0.36	0.31	0.25	0.08	0.16	0.07	0.20	0.23	0.25	0.16	
NiO	0.02	0.00	0.03	0.02	0.00	0.02	0.00	0.00	0.03	0.01	0.04	0.00	0.07	0.00	0.00	0.02	
Total	99.82	99.20	97.15	97.94	100.28	99.57	99.03	99.46	100.89	98.28	99.92	100.05	98.23	98.87	98.54	99.74	
Volatile (ppm)																	
SO <sub>3</sub>	90	70	90	60	230	110	140	230	320	250	150	160	90	30	60	310	
F	90	260	230	450	160	360	520	570	300	140	160	230	820	40	40	660	
Cl	1690	1130	1340	1670	1530	1420	1530	1780	1440	1080	1490	940	1430	1430	1850	1690	

**Table 4. 4.** (continued).

Sample	NTWP				TWP			TPP			TGP			S	
Spot no.	16-13	16-12	21-14	7-7	23-4	24-5	24-4	24-2	16-3	26-7	28-25	28-2	4-27	4-17	4-37
Eruption	2014				2014			2014			2014			2014	
Stage	II (CPF)				II (CPF)			II (CPF)			II (CPF)			II (CPF)	
Major element (wt.%)															
SiO <sub>2</sub>	70.43	69.31	68.97	70.82	69.13	65.96	70.93	68.98	66.93	69.09	67.75	65.05	71.40	70.43	70.35
TiO <sub>2</sub>	0.72	1.53	1.90	0.45	0.56	0.59	1.45	1.73	2.28	0.73	1.27	1.37	1.35	1.08	0.72
Al <sub>2</sub> O <sub>3</sub>	13.98	13.89	14.93	14.97	14.75	16.16	14.24	14.59	14.73	14.09	15.15	15.32	13.60	13.87	13.75
Cr <sub>2</sub> O <sub>3</sub>	0.07	0.00	0.00	0.00	0.00	0.00	0.00	0.03	0.00	0.00	0.01	0.00	0.00	0.00	0.00
FeO*	3.93	4.05	3.93	3.54	3.90	4.74	3.53	3.58	4.93	4.40	3.98	4.96	3.84	3.79	3.62
MnO	0.18	0.22	0.16	0.11	0.16	0.18	0.12	0.15	0.13	0.16	0.16	0.14	0.17	0.06	0.11
MgO	0.98	1.07	1.21	0.99	1.11	1.21	1.04	1.08	1.40	0.96	1.26	1.58	0.79	0.88	0.76
CaO	3.31	3.49	3.91	3.64	3.47	4.26	3.32	3.51	4.11	3.01	3.62	4.38	2.76	2.82	2.94
Na <sub>2</sub> O	3.79	3.74	3.79	4.02	3.89	4.36	3.52	3.90	3.56	3.56	4.26	4.31	3.88	3.80	4.08
K <sub>2</sub> O	1.82	1.78	1.66	1.67	1.71	1.68	1.67	1.67	1.64	1.93	1.61	1.55	1.79	1.84	1.80
P <sub>2</sub> O <sub>5</sub>	0.23	0.22	0.21	0.21	0.26	0.29	0.14	0.17	0.26	0.27	0.16	0.26	0.21	0.26	0.15
NiO	0.00	0.01	0.00	0.02	0.02	0.03	0.00	0.00	0.03	0.03	0.00	0.00	0.00	0.00	0.04
Total	99.44	99.31	100.67	100.43	98.96	99.47	99.96	99.37	99.99	98.23	99.21	98.91	99.78	98.81	98.31
Volatile (ppm)															
SO <sub>3</sub>	100	280	190	80	60	20	260	130	70	270	10	350	140	160	20
F	520	180	510	440	200	960	n.d.	250	420	550	140	n.d.	200	230	390
Cl	1500	1600	1460	1430	1830	1640	1470	1570	1650	1430	1630	1290	1400	1450	1560

n.d. Not detected.



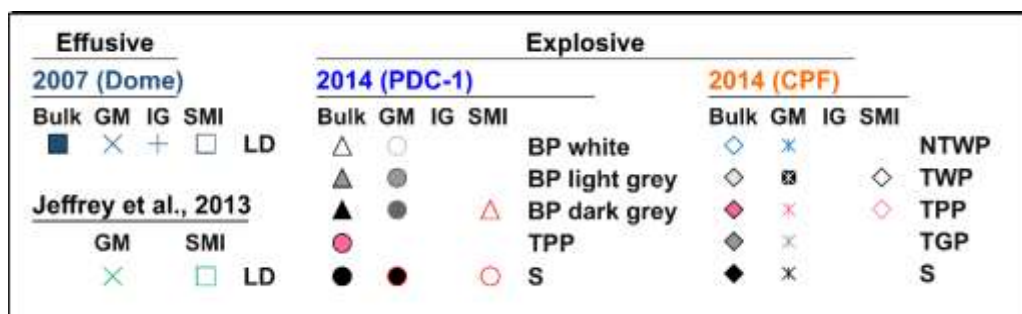


**Figure 4. 5.** Major element variation diagrams of bulk, groundmass glass, and SMI of 2007/08 and 2014 eruptions of Kelud. Melt inclusion compositions are corrected for PEC. All whole-rock, groundmass glass, and SMI values are normalized to 100 wt.% on a basis of volatile-free. FeO\* is all iron values reported as FeO.

#### 4.3.2. Volatile concentrations

##### *H<sub>2</sub>O and CO<sub>2</sub>*

SIMS results show that the highest H<sub>2</sub>O content occurs in SMIs from the 2014 TWP (up to 5.89 wt.%) and 2014 BP DG (up to 5.46 wt.%; Table 4.3). The 2007/08 SMIs generally have lower water contents (average 1.40 wt.%), although the highest measured H<sub>2</sub>O is 3.96 wt.%. (Fig. 4.6) The CO<sub>2</sub> concentrations of analyzed SMIs are typically < 200 ppm, but they may reach up to ~1,500 ppm in some melt inclusions from the 2014 eruption. Several melt inclusions in the dome sample appear to have high CO<sub>2</sub> concentrations (up to ~1,800 ppm) at low (~1 wt%) H<sub>2</sub>O contents. The maximum CO<sub>2</sub> values in the 2007 and 2014 melt inclusions are 1488 ppm and 1733 ppm, respectively.

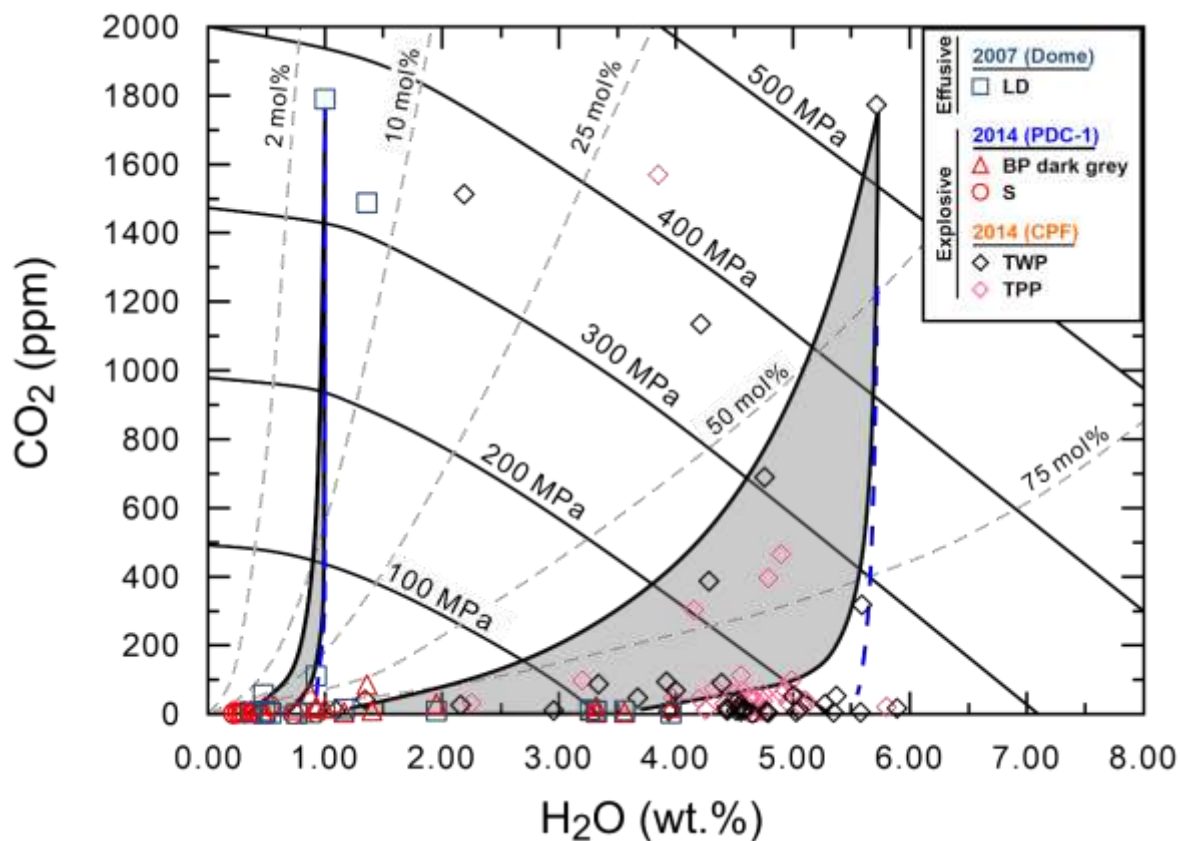


**Figure 4. 6.** CO<sub>2</sub> and H<sub>2</sub>O contents in melt inclusions measured by SIMS. Isobars curves (*fine black lines*) and vapor isopleths (*grey dashed lines*) are calculated at 1050°C using the *VolatileCalc 2.0* (Newman and Lowenstern, 2002). Bold solid lines represent closed-system degassing pathway, while blue dashed line for open-system degassing. The grey area is obtained simulating the degassing of the two groups of melt inclusions having the highest H<sub>2</sub>O and CO<sub>2</sub> contents, using closed system condition and initial excess of fluid from 0.5 to 3%.

#### *F, SO<sub>3</sub>, and Cl*

F concentrations show similarity among the 2007/08 and 2014 melt inclusions, with values ranging from 265 to 1,678 ppm (Fig. 4.7A). 2007/08 and 2014 CPF samples have narrow fluorine compositional ranges from 265 to 883 ppm and 322 to 635 ppm, respectively, while the 2014 PDC-1 inclusions have broader ranges from 121 to 1,678 ppm. Groundmass glass in the 2007/08 sample contains 90–940 ppm F, with a peak between 340 and 590 ppm (Table 4.4). Similarly, the groundmass glass in the 2014 samples has fluorine concentrations between 70–980 ppm, although they have relatively higher concentrations at the peak of 800–860 ppm than

the 2007/08 dome (Fig. 4.7A).

Melt inclusions generally have higher  $\text{SO}_3$  concentrations than their respective groundmass, ranging up to 413 ppm in 2007/08 samples and up to 644 ppm in 2014 samples (Fig. 4.7B). In comparison,  $\text{SO}_3$  from the previous study on plagioclase-hosted inclusions from the 2007/08 eruption reveals similar sulfur contents, although  $\text{SO}_3$  values are slightly lower, with the highest concentration up to 184 ppm (Jeffrey et al., 2013). The low sulfur concentration compared to the results presented in this study may result from the small population samples reported.

Chlorine concentrations in melt inclusions are relatively similar and resemble the concentration in their respective groundmass glass (Fig. 4.7C). In the 2007 melt inclusions, the Cl concentration ranges from 1,750 to 2,177 ppm, although some inclusion may have lower (511 ppm) or higher (3,932 ppm) concentrations. The 2014 inclusions have more restricted Cl concentrations, ranging from 1,161 to 2,816 ppm. The highest Cl concentrations are found in cpx-hosted melt inclusions in banded pumice samples (BP DG). The Cl concentrations in groundmass glass range from 1,130 ppm to 2,330 ppm in 2007/08 samples, while the concentration in 2014 samples varies from 840 to 2,660 ppm. The Cl concentrations in the 2007 cpx-hosted melt inclusions are slightly lower than those reported for plagioclase-hosted melt inclusions (Jeffrey et al., 2013), although the variations could occur as the consequences of different entrapment environments.



## 4.4. Discussion

### 4.4.1. Melt inclusion entrapment and crystallization of clinopyroxene hosts.

The crystallization temperature and pressure of clinopyroxene crystal hosts are calculated using various thermobarometer models (Fig. 4.8). The first thermobarometer used is Putirka (2008), which is a recalibrated version of Nimis (1995) based clinopyroxene composition on hydrous system (equation 32b), with SEE is  $\pm 260$  MPa. The temperature input of 1,050 °C (range between 1,010 and 1,052 °C) was calculated using equation 33 of Putirka (2008). The second model is based upon the Al partitioning between clinopyroxene and melt that is calibrated for hydrous systems (equation 32c; Putirka, 2008). This model requires temperature and H<sub>2</sub>O inputs (3.96 to 5.89 wt.% used based on H<sub>2</sub>O measurement) with a SEE of  $\pm 150$  MPa. Using Neave and Putirka (2017), which has 140 MPa of SEE, an additional test has been conducted to evaluate the crystallization depth of clinopyroxene. By utilizing all three geobarometer models above, the ranges of crystallization pressure for 2007/08 clinopyroxene are 280–400 MPa (Putirka 2008 equation 32b), 270–450 MPa (Putirka 2008 equation 32c), and 170–370 MPa (Neave and Putirka, 2017). These values are equivalent to depths of 10.7–15.76 ( $\pm 9.5$ ) km, 13.0–17.6 ( $\pm 5.5$ ) km, and 6.5–14.1 ( $\pm 5.4$ ), assuming a crustal density of 2,640 kg m<sup>-3</sup> beneath Kelud (Smyth et al., 2007). These results are consistent with previous clinopyroxene-derived pressure estimation by Jeffrey et al. (2013), suggesting the volatiles contained in the 2007/08 melt inclusions was derived from a deep magma reservoir. By applying similar geothermometer models, the crystallization pressure of 2014 clinopyroxenes lies on wider range of 40–550 MPa, equivalent to depths of 1.5 to 21.5 km.

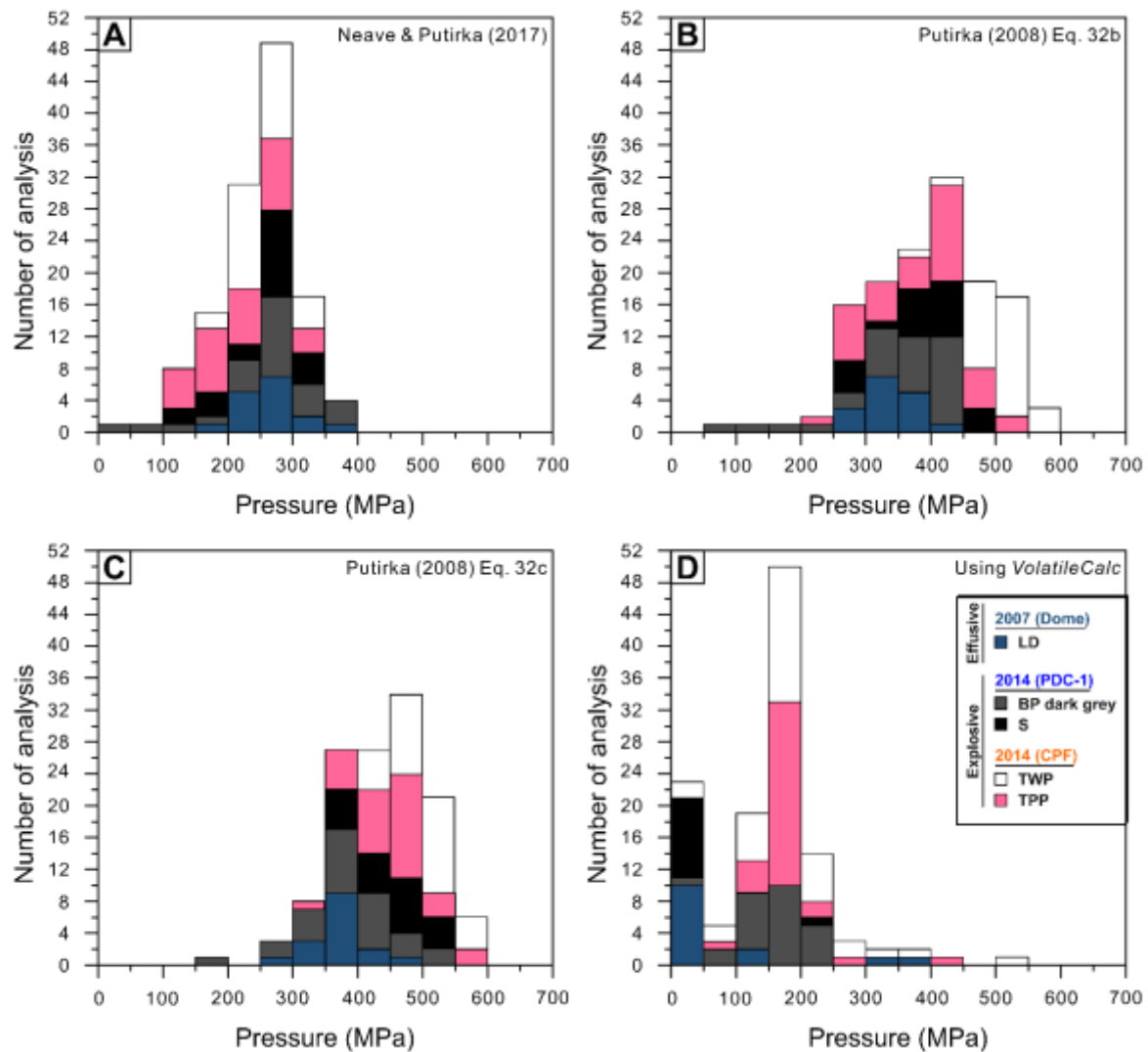


**Figure 4. 8.** Histograms of pressure at which clinopyroxene hosts were crystallized. A) Calculated using Neave and Putirka (2017) clinopyroxene barometer. B) calculated pressure using B) Equation 32b of Putirka (2008) and C) using Equation 32c of Putirka (2008). Histogram of saturation pressures based on H<sub>2</sub>O and CO<sub>2</sub> concentrations in 2007/08 and 2014 SMIs computed using VolatileCalc 2.0 (Newman and Lowenstern, 2002) at 1050 °C.

The wide variation of H<sub>2</sub>O concentrations in melt inclusions, particularly in the 2007/08 dome, suggests that some inclusions have undergone partial diffusion or rupture over extended periods of time, allowing the H<sub>2</sub>O loss after the entrapment. (Fig. 4.9). Plot of H<sub>2</sub>O against SiO<sub>2</sub> and K<sub>2</sub>O suggest that the 2007/08 and 2014 melt inclusions are entrapped from vapor saturated magma with most inclusions in dome samples and some in scoria have depleted water content with increasing SiO<sub>2</sub> and K<sub>2</sub>O. This is consistent with the fact that the 2007/08 melt inclusions and scoria from PDC deposits have experienced an extended cooling history at low pressure during their emplacement. Additionally, individual melt inclusion entrapment and last re-equilibration pressures were calculated using *VolatileCalc 2.0* (Newman and Lowenstern 2002) at temperature 1,050 °C, based on the clinopyroxene-melt thermometry. Assuming all melt inclusions are vapor-saturated, the minimum equilibration pressures range from <10 to 408 MPa. However, as mentioned above, some inclusions may have undergone partial diffusion or rupture during the ascent and thus the lowest values obtained from this modelling seem irrelevant. I then used the most evolved SMI composition in figure 4.9 to calculate the minimum equilibrium pressure, which suggests a pressure of ~100 MPa. Therefore, the equilibration depths from 2007/08 and 2014 melt inclusions range between ~3.8 and 15.7 km.

Overall, the clinopyroxene barometry results are consistent with previous barometry results on recent eruptive products from Kelud (i.e., Jeffrey et al., 2013; Cassidy et al., 2019) and geophysical evidence that suggests multi-level plumbing system (e.g., Hidayati et al., 2009; Hidayati et al., 2019), although the volatile-based pressure estimations show consistently lower crystallization pressures than the calculations derived from host clinopyroxene phenocrysts. Several scenarios can explain such differences: 1) melt inclusions were entrapped under vapor-undersaturated conditions; 2) partial dissolution of clinopyroxene hosts that formed the inclusions; or 3) melt inclusions have experienced continuous re-equilibration after the entrapment. Scenarios 1 and 2 may favor pressure estimations from volatile components to be significantly lower than those of actual entrapments. However, these scenarios are not

considered possible as they do not justify the vapor-saturated crystallization shown in the figure. 4.9, nor supported by any evidence of dissolution (i.e., melt channel or embayment) at clinopyroxene phenocrysts. Thus, the most probable explanation for the pressure difference is due to the re-equilibration of melt inclusions after initial entrapment. Unlike scenario 1, scenario 3 can accommodate vapor-saturated crystallization trends, as shown in figure 4.9. The melt inclusions re-equilibrated over a range of pressures less than 408 MPa, indicating that re-equilibration happened during ascent because of slow ascending magma at the depth or that magmas were temporarily stored at this pressure range before the eruption occurred; though this process needs to be further investigated. The maximum melt inclusion re-equilibration depth of ~15 km is consistent with previous studies on Kelud's plumbing system, suggesting that prior to both the 2007/08 and 2014 eruptions, magmas were stalled at these depths (Jeffrey et al., 2013; Cassidy et al., 2019).

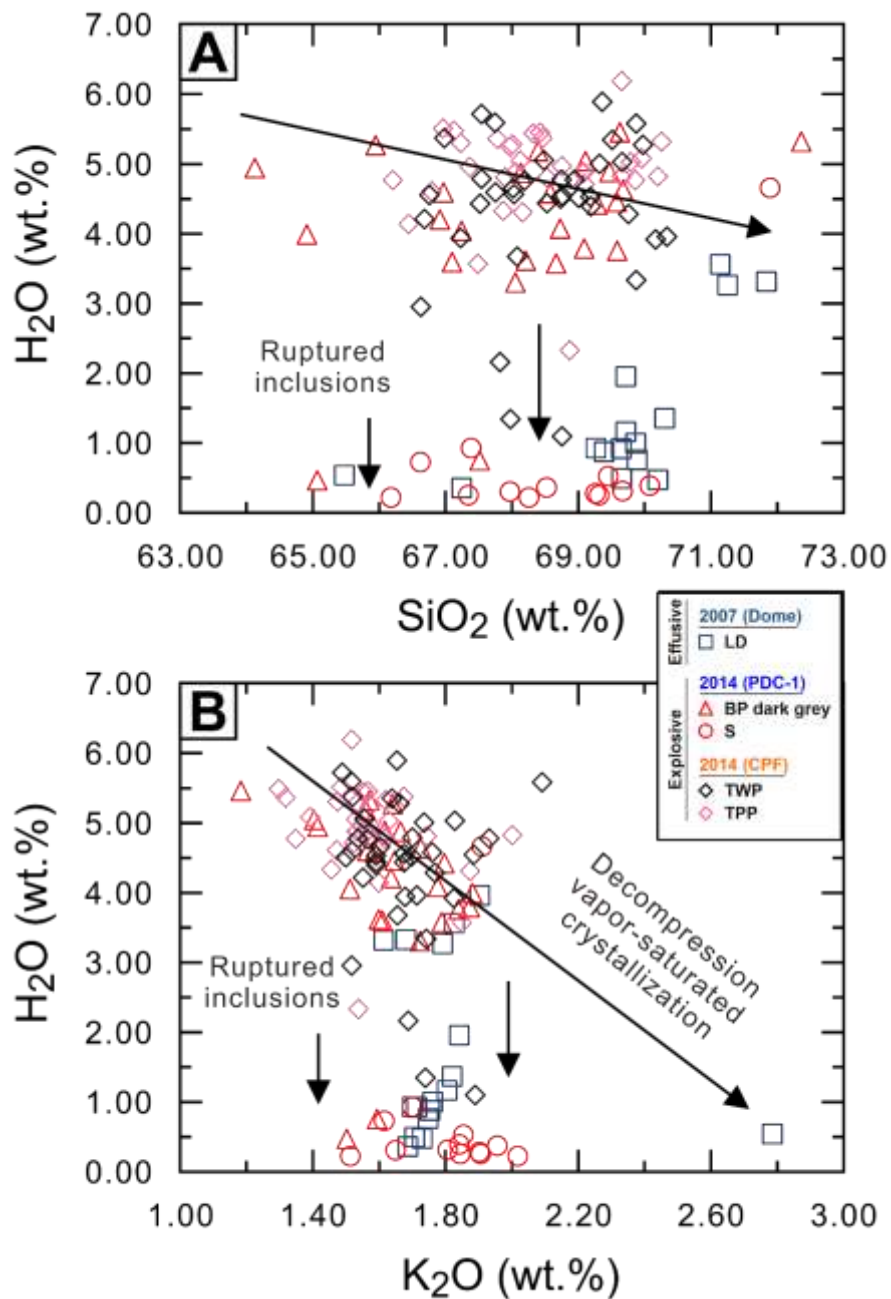


**Figure 4. 9.** Plots of water content versus A) SiO<sub>2</sub> and B) K<sub>2</sub>O, as the indicators for magmatic differentiation. H<sub>2</sub>O has negative correlations with SiO<sub>2</sub> and K<sub>2</sub>O, indicating last equilibrium stage of melt inclusion following vapor-saturated crystallization during decompression. Some inclusions might have experienced ruptured during ascent as suggested from low water contents.

#### 4.4.2. Deep and shallow-level degassing history

The degassing patterns of Kelud melt inclusions data were evaluated using *VolatileCalc 2.0* at 1,050 °C. Generally, volatiles will be outgassed after exsolving from the melt in the open-system model, whereas in the closed-system model, the exsolved vapor remains in the solution and acts as a buffer on the residual melt. An open-system model fits the data well for the 2007/08 inclusions, with the initial starting point at 1.0 wt.% H<sub>2</sub>O and 1790 ppm CO<sub>2</sub>. On the contrary, 2014 inclusions data fit the closed-system models better than the open-system, with the initial starting point of 5.7 wt% H<sub>2</sub>O, 1773 ppm CO<sub>2</sub>, and 0.5 to 3% exsolved vapor (Fig. 4.6). This closed-system trend commonly observed in 2014 CPF inclusions, suggesting that closed-system degassing occurred prior to the plinian event in 2014 eruption, with the exsolved volatiles remained in the system. The accumulation of exsolved volatile in the system then increased the overall pressure and caused the eruption to have a higher explosivity. The result is consistent with the behavior of SO<sub>3</sub> and F relative to the H<sub>2</sub>O with an overall positive correlations (Fig. 4.10 A and B). However, some inclusions in explosive products have lower H<sub>2</sub>O values than the degassing trendline. This indicate during closed-system degassing, H<sub>2</sub>O may also be lost due to diffusion through the crystals.

Fluorine concentrations in melt inclusions and groundmass glass (Fig. 4.7) are comparable with typical range for subduction-related magmas (Aiuppa et al. 2009). The results are consistent with the fact that F has high solubility in silicate melts and, thus it is not exsolved via degassing (e.g., Preece et al., 2014; Shimizu et al., 2017). The Cl contents of the groundmass glass generally share similar overall ranges with Cl in the melt inclusions; yet slightly lower than melt inclusion population, indicating Cl remained dissolved in the melt and only exsolved during syn-eruptive degassing at low pressures (Fig. 4.10C; Christopher et al., 2015; Thomas et al., 2021). The Cl concentrations in the melt inclusions of 2007/08 and 2014 products generally are in a range of 1,750 to 2,177 ppm that relatively constant with H<sub>2</sub>O content (Fig. 4.10C), comparable with other subduction-related magmas (Aiuppa et al. 2009). The simplest

explanation for a restricted Cl concentrations in the melt inclusions could be that the magma has undergone degassing with preferential exsolved H<sub>2</sub>O (e.g., [Mann et al., 2013](#)). However, it seems implausible given the chlorine degassing profile is pressure, temperature, and compositions dependent ([Botcharnikov et al., 2015](#); [Thomas and Wood, 2021](#)). Alternately, the silicate melt may have been in equilibrium with a magmatic hydrosaline chloride liquid ± vapor when degassing occurred (e.g., [Preece et al., 2014](#)). When magma rises and exsolves H<sub>2</sub>O, the water will interact with Cl in the melt, thus for every reacted H<sub>2</sub>O molecule, 2 molecules of HCl are produced (Eq. 19 of [Thomas and Wood, 2021](#)). This results in a large increase in volume that causes Cl to be less-degassed as the decompression increases. Therefore, I infer that chlorine concentrations are “buffered” by hydrosaline chloride that resulting in the relatively constant Cl values in silicate melt through the groundmass.

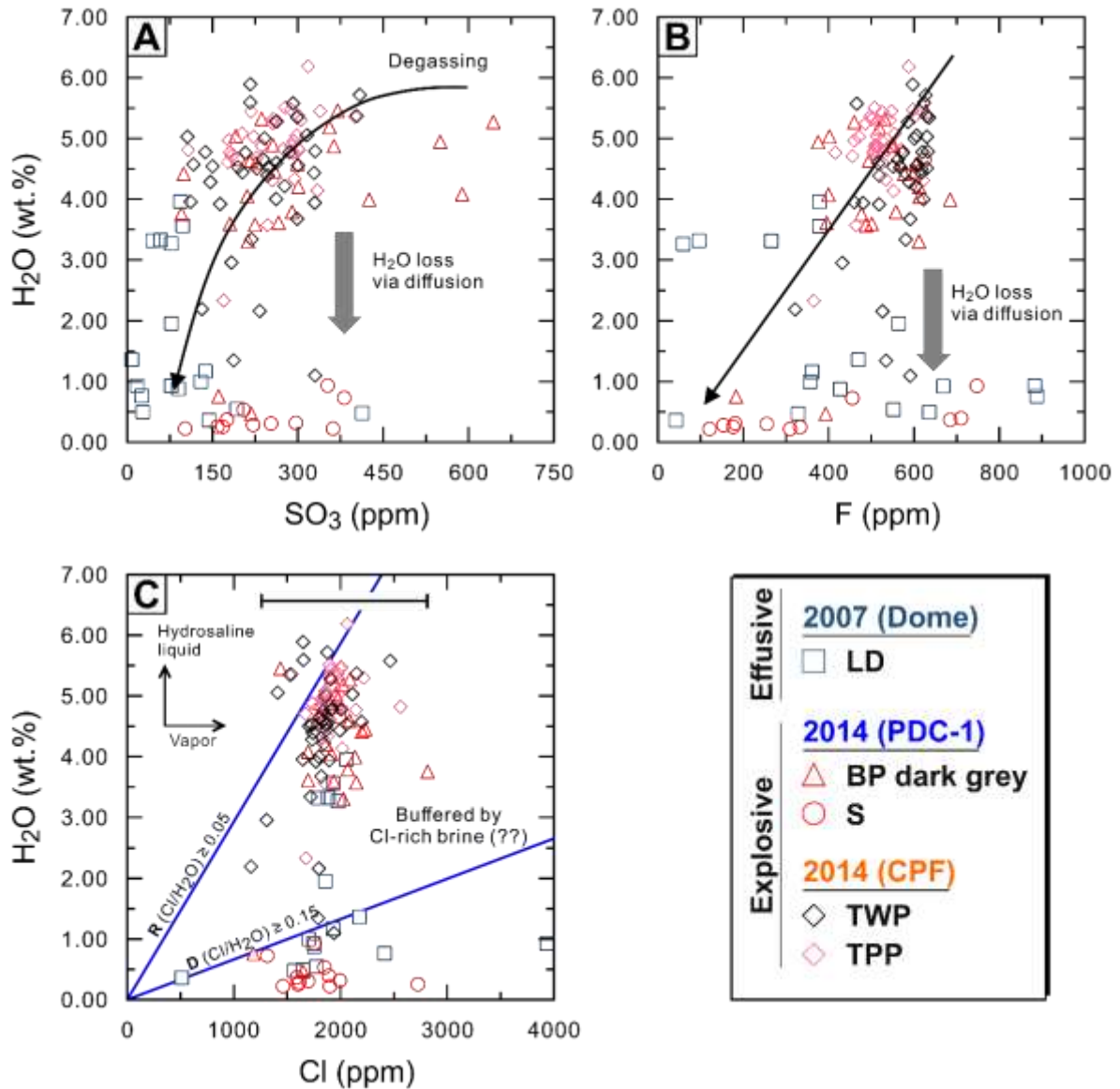


**Figure 4. 10.** Variations of volatile concentrations against H<sub>2</sub>O content. A) sulfur, B), fluorine, and C) chlorine. R represents ratio of Cl and H<sub>2</sub>O for rhyolite melts, whereas D for dacite melts (Webster, 2004)

#### 4.5. Summary and origin of effusive-explosive transition at Kelud

In general, the contrasting behavior of the 2007/08 dome-forming and 2014 plinian eruptions is reflected in their eruptive products. Major element concentrations in the whole rock compositions are similar, indicating that the overall magmatic composition does not significantly contribute to the changes in eruption style at Kelud. However, there are distinctions in the volatile behavior between the two eruptions. Melt inclusion analysis reveals that volatile concentrations in the 2007/08 samples align with a degassing path modeled for an open system, with initial H<sub>2</sub>O content lower than that of the 2014 eruption. In the case of the 2014 eruption, closed-system degassing seems to be sustained through the shallower depth and led to an explosive eruption that generated a plinian convective column on 13–14 February. In contrast, the open-system degassing in 2007/08 promoted magma to ascend slower (based on [Hidayati et al., 2019](#)) and erupt effusively. Additionally, the wide range of melt inclusion equilibration pressure at 3.8–15.7 km suggests that the melts have experienced continuous re-equilibration at depth and possibly derived from multiple magma reservoirs, as proposed by [Jeffrey et al. \(2013\)](#).

Silicate melt from 2007/08 and 2014 products was saturated in Cl, preserving evidence of hydrosaline fluids within the magmatic system prior to each eruption. Although the melt inclusions and their clinopyroxene hosts in this study have shed light on the magmatic system and magmatic contributions to the eruptive behavior of Kelud, other factors are likely to have also contributed to the eruptive dynamics (i.e., crystallization of microlites and degassing at the shallower level) that is not reflected in melt inclusion data. Thus, microlite crystallization is investigated in the following chapter (Chapter 5) to give some insight into pre-eruptive degassing and crystallization in the conduit.

## References

- Aiuppa, A., Baker, D.R., Webster J. D., 2009. Halogens in volcanic systems. *Chem. Geol.* 263:1–18. <https://doi.org/10.1016/j.chemgeo.2008.10.005>
- Botcharnikov, R.E., Holtz, F., Behrens, H., 2015. Solubility and fluid-melt partitioning of H<sub>2</sub>O and Cl in andesitic magmas as a function of pressure between 50 and 500 MPa. *Chem. Geol.*, 418, 117–131. <https://doi.org/10.1016/j.chemgeo.2015.07.019>
- Bucholz, C. E., Gaetani, G. A., Behn, M. D., Shimizu, N., 2013. Post-entrapment modification of volatiles and oxygen fugacity in olivine-hosted melt inclusions. *Earth Planet. Sci. Lett.* 374, 145–155. <https://doi.org/10.1016/j.epsl.2013.05.033>
- Cassidy, M., Ebmeier, S. K., Helo, C., Watt, S. F. L., Caudron, C., Odell, A., Spaans, K., Kristianto, P., Triastuty, H., Gunawan, H., Castro, J.M., 2019. Explosive eruptions with little warning: Experimental petrology and volcano monitoring observations from the 2014 eruption of Kelud, Indonesia. *Geochem. Geophys. Geosystems*, 20, 4218–4247. <https://doi.org/10.1029/2018GC008161>
- Caudron, C., Mazot, A., Bernard, A., 2012. Carbon dioxide dynamics in Kelut volcanic lake. *J. Geophys. Res.* 117:B05102. <https://doi.org/10.1029/2011JB008806>
- Christopher, T., E., Blundy, J., Cashman, K., Cole, P., Edmonds, M., Smith, P., J., Sparks, R., S., J., 2015. Crustal-scale degassing due to magma system destabilization and magma-gas decoupling at Soufrière Hills Volcano, Montserrat. *Geochem. Geophys. Geosystems*, 16, 267–300. <https://doi.org/10.1002/2015GC005791>
- Global Volcanism Program, 2008. Report on Kelud (Indonesia) (Wunderman, R., ed.). *Bulletin of the Global Volcanism Network*, 33:3. Smithsonian Institution. <https://doi.org/10.5479/si.GVP.BGVN200803-263280>
- Hammer, J. E., Cashman, K. V., Hoblitt, R. P., Newman, S. 1999. Degassing and microlite crystallization during pre-climactic events of the 1991 eruption of Mt. Pinatubo, Philippines. *Bull. Volcanol.* 60: 355. <https://doi.org/10.1007/s004450050238>

- Hidayati, S., Kristianto, Basuki, A., Mulyana, I., 2009. A new lava dome emerged from crater lake of Kelud volcano, East Java, Indonesia. *Jurnal Geologi Indonesia* 4 (4), 229–238. <http://dx.doi.org/10.17014/ijog.vol4no4.20091>.
- Hidayati, S., Triastuty, H., Mulyana, I., Adi, S., Ishihara, K., Basuki, A., Kuswandarto, H., Priyanto, B., Solikhin, A., 2019. Differences in the seismicity preceding the 2007 and 2014 eruptions of Kelud volcano, Indonesia. *J. Volcanol. Geotherm. Res.* 382, 50–67. <https://doi.org/10.1016/j.jvolgeores.2018.10.017>
- Jeffery, A.J., Gertisser, R., Troll, V.R. et al., 2013. The pre-eruptive magma plumbing system of the 2007–2008 dome-forming eruption of Kelut volcano, East Java, Indonesia. *Contrib. Mineral. Petrol.* 166, 275–308. <https://doi.org/10.1007/s00410-013-0875-4>
- Kawaguchi, M., Hasenaka, T., Koga, K. T., Rose-Koga, E. F., Yasuda, A., Hokanishi, N., Mori, Y., Shimizu, K., & Ushikubo, T., 2021. Persistent gas emission originating from a deep basaltic magma reservoir of an active volcano: the case of Aso volcano, Japan. *Contrib. Mineral. Petrol.* 176(1), 1–24. <https://doi.org/10.1007/s00410-020-01761-6>
- Le Maitre, R.W., Streckeisen, A., Zanettin, B., La Bas, M.J., Bonin, B., Bateman, P., Bellieni, G., Dudek, A., Efremova, J., Keller, J., Lameyre, J., Sabine, P.A., Schmidt, R., Sørensen, H., Woolley, A.R., 2002. *Igneous Rocks. A classification and Glossary of Terms. Recommendations of the International Union of Geological Sciences subcommission on the systematics of igneous rocks.* Cambridge University Press, Cambridge, 252 pp.
- Lormand, C., Zellmer, G. F., Sakamoto, N., Ubide, T., Kilgour, G., Yurimoto, H., Palmer, A., Németh, K., Iizuka, Y., & Moebis, A., 2021. Shallow magmatic processes revealed by cryptic microantecrysts: a case study from the Taupo Volcanic Zone. *Contrib. Mineral. Petrol.* 176(11), 97. <https://doi.org/10.1007/s00410-021-01857-7>
- Maeno, F., Nakada, S., Yoshimoto, M., Shimano, T., Hokanishi, N., Zaenuddin, A., Iguchi, M., 2019a. A sequence of a plinian eruption preceded by dome destruction at Kelud volcano, Indonesia, on 13 February, 2014, revealed from tephra fallout and pyroclastic density

- current deposits. *J. Volcanol. Geotherm. Res.* 382, 24–41. <https://doi.org/10.1016/j.jvolgeores.2017.03.002>
- Maeno, F., Nakada, S., Yoshimoto, M., Shimano, T., Hokanishi, N., Zaenuddin, A., Iguchi, M., 2019b. Eruption pattern and a long-term magma discharge rate over the past 100 years at Kelud volcano, Indonesia. *J. Disaster. Res.* 14 (1), 27–39. <https://doi.org/10.20965/jdr.2019.p0027>
- Mann, C.P., Wallace, P.J., Stix, J., 2013. Phenocryst-hosted melt inclusions record stalling of magma during ascent in the conduit and upper magma reservoir prior to vulcanian explosions, Soufrière Hills volcano, Montserrat, West Indies. *Bull. Volcanol.* 75:1–16. <https://doi.org/10.1007/s00445-013-0687-4>
- Morimoto, N., 1989. Nomenclature of pyroxenes. *Mineral. J.* 14 (5):198– 221. <https://doi.org/10.2465/minerj.14.198>
- Murch, A.P. and Cole, P.D., 2019. Using microlites to gain insights into ascent conditions of differing styles of volcanism at Soufrière Hills Volcano, *J. Volcanol. Geotherm. Res.* 384, 221–231. <https://doi.org/10.1016/j.jvolgeores.2019.07.022>
- Nielsen, R. L., Davidson, P. M., Grove, T.L., 1988. Pyroxene-melt equilibria: an updated model. *Contrib. Mineral. Petrol.* 100, 361–373 (1988). <https://doi.org/10.1007/BF00379745>
- Neave, D. A., & Putirka, K. D., 2017. A new clinopyroxene-liquid barometer, and implications for magma storage pressures under Icelandic rift zones. *Am. Mineral.* 102(4), 777–794. <https://doi.org/10.2138/am-2017-5968>
- Nimis, P., 1995. A clinopyroxene geobarometer for basaltic systems based on crystal-structure modelling. *Contrib. Miner. Petrol.* 121:115–125. <https://doi.org/10.1007/s004100050093>
- Noguchi, S., Toramaru, A., Nakada, S., 2008. Relation between microlite textures and discharge rate for the 1991–1995 eruptions at Unzen, Japan. *J. Volcanol. Geotherm.*

- Res.175, 141–155. <https://doi.org/10.1016/j.jvolgeores.2008.03.025>
- Preece, K., Gertisser, R., Barclay, J., Berlo, K., Herd, R. A., Edinburgh Ion Microprobe Facility. 2014. Pre- and syn-eruptive degassing and crystallisation processes of the 2010 and 2006 eruptions of Merapi volcano, Indonesia. *Contrib. Miner. Pet.*, 168(4), 1–25. <https://doi.org/10.1007/s00410-014-1061-z>
- Preece, K., Gertisser, R., Barclay, J., Charbonnier, S.J., Komorowski, J.-C., Herd, R.A., 2016. Transitions between explosive and effusive phases during the cataclysmic 2010 eruption of Merapi volcano, Java, Indonesia. *Bull. Volcanol.* 78, 54. <https://doi.org/10.1007/s00445-016-1046-z>
- Putirka, K.D., 2008. Thermometers and barometers for volcanic systems. *Rev. Mineral. Geochem.* 69:61–120. <https://doi.org/10.2138/rmg.2008.69.3>
- Shimizu, K., Ushikubo, T., Hamada, M., Itoh, S., Higashi, Y., Takahashi, E., Ito, M., 2017. H<sub>2</sub>O, CO<sub>2</sub>, F, S, Cl, and P<sub>2</sub>O<sub>5</sub> analyses of silicate glasses using SIMS: report of volatile standard glasses. *Geochem. J.* 51:299–313. [https://doi.org/10.2343/geoch\\_emj.2.0470](https://doi.org/10.2343/geoch_emj.2.0470)
- Siebert, L., Simkin, T., Kimberly, P., 2011. *Volcanoes of the world*, 3rd edn. University of California Press, Los Angeles, p 551
- Smyth, H.R., Hamilton, P.J., Hall, R., Kinny, P.D., 2007. The deep crust beneath island arcs: inherited zircons reveal a Gondwana continental fragment beneath East Java, Indonesia. *Earth Planet Sci, Lett.* 258:269–282. <https://doi.org/10.1016/j.epsl.2007.03.044>
- Surono, 2007, Pusat Vulkanologi Dan Mitigasi Bencana Geologi, Pos Pengamatan Gunungapi Kelut (Hasil evaluasi tingkat kegiatan G. Kelut): Departemen Energi Dan Sumber Daya Mineral, Republik Indonesia, Badan Geologi, Nomor, 112/GK/X/2007, 30 Oktober 2007. In Indonesian.
- Thomas, R. W., & Wood, B. J., 2021. The chemical behaviour of chlorine in silicate melts. *Geochim. Cosmo. Acta*, 294, 28–42. <https://doi.org/10.1016/J.GCA.2020.11.018>
- Toramaru, A., Noguchi, S., Oyoshihara, S., Tsune, A., 2008. MND (microlite number density)

- water exsolution rate meter. *J. Volcanol. Geotherm. Res.* 175(1–2), 156–167.  
<https://doi.org/10.1016/j.jvolgeores.2008.03.035>
- Van der Plas, L., Tobi, A.C., 1965. A chart for judging the reliability of point counting results. *Am. J. Sci.* 263, 87–90. <https://doi.org/10.2475/ajs.263.1.87>.
- Waelkens, C.M., Stix, J., Eves, E., Gonzalez, C., Martineau, D., 2021. H<sub>2</sub>O and CO<sub>2</sub> evolution in the Bandelier Tuff sequence reveals multiple and discrete magma replenishments. *Contrib. Mineral. Petrol.* 177:1, 177(1), 1–23. <https://doi.org/10.1007/S00410-021-01866-6>
- Webster, J.D., 2004. The exsolution of magmatic hydrosaline chloride liquids. *Chem. Geol.*, 210 (1–4), 33–48. <https://doi.org/10.1016/j.chemgeo.2004.06.003>
- Zurek, J., Moune, S., Williams-Jones, G., Vigouroux, N., Gauthier, P. J., 2019. Melt inclusion evidence for long term steady-state volcanism at Las Sierras-Masaya volcano, Nicaragua. *J. Volcanol. Geotherm. Res.* 378, 16–28.  
<https://doi.org/10.1016/J.JVOLGEORES.2019.04.007>

## Chapter 5

# Syn-eruptive degassing and crystallization process of the 2007/08 and 2014 eruptions of Kelud volcano, Indonesia

### 5.1. Introduction

Transitions between effusive and explosive eruption of compositionally similar magma are commonly observed at many subduction-related volcanoes around the world. These are typical phenomena, especially in viscous, silicic magmas (e.g., Pinatubo, and Merapi; [Hammer et al., 1999](#); [Preece et al., 2016](#)), although similar phenomena can also occur in less-viscous magmas (e.g., [Suzuki and Fujii, 2010](#)). Previous studies have linked effusive-explosive transitions to various pre-eruptive aspects, such as magma influx, degassing pattern, initial volatile and crystal contents ([Preece et al., 2014](#); [Cassidy et al., 2018](#); [Popa et al., 2021](#)), and various factors during ascent, including ascent rate, and decompression- and degassing-induced crystallization in the conduit ([Preece et al., 2016](#); [Bernard and de Maisonneuve, 2020](#)).

This chapter investigates the volcanic products from 2007/08 and 2014 eruptions of Kelud, Indonesia. The investigation focusses on magma dynamic of each eruption and the driving force behind the effusive-explosive transition during the 2007/08 and 2014 eruptions of Kelud volcano via textural and compositional analysis of groundmass phases from the respective eruptive products. In the last 100 years, Kelud has experienced at least seven eruptions that cover effusive and explosive styles with similar magma compositions (Fig. 5.1; i.e., [Indriyanto et al., 2023](#)), providing an excellent opportunity to study the relationship between the ascending rates and decompression- and degassing-induced crystallization in the conduit. The textural and compositional analysis are used to evaluate magma ascent rates, which is considered as important factors controlling degassing and crystallization behaviors, and ultimately affecting

the styles of eruption (Preece et al., 2016; Cassidy et al., 2018; Matsumoto and Geshi, 2021). Additionally, comparison of the products from two most recent and contrasting eruptions of Kelud elucidates syn-eruptive processes involved during the formation and transition between effusive and explosive eruption styles. Results of this work are beneficial for hazard assessment at Kelud and possibly other volcanoes with similar eruptive behavior worldwide.

## **5.2. Samples and analytical methods**

### **5.2.1. Sample selection and preparation**

In order to understand the driving force behind the transition between explosive and effusive eruption activity, the volcanic products from 2007 and 2014 eruptions of Kelud were examined. Time-controlled samples were collected from both pyroclastic density current and tephra fallout deposits during two episodes of field survey in August 2018 and October 2018 and samples acquired by Astiti Anggorowati in 2017 (personal communication). These samples were acquired from one unit of 2007/08 lava dome, and PDC-1 (Stage I) and CPF (Stage II) phase of 2014 eruption at the available exposures (Fig. 5.2). Lithologies are dominated by basalt for 2007/08 eruption and pumice and scoria for 2014 eruption, respectively.

A total 45 samples were collected using small scoop and placed into plastic bags. Each sample was manually sieved with 1 phi interval (from -1 to 4) and subsequently dried overnight at 60°C after being cleaned and purified under wet condition using W-170-ST ultrasonic cleaner. The samples were then molded and cast in form of polished thin sections for chemical and textural analysis.

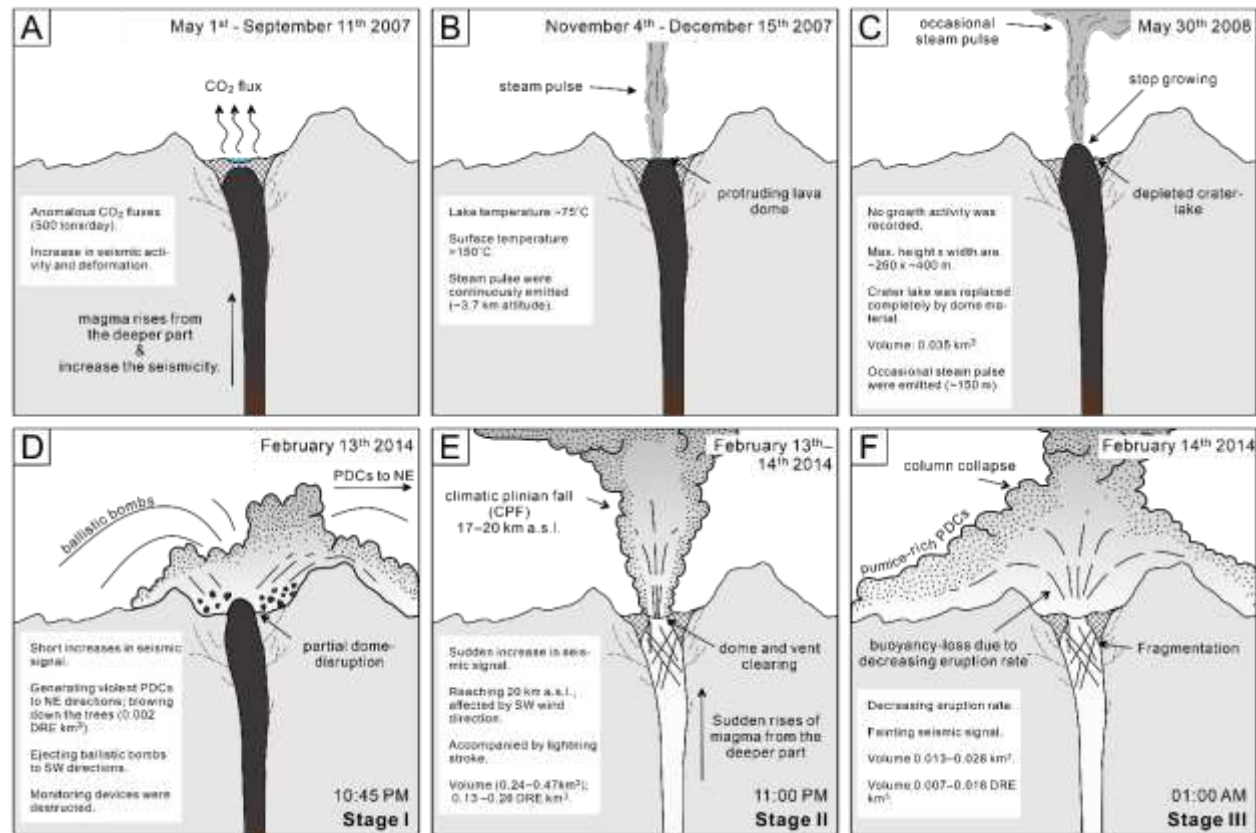


**Figure 5. 1.** Simplified sketch of the evolution of the 2007/08 lava dome and 2014 explosive eruptions. A) Increase in seismic activity and measured CO<sub>2</sub> fluxes denoted the unrest of the volcano prior to the 2007/08 eruption. B) Early stage of lava dome effusion was recorded from a sudden increase in surface temperature and emission of a steam pulse from a fresh protruding dome material in the lake area. C) Lava dome continuously grew until 30 May 2008, with a height reaching ~200 m from the crater surface. D) Seven years later, the 2007/08 dome was destroyed by an eruption on 13 February 2014 and produced ballistic bombs and PDCs towards the NE flanks of Kelud. E) At 11 PM on the same day, the plinian eruption column was developed and completely destroyed the 2007/08 dome, producing 0.24–0.47 km<sup>3</sup> pumice fallout deposits along the WSW and W directions. F) The marginal column collapse occurred on 14 February, emplacing pumice-rich PDC deposits along the main river flow around Kelud volcano.

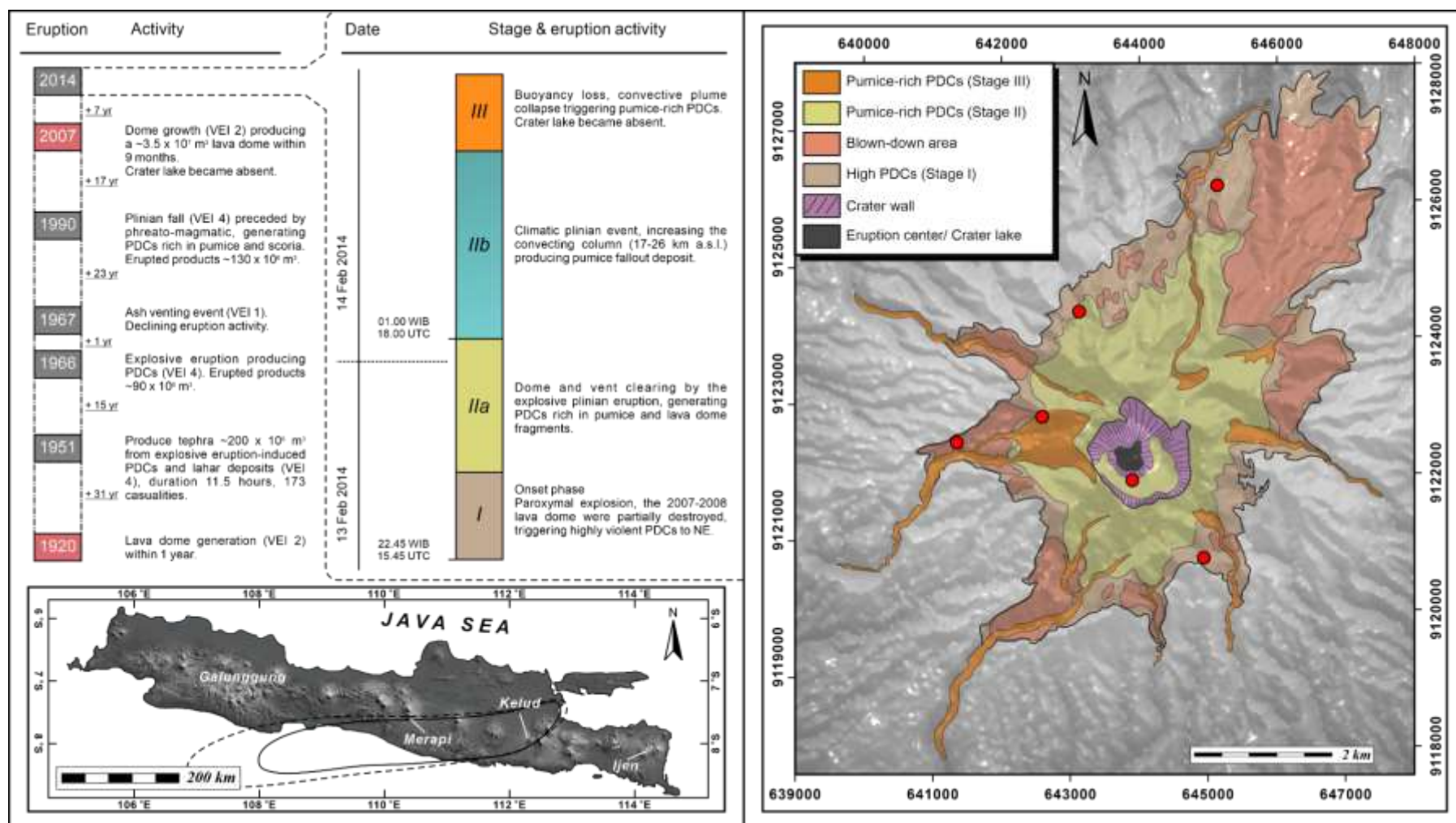


**Figure 5. 2.** Stages and distribution maps of 2014 eruption deposits (after Maeno et al., 2019a; Goode et al., 2019). Roman numerals indicate eruption stages in the center column and distribution map. The inset map shows the location of Kelud volcano, alongside other volcanoes on Java Island, and the distribution of fallout deposits of the 2014 eruption produced during stage II (CPF). Sample localities are marked with red circles.

### 5.2.2. Geochemical analysis

Whole-rock compositions of 2007 and 2014 eruption samples were acquired from fresh fraction of selected samples. A total of 30 samples were cleaned and purified under wet condition using W-170-ST ultrasonic cleaner, then dried overnight at 60°C before preparing fused glass beads for major and trace element measurements. Loss on ignition (LOI) was measured by weighing 3 g of powdered sample after furnacing at 900 °C for 3 hours. The element concentrations were measured using Rigaku ZSX Primus II X-ray fluorescence (XRF) spectrometer at the Faculty of International Resource Sciences, Akita University.

Mineral and glass major elements and volatiles were determined using JEOL JXA-8230 electron probe microanalyzer (EPMA) at the Faculty of International Resource Sciences, Akita University. Feldspar and pyroxene microlites were analyzed with a 15 kV accelerating voltage, a 20 nA beam current and applying a beam diameter of 2, 3 or 5 µm. Peak counting times per element were set on 10 to 20 s. Groundmass glass was analyzed using 5–10 µm defocused beam, with a 15 kV accelerating voltage, and a 6 nA beam current. Peak counting times range from 10 to 20 s for the major elements and 40 to 80 s for the volatiles. Natural minerals and synthetic compounds were used as the standard in order to calibrate the instrument, as well as checking the accuracy and precision during element analysis. In order to minimize the alkali migration during acquisition, sodium (*Na*) was always measured first. Detection limits are ~180–250 ppm for major elements, ~35 ppm for Cl, ~70 ppm for S, and ~470 ppm for F. Analytical uncertainties based upon repetitive analysis on natural and synthetic standards were in order of <5 % (relative) for major elements, S, and Cl, and <15 % (relative) for F.

### 5.2.3. Textural analysis

The textural analysis of microlite were conducted using back-scattered electron (BSE) images which were acquired with JEOL JSM-IT300LV SEM and JEOL JXA-8230 EPMA at Faculty of International Resource Sciences, Akita University. The observation of carbon-coated,

polished thin sections was carried out under 20 kV accelerating voltage at higher than  $\times 1000$  magnification to get high-resolution multiple BSE images over a continuous area. Twenty-three images of plagioclase feldspar and pyroxene microlites were acquired using EPMA elemental imaging to classify the textural types of feldspar (six types of textural and chemical zonation on 17 images) and pyroxene (five types of textural and chemical zonation on 6 images), where a given crystal may display more than one feature. The quantification of feldspar microlite textures however has become challenging because they have an average atomic value that is close to groundmass glass, therefore there was bias in determining each species based on the density value in BSE images. The images were subsequently digitally stitched and manually outlined using *CorelDRAW 2019* to separate the feldspar, pyroxene, and Fe-Ti oxide microlites from groundmass glass and vesicles. Around 800–900 feldspar microlite crystals and 150–1010 pyroxene crystals were measured for each sample to reduce statistical uncertainty. The digitized image was then exported to high-resolution tiff image in order to do measurement of crystal parameters using *ImageJ (version 1.51w)*. Edge-intersecting crystals were discarded from the estimation, as their shapes are incomplete and does not represent their actual shape. Vesicularity was defined as the area of vesicles that occupies the total area of the outlined image. The individual crystal area, mean crystal area, crystal dimension (short and long axis), including percentages of area covered by each crystal species were all measured under best fit ellipsoid condition (see [Hammer, 2000](#); [Preece et al., 2016](#); and [Murch et al., 2019](#)). The 2D quantitative textural analysis covered up measurement of areal number density ( $N_A$ ) of microlite phase and groundmass crystallinity ( $\phi$ ) under phenocryst- and bubble-free basis.

The stereological conversion from 2D to 3D crystal habit to get the characteristic aspect ratio was made by applying best fit shape curve of crystal length and width through the *CSDslice* software ([Morgan and Jerram, 2006](#)). The reliability of each best-fit was assessed with an  $R^2$  value, where an  $R^2 > 0.8$  are considered a good statistical fit. Out of 52 stereological conversion samples (26 feldspar and 26 pyroxenes), 26 samples have an  $R^2 > 0.8$ . Sixteen samples have an

$R^2$  between 0.7 and 0.8, and ten have an  $R^2 < 0.7$ , although three of these ten samples had more than 400 measured crystals. *CSDcorrections* v1.61 was used for generating crystal size distribution (CSD) graphs by inputting the characteristic aspect ratio (S: short; I: intermediate; and L: long axis). The measurement was utilized by applying an ellipsoid minor-axis for all analyzed samples. The fabric was set to be massive for all analyzed samples with a roundness of 0.1 out of 1 (scale: 0 to 1, where 0 is an equant block and 1 is an ellipsoid). The vesicles or voids correction were varied by considering the covered area (%) in the areal number density measurement. The logarithmic size scale was set to be 5 bins per decade so that the bin size would be 1.6 times bigger than the next smaller bin. Further, any bin with a crystal population of  $< 5$  was eliminated from the CSD graph (Higgins, 2000).

#### 5.2.4. Magma ascent rates

The magma decompression and ascent rates were estimated following the microlite number density (MND) water exsolution rate meter (Toramaru et al., 2008). The estimated values are considered as average ascent rates based on the assumptions that the microlite nucleation occurred under homogenous nucleation at the microlite nucleation depth. This model is defined by a set of three empirical equations (equations 10, 11, and 12 in Toramaru et al., 2008):

$$\left| \frac{dP_w}{dt} \right| = ckN_v^{2/3} \quad (5a)$$

where

$$c = 11.2 \times 10^6 \times C_w,$$

$$k = 1.2 \times 10^{(-12 - 0.23\Delta C_{Si} + 0.43C_w)} \text{ for plagioclase feldspars,}$$

$$k = 2.8 \times 10^{(-12 - 0.23\Delta C_{Si} + 0.43C_w)} \text{ for pyroxenes,}$$

$$\Delta C_{Si} = C_{Si} - 50,$$

$C_{Si}$  is  $\text{SiO}_2$  concentration of the melt in wt.%, and

$C_w$  is water content of the melt in wt.%.

$$\left. \frac{dP}{dt} \right|_{z=z_n} = \left. \frac{dP_w}{dt} \right|_{z=z_n} = v_n \left. \frac{dP}{dz} \right|_{z=z_n} \quad (5b)$$

with  $|dP/dz|$  being the pressure gradient at microlite nucleation depth;  $|dP/dz| = \rho \times g$ ;  $\rho$  is bulk density of the vesiculated magma at the nucleation depth and  $g$  as the gravitational acceleration; and  $v_n$ , being the ascent velocity of magma, can be calculated using Eq. (5c).

$$v_n = \frac{1}{\rho g} \left. \frac{dP_w}{dt} \right|_{z=z_n} \quad (5c)$$

This method assumes the decompression process is at a steady state, the degree of undercooling ( $\Delta T$ ) correlates positively with MND, and insignificant changes in velocity gradient ( $dv/dz$ ), so  $dv/dz$  can be neglected. The calculated average ascent velocity at the microlite nucleation depth from Eq. 5c is valid as long as the microlite does not nucleate at the fragmentation zone.

### 5.3. Results

#### 5.3.1. Petrographic overview

Surface and microscopic features of 30 thin sections from 2007/08 and 2014 eruptions were observed for this study. Visual inspection of mineral abundance in representative sample revealed that pumice, scoria, and dome samples show porphyritic textures, consisting of phenocryst and microphenocryst (length  $\sim 50$ -1500  $\mu\text{m}$ ), microlite (length  $< 50$   $\mu\text{m}$ ), and nanolite phase. However, due to the limitation of the instruments used, the nanolite could not be adequately observed. Plagioclase, clinopyroxene, and orthopyroxene appear as dominant phenocrysts and micro-phenocrysts alongside the occurrence of titanomagnetite (Figs. 5.3). Similarly, the groundmass consists of feldspar microlite, clinopyroxene, orthopyroxene, titanomagnetite, and volcanic glass (Fig. 5.4). Apatite presents as an accessory mineral and often occurs as a microlite phase together with cristobalite, which infills the vesicle and alters volcanic glass in some dome samples. Furthermore, the mineral proportion of selected samples

displays relative consistency through the eruption events, and each eruption stage is shown in Figure 5.3.

The quantitative modal abundance of the analyzed volcanic products reveals that dome samples have a relatively high phenocryst content of 49–64 vol.% and low vesicularity (5–23 vol.%; Fig. 5.3). Tephra from PDC-1 have phenocryst content ranging from 31 to 42 vol.% with moderate vesicularity of 31–55 vol.%, whereas samples from CPF have the lowest phenocryst content (23–36 vol.%) along with highest vesicularity values (41–66 vol.%). There is an increase in phenocryst content with decreasing explosivity, from plinian fallout to PDC deposits and lava domes. The vesicularity, on the other hand, shows a negative trend with decreasing explosivity. There is a clear transition from an effusive to explosive region at the ~45 vol.% phenocryst content, with the effusive products having less than ~25 vol.% vesicularity.

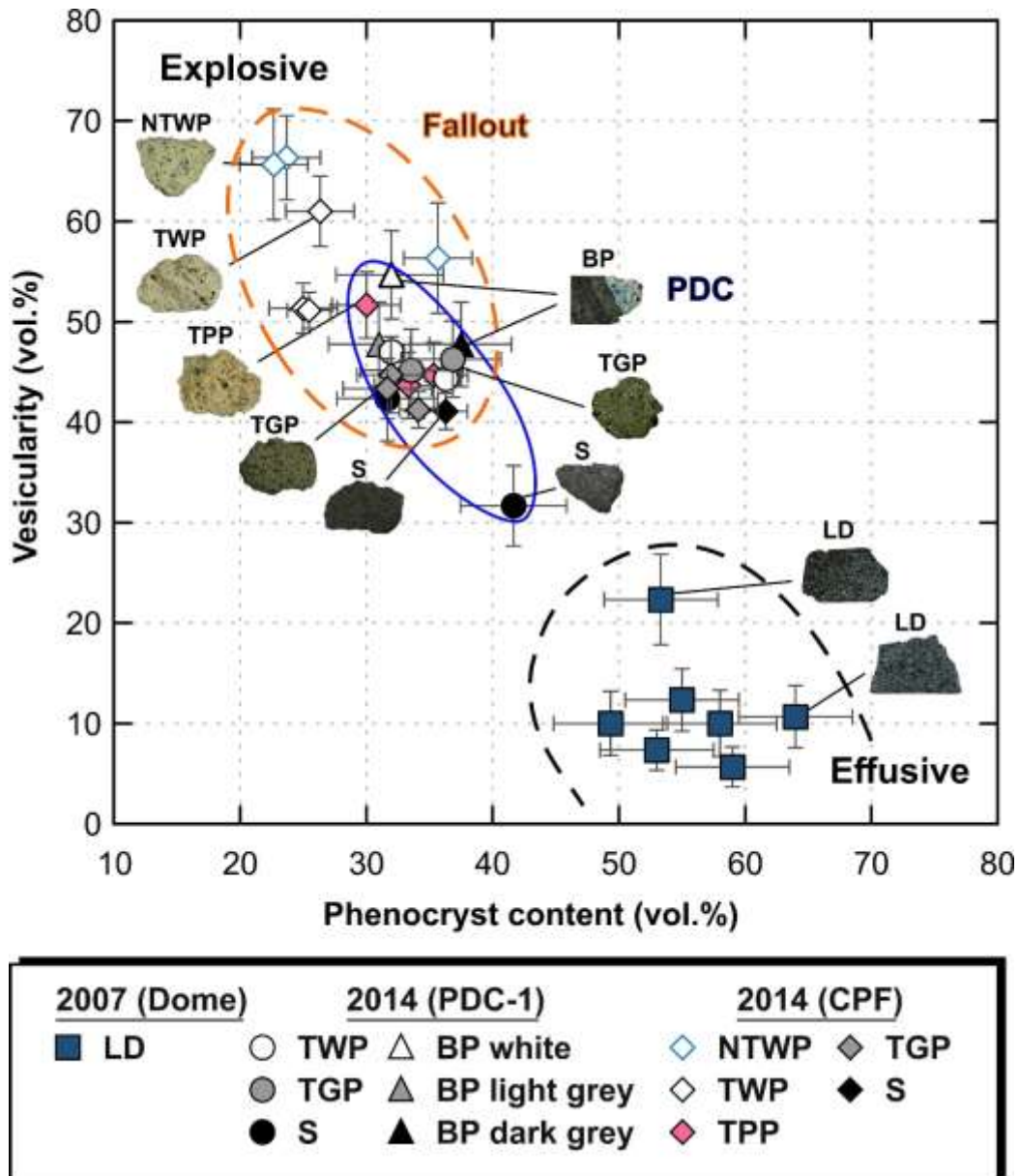


**Figure 5. 3.** Plot of vesicularity as a function of total phenocryst content showing the difference between effusive and explosive eruption products. The distribution of modal proportion is displayed in volume percent (vol.%) by counting >1000 points for the selected clast types from the studied eruption products. Error bars representing ( $2\sigma$ ) were obtained by applying the method of Van der Plas and Tobi (1965).

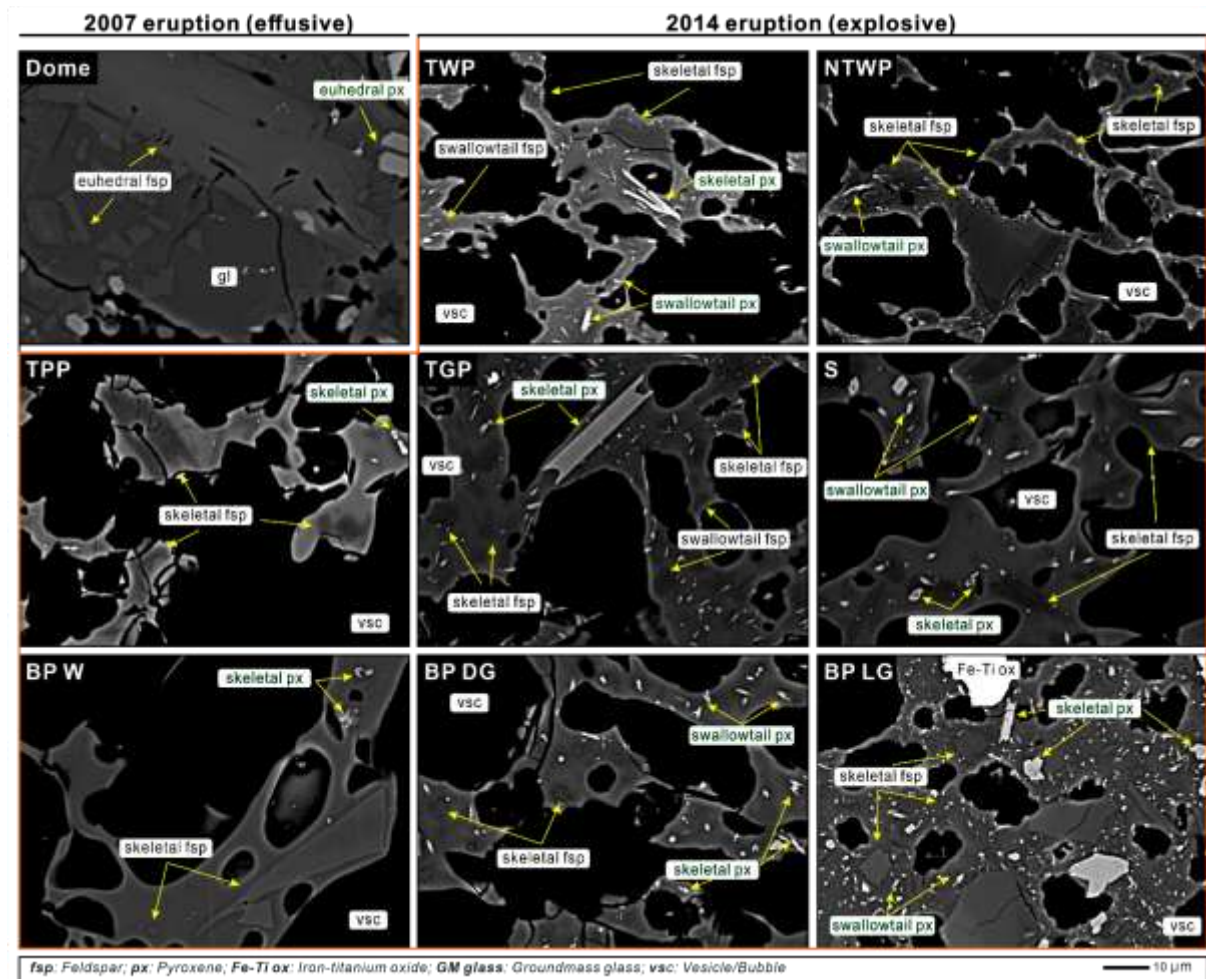


**Figure 5. 4.** Mineral assemblages contained in groundmass of 2007/08 and 2014 eruptions of Kelud. The groundmass mostly consists of plagioclase feldspar, pyroxene, and Fe-Ti oxide microlites, with occasional observed nanolite phase.

### 5.3.2. Microlite texture and composition

In general, the groundmass shares similar mineralogy with the one observed as phenocrysts, consisting of microlites of plagioclase feldspar, orthopyroxene, clinopyroxene, Fe-Ti oxide, and accessory apatite. Visual inspection of the groundmass texture in the representative samples reveals distinguishing features between each clast type. The microlite is rarely present, filling the groundmass within the pumice and scoria samples. However, the microlites may occupy >35 vol.% of the groundmass fraction in the dome samples.

#### *Feldspar microlite texture, zonation, and composition*

Feldspar microlites in effusive and explosive products usually show different characteristics, as reflected in their morphologies, internal zonations, and compositions. For the 2007/08 dome, crystals with >20  $\mu\text{m}$  length usually have euhedral blocky morphology, while the  $\leq 20$   $\mu\text{m}$  are dominated by euhedral prismatic (Fig. 5.5). The feldspar microlites of 2014 eruptions are typically skeletal/box-work, although in banded pumice samples (BP W, BP LG, and BP DG) of PDC-1, euhedral blocky present as dominant morphology consisting of bigger microlite crystals (>20  $\mu\text{m}$ ), followed by the skeletal shape in the crystal less than 20  $\mu\text{m}$  in length.

The internal textures and zonations of feldspar microlites also show slight differences among the effusive and explosive products (Fig. 5.6). The 2007/08 dome usually has feldspar microlites with normal and oscillatory zonations, while the 2014 explosive products have more variable features from normal zoning, oscillatory zoning, and hollow texture. Resorption and overgrowth are typical in feldspar microlites of 2007/08 and 2014 eruptions. Each textural classification is described below.

1. *Resorption and overgrowth.* Resorption and overgrowth are the most common textures observed in feldspar microlites. Two levels of resorption can be identified: complex and restricted resorptions. Crystals with complex resorption are commonly found in 2007/08 effusive products, whereas simple and restricted resorptions are common in 2014

explosive products. Complex resorption affects some crystals, showing an anhedral core with several growth layers and a euhedral outer rim (Fig. 5.6a). On the other hand, crystals with limited resorption often show a rounded anhedral core, which reflects a single resorption event, followed by continuous overgrowth of a euhedral to subhedral rim (Fig. 5.6d).

2. *Oscillatory zoning.* Oscillatory zonation is a common feature in both effusive and explosive products. Oscillatory zoned microlites are characterized by various amplitudes and frequencies of compositional cycles up to 10  $\mu\text{m}$  wide, parallel to the crystal edges (Figs. 5.6a, b, and e). Most of the feldspar microlites from the explosive eruption have multiple thin (1–15  $\mu\text{m}$ ) oscillations with zoning patterns of rim zones, often mantling a small unzoned (sometimes resorbed) core. A few zoned crystals, ranging from 40  $\mu\text{m}$  to  $\sim 80 \mu\text{m}$  in length, display uninterrupted zoning where an oscillation continuously develops (Fig. 5.6b).
3. *Normal zoning.* Most crystals without oscillatory zoning occur as normally zoned with a steep concentration gradient defining the compositional difference between two growth zones (Fig. 5.6c). The growth zones can reach up to 20  $\mu\text{m}$  in width. About 90% of the crystals identified with this texture present euhedral calcic cores that are overgrown by more sodic outer layer.
4. *Hollow texture.* Hollow textures in feldspar microlites present as elongated hollow formations in basal cuts, or as rounded void spaces in elongated cuts (Fig. 5.6f). The void usually filled with matrix glass and may be associated with a normal zoning and skeletal overgrowth rim. This texture, which we identify as the remnant of early skeletal growth, is predominant in the 2014 explosive products.

Representative analytical results of feldspar microlites from 2007/08 and 2014 products are shown in Table 5.1. Feldspar microlites in most samples have general compositional ranges from  $\text{An}_{89}\text{Ab}_{11}\text{Or}_0$  to  $\text{An}_{22}\text{Ab}_{68}\text{Or}_{10}$  with frequent more sodic rim (Fig. 5.7). Further, all feldspar

compositions were plotted separately in the feldspar ternary diagram, revealing that all samples cover a wide range of compositions (from bytownite to andesine), except for the BP LG of PDC-1 and CPF scoria, which have bytownite to labradorite compositions, ranging from  $An_{83}Ab_{16}Or_1$  to  $An_{56}Ab_{44}Or_1$  and  $An_{88}Ab_{12}Or_0$  to  $An_{54}Ab_{45}Or_1$ , respectively (Fig. 5.7). The dome samples from the 2007/08 eruption show the widest compositional range from  $An_{87}Ab_{12}Or_1$  to  $An_{22}Ab_{68}Or_{10}$ , reaching the high-K field of oligoclase (Fig. 5.7). Feldspar microlite from BP W of PDC-1 range between  $An_{89}Ab_{11}Or_0$  and  $An_{42}Ab_{57}Or_1$ , BP DG of PDC-1 between  $An_{88}Ab_{12}Or_0$  to  $An_{49}Ab_{48}Or_3$ , and SB of PDC-1 between  $An_{84}Ab_{16}Or_0$  to  $An_{43}Ab_{53}Or_4$ , although nearly 90% of measured microlites in SB samples have  $\leq An_{70}$ . CPF NTWP, TWP, TPP, and TGP microlites have a similar overall range in composition between  $An_{82}Ab_{18}Or_0$  to  $An_{45}Ab_{50}Or_5$ .



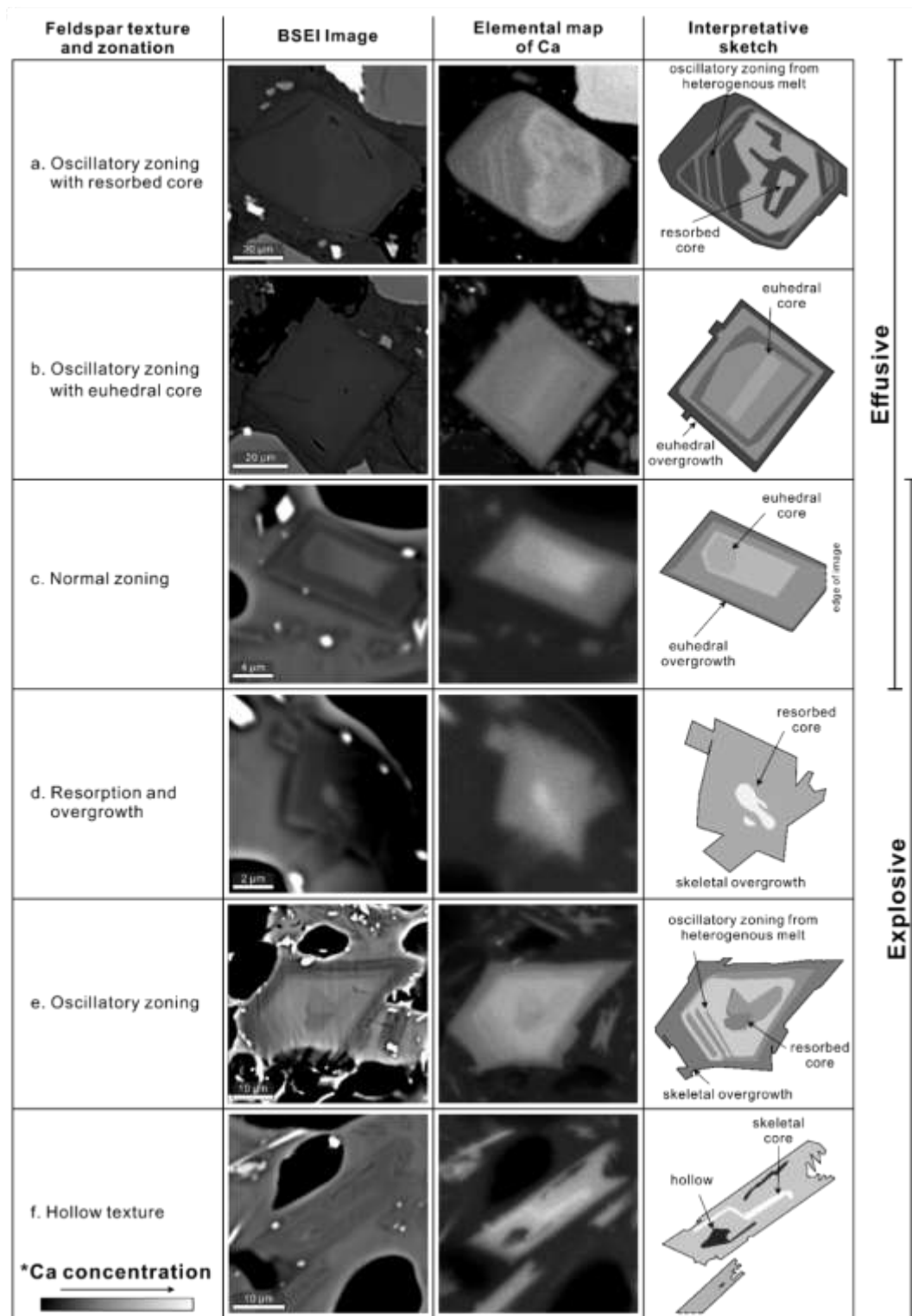


**Figure 5. 6.** Textures and zonation of feldspar microlites observed in the 2007/08 and 2014 products, including descriptions and interpretative sketches: oscillatory zoning with a) resorbed core or b) euhedral core and euhedral to subhedral overgrowth rim; normal zoning with distinct compositional variation between c) euhedral or d) resorbed core and growing rim; e) oscillatory zoning with resorbed core, where the overgrowth rim has skeletal morphology; and f) hollow texture highlighting a remnant core of skeletal crystallization. All elemental images use distribution of calcium in the analyzed feldspar microlites. Note different scales of each crystal.

**Table 5. 1.** Representative feldspar microlite composition of products from 2007/08 and 2014 eruptions analyzed using electron microprobe. FeO\*= total iron LD: lava dome; BP W: banded pumice white part; BP LG: banded pumice light grey; BP DG: banded pumice dark grey; SB: scoria bomb; NTWP: non-transparent white pumice; TWP: transparent white pumice; TPP: transparent pink pumice; TGP: transparent grey pumice; and S: scoria.

Sample	LD C-4			BP W			BP LG			BP DG	
Spot no.	468	507	28	67	30	63	126	150	160	114	108
Eruption	2007/08			2014			2014			2014	
Stage	-	-	-	I (PDC-1)			I (PDC-1)			I (PDC-1)	
Major element (wt.%)											
SiO <sub>2</sub>	45.88	56.55	62.32	45.75	54.37	58.42	48.82	50.68	53.94	46.30	51.25
TiO <sub>2</sub>	0.03	0.16	0.14	0.02	0.03	0.03	0.02	0.01	0.03	0.01	0.05
Al <sub>2</sub> O <sub>3</sub>	33.67	26.69	21.91	34.14	28.63	25.70	31.69	30.52	28.29	34.30	30.58
Cr <sub>2</sub> O <sub>3</sub>	0.00	0.00	0.00	0.00	0.00	0.00	0.02	0.01	0.01	0.00	0.00
FeO*	0.72	0.96	0.80	0.67	0.58	0.51	0.63	0.61	0.67	0.66	0.67
MnO	0.03	0.00	0.00	0.02	0.01	0.00	0.03	0.02	0.01	0.03	0.00
MgO	0.09	0.41	0.39	0.03	0.07	0.04	0.04	0.04	0.11	0.03	0.06
CaO	17.30	8.99	4.61	17.14	11.32	8.32	15.00	13.76	11.42	17.24	13.54
Na <sub>2</sub> O	1.34	5.79	7.79	1.22	4.57	6.24	2.72	3.48	4.56	1.29	3.57
K <sub>2</sub> O	0.04	0.28	1.35	0.03	0.16	0.25	0.05	0.07	0.14	0.03	0.08
NiO	0.03		0.00	0.01	0.00	0.00	0.00	0.00	0.00	0.00	0.00
Total	99.12	99.82	99.31	99.02	99.73	99.51	99.00	99.19	99.19	99.88	99.79
Structural formula based on O=8 (apfu)											
Si	2.13	2.55	2.80	2.13	2.46	2.63	2.26	2.33	2.46	2.13	2.34
Ti	0.00	0.01	0.00	0.00	0.00	0.00	0.00	0.00	0.00	0.00	0.00
Al	1.85	1.42	1.16	1.87	1.53	1.36	1.73	1.65	1.52	1.86	1.64
Cr	0.00	0.00	0.00	0.00	0.00	0.00	0.00	0.00	0.00	0.00	0.00
ΣFe	0.03	0.04	0.03	0.03	0.02	0.02	0.02	0.02	0.03	0.03	0.03
Mn	0.00	0.00	0.00	0.00	0.00	0.00	0.00	0.00	0.00	0.00	0.00
Mg	0.01	0.03	0.03	0.00	0.00	0.00	0.00	0.00	0.01	0.00	0.00
Ca	0.86	0.43	0.22	0.85	0.55	0.40	0.74	0.68	0.56	0.85	0.66
Na	0.12	0.51	0.68	0.11	0.40	0.54	0.24	0.31	0.40	0.12	0.32
K	0.00	0.02	0.08	0.00	0.01	0.01	0.00	0.00	0.01	0.00	0.00
Ni	0.00	0.00	0.00	0.00	0.00	0.00	0.00	0.00	0.00	0.00	0.00
ΣCation	5.00	5.00	5.00	4.99	4.98	4.97	5.00	5.00	4.98	4.99	5.00
XAn	0.87	0.45	0.23	0.88	0.57	0.42	0.75	0.68	0.58	0.88	0.67
XAb	0.12	0.53	0.69	0.11	0.42	0.57	0.25	0.31	0.42	0.12	0.32
XOr	0.00	0.02	0.08	0.00	0.01	0.02	0.00	0.00	0.01	0.00	0.00
Total	1.00	1.00	1.00	1.00	1.00	1.00	1.00	1.00	1.00	1.00	1.00

**Table 5. 1.** (continued).

Sample	SB			NTWP			TWP			TPP	
Spot no.	450	19	63	72	20	80	185	200	13	428	441
Eruption	2014			2014			2014			2014	
Stage	I (PDC-1)			II (Climactic Plinian Fall; CPF)							
Major element (wt.%)											
SiO <sub>2</sub>	47.18	56.27	59.28	46.31	52.04	56.97	46.81	51.54	56.75	46.22	49.84
TiO <sub>2</sub>	0.00	0.17	0.28	0.02	0.02	0.05	0.02	0.00	0.06	0.00	0.02
Al <sub>2</sub> O <sub>3</sub>	33.79	26.23	23.49	33.49	29.64	26.46	33.19	30.27	27.19	33.76	31.46
Cr <sub>2</sub> O <sub>3</sub>	0.00	0.00	0.00	0.00	0.04	0.00	0.00	0.00	0.00	0.00	0.00
FeO*	0.60	0.99	1.38	0.55	0.54	0.73	0.63	0.62	0.63	0.64	0.64
MnO	0.01	0.00	0.00	0.00	0.02	0.00	0.00	0.00	0.03	0.02	0.00
MgO	0.03	0.76	0.89	0.04	0.07	0.17	0.01	0.04	0.08	0.04	0.05
CaO	16.73	9.95	8.13	17.12	13.03	9.76	16.65	13.27	10.20	16.94	14.66
Na <sub>2</sub> O	1.74	5.74	5.56	1.46	4.01	5.63	1.63	3.77	5.47	1.49	3.02
K <sub>2</sub> O	0.03	0.29	0.62	0.03	0.10	0.19	0.05	0.09	0.18	0.02	0.06
NiO	0.01	0.00	0.00	0.01	0.01	0.00	0.01	0.02	0.00	0.00	0.00
Total	100.11	100.38	99.63	99.02	99.51	99.96	99.01	99.63	100.57	99.13	99.75
Structural formula based on O=8 (apfu)											
Si	2.17	2.54	2.67	2.15	2.38	2.56	2.17	2.35	2.54	2.15	2.28
Ti	0.00	0.01	0.01	0.00	0.00	0.00	0.00	0.00	0.00	0.00	0.00
Al	1.83	1.39	1.25	1.83	1.60	1.40	1.82	1.63	1.43	1.85	1.70
Cr	0.00	0.00	0.00	0.00	0.00	0.00	0.00	0.00	0.00	0.00	0.00
ΣFe	0.02	0.04	0.05	0.02	0.02	0.03	0.02	0.02	0.02	0.02	0.02
Mn	0.00	0.00	0.00	0.00	0.00	0.00	0.00	0.00	0.00	0.00	0.00
Mg	0.00	0.05	0.06	0.00	0.00	0.01	0.00	0.00	0.01	0.00	0.00
Ca	0.82	0.48	0.39	0.85	0.64	0.47	0.83	0.65	0.49	0.84	0.72
Na	0.15	0.50	0.49	0.13	0.36	0.49	0.15	0.33	0.47	0.13	0.27
K	0.00	0.02	0.04	0.00	0.01	0.01	0.00	0.01	0.01	0.00	0.00
Ni	0.00	0.00	0.00	0.00	0.00	0.00	0.00	0.00	0.00	0.00	0.00
ΣCation	5.00	5.02	4.96	5.00	5.00	4.98	4.99	5.00	4.98	5.00	5.00
XAn	0.84	0.48	0.43	0.86	0.64	0.48	0.85	0.66	0.50	0.86	0.73
XAb	0.16	0.50	0.53	0.13	0.36	0.50	0.15	0.34	0.49	0.14	0.27
XOr	0.00	0.02	0.04	0.00	0.01	0.01	0.00	0.01	0.01	0.00	0.00
Total	1.00	1.00	1.00	1.00	1.00	1.00	1.00	1.00	1.00	1.00	1.00

**Table 5. 1.** (continued).

Sample	TPP	TGP			S		
Spot no.	423	381	376	371	299	278	301
Eruption	2014	2014			2014		
Stage	II (Climactic Plinian Fall; CPF)						
Major element (wt.%)							
SiO <sub>2</sub>	57.86	47.74	51.29	54.29	45.91	50.72	55.37
TiO <sub>2</sub>	0.00	0.02	0.00	0.06	0.00	0.04	0.06
Al <sub>2</sub> O <sub>3</sub>	25.81	33.32	30.20	27.90	34.09	30.97	27.06
Cr <sub>2</sub> O <sub>3</sub>	0.00	0.00	0.01	0.03	0.00	0.01	0.00
FeO*	0.42	0.68	0.70	0.88	0.58	0.65	0.85
MnO	0.01	0.00	0.03	0.03	0.00	0.00	0.00
MgO	0.04	0.03	0.04	0.13	0.06	0.07	0.14
CaO	8.13	16.41	13.18	11.20	17.42	14.02	10.74
Na <sub>2</sub> O	6.56	1.93	3.66	4.82	1.34	3.39	5.01
K <sub>2</sub> O	0.21	0.03	0.10	0.16	0.03	0.08	0.22
NiO	0.00	0.00	0.00	0.00	0.02	0.00	0.00
Total	99.03	100.15	99.20	99.51	99.45	99.95	99.45
Structural formula based on O=8 (apfu)							
Si	2.62	2.19	2.35	2.47	2.13	2.31	2.52
Ti	0.00	0.00	0.00	0.00	0.00	0.00	0.00
Al	1.37	1.80	1.63	1.50	1.86	1.67	1.45
Cr	0.00	0.00	0.00	0.00	0.00	0.00	0.00
ΣFe	0.02	0.03	0.03	0.03	0.02	0.02	0.03
Mn	0.00	0.00	0.00	0.00	0.00	0.00	0.00
Mg	0.00	0.00	0.00	0.01	0.00	0.00	0.01
Ca	0.39	0.81	0.65	0.55	0.86	0.69	0.52
Na	0.57	0.17	0.33	0.43	0.12	0.30	0.44
K	0.01	0.00	0.01	0.01	0.00	0.00	0.01
Ni	0.00	0.00	0.00	0.00	0.00	0.00	0.00
ΣCation	4.99	5.00	5.00	5.00	5.00	5.00	4.99
XAn	0.40	0.82	0.66	0.56	0.88	0.69	0.54
XAb	0.59	0.18	0.33	0.43	0.12	0.30	0.45
XOr	0.01	0.00	0.01	0.01	0.00	0.00	0.01
Total	1.00	1.00	1.00	1.00	1.00	1.00	1.00

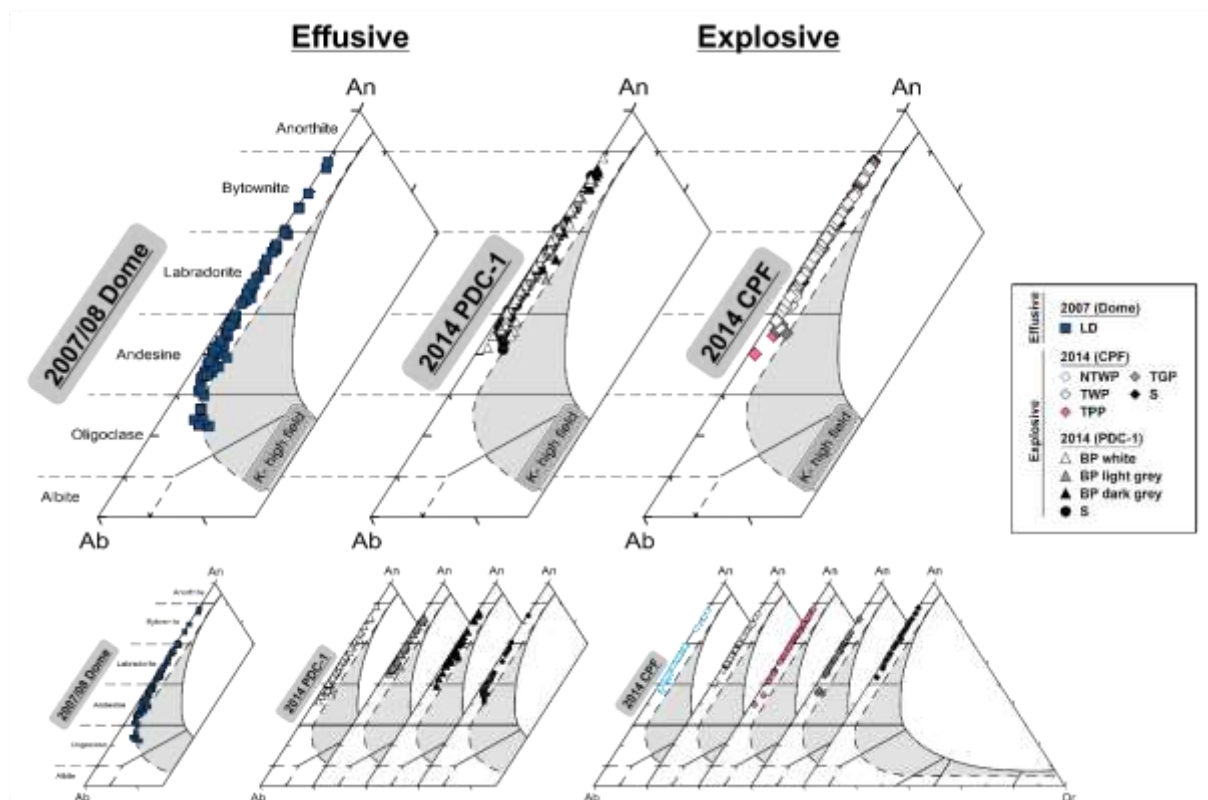


**Figure 5. 7.** Feldspar microlite compositions of analyzed samples plotted on ternary (An-Ab-Or) diagram show (upper) the general distribution of all microlite compositions from different eruption events and (lower) the microlite composition plotted separately for each defined clast type.

### *Pyroxene microlite texture, zonation, and composition*

Similar to the feldspar microlites, the pyroxenes also show different morphologies, internal zonations, and compositions among the effusive and explosive products. For the 2007/08 dome, the euhedral blocky shape dominates the morphology of crystals, although the euhedral prismatic shape can sometimes be observed on the crystals between 20 to 30  $\mu\text{m}$  (Fig. 5.5). The pyroxene microlites of 2014 eruptions are typically skeletal/box-work or swallowtail and relatively consistent through the smaller size.

The internal textures and zonations of pyroxene microlites also show slight differences among the effusive and explosive products (Fig. 5.8). The 2007/08 dome usually has pyroxene microlites with normal, oscillatory, and sectoral zonations, while the 2014 explosive products have normal zoning and hollow texture. Resorption and overgrowth are also typical in pyroxene microlite of 2007/08 and 2014 eruptions. Each textural classification is described below.

1. *Resorption and overgrowth.* Resorption and overgrowth are commonly observed in pyroxenes microlites. Unlike the feldspars, pyroxenes are smaller, less complex, and typically have a resorbed rounded core with euhedral overgrowth (Fig. 5.8d).
2. *Calcium-rich bands.* Ca-rich bands are invisible via BSE observation and can only be observed through elemental maps of Ca. The bands are often present in pyroxene microlites as thin layers at the rims and parallel to the (100) plane ( $\sim 1 \mu\text{m}$  in width; Figs. 5.8c & d). In most cases, Ca-rich rims have low Fe, Ti, and Mg, and are enriched in Al. These Ca-rich bands are not always continuous, especially in the cases where Ca-rich minerals (i.e., plagioclase feldspar) have crystallized close to the pyroxene rim (Fig. 5.8d).
3. *Hollow texture.* Hollow textures in pyroxene microlites are present as elongated or irregular voids perpendicular to the (001) plane (Fig. 5.8f). The voids are filled with matrix glass and are sometimes associated with a skeletal and normally zoned overgrowth rim. This texture can be found restricted only to the 2014 explosive products.

4. *Normal zoning.* Most pyroxene crystals with normal zoning have a euhedral core with no sign of resorption (Figs. 5.8a and e). The cores are generally Fe- and Si-rich with depleted Mg and Al values, while the rims have Mg-rich and depleted Fe. The compositional boundary between core and rim is generally sharp but also appears diffuse in several crystals.
5. *Oscillatory zoning.* Pyroxene with oscillatory zoning is prevalent in effusive materials, but not as abundant as feldspar microlite (Fig. 5.8b). The oscillations are thin (1–15  $\mu\text{m}$ ) and comprise distinct amounts of Fe, Mg, Al, and Si. Mg has a negative correlation with Fe and Si, but a positive correlation with Al. Frequently, the oscillations are accompanied by a tiny (occasionally resorbed) core.
6. *Sector zoning.* Sector zoning in pyroxene microlites is characterized by the intergrowth of Mg-rich (i.e., orthopyroxene) and Ca-rich (clinopyroxene) crystals (Fig. 5.8c). The sectors are usually calcic hourglass shapes that can be observed perpendicular to the c-axis. This texture is limited to the small crystals  $<10 \mu\text{m}$  and is cryptic in BSE images.
7. *Unzoned.* Besides the textures described above, unzoned pyroxenes are also common.

They are euhedral to subhedral and massive with no obvious zonation or internal texture.

Representative analytical results of pyroxene microlites from 2007/08 and 2014 products are shown in Table 5.2. Pyroxene microlites in most samples define the main population of orthopyroxenes (i.e., ~85% of enstatite) and a smaller population of clinopyroxenes (i.e., ~4% pigeonite and ~11% augite; see Fig. 5.9). Further, the orthopyroxene microlites have Mg# ranging from 60 to 76, with average Mg# of  $76 \pm 3$  ( $1\sigma$ ),  $69 \pm 3$  ( $1\sigma$ ),  $72 \pm 2$  ( $1\sigma$ ),  $72 \pm 1$  ( $1\sigma$ ),  $72 \pm 1$  ( $1\sigma$ ), and  $69 \pm 5$  ( $1\sigma$ ) for 2007/08 dome, PDC-1 BP W, BP LG, BP DG, and SB, respectively. The orthopyroxenes of CPF have Mg# averages of  $72 \pm 2$  ( $1\sigma$ ),  $71 \pm 2$  ( $1\sigma$ ),  $72 \pm 2$  ( $1\sigma$ ),  $72 \pm 2$  ( $1\sigma$ ), and  $70 \pm 1$  ( $1\sigma$ ) for NTWP, TWP, TPP, TGP, and S of CPF, respectively. The clinopyroxenes of the 2007/08 dome have an average Mg# value of  $76 \pm 1$  ( $1\sigma$ ). Clinopyroxenes of PDC-1 have variable Mg# averages of  $78 \pm 2$  ( $1\sigma$ ),  $74 \pm 5$  ( $1\sigma$ ), and  $75 \pm 1$

(1 $\sigma$ ) for BP W, BP LG, and BP DG. CPF NTWP, TWP, TPP, TGP, and S clinopyroxenes have relatively similar Mg#, with average values of  $76 \pm 2$  (1 $\sigma$ ),  $76 \pm 2$  (1 $\sigma$ ),  $74 \pm 2$  (1 $\sigma$ ),  $74 \pm 1$  (1 $\sigma$ ), and  $75 \pm 2$  (1 $\sigma$ ), respectively.

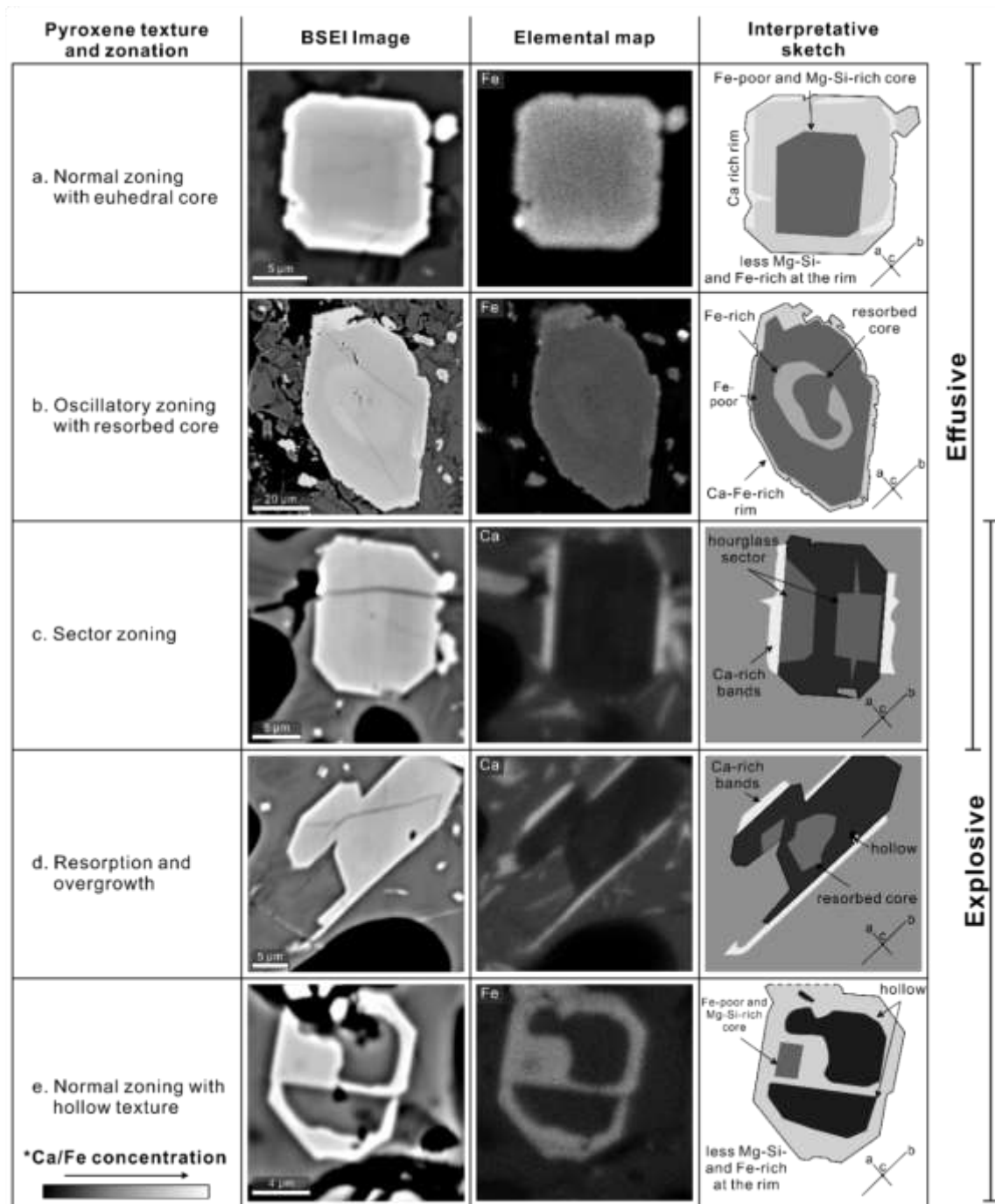


**Figure 5. 8.** Textures and zonation of pyroxene microlites observed in the 2007/08 and 2014 products, including descriptions and interpretative sketches: a) normal zoning sharp boundary between Fe-poor euhedral core and Fe-rich overgrowth rim; b) oscillatory zoning that show successive growth of Fe-poor and Fe-rich rims over the resorbed core; c) sector zoning in basal cut as hourglass sector around an unzoned core and often appear with thin Ca-rich bands due to local partitioning effect of feldspar crystallization; d) resorbed core and skeletal overgrowth with thin Ca-rich band; and e) hollow texture highlighting a normal zoning from the remnant core of euhedral/hopper crystallization. The elemental images mostly use distribution of calcium and iron to distinguish textural variation in the analyzed pyroxene microlites. Note different scales of each acquired crystal.

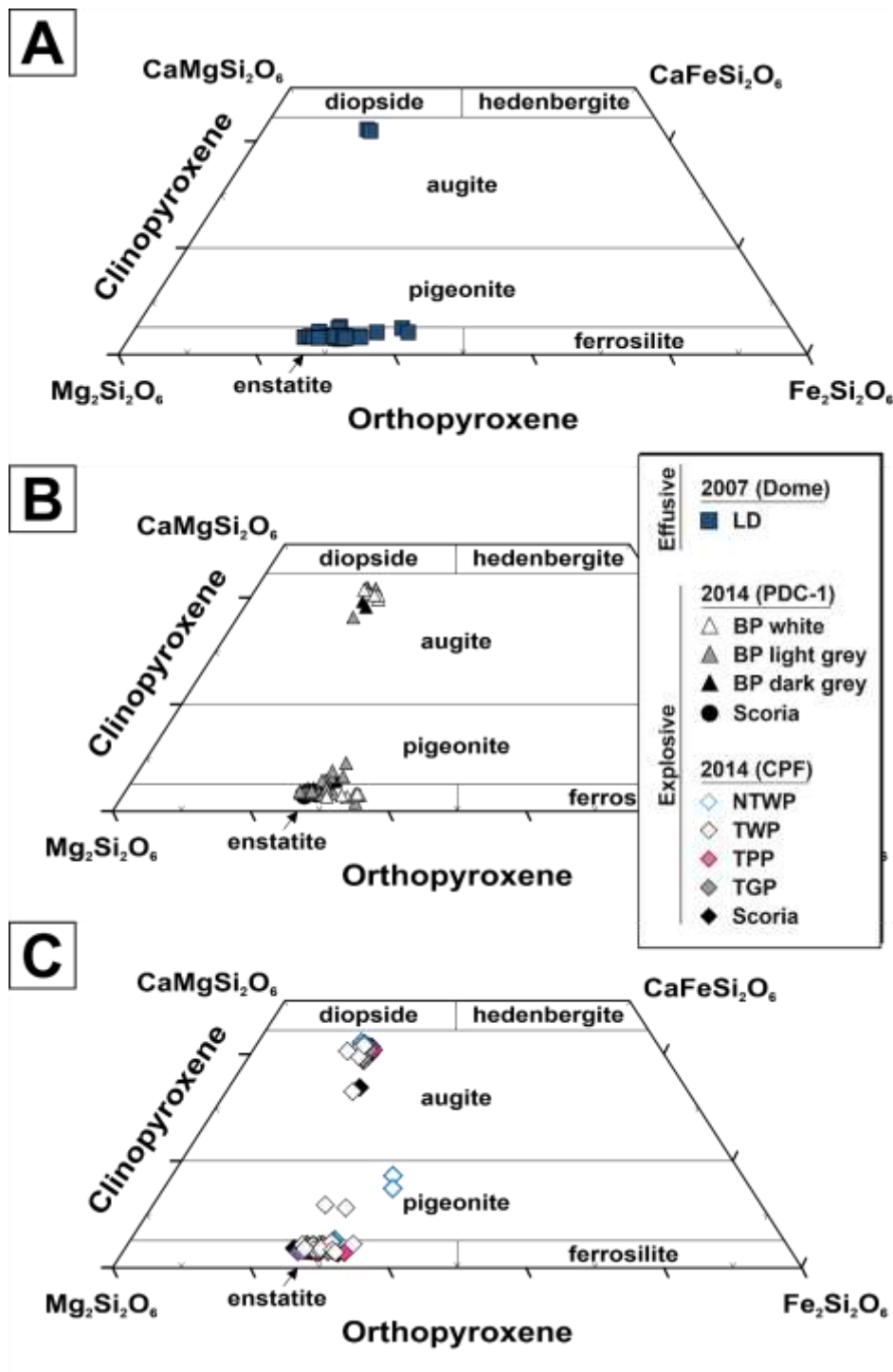


**Figure 5. 9.** Pyroxene microlite compositions of analyzed samples plotted on quadrilateral (Di-Hd-En-Fs) diagram show the discrimination of pyroxene species in A) 2007/08 lava dome, B) 2014 PDC-1, and C) 2014 CPF (Morimoto, 1989).

**Table 5. 2.** Representative pyroxene microelite composition of products from 2007/08 and 2014 eruptions analyzed using electron microprobe. FeO\*= total iron. LD: lava dome; BP W: banded pumice white part; BP LG: banded pumice light grey; BP DG: banded pumice dark grey; SB: scoria bomb; NTWP: non-transparent white pumice; TWP: transparent white pumice; TPP: transparent pink pumice; TGP: transparent grey pumice; and S: scoria.

Sample	LD C-4			BP W			BP LG			BP DG		
Spot no.	1	497	483	40	76	79	123	155	169	97	118	
Eruption	2007/08			2014			2014			2014		
Stage	-	-	-	I (PDC-1)			I (PDC-1)			I (PDC-1)		
Mineral	Cpx	Opx	Opx	Cpx	Cpx	Opx	Cpx	Opx	Opx	Cpx	Opx	
Major element (wt.%)												
SiO <sub>2</sub>	51.62	52.71	53.68	51.95	52.79	52.70	52.03	52.95	54.07	52.65	53.32	
TiO <sub>2</sub>	0.41	0.23	0.12	0.25	0.32	0.22	0.34	0.21	0.17	0.43	0.27	
Al <sub>2</sub> O <sub>3</sub>	2.48	2.15	0.59	1.40	1.69	0.85	2.09	2.43	1.44	3.01	1.41	
Cr <sub>2</sub> O <sub>3</sub>	0.01	0.00	0.00	0.02	0.01	0.02	0.05	0.00	0.00	0.01	0.00	
FeO*	8.87	16.63	18.92	9.12	10.38	19.88	9.71	17.02	17.20	9.89	17.27	
MnO	0.35	0.67	0.91	0.53	0.56	1.10	0.49	0.67	0.77	0.48	0.71	
MgO	14.81	24.75	23.98	14.75	13.89	21.99	16.13	24.02	23.42	14.70	24.33	
CaO	20.35	2.20	1.47	19.95	18.93	1.58	17.39	1.64	2.05	17.74	1.83	
Na <sub>2</sub> O	0.26	0.05	0.00	0.28	0.39	0.01	0.17	0.11	0.18	0.43	0.04	
K <sub>2</sub> O	0.02	0.03	0.01	0.02	0.09	0.01	0.03	0.05	0.07	0.09	0.01	
NiO	0.02	0.00	0.01	0.00	0.00	0.00	0.00	0.01	0.00	0.02	0.00	
Total	99.19	99.41	99.69	98.26	99.03	98.36	98.42	99.11	99.37	99.45	99.18	
Structural formula based on O=6 (apfu)												
Si	1.93	1.94	1.98	1.97	1.98	1.98	1.95	1.95	1.99	1.96	1.96	
Ti	0.01	0.01	0.00	0.01	0.01	0.01	0.01	0.01	0.00	0.01	0.01	
Al	0.11	0.09	0.03	0.06	0.07	0.04	0.09	0.11	0.06	0.13	0.06	
Cr	0.00	0.00	0.00	0.00	0.00	0.00	0.00	0.00	0.00	0.00	0.00	
Fe <sup>3+</sup>	0.03	0.04	0.01	0.02	0.00	0.00	0.00	0.00	0.00	0.00	0.00	
Fe <sup>2+</sup>	0.25	0.47	0.58	0.27	0.33	0.63	0.31	0.52	0.53	0.31	0.53	
Mn	0.01	0.02	0.03	0.02	0.02	0.04	0.02	0.02	0.02	0.02	0.02	
Mg	0.83	1.35	1.32	0.83	0.78	1.23	0.90	1.32	1.28	0.81	1.34	
Ca	0.82	0.09	0.06	0.81	0.76	0.06	0.70	0.06	0.08	0.71	0.07	
Na	0.02	0.00	0.00	0.02	0.03	0.00	0.01	0.01	0.01	0.03	0.00	
K	0.00	0.00	0.00	0.00	0.00	0.00	0.00	0.00	0.00	0.00	0.00	
Ni	0.00	0.00	0.00	0.00	0.00	0.00	0.00	0.00	0.00	0.00	0.00	
ΣCation	4.01	4.01	4.00	4.01	3.99	3.99	4.00	4.00	3.99	3.98	4.00	
XWo	0.42	0.04	0.03	0.42	0.03	0.40	0.36	0.03	0.04	0.38	0.04	
XEn	0.43	0.69	0.66	0.43	0.63	0.41	0.47	0.68	0.67	0.44	0.68	
XFfs	0.15	0.27	0.31	0.16	0.34	0.18	0.17	0.28	0.29	0.18	0.28	
Total	1.00	1.00	1.00	1.00	1.00	1.00	1.00	1.00	1.00	1.00	1.00	
Mg#	76.78	74.18	69.54	75.32	70.38	66.30	74.74	71.54	70.74	72.51	71.51	

**Table 5. 2.** (continued).

Sample	SB			NTWP			TWP			TPP	
Spot no.	340	341	345	97	118	169	213	179	17	440	433
Eruption	2014			2014			2014			2014	
Stage	I (PDC-1)			II (CPF)			II (CPF)			II (CPF)	
Mineral	Opx	Opx	Opx	Cpx	Opx	Opx	Opx	Opx	Opx	Cpx	Opx
Major element (wt.%)											
SiO <sub>2</sub>	52.77	53.95	52.99	51.62	54.26	54.14	52.80	54.37	53.37	52.70	54.11
TiO <sub>2</sub>	0.27	0.16	0.22	0.41	0.15	0.18	0.40	0.28	0.23	0.36	0.16
Al <sub>2</sub> O <sub>3</sub>	2.41	0.69	1.44	2.48	0.96	1.39	1.95	2.45	1.11	2.32	0.90
Cr <sub>2</sub> O <sub>3</sub>	0.00	0.00	0.01	0.01	0.04	0.00	0.00	0.05	0.00	0.02	0.00
FeO*	16.06	16.92	17.65	8.87	15.88	16.17	15.13	16.92	16.80	9.37	16.57
MnO	0.60	0.77	0.74	0.35	0.63	0.61	0.64	0.71	0.84	0.51	0.71
MgO	25.14	24.62	23.98	14.81	25.67	25.32	22.41	23.45	21.32	14.44	24.90
CaO	1.50	1.67	1.58	20.35	1.65	1.73	5.80	2.01	5.50	19.39	1.87
Na <sub>2</sub> O	0.00	0.01	0.03	0.26	0.03	0.04	0.06	0.23	0.06	0.35	0.03
K <sub>2</sub> O	0.00	0.01	0.01	0.02	0.01	0.01	0.03	0.07	0.02	0.04	0.01
NiO	0.00	0.00	0.00	0.02	0.02	0.01	0.01	0.02	0.02	0.00	0.00
Total	98.74	98.80	98.65	99.19	99.29	99.58	99.22	100.56	99.24	99.50	99.26
Structural formula based on O=6 (apfu)											
Si	1.94	1.99	1.97	1.93	1.98	1.97	1.95	1.97	1.98	1.96	1.98
Ti	0.01	0.00	0.01	0.01	0.00	0.00	0.01	0.01	0.01	0.01	0.00
Al	0.10	0.03	0.06	0.11	0.04	0.06	0.08	0.10	0.05	0.10	0.04
Cr	0.00	0.00	0.00	0.00	0.00	0.00	0.00	0.00	0.00	0.00	0.00
Fe <sup>3+</sup>	0.00	0.00	0.00	0.03	0.00	0.00	0.00	0.00	0.00	0.00	0.00
Fe <sup>2+</sup>	0.49	0.52	0.55	0.25	0.49	0.49	0.47	0.51	0.52	0.29	0.51
Mn	0.02	0.02	0.02	0.01	0.02	0.02	0.02	0.02	0.03	0.02	0.02
Mg	1.38	1.35	1.33	0.83	1.40	1.38	1.23	1.27	1.18	0.80	1.36
Ca	0.06	0.07	0.06	0.82	0.06	0.07	0.23	0.08	0.22	0.77	0.07
Na	0.00	0.00	0.00	0.02	0.00	0.00	0.00	0.02	0.00	0.03	0.00
K	0.00	0.00	0.00	0.00	0.00	0.00	0.00	0.00	0.00	0.00	0.00
Ni	0.00	0.00	0.00	0.00	0.00	0.00	0.00	0.00	0.00	0.00	0.00
ΣCation	4.00	3.99	4.00	4.01	4.00	4.00	4.00	3.98	3.99	3.99	3.99
XWo	0.03	0.03	0.03	0.42	0.03	0.03	0.12	0.04	0.11	0.41	0.04
XEn	0.71	0.69	0.68	0.43	0.71	0.70	0.63	0.67	0.61	0.43	0.69
XF <sub>s</sub>	0.26	0.28	0.29	0.15	0.26	0.26	0.25	0.29	0.28	0.16	0.27
Total	1.00	1.00	1.00	1.00	1.00	1.00	1.00	1.00	1.00	1.00	1.00
Mg#	73.67	72.12	70.77	76.78	74.20	73.59	72.55	71.08	69.28	73.25	72.78

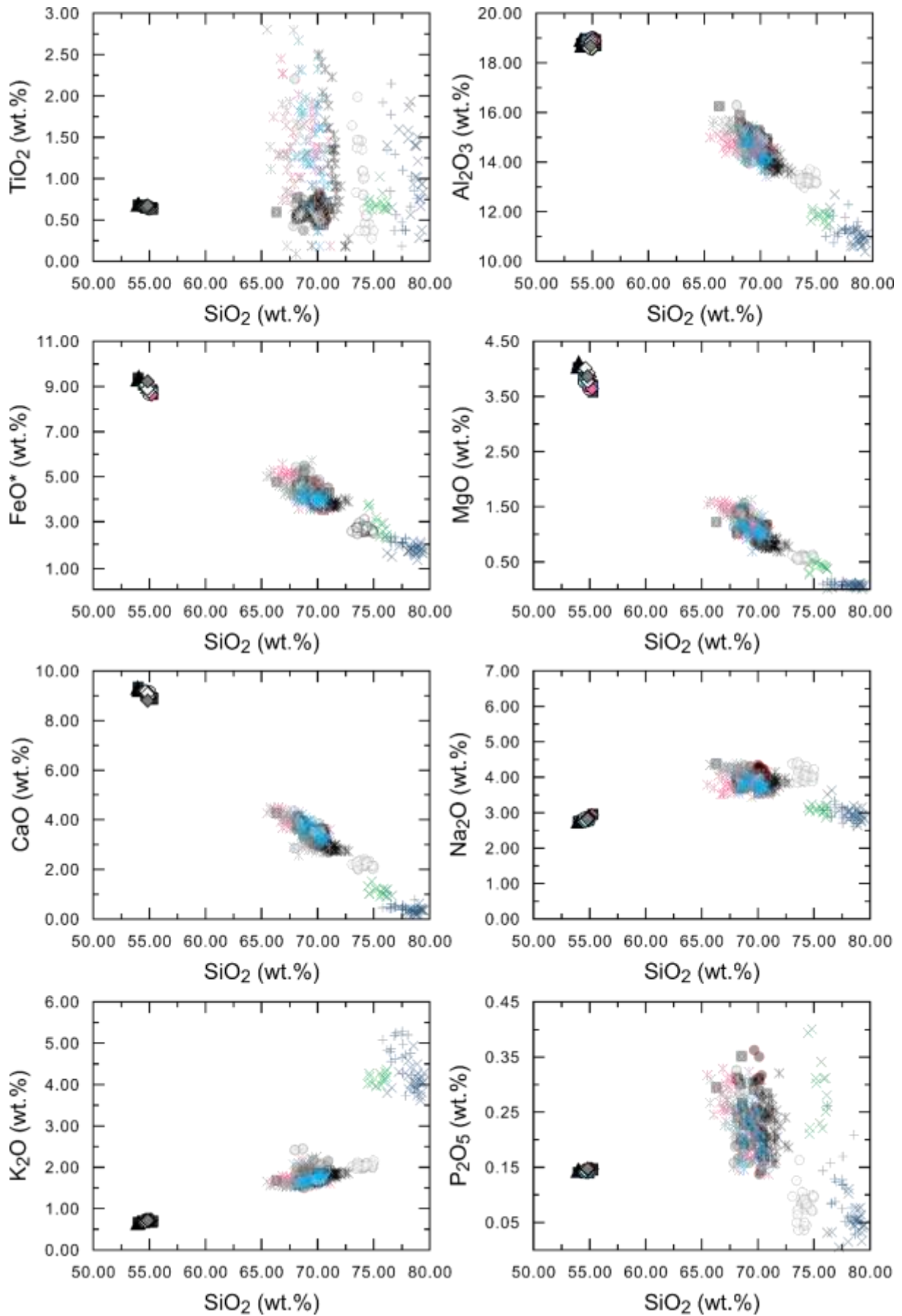
Table 5. 2. (continued).

Sample	TPP	TGP			S		
Spot no.	443	375	380	379	275	315	331
Eruption	2014		2014			2014	
Stage	CPF		II (CPF)			II (CPF)	
Mineral	Opx	Cpx	Opx	Opx	Cpx	Opx	Opx
Major element (wt.%)							
SiO <sub>2</sub>	53.16	50.54	54.52	53.63	52.20	53.76	53.19
TiO <sub>2</sub>	0.25	0.77	0.24	0.26	0.35	0.15	0.22
Al <sub>2</sub> O <sub>3</sub>	1.04	3.30	2.61	2.24	1.78	0.96	1.13
Cr <sub>2</sub> O <sub>3</sub>	0.02	0.00	0.00	0.01	0.00	0.00	0.00
FeO*	19.29	9.82	16.21	17.23	9.40	15.98	18.94
MnO	0.91	0.49	0.60	0.72	0.50	0.70	0.83
MgO	22.93	15.00	24.09	23.97	14.80	25.69	23.45
CaO	1.39	18.35	2.09	2.16	20.32	1.74	1.33
Na <sub>2</sub> O	0.03	0.28	0.17	0.07	0.27	0.02	0.02
K <sub>2</sub> O	0.01	0.01	0.05	0.02	0.00	0.01	0.00
NiO	0.01	0.00	0.00	0.00	0.03	0.01	0.01
Total	99.03	98.55	100.58	100.31	99.65	99.01	99.13
Structural formula based on O=6 (apfu)							
Si	1.98	1.91	1.97	1.95	1.95	1.97	1.97
Ti	0.01	0.02	0.01	0.01	0.01	0.00	0.01
Al	0.05	0.15	0.11	0.10	0.08	0.04	0.05
Cr	0.00	0.00	0.00	0.00	0.00	0.00	0.00
Fe <sup>3+</sup>	0.00	0.02	0.00	0.00	0.03	0.01	0.00
Fe <sup>2+</sup>	0.60	0.29	0.49	0.53	0.27	0.48	0.59
Mn	0.03	0.02	0.02	0.02	0.02	0.02	0.03
Mg	1.27	0.84	1.29	1.30	0.82	1.40	1.30
Ca	0.06	0.74	0.08	0.08	0.81	0.07	0.05
Na	0.00	0.02	0.01	0.00	0.02	0.00	0.00
K	0.00	0.00	0.00	0.00	0.00	0.00	0.00
Ni	0.00	0.00	0.00	0.00	0.00	0.00	0.00
ΣCation	3.99	4.01	3.98	4.00	4.01	4.00	4.00
XWo	0.03	0.39	0.04	0.04	0.42	0.03	0.03
XEn	0.65	0.44	0.69	0.67	0.42	0.71	0.66
XF <sub>s</sub>	0.32	0.17	0.27	0.28	0.16	0.26	0.31
Total	1.00	1.00	1.00	1.00	1.00	1.00	1.00
Mg#	67.88	74.63	72.49	71.24	75.55	74.62	68.79

### 5.3.3. Whole-rock and groundmass composition

As previously mentioned in Chapter 4, the bulk-chemical composition of 2007/08 and 2014 products have similar concentrations ( $\text{SiO}_2$  ranges from 54.01 to 55.43 wt.%) and lie within the basaltic andesite field in the total alkali vs. silica diagram (Le Maitre et al., 2002) (Fig. 5.10; Table 3.2). The bulk compositions are also comparable to the products from various eruption styles in historical records (i.e., Bourdier et al., 1997; Indriyanto et al., 2023). The groundmass glass compositions, on the other hand, have compositions of dacite to rhyolite with  $\text{SiO}_2$  ranging from 63.7 to 78.8 wt.% (Table 4.4). The most evolved melt compositions observed in this study come from the 2007/08 domes, which have the  $\text{SiO}_2$  between 75.0 and 78.8 wt.%, while the glass compositions of 2014 products have slightly lower  $\text{SiO}_2$  values ranging from 63.7 to 75.7 wt.%. Furthermore, the major oxides of whole-rock and groundmass are plotted against silica value concerning 100% anhydrous condition (Fig. 5.11). The overall trend of  $\text{K}_2\text{O}$  displays a positive correlation with the increase of  $\text{SiO}_2$ , while  $\text{Al}_2\text{O}_3$ ,  $\text{FeO}^*$  (total iron calculated as  $\text{FeO}$ ),  $\text{MgO}$ , and  $\text{CaO}$  correlate negatively with  $\text{SiO}_2$  concentrations.  $\text{TiO}_2$  and  $\text{P}_2\text{O}_5$  show no systematic correlation with the  $\text{SiO}_2$  concentration. The  $\text{Na}_2\text{O}$  trend is inflexed with  $\text{Na}_2\text{O}$  positively correlates with silica concentrations until ~69 wt.%  $\text{SiO}_2$  before  $\text{Na}_2\text{O}$  begins to decrease with an increase in  $\text{SiO}_2$ .







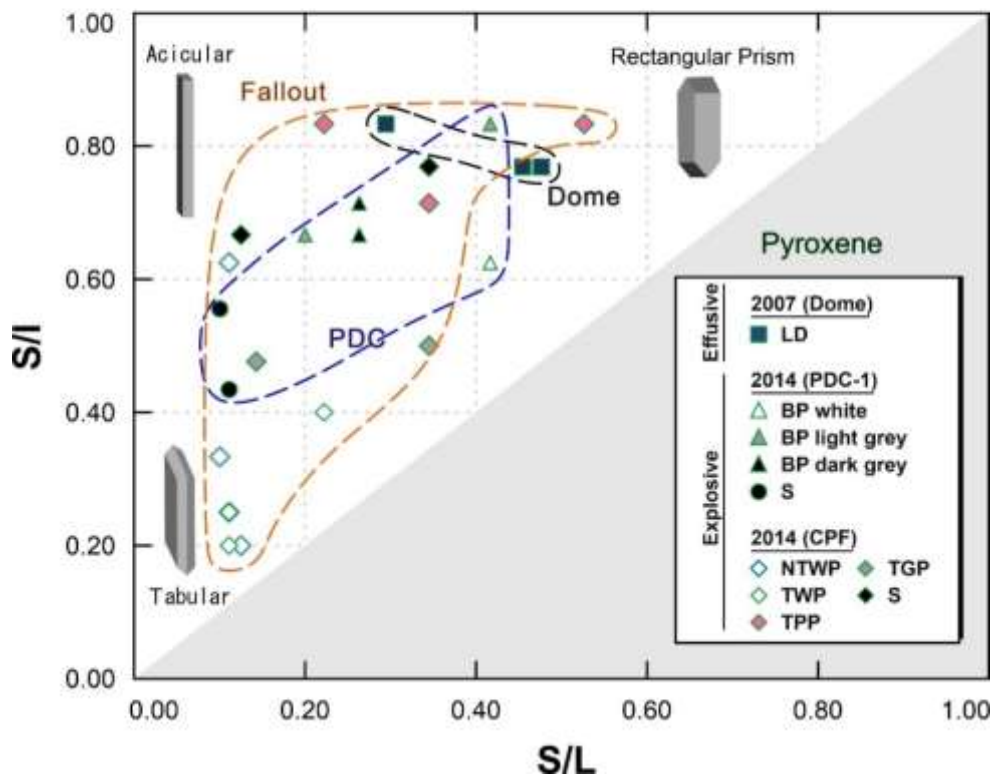
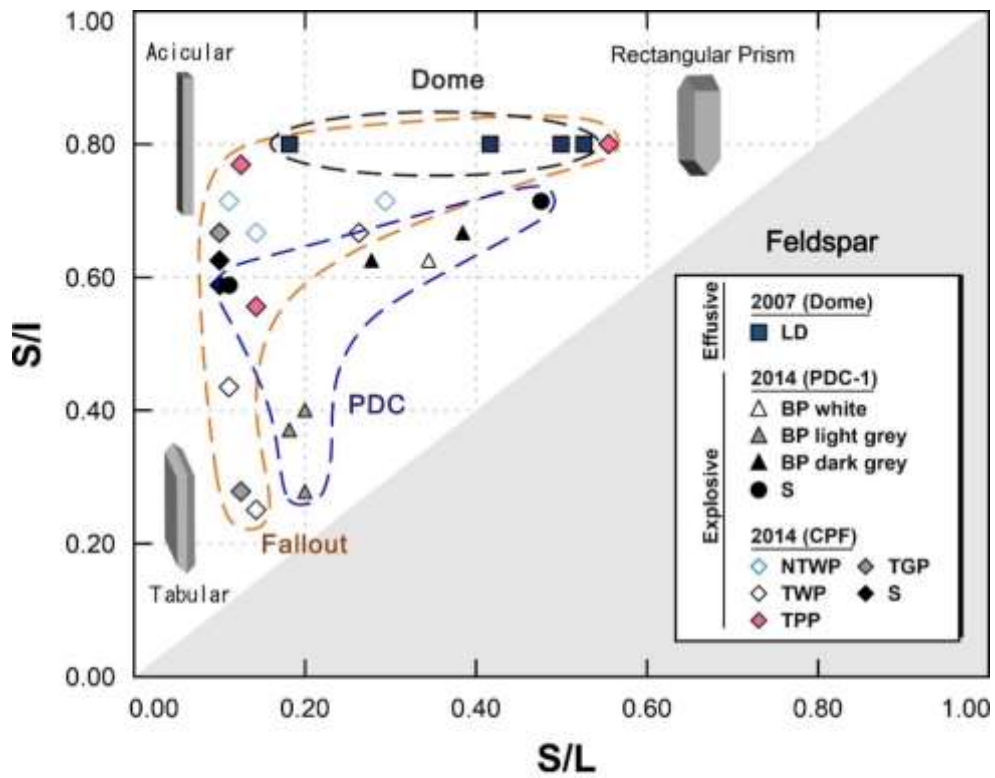


**Figure 5. 12.** Plot of microlite aspect ratios (Short axis over Intermediate axis (S/I) vs Short axis over Long axis (S/L)) for (upper) plagioclase feldspar microlites and (lower) pyroxene microlites. The feldspar and pyroxene microlites share similar aspect ratios and have wide ranges of crystal habits, covering rectangular prism, acicular, and tabular.

**Table 5. 3.** Summary of quantitative textural analysis of feldspar microlite. Lithology types are LD: lava dome; BP W: banded pumice white part; BP LG: banded pumice light grey; BP DG: banded pumice dark grey; SB: scoria bomb; NTWP: non-transparent white pumice; TWP: transparent white pumice; TPP: transparent pink pumice; TGP: transparent grey pumice; and S: scoria.

Eruption	Stage	Sample	2D areal measurements								3D volumetric measurements			
			$n^a$	GM glass area (%)	$N_A$ (mm <sup>-2</sup> )	$\phi$	Mean crystal area (μm <sup>2</sup> )	$S/I$	$S/L$	$S_n$ (μm)	3d Crystal shape	Aspect ratio (S:I:L)	R <sup>2</sup>	$N_V$ (mm <sup>-3</sup> )
2007/08	-	LD_2-1	829	84.45	13,039	0.37	26.86	0.80	0.53	5.30	Rectangular Prism	1.00 : 1.30 : 2.10	0.8522	2,461,985
2007/08	-	LD_2-2	824	94.19	13,646	0.29	20.77	0.80	0.50	4.58	Rectangular Prism	1.00 : 1.20 : 3.40	0.9159	2,981,958
2007/08	-	LD_3-1	826	99.77	7,774	0.33	32.72	0.80	0.42	6.52	Rectangular Prism	1.00 : 1.30 : 2.10	0.8522	1,191,881
2007/08	-	LD_3-2	820	99.55	7,975	0.31	38.72	0.80	0.18	6.25	Acicular	1.00 : 1.30 : 2.20	0.7592	1,276,487
2014	I (PDC-1)	BP_W	898	18.43	4,182	0.12	27.68	0.63	0.34	5.31	Rectangular Prism	1.00 : 1.60 : 2.40	0.8914	788,259
2014	I (PDC-1)	BP_DG-1	834	64.69	58,678	0.33	5.41	0.67	0.38	2.38	Rectangular Prism	1.00 : 1.40 : 3.80	0.8623	24,632,310
2014	I (PDC-1)	BP_DG-3	842	56.40	63,716	0.36	5.30	0.63	0.28	2.39	Rectangular Prism	1.00 : 1.50 : 3.80	0.8062	26,690,166
2014	I (PDC-1)	BP_LG-1	850	39.30	60,956	0.21	3.43	0.40	0.20	1.86	Rectangular Prism	1.00 : 1.50 : 5.00	0.8311	32,747,643
2014	I (PDC-1)	BP_LG-2	828	39.79	44,691	0.21	3.12	0.28	0.20	2.16	Rectangular Prism	1.00 : 1.20 : 2.40	0.7942	20,648,959
2014	I (PDC-1)	BP_LG-4	825	33.35	36,634	0.24	4.51	0.37	0.18	2.53	Rectangular Prism	1.00 : 1.40 : 3.80	0.7740	14,461,658
2014	I (PDC-1)	SB_1	917	40.26	14,830	0.17	11.56	0.59	0.10	3.43	Acicular	1.00 : 1.50 : 8.00	0.7479	4,328,014
2014	I (PDC-1)	SB_3	837	43.21	11,137	0.18	15.87	0.63	0.10	3.98	Acicular	1.00 : 1.30 : 2.90	0.7785	2,796,945
2014	II (CPF)	NTWP-2_14	834	32.96	27,334	0.26	8.83	0.80	0.56	3.11	Rectangular Prism	1.00 : 1.60 : 9.00	0.8486	8,790,898
2014	II (CPF)	NTWP-2_18	830	32.79	38,395	0.16	4.19	0.71	0.29	2.07	Acicular	1.00 : 3.00 : 10.00	0.8403	18,590,719
2014	II (CPF)	NTWP-2_20	882	30.00	29,871	0.17	5.49	0.71	0.11	2.41	Acicular	1.00 : 4.00 : 9.00	0.6761	12,400,337
2014	II (CPF)	NTWP-2_22	865	51.92	36,290	0.16	4.47	0.67	0.14	2.12	Acicular	1.00 : 5.00 : 8.00	0.8131	17,126,231
2014	II (CPF)	TWP-2_2	890	27.11	17,244	0.09	5.18	0.67	0.26	2.34	Acicular	1.00 : 5.00 : 9.00	0.6879	7,368,854
2014	II (CPF)	TWP-2_3	850	39.49	28,684	0.13	4.43	0.25	0.14	2.14	Acicular	1.00 : 2.50 : 4.50	0.7212	13,426,672
2014	II (CPF)	TWP-2_24	807	23.72	20,165	0.10	4.80	0.43	0.11	2.27	Acicular	1.00 : 4.00 : 9.00	0.5674	8,891,725
2014	II (CPF)	TPP_16	898	21.44	14,153	0.11	7.75	0.56	0.14	2.83	Acicular	1.00 : 1.40 : 2.90	0.6734	5,001,301
2014	II (CPF)	TPP_31	828	24.78	9,502	0.07	7.08	0.77	0.13	2.71	Acicular	1.00 : 1.20 : 4.50	0.8336	3,505,340
2014	II (CPF)	TPP_46	849	36.47	35,760	0.34	5.93	0.80	0.56	3.09	Acicular	1.00 : 1.20 : 1.90	0.8640	11,559,832
2014	II (CPF)	TGP_26	900	43.23	31,688	0.17	5.31	0.67	0.10	2.33	Rectangular Prism	1.00 : 2.10 : 7.00	0.7694	13,624,468
2014	II (CPF)	TGP_27	915	37.29	30,598	0.24	7.96	0.28	0.13	2.79	Rectangular Prism	1.00 : 2.00 : 2.90	0.8737	10,986,882
2014	II (CPF)	S_2	821	34.42	16,949	0.22	11.89	0.71	0.48	3.59	Rectangular Prism	1.00 : 1.80 : 10.00	0.8563	4,717,475
2014	II (CPF)	S_4	829	46.36	16,501	0.17	10.13	0.59	0.11	3.17	Acicular	1.00 : 2.30 : 9.00	0.7771	5,204,492

<sup>a</sup>Number of measured crystals.

$N_A$ : areal number density.  $N_V$ : volumetric number density (MND).

**Table 5. 4.** Summary of quantitative textural analysis of pyroxene microlite. Lithology types are LD: lava dome; BP W: banded pumice white part; BP LG: banded pumice light grey; BP DG: banded pumice dark grey; SB: scoria bomb; NTWP: non-transparent white pumice; TWP: transparent white pumice; TPP: transparent pink pumice; TGP: transparent grey pumice; and S: scoria.

Eruption	Stage	Sample	2D areal measurements								3D volumetric measurements			
			$n^a$	GM glass area (%)	$N_A$ (mm <sup>-2</sup> )	$\phi$	Mean crystal area (μm <sup>2</sup> )	$S/I$	$S/L$	$S_n$ (μm)	3d Crystal shape	Aspect ratio (S:I:L)	R <sup>2</sup>	$N_V$ (mm <sup>-3</sup> )
2007/08	-	LD_2-1	183	84.45	2,878	0.04	13.70	0.77	0.48	3.89	Rectangular Prism	1.00 : 1.30 : 2.10	0.8109	740,809
2007/08	-	LD_2-2	162	94.19	2,683	0.07	27.09	0.83	0.29	5.18	Acicular	1.00 : 1.20 : 3.40	0.6877	517,972
2007/08	-	LD_3-1	402	99.77	3,784	0.05	15.09	0.77	0.48	3.64	Rectangular Prism	1.00 : 1.30 : 2.10	0.8109	1,038,580
2007/08	-	LD_3-2	349	99.55	3,394	0.05	12.09	0.77	0.45	3.65	Rectangular Prism	1.00 : 1.30 : 2.20	0.8701	931,154
2014	I (PDC-1)	BP_W	199	18.43	927	0.03	34.80	0.63	0.42	6.02	Acicular	1.00 : 1.60 : 2.40	0.7699	153,840
2014	I (PDC-1)	BP_DG-1	684	64.69	48,124	0.10	2.00	0.71	0.26	1.41	Acicular	1.00 : 1.40 : 3.80	0.8284	34,046,140
2014	I (PDC-1)	BP_DG-3	639	56.40	48,355	0.10	1.92	0.67	0.26	1.41	Acicular	1.00 : 1.50 : 3.80	0.6286	34,395,768
2014	I (PDC-1)	BP_LG-1	301	39.30	21,586	0.06	2.87	0.67	0.20	1.70	Acicular	1.00 : 1.50 : 5.00	0.7475	12,675,727
2014	I (PDC-1)	BP_LG-2	150	39.79	8,096	0.02	1.62	0.83	0.42	1.61	Acicular	1.00 : 1.20 : 2.40	0.8194	5,043,976
2014	I (PDC-1)	BP_LG-4	151	33.35	6,705	0.03	3.64	0.71	0.26	1.98	Acicular	1.00 : 1.40 : 3.80	0.6749	3,380,020
2014	I (PDC-1)	SB_1	987	40.26	15,962	0.05	2.76	0.67	0.13	1.70	Acicular	1.00 : 1.50 : 8.00	0.8157	9,382,378
2014	I (PDC-1)	SB_3	1071	43.21	14,251	0.06	3.98	0.77	0.34	2.01	Acicular	1.00 : 1.30 : 2.90	0.8847	7,072,487
2014	II (CPF)	NTWP-2_14	143	32.96	4,687	0.04	6.76	0.63	0.11	2.78	Acicular	1.00 : 1.60 : 9.00	0.5566	1,688,588
2014	II (CPF)	NTWP-2_18	434	32.79	20,076	0.03	1.59	0.33	0.10	1.32	Acicular	1.00 : 3.00 : 10.00	0.6571	15,256,269
2014	II (CPF)	NTWP-2_20	785	30.00	26,586	0.04	1.49	0.25	0.11	1.26	Acicular	1.00 : 4.00 : 9.00	0.7631	21,152,003
2014	II (CPF)	NTWP-2_22	479	51.92	20,096	0.07	3.24	0.20	0.13	1.81	Rectangular Prism	1.00 : 5.00 : 8.00	0.8155	11,132,344
2014	II (CPF)	TWP-2_2	437	27.11	8,467	0.03	2.72	0.20	0.11	1.84	Rectangular Prism	1.00 : 5.00 : 9.00	0.8781	4,593,141
2014	II (CPF)	TWP-2_3	119	39.49	4,016	0.01	1.74	0.40	0.22	1.53	Rectangular Prism	1.00 : 2.50 : 4.50	0.9068	2,629,086
2014	II (CPF)	TWP-2_24	300	23.72	7,496	0.03	3.51	0.25	0.11	1.97	Rectangular Prism	1.00 : 4.00 : 9.00	0.8451	3,805,402
2014	II (CPF)	TPP_16	347	21.44	5,469	0.02	2.18	0.71	0.34	1.73	Rectangular Prism	1.00 : 1.40 : 2.90	0.7240	3,165,423
2014	II (CPF)	TPP_31	320	24.78	3,672	0.01	2.04	0.83	0.22	1.69	Acicular	1.00 : 1.20 : 4.50	0.8012	2,172,431
2014	II (CPF)	TPP_46	357	36.47	15,037	0.04	2.54	0.83	0.53	1.69	Acicular	1.00 : 1.20 : 1.90	0.7225	8,886,889
2014	II (CPF)	TGP_26	977	43.23	34,399	0.07	1.85	0.48	0.14	1.39	Acicular	1.00 : 2.10 : 7.00	0.7919	24,760,864
2014	II (CPF)	TGP_27	36	37.29	1,204	0.01	2.68	0.50	0.34	2.41	Rectangular Prism	1.00 : 2.00 : 2.90	0.6082	500,244
2014	II (CPF)	S_2	752	34.42	15,524	0.03	2.07	0.56	0.10	1.50	Acicular	1.00 : 1.80 : 10.00	0.7266	10,359,255
2014	II (CPF)	S_4	526	46.36	10,470	0.03	2.46	0.43	0.11	1.60	Rectangular Prism	1.00 : 2.30 : 9.00	0.7880	6,524,291

<sup>a</sup>Number of measured crystals.

$N_A$ : areal number density.  $N_V$ : volumetric number density (MND).

*Feldspar microlite*

Feldspar microlites are the most abundant microlite phase in the groundmass. Quantitative textural analysis of the feldspar microlites revealed that there are significant variations in textural parameters among the products from effusive and explosive eruptions (Fig 5.13 and Table 5.3). Feldspar abundance is expressed as  $N_A$  (in number·mm<sup>-2</sup>) and MND (in number·m<sup>-3</sup>), which describes the microlite number density over a certain unit area and volume on the basis of phenocryst- and bubble-free, respectively. Sample with the highest number density is recorded from BP dark grey of PDC-1 (2014) with 58,677 to 63,716 crystals mm<sup>-2</sup> and  $3.27 \times 10^{16}$  m<sup>-3</sup>, whereas the lowest number density is from BP white of PDC-1 (2014) and lava dome (2007/08) with 4,182 to 13,646 crystals mm<sup>-2</sup> or  $7.88 \times 10^{14}$  m<sup>-3</sup> to  $2.98 \times 10^{15}$  m<sup>-3</sup>. For samples from the explosive phase, the mean crystal area ranges between ~3–16 μm<sup>2</sup>, even though the average value of crystal size in BP white of PDC-1 is larger (up to 27.68 μm<sup>2</sup>). Conversely, the products from the effusive phase have the biggest crystal area, with the average crystal area ranging from 20.77 to 38.72 μm<sup>2</sup>. There is an overall decrease in crystal size with increasing number density (Fig. 5.13B). Feldspar microlite crystallinity is expressed as  $\phi$ , describing the fraction of groundmass area covered by feldspar microlite as a function of crystal size and abundance. By following the calculation of Hammer et al. (2000), Preece et al. (2016), and Bernard & Bouvet de Maisonneuve (2020), the crystallinity is measured on the basis of phenocryst-, vesicle- and microlite other than feldspar-free by dividing the area of feldspar microlite against the area occupied only by groundmass glass. Generally, the products from effusive phase have high feldspar microlite crystallinity (0.29–0.37), while the explosive phase has lower crystallinity values ranging from 0.10 to 0.36 (average 0.19).

Eruptions with different explosivity can be explicitly distinguished on a  $N_A$  vs.  $\phi$  plot (Fig. 5.13A). On this particular plot, the data population in the lower right region corresponds to growth-dominated crystallization with limited nucleation. In contrast, in the upper left, the crystallization regime is dominated by nucleation rather than growth. Further, the upper right

region correlates with the crystallization regime in which both nucleation and growth are dominant. The 2007/08 dome samples plots in the lower right region, which corresponds to the lower areal number density with higher crystallinity. However, the 2014 products (from both PDC-1 and CPF) display relatively higher overall  $N_A$  ranges with lower feldspar crystallinity in comparison to the dome products.

3D crystal aspect ratio is expressed as  $S/I$  and  $S/L$ , describing the ratio between the short axis with the intermediate and long axis acquired from the stereological conversion of 2D  $S$  and  $L$  values from the measurement (Morgan and Jerram, 2006). The crystals tend to have a more equant and blocky habit with a higher ratio between short and intermediate or long axis. In contrast, the crystals will show more elongated and prismatic habits as the aspect ratio decreases. Generally, short to intermediate axis ratios ( $S/I$ ) show no systematic correlation with  $N_A$  values (Fig. 5.13C). However, a plot of  $S/L$  against  $N_A$  and mean crystal area (Fig. 5. 13D) highlights that the more equant and blocky crystals correlate with lower number density and bigger crystal size, whereas the more elongated crystal associated with higher number density and smaller crystal size.

Plots of volumetric number density versus crystallinity and crystal size ( $S_n$ ) show nearly identical trends and confirm the areal number density results (Fig. 5.13E). Dome samples have larger crystals with a lower number per volume unit, whereas pumices and scoria from explosive products have a greater number of smaller crystals. A similar pattern can be seen in the MND vs. characteristic length of feldspar microlites, which show an anti-correlation between number density and crystal size (Fig. 5. 13F).

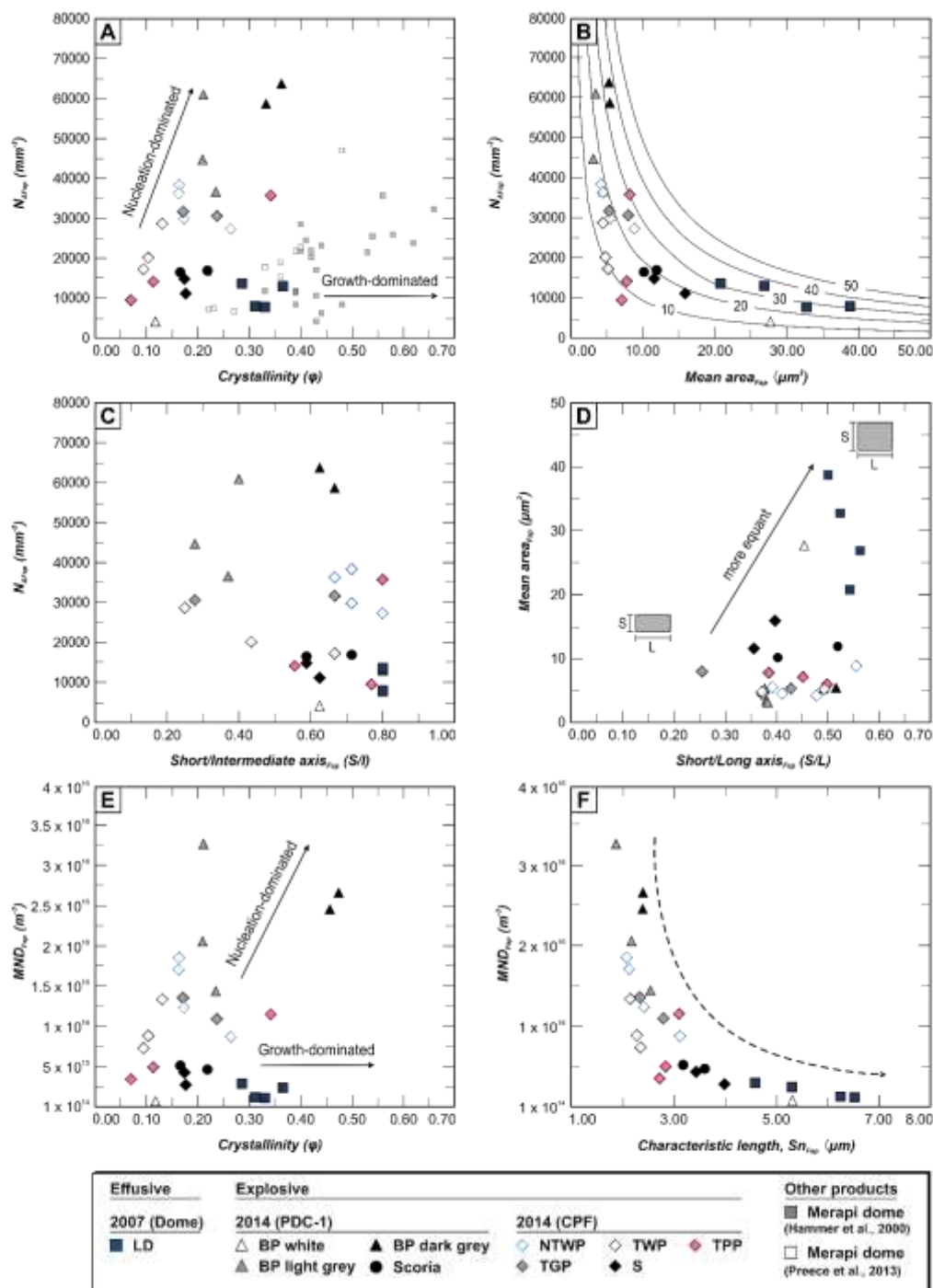


**Figure 5. 13.** Variation in 2D and 3D textural parameters of 2007/08 and 2014 products. Areal number density of feldspar microlite ( $N_A$ ,  $\text{mm}^{-2}$ ) plotted against A) feldspar microlite crystallinity ( $\phi$ ), together with products from other dome-forming eruption of Merapi volcano, Indonesia (Hammer, 2000; Preece et al., 2013), B) feldspar microlite mean crystal area in  $\mu\text{m}^{-2}$ , and C) short/intermediate axis ratio ( $S/I$ ). D) Feldspar microlite mean crystal area ( $\mu\text{m}^{-2}$ ) vs.  $S/L$ . Volumetric number density of feldspar microlite (MND,  $\text{m}^{-3}$ ) plotted against E) feldspar microlite crystallinity ( $\phi$ ) and F) characteristic length of feldspar microlite in  $\mu\text{m}$ . Curves on plots B) represent isocrystallinity curves (in percentage values) calculated using a simple model of circular crystal sections at a particular  $N_A$  and crystal size.

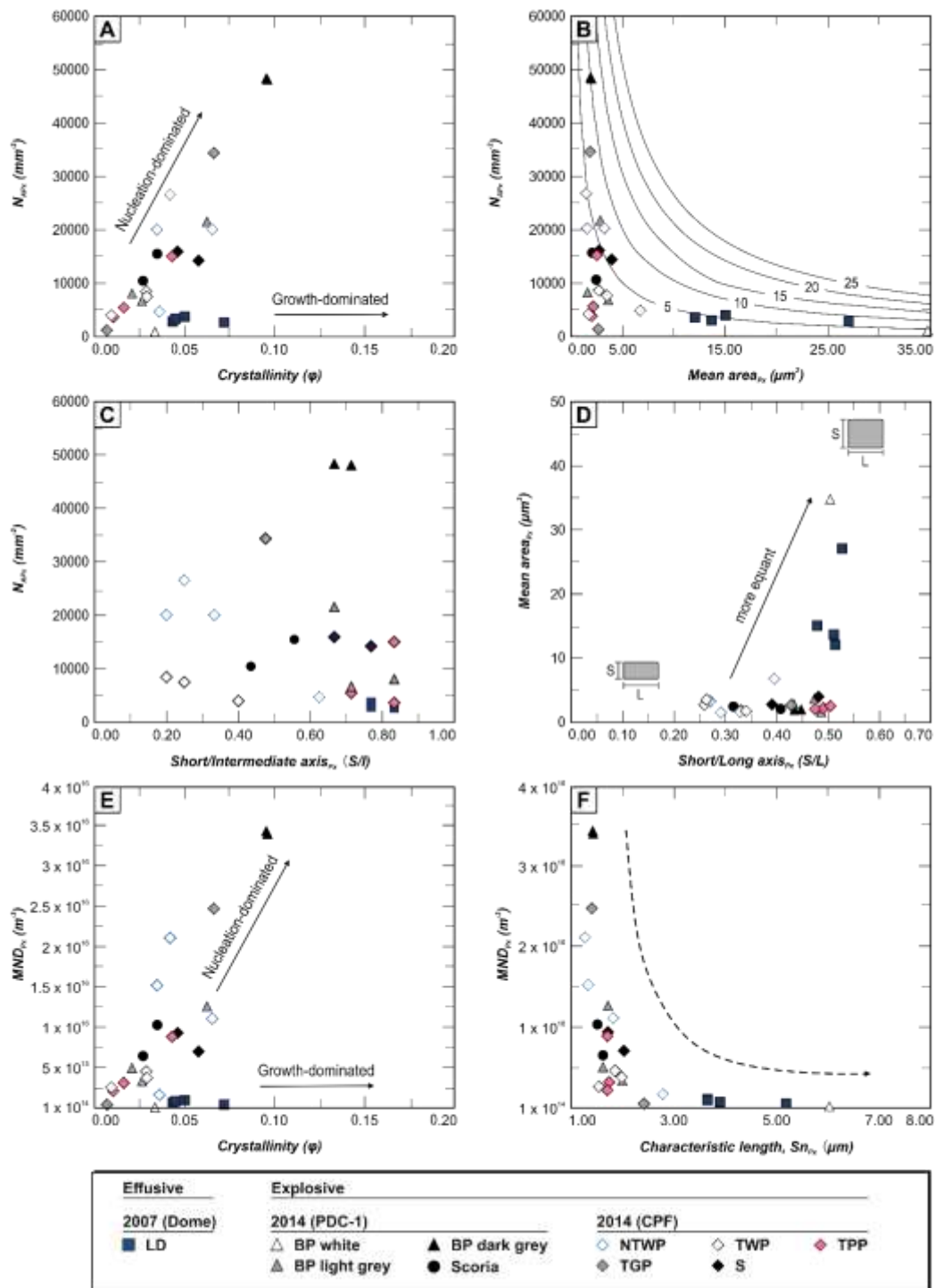


**Figure 5. 14.** Variation in 2D and 3D textural parameters of 2007/08 and 2014 products. Areal number density of pyroxene microlite ( $N_A$ ,  $\text{mm}^{-2}$ ) plotted against A) pyroxene microlite crystallinity ( $\phi$ ), B) pyroxene microlite mean crystal area in  $\mu\text{m}^{-2}$ , and C) short/intermediate axis ratio ( $S/I$ ). D) Pyroxene microlite mean crystal area ( $\mu\text{m}^{-2}$ ) vs.  $S/L$ . Volumetric number density of pyroxene microlite ( $\text{MND}$ ,  $\text{m}^{-3}$ ) plotted against E) pyroxene microlite crystallinity ( $\phi$ ) and F) characteristic length of pyroxene microlite in  $\mu\text{m}$ . Curves on plots B) represent isocrystallinity curves (in percentage values) calculated using a simple model of circular crystal sections at a particular  $N_A$  and crystal size.

### *Pyroxene microlite*

Pyroxene microlites have slightly lower number densities but exhibit remarkably similar trends to feldspar plots (Fig. 5.14; Table 5.4). Samples from the explosive phase have the broadest range of pyroxene number density, covering the lowest values of 926 crystals  $\text{mm}^{-2}$  or  $1.54 \times 10^{14} \text{ m}^{-3}$  (BP white of PDC-1) and 1,203 crystals  $\text{mm}^{-2}$  or  $5.00 \times 10^{14} \text{ m}^{-3}$  (TGP of CPF) and the highest value of 48,354 crystals  $\text{mm}^{-2}$   $5.00 \times 10^{14} \text{ m}^{-3}$  (BP dark grey of PDC-1; Fig. 3.14A). The mean crystal area varies from  $\sim 2$  to  $7 \mu\text{m}^2$ , although the BP white of PDC-1 has a larger average crystal size (up to  $35 \mu\text{m}^2$ ). In contrast, the 2007/08 dome generally has low number densities, ranging from 2,682 to 3,783 crystals  $\text{mm}^{-2}$  or  $5.18 \times 10^{14} \text{ m}^{-3}$  to  $1.04 \times 10^{15} \text{ m}^{-3}$  with a relatively bigger crystal area (12 to  $27 \mu\text{m}^2$ ).

Pyroxenes also exhibit the same negative correlation trend between  $N_A$  (and MND) and mean surface area (and  $S_n$ ) as for feldspars, but with lower microlite fractions and smaller sizes (Fig. 5.14 B–F). Microlite aspect ratios ( $S/I$ ) do not correlate with number density ( $N_A$  or MND) or eruption style (Fig. 5.14C) but show a positive correlation with size (Fig. 5.14D). Overall, feldspar and pyroxene microlites behave very similarly in the Kelud system, confirming that they can be used concurrently to probe the system.

### *Bubble number density (BND) and its relationship with MND*

The abundance of bubbles is expressed as BND (in  $\text{m}^{-3}$ ) portrays records of degassing processes in magmas. Therefore, their sizes, shapes, and numbers can be correlated with the physical processes that drive magma ascent and eruption. Due to uncertainties of vesicle boundary (i.e., post-eruption modifications during emplacement or erosion during sample preparations; [Cashman et al., 1994](#)) in effusive products (dome) and limited bubbles that can be examined, BND measurements can only be performed on explosive products. In the PDC-1, BND values range from  $2.08 \times 10^{15} \text{ m}^{-3}$  to  $8.12 \times 10^{15} \text{ m}^{-3}$ , while CPF products have BND values between  $3.40 \times 10^{15} \text{ m}^{-3}$  to  $2.01 \times 10^{16} \text{ m}^{-3}$  (Fig. 5.15). For both feldspar and pyroxene microlite phases,

the MNDs exhibit positive correlations with increasing BNDs. Our results show that there is a distinct population of PDC and plinian fall, with CPF samples having marginally higher BNDs than PDC-1 and a steeper slope for feldspar microlites (Fig. 5.15A).

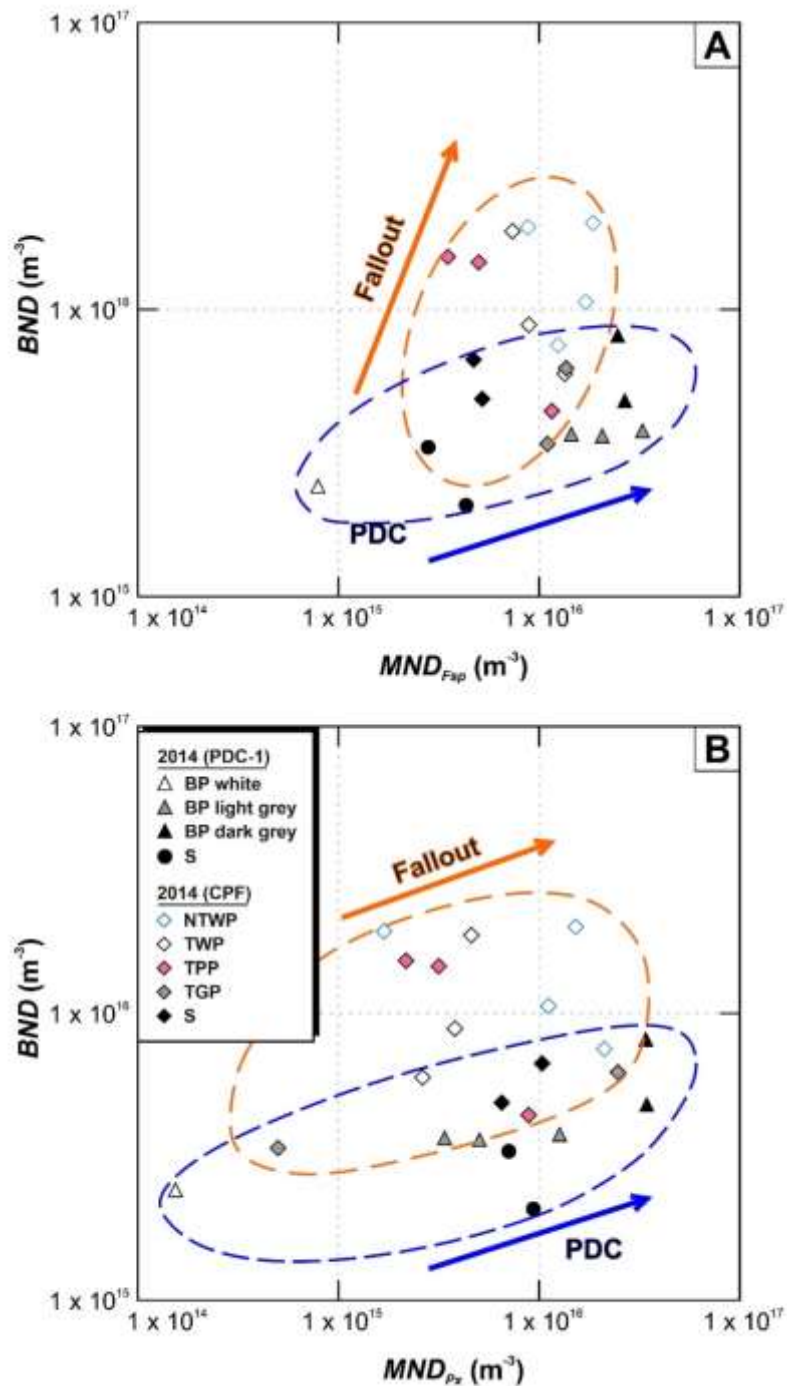


**Figure 5. 15.** BND and MND relationship for A) feldspar microlite and B) pyroxene microlites in the 2014 eruption's products.

### 5.3.5. Microlite size distributions (MSDs)

Conversion from 2D intersection data acquired by axis measurement into 3D data is necessary to fully examine all the information from crystal population. The microlite size distributions (MSDs) are defined as the number of microlites per unit volume within a specific crystal size interval. The MSD diagrams utilized in this study consider the crystal population density (in  $\ln$  population density  $\text{mm}^{-4}$ ) plotted against the bin of crystal size (in mm). All MSDs show curved trendlines, which can be divided into two or three segments based on the gradient of each segment (Fig 5.16; Tables 5.5 and 5.6).

All samples can be divided into two main groups based on the population density value and the crystal size. The first group, growth-dominated, shows the low value of the final stage crystallization ( $n^0$  of segment 1) and relatively less-steep slopes that accommodate bigger crystal size (Fig. 5.16), which indicates the final nucleation ranges from  $2.36 \times 10^8$  to  $3.96 \times 10^9$  crystal  $\text{mm}^{-4}$  (Tables 5.5 and 5.6). Samples contained in this group include feldspar microlites of 2007/08 dome and BP white and scoria bombs of 2014 PDC-1. In contrast, the second group (nucleation-dominated) exhibits a high value of the final stage crystallization, ranging from  $8.00 \times 10^8$  to  $5.61 \times 10^{10}$  crystal  $\text{mm}^{-4}$ , with relatively steeper slopes and accommodating smaller intervals of crystal size. This group covers feldspar microlites from BP dark grey and BP light grey of 2014 PDC-1 and all samples from 2014 CPF. Pyroxene microlites show relatively homogenous MSD graphs over the different eruption events and stages (Figs. 5.16D–F), although the  $n^0$  of segment one ranges from  $1.38 \times 10^8$  to  $2.54 \times 10^{11}$  crystal  $\text{mm}^{-4}$ .

Similar to feldspars, MSDs of pyroxene can also be divided into growth-dominated and nucleation-dominated groups, although the latter appears as the dominant crystallization regime in both effusive and explosive phases ( $n^0$  of segment one ranges from  $1.06 \times 10^9$  to  $2.54 \times 10^{11}$  crystal  $\text{mm}^{-4}$ ). The growth-dominated crystallization was restricted only in BP white of 2014 PDC-1 with  $1.38 \times 10^8$  crystal  $\text{mm}^{-4}$  as  $n^0$  of segment one and TPP\_46 of CPF that has  $3.59 \times 10^8$  crystal  $\text{mm}^{-4}$  as  $n^0$  of segment 1 (Table 5.6).

**Table 5. 5.** Summary of MSD results and calculated growth rates (G) and nucleation rates (J) for feldspar microlites. Lithology types are LD: lava dome; BP W: banded pumice white part; BP LG: banded pumice light grey; BP DG: banded pumice dark grey; SB: scoria bomb; NTWP: non-transparent white pumice; TWP: transparent white pumice; TPP: transparent pink pumice; TGP: transparent grey pumice; and S: scoria.

Eruption	Stage	Sample	Segment 1				Segment 2				Segment 3			
			$\ln(n^0)$ ( $\text{mm}^{-4}$ )	Slope ( $^{\circ}$ )	$R^2$	J ( $\text{mm}^{-3}\text{s}^{-1}$ )	$\ln(n^0)$ ( $\text{mm}^{-4}$ )	Slope ( $^{\circ}$ )	$R^2$	J ( $\text{mm}^{-3}\text{s}^{-1}$ )	$\ln(n^0)$ ( $\text{mm}^{-4}$ )	Slope ( $^{\circ}$ )	$R^2$	G ( $\text{mm s}^{-1}$ )
2007/08	-	LD_2-1	22.10	-452.52	0.99	22.10	20.86	-297.45	0.97	20.86	11.24	-11.61	1.00	$3.99 \times 10^{-8}$
2007/08	-	LD_2-2	20.74	-249.56	0.95	20.74	22.49	-448.65	1.00	22.49				-
2007/08	-	LD_3-1	19.56	-110.06	0.99	19.56	15.09	-44.055	0.99	15.09				-
2007/08	-	LD_3-2	19.33	-109.00	1.00	19.33	14.88	-43.62	1.00	14.88	15.28	-46.14	1.00	$1.00 \times 10^{-8}$
2014	I (PDC-1)	BP_W	21.27	-526.82	1.00	21.27	18.69	-254.54	1.00	18.69	13.85	-59.06	0.97	$2.45 \times 10^{-8}$
2014	I (PDC-1)	BP_DG-1	24.75	-664.72	0.99	24.75	18.23	-155.63	1.00	18.23	14.49	-41.97	1.00	$3.45 \times 10^{-8}$
2014	I (PDC-1)	BP_DG-3	24.48	-495.95	0.99	-	19.11	-189.62	1.00	-				-
2014	I (PDC-1)	BP_LG-1	23.82	-374.11	0.99	-	23.70	-329.17	1.00	-				-
2014	I (PDC-1)	BP_LG-2	24.86	-479.99	1.00	-	20.94	-240.86	1.00	-				-
2014	I (PDC-1)	BP_LG-4	23.49	-351.77	0.99	-	17.93	-123.93	1.00	-				-
2014	I (PDC-1)	SB_1	20.04	-118.60	1.00	20.04	19.00	-87.294	1.00	19.00	16.08	-50.75	1.00	$2.85 \times 10^{-8}$
2014	I (PDC-1)	SB_3	19.28	-93.22	0.98	19.28	17.34	-64.75	1.00	17.34	14.38	-29.47	0.99	$4.91 \times 10^{-8}$
2014	II (CPF)	NTWP-2_14	23.33	-634.07	0.97	-	17.23	-169.77	0.99	-				-
2014	II (CPF)	NTWP-2_18	23.98	-542.21	0.99	-	21.42	-302.66	1.00	-				-
2014	II (CPF)	NTWP-2_20	22.02	-214.45	1.00	-	18.44	-94.616	1.00	-				-
2014	II (CPF)	NTWP-2_22	22.82	-278.17	1.00	22.82	19.73	-143.88	1.00	19.73	13.21	-26.52	1.00	$5.45 \times 10^{-8}$
2014	II (CPF)	TWP-2_2	22.31	-443.87	0.99	22.31	19.73	-231.40	1.00	19.73	15.11	-78.65	1.00	$1.84 \times 10^{-8}$
2014	II (CPF)	TWP-2_3	23.89	-376.69	1.00	23.89	21.41	-202.77	1.00	21.41	16.52	-63.29	1.00	$2.29 \times 10^{-8}$
2014	II (CPF)	TWP-2_24	22.23	-232.45	1.00	22.23	21.02	-165.40	1.00	21.02	16.04	-56.02	1.00	$2.58 \times 10^{-8}$
2014	II (CPF)	TPP_16	21.81	-230.76	1.00	21.81	20.45	-171.76	1.00	20.45	18.37	-113.04	1.00	$1.28 \times 10^{-8}$
2014	II (CPF)	TPP_31	20.50	-197.72	0.97	20.50	18.46	-127.83	0.99	18.46	10.92	-8.80	1.00	$1.64 \times 10^{-7}$
2014	II (CPF)	TPP_46	25.11	-1109.00	0.99	-	21.88	-554.55	0.99	-				-
2014	II (CPF)	TGP_26	21.48	-160.35	0.99	-	16.61	-56.987	0.99	-				-
2014	II (CPF)	TGP_27	22.19	-177.69	1.00	-	12.80	-24.00	1.00	-				-
2014	II (CPF)	S_2	23.27	-613.21	0.99	23.27	19.46	-264.25	0.98	19.46	13.92	-51.28	1.00	$2.82 \times 10^{-8}$
2014	II (CPF)	S_4	20.66	-143.39	0.99	-	11.37	-10.90	1.00	-	11.24			-

$n^0$  population density in which the MSD trends intercept y-axis. Crystallization times were determined from the seismic data (tremor, VB, and VT signals) prior to both eruptions: 2007/08=25 days; 2014=8 days ([Hidayati et al., 2019](#)).

**Table 5. 6.** Summary of MSD results and calculated growth rates (G) and nucleation rates (J) for pyroxene microlites. Lithology types are LD: lava dome; BP W: banded pumice white part; BP LG: banded pumice light grey; BP DG: banded pumice dark grey; SB: scoria bomb; NTWP: non-transparent white pumice; TWP: transparent white pumice; TPP: transparent pink pumice; TGP: transparent grey pumice; and S: scoria.

Eruption	Stage	Sample	Segment 1				Segment 2				Segment 3			
			ln ( $n^0$ ) (mm <sup>-4</sup> )	Slope (°)	R <sup>2</sup>	J (mm <sup>-3</sup> s <sup>-1</sup> )	ln ( $n^0$ ) (mm <sup>-4</sup> )	Slope (°)	R <sup>2</sup>	J (mm <sup>-3</sup> s <sup>-1</sup> )	ln ( $n^0$ ) (mm <sup>-4</sup> )	Slope (°)	R <sup>2</sup>	G (mm s <sup>-1</sup> )
2007/08	-	LD_2-1	20.78	-488.69	0.99	-	18.45	-262.90	1.00	-				
2007/08	-	LD_2-2	20.86	-475.11	0.99	-	19.32	-316.95	1.00	-				
2007/08	-	LD_3-1	21.41	-423.07	1.00	-	21.76	-445.45	1.00	-				
2007/08	-	LD_3-2	21.29	-461.20	1.00	-	20.45	-407.69	1.00	-				
2014	I (PDC-1)	BP_W	18.74	-372.76	0.98	-	13.02	-60.83	1.00	-				
2014	I (PDC-1)	BP_DG-1	23.30	-438.16	0.99	-	16.19	-99.21	1.00	-				
2014	I (PDC-1)	BP_DG-3	26.26	-1006.70	1.00	-	23.40	-609.30	1.00	-				
2014	I (PDC-1)	BP_LG-1	24.28	-727.67	1.00	-	19.07	-224.46	0.99	-				
2014	I (PDC-1)	BP_LG-2	24.07	-1235.20	0.98	-	16.25	-177.27	1.00	-				
2014	I (PDC-1)	BP_LG-4	23.96	-960.98	0.97	-	19.18	-328.17	1.00	-				
2014	I (PDC-1)	SB_1	22.50	-323.78	1.00	-	21.74	-290.04	1.00	-				
2014	I (PDC-1)	SB_3	23.58	-740.59	0.99	-								
2014	II (CPF)	NTWP-2_14	21.25	-312.63	1.00	-	15.52	-77.38	1.00	-				
2014	II (CPF)	NTWP-2_18	21.61	-269.14	0.99	-								
2014	II (CPF)	NTWP-2_20	24.82	-484.50	1.00	-	18.09	-109.43	1.00	-				
2014	II (CPF)	NTWP-2_22	24.50	-479.47	1.00	-								
2014	II (CPF)	TWP-2_2	22.96	-405.41	0.98	22.96	19.13	-183.96	1.00	19.13	15.31	-48.84	1.00	2.96×10 <sup>-8</sup>
2014	II (CPF)	TWP-2_3	24.39	-977.74	1.00	-								
2014	II (CPF)	TWP-2_24	21.44	-255.91	0.97	-								
2014	II (CPF)	TPP_16	23.52	-962.62	1.00	-								
2014	II (CPF)	TPP_31	24.49	-1139.30	1.00	-	14.99	-94.34	1.00	-				
2014	II (CPF)	TPP_46	19.70	-390.44	0.95	-	15.18	-85.39	1.00	-				
2014	II (CPF)	TGP_26	24.48	-536.12	0.98	-	11.80	-47.33	1.00	-				
2014	II (CPF)	TGP_27	23.17	-1353.00	1.00	-	16.52	.201.12	1.00	-				
2014	II (CPF)	S_2	22.77	-369.61	1.00	22.77	17.67	-103.73	0.98	17.67	14.27	-38.31	1.00	3.78×10 <sup>-8</sup>
2014	II (CPF)	S_4	23.30	-396.83	0.99	-	20.51	-238.68	1.00	-				

$n^0$  population density in which the MSD trends intercept y-axis. Crystallization times were determined from the seismic data (tremor, VB, and VT signals) prior to both eruptions: 2007/08=25 days; 2014=8 days (Hidayati et al., 2019).

Furthermore, these two groups observed at feldspar and pyroxene microlites correspond thoroughly with the variation in the 2D crystallinity group (Figs. 5.13A and 5.14A). Samples with a nucleation-dominated crystallization regime will also have low  $\phi$  values, whereas the growth-dominated group corresponds to the high  $\phi$  samples. In addition, most of the MSD graphs show a decrement in population density at the smallest crystal sizes has been attributed to either an insufficient resolution to image the smallest crystal sizes (Marsh, 1998; Hammer et al., 1999; Murch and Cole, 2019) or the probability error during conversion in CSD software (i.e., Higgins, 2000; Bernard and de Maisonneuve, 2020). Therefore, these values will not be discussed in further sections.

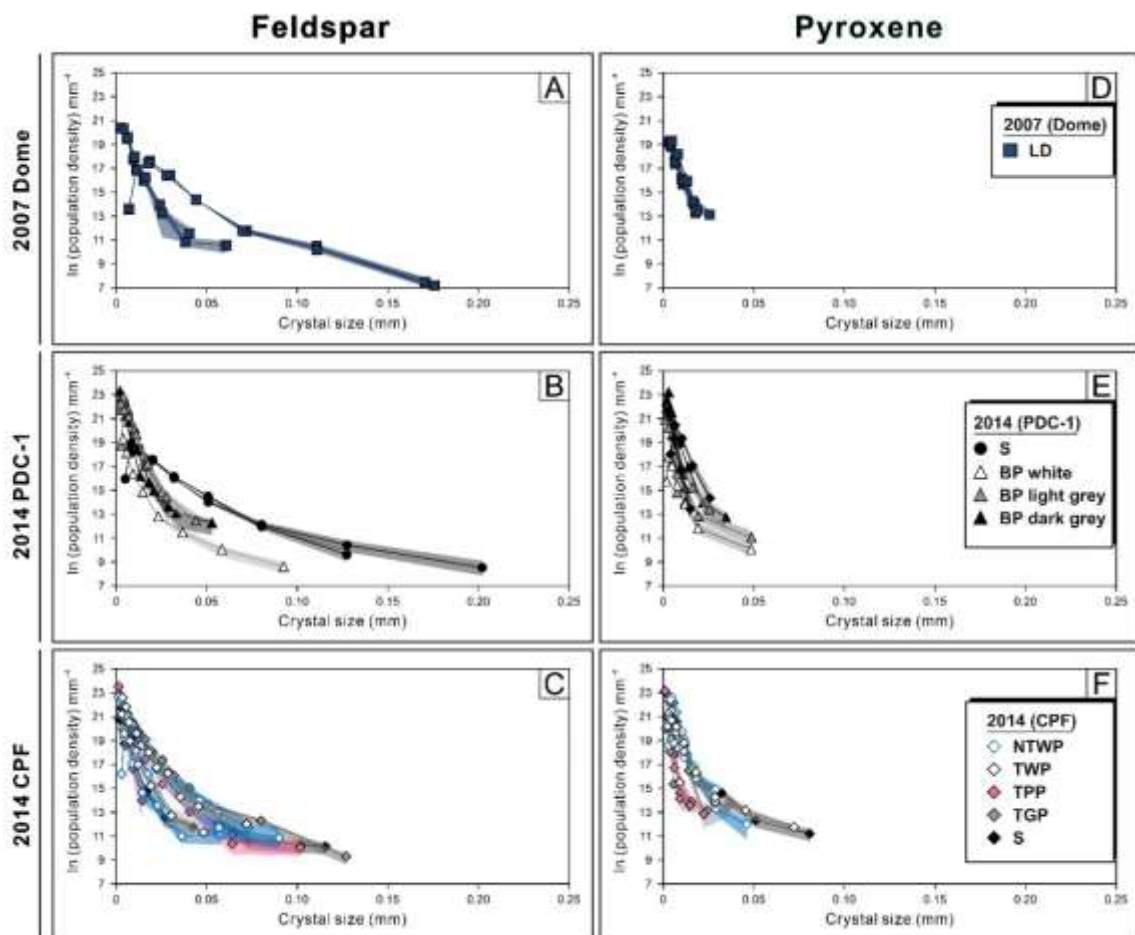


**Figure 5. 16.** Microlite size distributions (MSDs) of feldspar (A–C) and pyroxene (D–F) microlites from different eruption event and stages plotted in binary population density ( $\text{mm}^{-4}$ ) vs. crystal size (mm). The linear best-fit slopes and intercepts of each MSD are reported in Tables 5.5 and 5.6. Envelopes around the distribution points represent the  $1\sigma$  standard deviation acquired from CSDcorrections v1.61 of Higgins (2000; 2006).

## 5.4. Discussion

This section will extensively discuss the relationship between the mineralogical, chemical, and textural variations of 2007/08 and 2014 products towards the related crystallization processes. The results will provide critical information about the driving force behind the changes in eruption styles. This section will elaborate on the chemical and textural variation of the feldspar and pyroxene microlites, the crystallization scheme from studied volcanic products, and the implication of this study for future hazard assessment on Kelud, particularly volcanoes with similar eruption styles.

### 5.4.1. Magma ascent and decompression rates

Average magma ascent and decompression rates in the microlite nucleation zones were calculated using the MND water exsolution rate meter of Toramaru et al. (2008). As previously mentioned in section 5.3.3, there are significant differences between whole-rock and groundmass glass compositions; glass compositions are highly differentiated, reaching dacite to rhyolite (63.7 to 78.8 wt.% SiO<sub>2</sub>). Thus, glass compositions were selected for the ascent and decompression rate, as they most likely represent the  $C_{si}$  that close to the actual silica concentrations of magma at the nucleation depth in addition of  $C_w$  acquired from melt inclusion in chapter 4.

Calculated  $dP/dt$  and  $v_n$  for feldspar and pyroxene microlites are systematically similar over eruptive styles and stages, although pyroxenes yield slightly higher values less than one order (Fig. 5.17; Table 5.7). Effusive products have lowest ascent average decompression rate ranging from  $2.15 \times 10^{-5}$  to  $4.57 \times 10^{-5}$  MPa/s with average ascent rates between 0.001 and 0.002 m/s. The calculated  $dP/dt$  and  $v_n$  values are consistent with estimated ascent rates based on monitoring records (0.0015 m/s; Siebert et al., 2011) and CO<sub>2</sub> fluxes 4 month prior the eruption (0.0004 m/s; Jeffrey et al., 2013). On the contrary, pumice and scoria examined from 2014 explosive eruption have higher ascent average decompression rates ( $4.58 \times 10^{-4}$  –  $3.09 \times$

$10^{-1}$  MPa/s) and time averaged ascent rates (0.03 – 18.70 m/s; average value of 4.38 m/s).

The consensus from visual observations and MND-derived ascent rates suggests that the assumption of equilibrium crystallization of feldspars and pyroxene microlites in all samples is valid. Therefore, the relationship between ascent-degassing conditions and crystallization trends during magma ascent will be further assessed in the following sections.

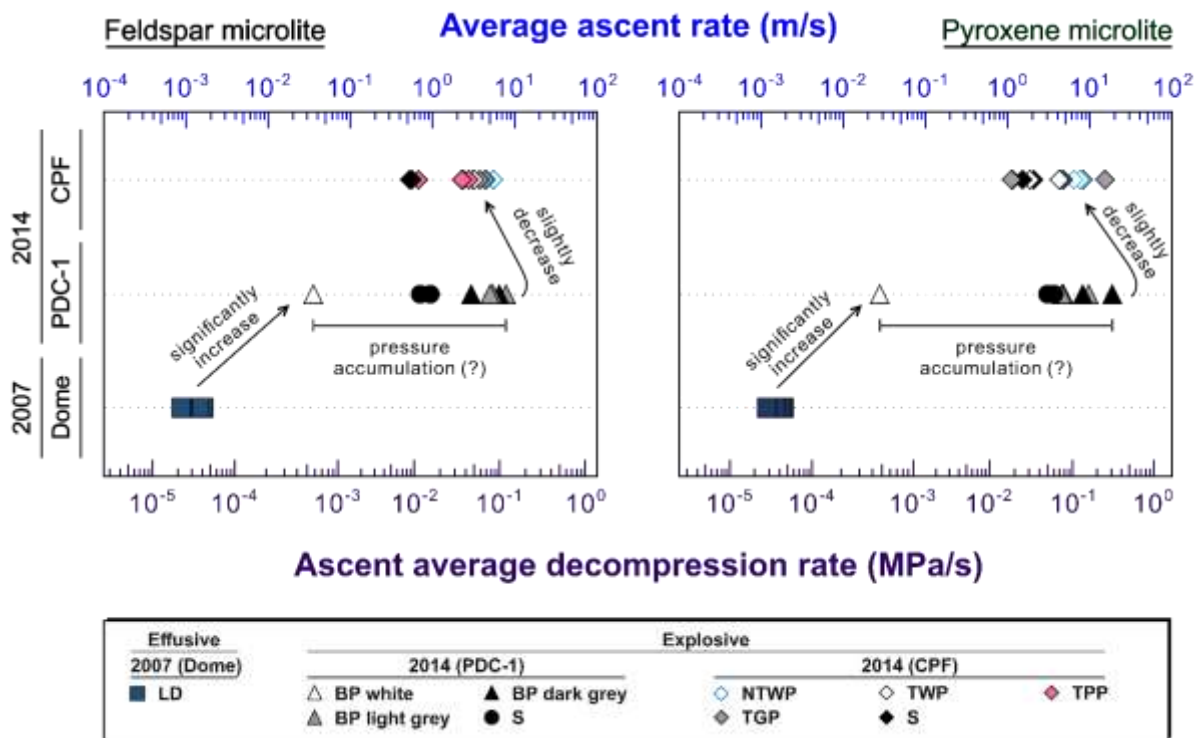


**Figure 5. 17.** Magma ascent rates and decompression rates calculated using MND water exsolution rate meter for plagioclase feldspars and pyroxenes. Ascent and decompression rates obtained from feldspar and pyroxenes are systematically similar, although pyroxenes have slightly higher values (less than one order).

**Table 5. 7.** Summary of input parameters and results for magma ascent and decompression rates calculated using Toramaru et al. (2008). Lithology types are LD: lava dome; BP W: banded pumice white part; BP LG: banded pumice light grey; BP DG: banded pumice dark grey; SB: scoria bomb; NTWP: non-transparent white pumice; TWP: transparent white pumice; TPP: transparent pink pumice; TGP: transparent grey pumice; and S: scoria.

Eruption	Stage	Sample	MND (m <sup>-3</sup> )		C <sub>w</sub> (wt.%)	C <sub>Si</sub> (wt.%)	dP <sub>w</sub> /dt (MPa s <sup>-1</sup> )		Bulk density* (kg m <sup>-3</sup> )	v <sub>n</sub> (m s <sup>-1</sup> )	
			Feldspar	Pyroxene			Feldspar	Pyroxene		Feldspar	Pyroxene
2007/08	-	LD_2-1	2.46 × 10 <sup>15</sup>	7.41 × 10 <sup>14</sup>	4.00	76.82	3.48 × 10 <sup>-5</sup>	3.65 × 10 <sup>-5</sup>	2500	0.001	0.001
2007/08	-	LD_2-2	2.98 × 10 <sup>15</sup>	5.18 × 10 <sup>14</sup>	4.00	76.82	3.95 × 10 <sup>-5</sup>	2.87 × 10 <sup>-5</sup>	2500	0.002	0.001
2007/08	-	LD_3-1	1.19 × 10 <sup>15</sup>	1.04 × 10 <sup>15</sup>	4.00	76.82	2.15 × 10 <sup>-5</sup>	4.57 × 10 <sup>-5</sup>	2500	0.001	0.002
2007/08	-	LD_3-2	1.28 × 10 <sup>15</sup>	9.31 × 10 <sup>14</sup>	4.00	76.82	2.25 × 10 <sup>-5</sup>	4.25 × 10 <sup>-5</sup>	2500	0.001	0.002
2014	I (PDC-1)	BP_W	7.88 × 10 <sup>14</sup>	1.54 × 10 <sup>14</sup>	5.89	74.33	5.83 × 10 <sup>-4</sup>	4.58 × 10 <sup>-4</sup>	1684	0.035	0.028
2014	I (PDC-1)	BP_DG-1	2.40 × 10 <sup>16</sup>	3.40 × 10 <sup>16</sup>	5.46	67.88	1.07 × 10 <sup>-2</sup>	3.09 × 10 <sup>-1</sup>	1684	6.459	18.699
2014	I (PDC-1)	BP_DG-3	2.67 × 10 <sup>16</sup>	3.44 × 10 <sup>16</sup>	5.46	69.46	4.87 × 10 <sup>-2</sup>	1.35 × 10 <sup>-1</sup>	1684	2.944	8.135
2014	I (PDC-1)	BP_LG-1	3.27 × 10 <sup>16</sup>	1.27 × 10 <sup>16</sup>	5.46	67.88	1.29 × 10 <sup>-1</sup>	1.60 × 10 <sup>-1</sup>	1684	7.806	9.674
2014	I (PDC-1)	BP_LG-2	2.06 × 10 <sup>16</sup>	5.04 × 10 <sup>15</sup>	5.46	68.15	8.25 × 10 <sup>-2</sup>	7.52 × 10 <sup>-2</sup>	1684	4.989	4.549
2014	I (PDC-1)	BP_LG-4	1.45 × 10 <sup>16</sup>	3.38 × 10 <sup>15</sup>	5.46	67.55	8.90 × 10 <sup>-2</sup>	7.88 × 10 <sup>-2</sup>	1684	5.382	4.765
2014	I (PDC-1)	SB_1	4.33 × 10 <sup>15</sup>	9.38 × 10 <sup>15</sup>	5.67	69.79	1.55 × 10 <sup>-2</sup>	6.08 × 10 <sup>-2</sup>	1684	0.940	3.674
2014	I (PDC-1)	SB_3	2.80 × 10 <sup>15</sup>	7.07 × 10 <sup>15</sup>	5.67	69.79	1.16 × 10 <sup>-2</sup>	5.03 × 10 <sup>-2</sup>	1684	0.703	3.043
2014	II (CPF)	NTWP-2_14	8.79 × 10 <sup>15</sup>	1.69 × 10 <sup>15</sup>	5.89	67.83	9.11 × 10 <sup>-2</sup>	7.07 × 10 <sup>-2</sup>	1684	5.506	4.277
2014	II (CPF)	NTWP-2_18	1.86 × 10 <sup>16</sup>	1.53 × 10 <sup>16</sup>	5.89	69.84	5.17 × 10 <sup>-2</sup>	1.06 × 10 <sup>-1</sup>	1684	3.128	6.397
2014	II (CPF)	NTWP-2_20	1.24 × 10 <sup>16</sup>	2.12 × 10 <sup>16</sup>	5.89	69.94	3.75 × 10 <sup>-2</sup>	1.25 × 10 <sup>-1</sup>	1684	2.270	7.561
2014	II (CPF)	NTWP-2_22	1.71 × 10 <sup>16</sup>	1.11 × 10 <sup>16</sup>	5.89	69.09	7.31 × 10 <sup>-2</sup>	1.28 × 10 <sup>-1</sup>	1684	4.422	7.742
2014	II (CPF)	TWP-2_2	7.37 × 10 <sup>15</sup>	4.59 × 10 <sup>15</sup>	5.89	67.86	7.98 × 10 <sup>-2</sup>	1.36 × 10 <sup>-1</sup>	1684	4.824	8.214
2014	II (CPF)	TWP-2_3	1.34 × 10 <sup>16</sup>	2.63 × 10 <sup>15</sup>	5.89	69.96	3.90 × 10 <sup>-2</sup>	3.07 × 10 <sup>-2</sup>	1684	2.361	1.857
2014	II (CPF)	TWP-2_24	8.89 × 10 <sup>15</sup>	3.81 × 10 <sup>15</sup>	5.89	68.87	5.28 × 10 <sup>-2</sup>	7.00 × 10 <sup>-2</sup>	1684	3.196	4.235
2014	II (CPF)	TPP_16	5.00 × 10 <sup>15</sup>	3.17 × 10 <sup>15</sup>	5.10	66.68	4.56 × 10 <sup>-2</sup>	7.84 × 10 <sup>-2</sup>	1684	2.755	4.739
2014	II (CPF)	TPP_31	3.51 × 10 <sup>15</sup>	2.17 × 10 <sup>15</sup>	5.10	68.89	1.12 × 10 <sup>-2</sup>	1.89 × 10 <sup>-2</sup>	1684	0.674	1.144
2014	II (CPF)	TPP_46	1.16 × 10 <sup>16</sup>	8.89 × 10 <sup>15</sup>	5.10	68.10	3.75 × 10 <sup>-2</sup>	7.35 × 10 <sup>-2</sup>	1684	2.271	4.446
2014	II (CPF)	TGP_26	1.36 × 10 <sup>16</sup>	2.48 × 10 <sup>16</sup>	5.70	68.40	7.23 × 10 <sup>-2</sup>	2.51 × 10 <sup>-1</sup>	1684	4.370	15.185
2014	II (CPF)	TGP_27	1.10 × 10 <sup>16</sup>	5.00 × 10 <sup>14</sup>	5.70	68.43	6.17 × 10 <sup>-2</sup>	1.84 × 10 <sup>-2</sup>	1684	3.733	1.111
2014	II (CPF)	S_2	4.72 × 10 <sup>15</sup>	1.04 × 10 <sup>14</sup>	5.67	71.01	8.65 × 10 <sup>-3</sup>	3.41 × 10 <sup>-2</sup>	1684	0.523	2.063
2014	II (CPF)	S_4	5.20 × 10 <sup>15</sup>	6.52 × 10 <sup>15</sup>	5.67	71.01	9.24 × 10 <sup>-3</sup>	2.51 × 10 <sup>-2</sup>	1684	0.559	1.516

\*Bulk densities used in this calculated based on average density of vesiculated magma for lavas and pyroclasts (e.g., Toramaru et al., 2008; Murch and Cole, 2019; Bernad and de Maisonneuve, 2020).

#### 5.4.2. Variable crystallizations during magma ascent

Two data populations are recognized from the variation diagrams of composition versus total crystallinity, which accommodate all microlite mineral phases (i.e., feldspars, pyroxenes, and Fe-Ti oxides; Fig. 5.18). Firstly, most of the major elements are plotted separately between effusive and explosive products, with effusive products having elevated values of  $\text{SiO}_2$  and  $\text{K}_2\text{O}$  in comparison to explosive products, while  $\text{Al}_2\text{O}_3$ ,  $\text{FeO}^*$ ,  $\text{MgO}$ ,  $\text{CaO}$ ,  $\text{Na}_2\text{O}$ , and  $\text{P}_2\text{O}_5$  have lower values. The  $\text{TiO}_2$  values share similarities between explosive and effusive products. These variations suggest that groundmass compositions from explosive and effusive phases are affected strongly by global equilibrium, with groundmass crystallinity varying as a function of each formation process (Couch et al., 2003a; Preece et al., 2013; Murch and Cole, 2019; Matsumoto et al., 2021). Secondly, in explosive products, two trends can be observed. Samples from the 2014 CPF phase generally have similar trends with increasing crystal content and are comparable with the 2007/08 samples.  $\text{SiO}_2$ ,  $\text{TiO}_2$ , and  $\text{Na}_2\text{O}$  positively correlate with increasing crystallinity, whereas  $\text{Al}_2\text{O}_3$ ,  $\text{FeO}^*$ ,  $\text{MgO}$ ,  $\text{CaO}$ ,  $\text{K}_2\text{O}$ , and  $\text{P}_2\text{O}_5$  show a negative correlation with crystal content (Fig. 3.18).  $\text{K}_2\text{O}$  shows relatively uniform values over increasing crystallinity. On the contrary, PDC-1 samples have  $\text{SiO}_2$ ,  $\text{TiO}_2$ , and  $\text{Na}_2\text{O}$  that negatively correlate with crystal content, while  $\text{Al}_2\text{O}_3$ ,  $\text{FeO}^*$ ,  $\text{MgO}$ , and  $\text{CaO}$  show positive correlations with crystallinity. This evidence implies that the groundmass compositions during the explosive phase were affected by local equilibrium (i.e., different crystallization times or undercooling temperatures). The fact that  $\text{K}_2\text{O}$ , as the differentiation indicator, in the PDC-1 samples has slightly higher concentrations with similar trends over  $\text{SiO}_2$  suggests that the microlites in 2014 products were derived from more fractionated portions of the same magmatic body (i.e., Preece et al., 2016; Matsumoto and Geshi, 2021). Higher overall  $\text{SiO}_2$ ,  $\text{Na}_2\text{O}$ , and  $\text{K}_2\text{O}$  values in PDC-1 samples (Fig. 5.11) along with lower  $\text{Al}_2\text{O}_3$ ,  $\text{FeO}^*$ ,  $\text{MgO}$ , and  $\text{CaO}$  in comparison to CPF products support the idea that groundmass glasses of PDC-1 were derived from more differentiated magma and significantly affected by microlite crystallization during

the early-stage of 2014 eruption (e.g., Hammer et al., 2000; Preece et al., 2013). Moreover, the abundant microlite crystal with equant morphology in PDC-1 in the coarser fraction confirms the sufficient time for the crystals to grow in the early crystallization stage via fractional crystallization (Fig. 5.5; e.g., Shea et al., 2010; Matsumoto et al., 2021).

Textural variation of groundmass microlites can provide critical information on crystallization regime and conduit dynamics during magma ascent (e.g., Hammer et al., 2000, Preece et al., 2016, Bernard and de Maisonneuve, 2020; Matsumoto and Geshi, 2021). Overall, the microlites contained in 2007/08 products display euhedral blocky that progressively changed to euhedral prismatic towards higher areal number density region (Figs. 5.13 & 5.14), whereas 2014 products mostly exhibit skeletal and swallowtail morphologies (Fig 5.5). Experimental studies (i.e., Lofgren, 1974; Couch et al., 2003a; Shea and Hammer, 2013) revealed that crystal morphology of plagioclase feldspar and pyroxene tends to shift from acicular dendritic to swallowtail to hopper to tabular/equant with increasing crystallization time and decrease of undercooling temperature ( $\Delta T$ , defined as  $T_{liquidus} - T_{magma}$ ) and decompression rate (Fig. 5.19). The restricted microlite morphology observed in the 2007/08 dome indicates that magma has experienced low  $\Delta T$  and  $dP/dt$  during ascending. However, the morphological transformation to euhedral prismatic is observed at size 20  $\mu\text{m}$  for feldspars and 30  $\mu\text{m}$  for pyroxenes (Fig. 5.5). Such transformation implies that there was a slight increase in decompression rate and  $\Delta T$ , as expected during the crystallization in the shallower conduit in which the decompression rate was affected by degassing. Slow ascent experienced during ascent prompted the microlites to have a longer crystallization time that produced dominant euhedral morphology. This evidence also explains the reason behind 2007/08 domes having low number density and high crystal contents (Table. 5.3).

The contrasting features observed in 2014 PDC-1 samples, which is dominated by euhedral block in bigger-sized crystal and transition into having swallowtail and skeletal morphologies throughout the smaller class size (Fig. 5.5 and 5.19). The abrupt transformation suggests that

the ascending magma has experienced low  $\Delta T$  and  $dP/dt$  at the early crystallization stage before experiencing sudden decompression. The calculated ascent and decompression rates corroborate the textural observations. In the early stage of microlite crystallization, magma rose from a velocity of 0.03 to 18.70 m/s, coupled with increases in decompression rates to  $3.09 \times 10^{-1}$  MPa/s over three magnitudes. These phenomena are subsequently interpreted as pressure accumulation at the shallower level just before the eruption occurred. Similar to the field-based studies conducted on 2014 products (e.g., [Goode et al., 2019](#); [Maeno et al., 2019](#)), I infer that the 2007/08 dome acted as a “cap” to seal off the effective permeability for outgassing, thereby increasing the effective pressure prior to the 2014 eruption. The higher decompression and ascent rates were maintained, although slightly lower, during the 2014 climactic plinian event. The relatively homogenous morphology found in CPF samples indicates high decompression rates occurred continuously during the development of the climactic plinian phase (e.g., [Hammer et al., 2000](#); [Shea and Hammer, 2013](#)).

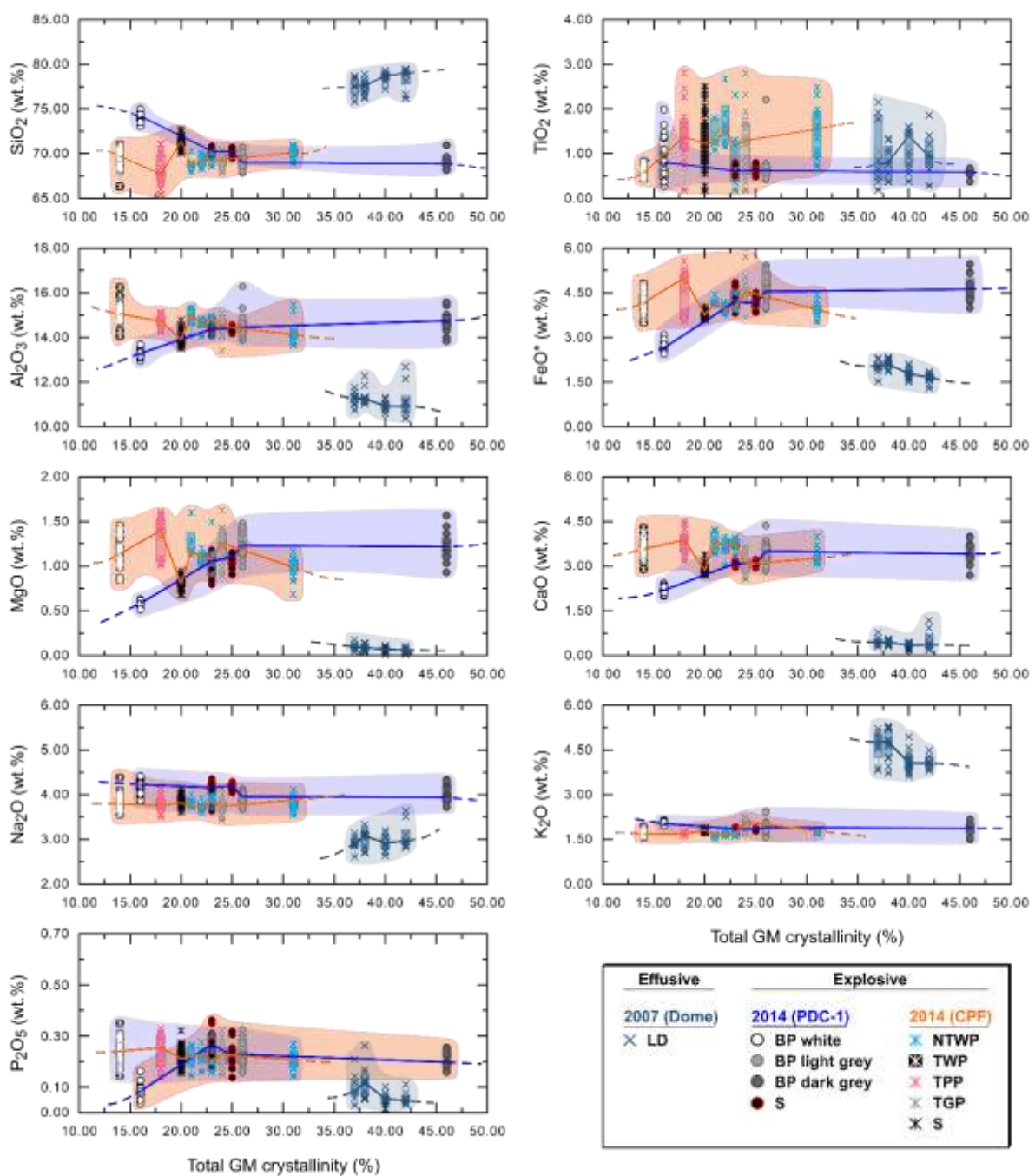


**Figure 5. 18.** Variation of groundmass glass compositions of 2007/08 and 2014 products plotted against total groundmass crystallinity that includes all microlite mineral phases present (feldspars, pyroxenes, and Fe-Ti oxides).

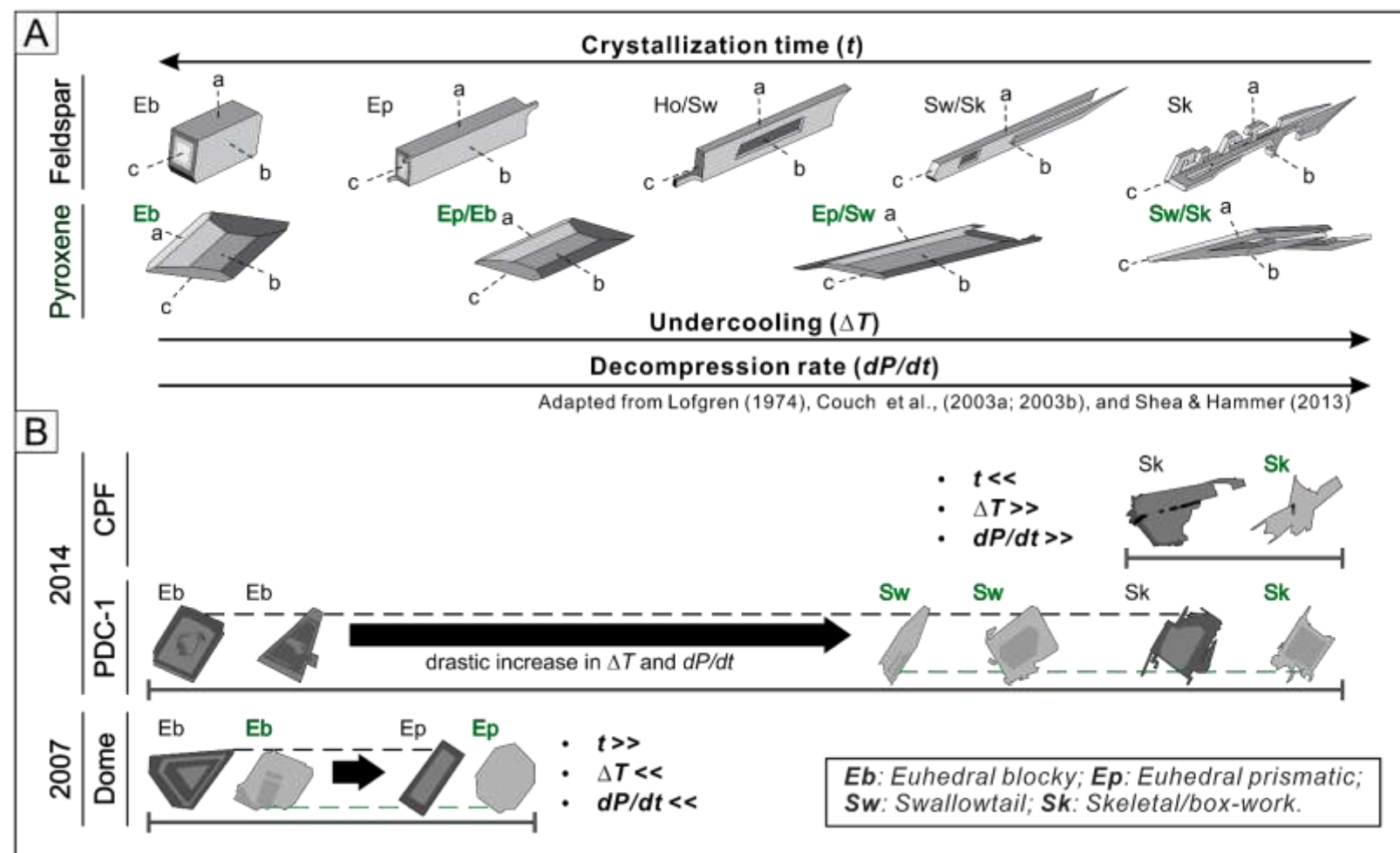


**Figure 5. 19.** Variation of microlite morphologies linked with crystallization time and decompression rate for every eruption types and stages. The variation of feldspar and pyroxene morphologies for every eruption type and stage. The shapes characterization based on the experimental result of Lofgren (1974), Couch et al., (2003a; 2003b), and Shea & Hammer (2013) through observing the size and abundance of feldspar and pyroxene microlite contained in the samples.

Additionally, the MSD analysis results revealed that the crystallization of analyzed samples could be categorized into so-called ‘nucleation-dominated’ and ‘growth-dominated’ groups. The growth-dominated group consists of 2007/08 dome and 2014 PDC-1 banded pumice and scoria bomb, which has experienced low undercooling temperature, while the nucleation-dominated group is composed of pumice and scoria from 2014 PDC-1 and CPF, and pyroxene microlites from both 2007/08 and 2014 eruptions. Although MSDs show curve appearances, they can be divided approximately into two or three straight segments. By knowing the slope of the shallowest segment from each MSD curve, the growth rate can be estimated following the equation from Marsh (1988):

$$\text{Slope} = -1/G\tau; \quad (5d)$$

where  $G$  is growth rate, and  $\tau$  is crystallization time. By using crystallization time inferred from tremor and VB signals on 16 October 2007 (25 days prior to the 2007/08 eruption), and VT and VB signals on 5 February 2014 (8 days prior to the 2014 eruption), the growth rates for 2007/08 and 2014 microlites can be calculated (Hidayati et al., 2019). The growth rates for feldspar microlites are estimated to be  $1.00 \times 10^{-8}$  to  $3.99 \times 10^{-8}$  mm s<sup>-1</sup>, between  $2.45 \times 10^{-8}$  and  $4.91 \times 10^{-8}$  mm s<sup>-1</sup>, and  $1.28 \times 10^{-8}$  to  $1.64 \times 10^{-7}$  mm s<sup>-1</sup> for 2007/08 dome, 2014 PDC-1, and 2014 CPF respectively (Table 5.5). These calculated rates are close to the low end of the growth rate ranges for plagioclase feldspar ( $10^{-6}$  to  $10^{-8}$  mm s<sup>-1</sup>) during syn-eruptive crystallization, proposed by Brugger and Hammer (2010), suggesting that the effusive and explosive phases could have similar initial crystallization conditions that started to crystallize from the deeper portion of the conduit. However, different growth rates are expected from late crystallization during ascent in the shallower conduit, which may have faster growth rates (e.g., Brugger and Hammer, 2010; Shea and Hammer, 2013). The calculated average ascent rates confirm that bigger microlites in effusive products were produced via slow ascent with higher growth rates, whereas higher ascent rates will lead to nucleation-dominated crystallization as observed in explosive products (Table 5.7).

The nucleation rate is calculated following an equation proposed by Marsh (1988):

$$J = n^o G; \quad (5e)$$

where  $J$  is the nucleation rate,  $n^o$  is the  $y$ -axis intercept of the slope in MSD graphs, and  $G$  is the growth rate. The calculation used only the steepest slope of CSD that exhibits the latest formed crystal before experiencing fragmentation. The estimated nucleation rates are 19.33 to 22.10 nuclei  $\text{mm}^{-3} \text{s}^{-1}$  for the 2007/08 dome, 19.28–20.14  $\text{mm}^{-3} \text{s}^{-1}$  for the onset phase of the 2014 eruption, and 20.50 to 23.89 nuclei  $\text{mm}^{-3} \text{s}^{-1}$  for the plinian phase of 2014 eruption. Moreover, growth and nucleation rates may be underestimated for the sample that has experienced higher undercooling temperature and continuous crystallization.

#### 5.4.3. Two-step crystallization timings

Variations in the microtextural features and chemical compositions of groundmass glass among the 2007/08 and 2014 eruptions reflect a two-step crystallization process during magma ascent in the conduit. Different undercooling paths can account for the disparities in particle texture among volcanic products. Since undercooling ( $\Delta T$ ) represents the difference between liquidus and magma/melt temperatures ( $T_{liq}-T_m$ ), the variations in  $\Delta T$  are highly affected by variable cooling rates or degassing that increases the liquidus temperature. Moreover, when degassing occurs during ascent, an increase in the liquidus temperature due to decompression-induced devolatilization is expected because the magma is in nearly isothermal condition (Couch et al., 2003a, 2003b; Shea and Hammer, 2013; Matsumoto and Geshi, 2021).

Figure 5.20 illustrates the relationship between water solubility in silicate melt and change in water concentrations towards groundmass crystallization (i.e., feldspar). The feldspar microlite compositions in the ternary diagram, coupled with the dry ternary solvus isothermal section, are generated using SOLV CALC software (Wen and Nekvasil, 1994) under the pressure condition of 0.5 kbar. These sections, in terms of dry solvus condition, are not sensitive to the pressure changes in depth of less than 3 km, the expected zone where decompression-induced

crystallization and degassing of H<sub>2</sub>O occurs in conduit (Hammer et al., 2000; Bernard and de Maisonneuve, 2020; Matsumoto and Geshi, 2021). Consequently, the microlite compositions vary as a function of H<sub>2</sub>O activity, with the residual melt compositions affecting the composition of crystallized feldspar microlites.

Assuming a magma that has certain phenocryst contents ascends with certain water content, the residual melt will start to exceed the water saturation point at P1 as the pressure decreases. The melt maintains its metastable water concentration in a supersaturated condition before dehydration occurs at P2. At this point, water starts to be exsolved that resulting in the increases in liquidus temperature ( $T_{liq}$ ) of the crystals. Consequently, the effective undercooling ( $\Delta T$ ) increases rapidly following the decompression and dehydration of melt (Matsumoto and Geshi, 2021). Depending on the degree of undercooling of silicate melt, the crystallization path will be either nucleation-dominant or growth-dominant (Brugger and Hammer, 2010; Shea and Hammer, 2013). The nucleation-dominant occurs at higher  $\Delta T$  as a result of the surface free energy, whereas the growth dominant could coincide at even lower  $\Delta T$ . The first-step crystallization occurs when  $\Delta T$  has reached the critical point for microlite nucleation, following the solubility curve at that pressure (P3). Starting from this particular pressure, the path of melt dehydration will differ between distinct eruption styles. For instance, the 2007/08 dome had experienced lower  $\Delta T$ , reflected from the homogenous microlite morphology and lower ascent rates, that decreased the nucleation rate to enter growth-dominated crystallization. The microlite crystallization occurred continuously following the water solubility curve, as observed in wide ranges of feldspar compositions. This particular evidence also corresponds to continuous degassing with a low decompression rate during the groundmass crystallization of the 2007/08 dome. On the contrary, 2014 CPF products have experienced nucleation-dominated crystallizations. The combination of skeletal morphology, short range of feldspar composition, and high ascent velocities implies that 2014 CPF products had experienced sudden decompression due to high water exsolution rates before fragmentation occurred at P4 (e.g.,

Couch et al., 2003a; 200b; Shea et al., 2013). The sudden decompression interrupted crystal growth, and accordingly forced the microlites to crystallize at higher  $\Delta T$ .

The second step of crystallization occurred only in 2014 PDC-1 samples, as indicated by two distinct microlite morphologies and the abundance nanolite phase (Fig. 5.4). The occurrence of nanolite has been attributed to the drastic increase in  $\Delta T$  that disrupt the crystallization of microlite phase (e.g., Matsumoto and Geshi, 2021). A drastic increase in  $\Delta T$  driven by magma fragmentation can be associated with a rise in oxygen fugacity due to sudden decompression and rapid cooling that affects microlite and nanolite crystallization during magma fragmentation in the conduit. However, since the nanolites and microlites share similar textural and chemical features, the processes attributed to the crystallization mechanism are also similar (i.e., decompression and rapid cooling; Shea and Hammer, 2013). In the case of 2014 PDC-1 products, I infer that pressure accumulation prior to fragmentation mainly affected the late-stage microlites and nanolites (Brugger and Hammer, 2010). Calculated ascent rates from the volumetric MNDs using the water exsolution rate meter of Toramaru et al. (2008) and abrupt transitions of microlite morphology confirm the second step crystallization occurred during the onset of the 2014 eruption via sudden decompression (Fig. 5.20). Following the sudden drop of pressure in P4A, the melt became supersaturated again with water in P4B. Consequently, when the melt started dehydrating, it increased the  $\Delta T$  and produced microlites with skeletal morphology (P4C). After magma reached the critical point for fragmentation (P5), the pressure dropped again, and the liquidus temperature ( $T_{liquid}$ ) rose, which led to nanolite nucleation (P6). Moreover, nanolite nucleation will not occur if the residual melt does not dehydrate efficiently or maintains its water content until quenching, as observed in nanolite-free 2007/08 dome and 2014 CPF.

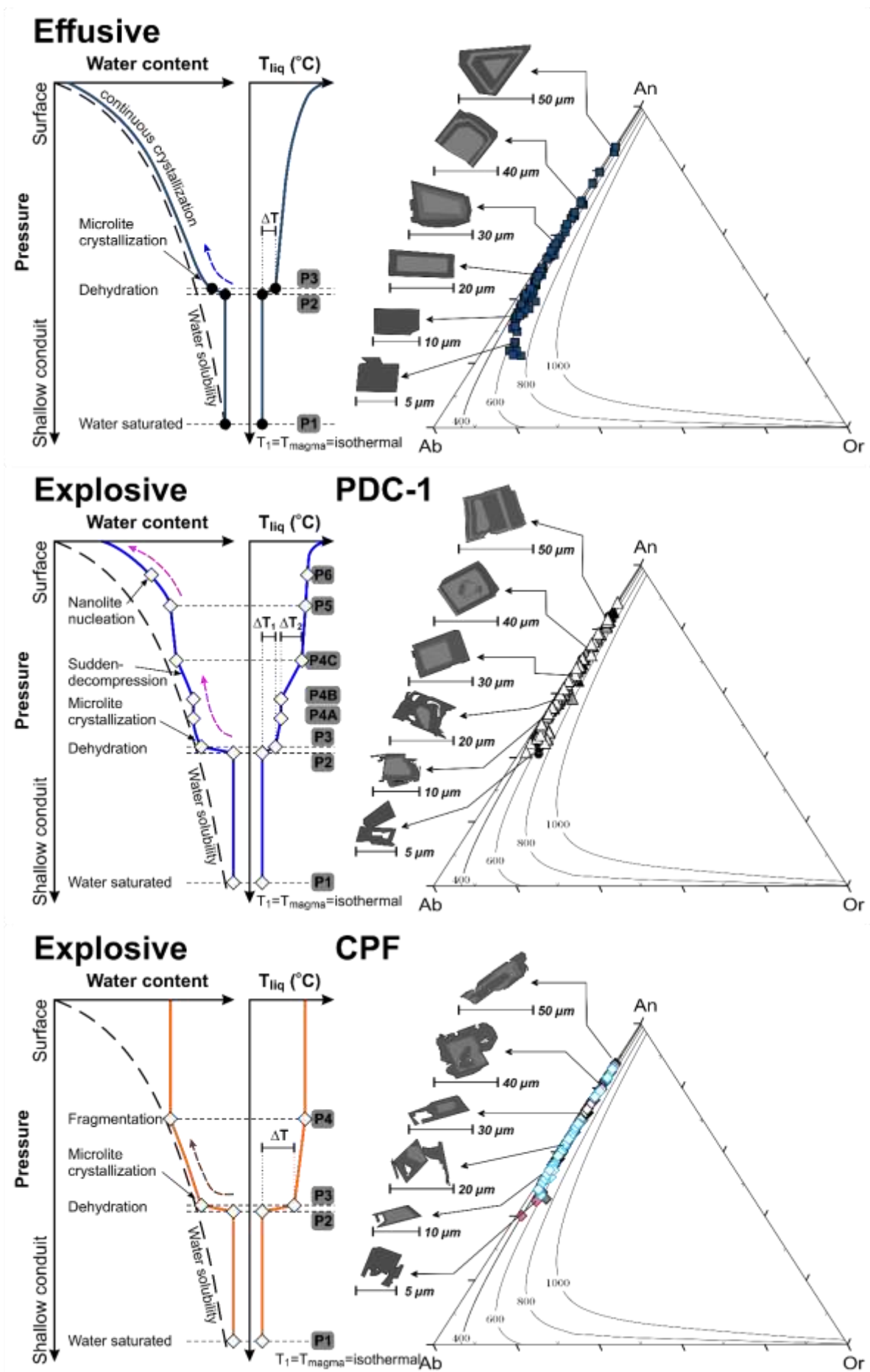


**Figure 5. 20.** Schematic illustrations showing the relationship between feldspar microlite crystallization and water saturation timing that produced studied volcanic products. Left graphs illustrate the water solubility in silicate melt (dashed lines) and effects of decompression during ascent on evolution of water content in magma (solid color lines). (Right graphs) feldspar microlite compositions coupled with morphological variations per size interval plotted in the feldspar ternary (An-Ab-Or) diagram display the compositionally differ towards different eruptive stages. Curves are generated using SOLV CALC (Wen and Nekvasil, 1994), representing isothermal sections of the dry ternary solvus at 400, 600, 800, and 1000 °C.

Additionally, some pyroxenes in 2014 products exhibit sector zoning, in which Ca-rich rims overgrowth unzoned cores during late-stage crystallization (e.g., Figs 5.8C & D). Previous studies have attributed sector zoning formation in phenocrysts to the low undercooling due to various kinetic effects during crystallization (Zellmer et al., 2016; 2018; Masotta et al., 2020). Using a similar process as an analog, sectoral zoning in pyroxene microlites could indicate that groundmass crystallization was affected mainly by cooling (Masotta et al., 2020). It is possible that prior to the eruption, the temperature of 2014 magma has decreased, therefore affecting the undercooling to crystallize pyroxene microlites with sector zoning. Alternatively, a low-undercooling temperature could also occur through degassing by increasing the liquidus temperature of magma (Shea and Hammer, 2013; Matsumoto and Geshi, 2021). As proposed by Klügel et al. (2020) and Lormand et al. (2021), the formation of sector zoning may be achieved following the volatile exsolution in late-stage crystallization at shallower depths. As a consequence, the residual melt composition became favorable to initiate the Ca-rich rims that overgrew Ca-poor cores described in this study (Figs. 5.8.A, C, & D). These processes potentially occurred in the shallowest portion of conduit, since the H<sub>2</sub>O-saturated melt started to exsolve its volatile and triggered decompression-induced crystallization at the low-pressure environments (e.g., Masotta et al., 2020; Matsumoto and Geshi, 2021).

#### 5.4.4. Effect of initial crystal content on the crystallization and degassing of ascending magma

As previously mentioned in section 5.3.1, figure 5.3 highlights the correlation between phenocryst content and vesicularity toward the explosivity of different eruption styles. The eruption with greater explosivity tends to have lower phenocryst contents and *vice versa*, with the 2007/08 dome and 2014 pumice as the two end-members of the eruption spectrum. The formation of phenocrysts in the deeper plumbing system through shallow reservoirs implies that initial ascent conditions profoundly control the eruption style produced. A crystal rich-magma batch with a 25–50 vol.% phenocryst content (i.e., effusive lava) will have an initial viscosity up to eight times greater than a quasi-aphyric magma batch (e.g., [Popa et al., 2021](#)). When the crystallinity threshold at which permeability outgassing is reached (~40% crystallinity), a dramatic increase in relative viscosity due to the rheological eruptibility limit causes volatiles to begin decoupling from magma ([Popa et al., 2021](#); [Ruth and Costa, 2021](#)). Therefore, the initial ascent rate of crystal-rich magma will be slower and became suitable conditions for the microlites to grow, increasing overall resistance for magma during ascent. Slow ascent rates (0.001–0.002 m/s) are expected for the 2007/08 dome, which has high total crystal content of combined phenocryst and microlite phases (up to 75 vol.%). Thus, when magma has a slow initial ascent rate, volatile components can be easily exsolved and outgassed from the melt, producing an eruption with lower explosivity ([Hammer et al., 2000](#); [Bernard and de Maisonneuve, 2020](#); [Popa et al., 2021](#)).

Moreover, recent studies have also demonstrated the mechanical effects of crystals (i.e., surface tensions) on bubble development, which promote coalescence and effective permeability for gas escape (e.g., [Shea, 2017](#)). The higher volume occupied by crystal phases, the tendency for the bubble to grow between crystals during the gas transfer also becomes higher. Consequently, bubble growth and effective permeability will be increased when crystal proportions are high enough, either due to higher initial crystal contents at the magma reservoir or by microlite crystallization in the conduit (e.g., [Shea et al., 2010](#)). It will further develop permeable pathways

near the surface for gas to escape the system, ultimately slowing down the ascent rate to produce an effusive eruption. By comparison, pumice and scoria issued from the 2014 plinian phase show slightly lower microlite contents ranging from 2 to 30 vol%, while the scoria is between 9 and 11 vol.% (Tables. 5.3 and 5.4). When the magma is quasi-aphyric and has a high initial ascent rate, the volatile outgassing and microlite crystallization will be suppressed. Consequently, it will increase the rate of volatile components to be simultaneously exsolved at the shallowest conduit and later produce an explosive eruption, similar to Rabaul (Bernard and de Maisonneuve, 2020) and Merapi (Preece et al., 2016).

#### 5.4.5. Controls on the effusive-explosive transition at Kelud

The 2007/08 and 2014 eruptions exhibited transitions between effusive and explosive behavior. Whole-rock compositions remained constant throughout the eruptions, indicating that bulk magmatic composition cannot be the main factor in the observed change in behavior. Instead, the initiation and cessation of each eruption were governed by magma flux from depth, with shallow conduit processes modulating eruptive style.

Although effusive eruptions have been studied in considerably less detail than explosive eruptions, certain parameters can be compared to shed light on the dynamics of this type of eruption. The 2007/08 dome had higher viscosity during its initial ascent, reflected by a high phenocryst content with >49 vol% (Fig. 5.3) and low decompression rates decompression rates ( $2.15 \times 10^{-5}$ – $4.57 \times 10^{-5}$  MPa/s; Fig. 3.20). This would subsequently trigger the microlite crystallization by lowering the surface tension necessary to form effective permeability (Fig. 5.21A). The ascent rates estimated for the 2007/08 dome have the same magnitude as other dome-forming eruptions suggested by Cassidy et al. (2018). Therefore, this would imply that effusive eruption could have resulted from the high outgassing mode and high crystallization rates in the shallower portion of the conduit driven by higher initial phenocryst content and low initial ascent rates. On the contrary, 2014 products bear the lowest phenocryst content with 15–

40 vol% (Fig. 3.3). This suggests that 2014 magmas had relatively lower viscosity and higher ascents compared to the 2007/08 dome. However, the decompression and ascent rates inferred from banded pumice and scoria bomb samples were at lower magnitudes during their initial ascent (Table 5.7). Both decompression and ascent rates were then tremendously increased, reaching values of  $3.09 \times 10^{-1}$  MPa/s and 18.7 m/s (i.e., BP dark and light grey). Here, I infer that magma recharged, as indicated by the presence of banded pumice with different textural and physical properties, occurred and intensified the magma mobilization and resulting in higher decompression and ascent rates (more than four times magnitudes of the 2007/08 dome; Fig. 5.21B). The higher ascent rates allowed the volatile components to be further exsolved simultaneously and increased the effective pressure on magma, producing more explosive eruptions. Moreover, the climactic plinian phase marks slightly lower decompression and ascent rates than PDC-1 (Fig. 5.21C). Such decrement is expected since the pressure gradually became stable after releasing the accumulated pressure sealed by the 2007/08 dome.

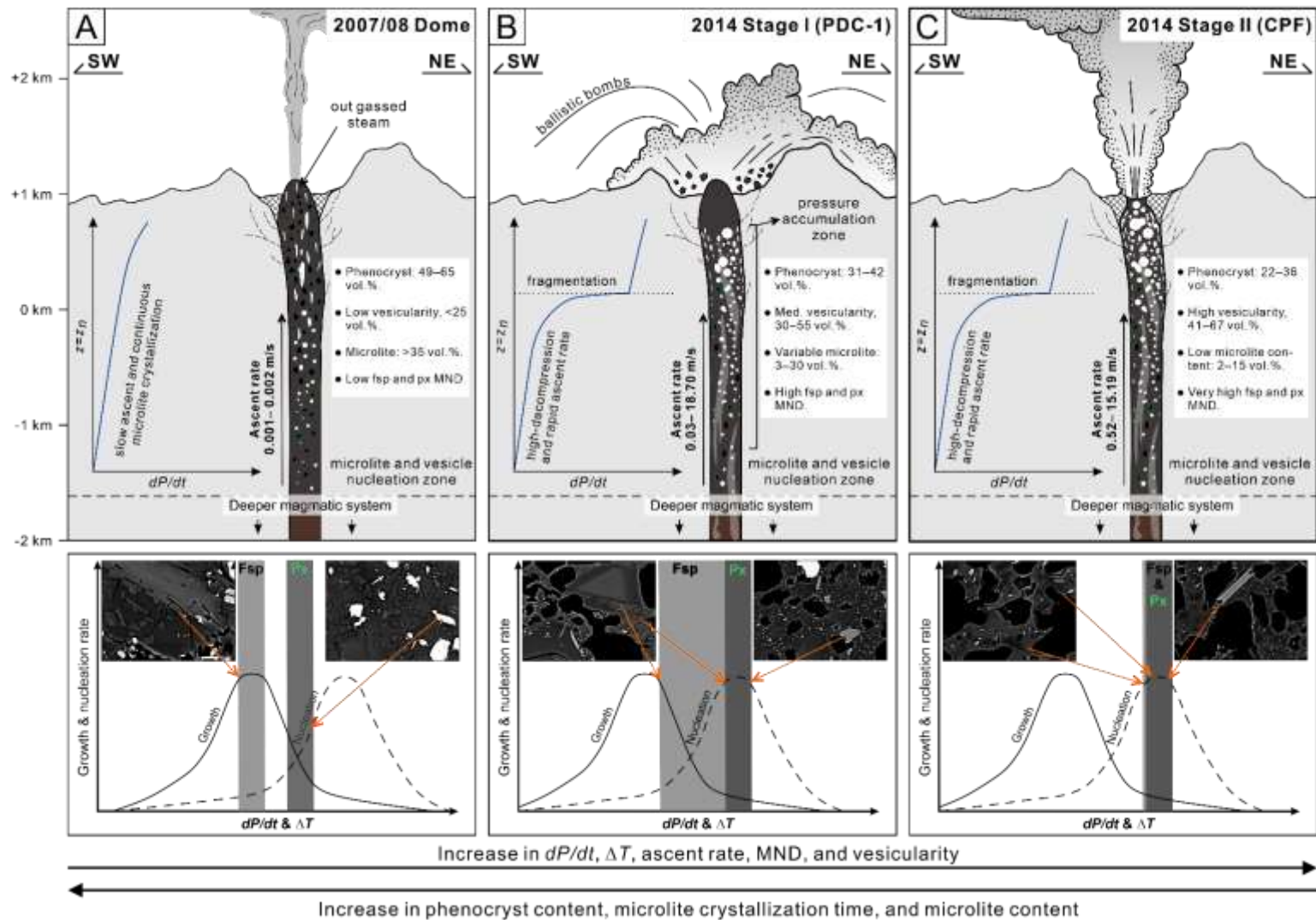


**Figure 5. 21.** Schematic illustrations of magma dynamics during ascent for A) 2007/08 dome-forming eruption, B) onset of 2014 eruption, C) climactic plinian event in 2014 eruption.

#### 5.4.6. Hazard implication

This study has demonstrated the variations of textural and chemical composition from the 2007/08 and 2014 products have a significant role in governing the eruption styles produced. A plot of  $\log(\text{MND})$  versus  $\text{SiO}_2$  concentrations indicates that both effusive and explosive phases of Kelud are comparable to other eruptions with similar styles around the world in terms of crystallinity and compositions (Fig. 5.22). With more evolved magma compositions, lower crystallinity, and higher microlite number densities, a volcano tends to produce an eruption with higher explosivity (i.e., Pinatubo and Merapi; [Hammer et al., 1999](#); [Preece et al., 2013](#); [2016](#)). On the contrary, higher crystal contents and lower microlite number densities will lead an eruption to be more effusive (i.e., producing lava flow or domes).

Further, the  $N_A-\phi$  relationship suggests that high values of decompression rates will lead to faster growth rates of microlites and high explosivity in explosive products, whereas lower values of decompression rates produce low explosivity eruptions via slower microlite crystallization (Fig. 5.22). Compared to the 1991 eruption of Pinatubo ([Hammer et al. 1999](#)), the products of the 2014 eruption of Kelud have lower overall  $N_A$  values, corroborated by the calculated growth rate of feldspar microlites from these two eruptions. The result indicates that the Kelud 2014 eruption has an intermediate explosivity compared to the climatic plinian eruption of Pinatubo and other effusive dome-forming eruptions (Merapi lava domes; [Hammer et al., 2000](#); [Preece et al., 2013](#)). However, Kelud had produced an eruption with VEI of 4 and  $\sim 0.28 \text{ km}^3$  DRE in volume that drifted  $\sim 600 \text{ km}$  westward over the Indonesian ocean. If based on the volume and intensity alone, theoretically, the 2014 eruption could not produce such a high-explosivity eruption. Nevertheless, such phenomena could be explained by pressure accumulation prior to the 2014 eruption, where the 2007/08 dome acted as a “plug” that sealed pressure under closed system degassing. Consequently, by the time pressure was released, it could produce higher explosivity than other eruptions with similar bulk ejected volumes (i.e., Sundoro; [Prambada et al., 2016](#)).

This study suggests that the condition of the volcanic vent (i.e., presence of lava dome, degassing, and crystallization behaviors) implies a significant contribution to the lava-tephra formation at Kelud. Therefore, eruptions with a similar pattern may also occur in the future. This point also emphasizes that Kelud should be considered a high-risk volcano and requires further studies to reconstruct a more sophisticated eruptive scenario.

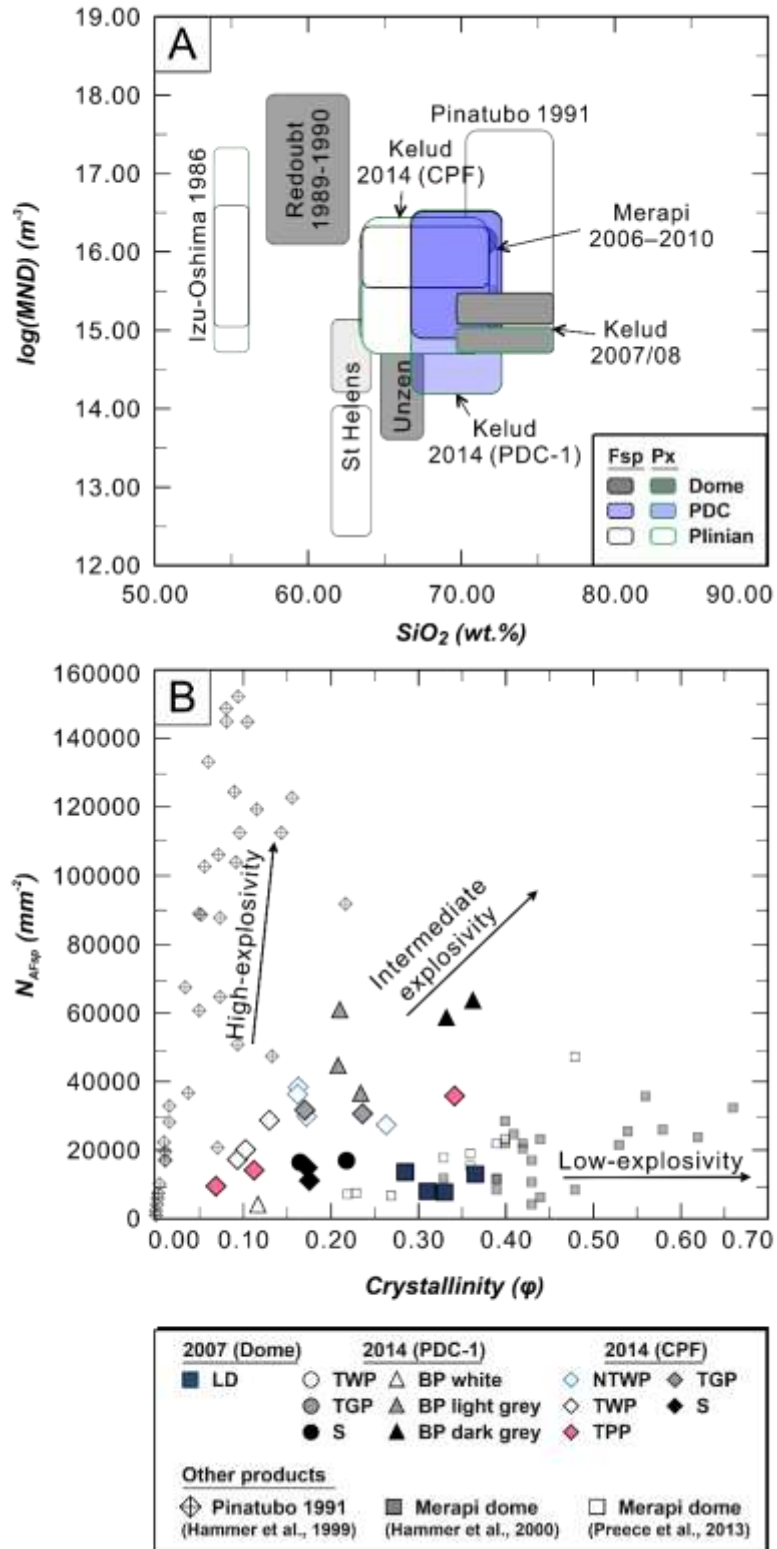


**Figure 5. 22.** A) Plot of  $\log(\text{MND})$  vs  $\text{SiO}_2$  concentration. MND data were compiled from previous publications of Redoubt (Wolf and Eichelberger, 1997), Mount St. Helens (Cashman, 1992), Pinatubo (Hammer et al., 1999; Borisova et al., 2005), Izu-Oshima (Toramaru et al., 2008), Unzen (Noguchi et al., 2008), and Merapi (Preece et al., 2013; 2016). B) Plot of  $N_{\text{A}}$  vs  $\phi$  in comparison with other eruptions with various explosivity.

## 5.5. Summary and conclusion

This study documented the physical, textural, and chemical variations of volcanic products from effusive and explosive events in 2007/08 and 2014, respectively. In summary, the dispersity of eruption styles at Kelud was initially controlled by different crystallization patterns from the depth that affected magma rheology during ascent. The crystallization processes were enhanced by rapid decompression and degassing in the shallower conduit, which in turn finalized the eruption style produced and responsible for the effusive-explosive transition. The 2007/08 was fed by a crystal-rich magma that has slow ascent ( $<0.002$  m/s) and decompression rates due to volatile outgassing at relatively higher viscosity. In contrast, the 2014 plinian eruption was derived from less crystalline magma that rapidly ascends (reaching over 18 m/s at the microlite nucleation depth) due to its low viscosity and effective permeability. Furthermore, the transition between effusive and explosive activity was driven primarily by conduit dynamics during magma ascent, with degassing and crystallization acting via a two-step crystallization mechanism. The presence of a 'plug' in the conduit, coupled with high ascent rates led to closed-system conditions, which increased the overall effective pressure accumulated in the system and led to explosive eruptions that produced climactic plinian fallout (CPF) in February 2014.

The 2007/08 and 2014 eruptions demonstrate the capacity of Kelud volcano to switch the eruptive behavior from dome-forming to explosive behavior with possible repetitions in the future and little warning time after the initial dome growth. This study also demonstrates that at Kelud, the conditions of magma storage and crystallization pathways are important for the final eruption style produced. Consequently, further characterization of magma reservoirs (e.g., permeability and vesicle studies) is required to gain a better understanding of the eruption dynamics and triggering factors at Kelud volcano and other volcanoes with similar eruption styles.

## References

- Bani, P., Kristianto, Kunrat, S., Syahbana, D. K., 2020. Insights into the recurrent energetic eruptions on Awu, one of the deadliest volcano on earth. *Nat. Hazards Earth Syst. Sci.* 20, 2119–2020. <https://doi.org/10.5194/nhess-20-2119-2020>
- Bernard, O., & Bouvet de Maisonneuve, C., 2020. Controls on eruption style at Rabaul, Papua New Guinea – Insights from microlites, porosity and permeability measurements. *J. Volcanol. Geotherm. Res.* 406. <https://doi.org/10.1016/j.jvolgeores.2020.107068>
- Borisova, A. Y., Pichavant, M., Beny, J. M., Rouer, O., & Pronost, J., 2005. Constraints on dacite magma degassing and regime of the 15 June, 1991, climactic eruption of Mount Pinatubo (Philippines): New data on melt and crystal inclusions in quartz. *J. Volcanol. Geotherm. Res.* 145(1–2), 35–67. <https://doi.org/10.1016/j.jvolgeores.2005.01.004>
- Bourdier, J. L., Pratomo, I., Thouret, J.-C., Boudon, G., Vincent, P.M. 1997. Observations, stratigraphy and eruptive processes of the 1990 eruption of Kelut volcano, Indonesia. *J. Volcanol. Geotherm. Res.* 79, 181–203. [https://doi.org/10.1016/S0377-0273\(97\)00031-0](https://doi.org/10.1016/S0377-0273(97)00031-0)
- Cashman, K. V., 1992. Groundmass crystallization of Mount St. Helens dacite, 1980-1986: a tool for interpreting shallow magmatic processes. *Contrib. Mineral. Petrol.* 109(4), 431–449. <https://doi.org/10.1007/BF00306547>
- Cashman, K. V, Mangan, M. T., Newman, S., 1994. Surface degassing and modifications to vesicle size distributions in active basalt flows. *J. Volcanol. Geotherm. Res.* 61(1), 45–68. [https://doi.org/https://doi.org/10.1016/0377-0273\(94\)00015-8](https://doi.org/https://doi.org/10.1016/0377-0273(94)00015-8)
- Cassidy, M., Manga, M., Cashman, K., Bachmann, O., 2018. Controls on explosive-effusive volcanic eruption styles. In *Nat. Commun.* (Vol. 9, Issue 1). Nature Publishing Group. <https://doi.org/10.1038/s41467-018-05293-3>
- Caudron, C., Mazot, A., Bernard, A., 2012. Carbon dioxide dynamics in Kelut volcanic lake. *J. Geophys. Res.* 117:B05102. <https://doi.org/10.1029/2011JB008806>

- Couch, S., Sparks, R.S.J., Carroll, M.R., 2003a. The kinetics of degassing-induced crystallization at Soufrière Hills volcano, Montserrat. *J. Petrol.* 44, 1477–1502. <https://doi.org/10.1093/petrology/44.8.1477>
- Couch, S., Harford, C.L., Sparks, R.S.J., Carroll, M.R., 2003b. Experimental constraints on the conditions of formation of highly calcic plagioclase microlites at the Soufrière Hills volcano, Montserrat. *J. Petrol.* 44, 1455–1475. <https://doi.org/10.1093/petrology/44.8.1455>
- Global Volcanism Program, 2008. Report on Kelud (Indonesia) (Wunderman, R., ed.). Bulletin of the Global Volcanism Network, 33:3. Smithsonian Institution. <https://doi.org/10.5479/si.GVP.BGVN200803-263280>
- Hammer, J. E., Cashman, K. V., Hoblitt, R. P., Newman, S. 1999. Degassing and microlite crystallization during pre-climactic events of the 1991 eruption of Mt. Pinatubo, Philippines. *Bull. Volcanol.* 60: 355. <https://doi.org/10.1007/s004450050238>
- Hammer, J.E., Cashman, K.V., Voight B., 2000. Magmatic processes revealed by textural and compositional trends in Merapi dome lavas. *J. Volcanol. Geotherm. Res.* 100, 165–192. [https://doi.org/10.1016/S0377-0273\(00\)00136-0](https://doi.org/10.1016/S0377-0273(00)00136-0)
- Hidayati, S., Kristianto, Basuki, A., Mulyana, I., 2009. A new lava dome emerged from crater lake of Kelud volcano, East Java, Indonesia. *Ind. J. Geo.* 4 (4), 229–238. <http://dx.doi.org/10.17014/ijog.vol4no4.20091>.
- Hidayati, S., Triastuty, H., Mulyana, I., Adi, S., Ishihara, K., Basuki, A., Kuswandarto, H., Priyanto, B., Solikhin, A., 2019. Differences in the seismicity preceding the 2007 and 2014 eruptions of Kelud volcano, Indonesia. *J. Volcanol. Geotherm. Res.* 382, 50–67. <https://doi.org/10.1016/j.jvolgeores.2018.10.017>
- Higgins, D.M., 2000. Measurement of crystal size distributions. *Am. Mineral.* 85, 1105–1116. <https://doi.org/10.2138/am-2000-8-901>.
- Higgins, M.D., 2006. Quantitative Textural Measurements in Igneous and Metamorphic

- Petrology. Cambridge University Press, Cambridge, 265 pp.  
<https://doi.org/10.1017/CBO9780511535574>
- Indriyanto, J. N., Ohba, T., Hoshide, T., Angkasa, S. S., Abdurrachman, M., 2023. Eruptive history of the last-1300-years activity of Kelud volcano , Indonesia : Inferences from stratigraphy , chronology , sedimentology , componentry , and geochemistry. *J. Volcanol. Geotherm. Res.*, 433, 107723.  
<https://doi.org/10.1016/j.jvolgeores.2022.107723>
- Jeffery, A. J., Gertisser, R., Troll, V. R., Jolis, E. M., Dahren, B., Harris, C., Tindle, A. G., Preece, K., O'Driscoll, B., Humaida, H., Chadwick, J. P., 2013. The pre-eruptive magma plumbing system of the 2007-2008 dome-forming eruption of Kelut volcano, East Java, Indonesia. *Contributions to Mineralogy and Petrology*, 166(1), 275–308.  
<https://doi.org/10.1007/s00410-013-0875-4>
- Klügel, A., Day, S., Schmid, M., Faria, B., 2020. Magma plumbing during the 201T 2015 eruption of Fogo (Cape Verde Islands). *Front. Earth. Sci.* 8:157.  
<https://doi.org/10.3389/feart.2020.00157>
- Le Maitre, R.W., Streckeisen, A., Zanettin, B., La Bas, M.J., Bonin, B., Bateman, P., Bellieni, G., Dudek, A., Efremova, J., Keller, J., Lameyre, J., Sabine, P.A., Schmidt, R., Sørensen, H., Woolley, A.R., 2002. *Igneous Rocks. A classification and Glossary of Terms. Recommendations of the International Union of Geological Sciences subcommission on the systematics of igneous rocks.* Cambridge University Press, Cambridge, 252 pp.
- Lofgren, G., 1974. An experimental study of plagioclase crystal morphology: isothermal crystallization. *Am. J. Sci.* 274, 243–273. <https://doi.org/10.2475/ajs.274.3.243>
- Lormand, C., Zellmer, G. F., Sakamoto, N., Ubide, T., Kilgour, G., Yurimoto, H., Palmer, A., Németh, K., Iizuka, Y., & Moebis, A., 2021. Shallow magmatic processes revealed by cryptic microantecrysts: a case study from the Taupo Volcanic Zone. *Contrib. Mineral. Petrol.* 176(11), 97. <https://doi.org/10.1007/s00410-021-01857-7>

- Maeno, F., Nakada, S., Yoshimoto, M., Shimano, T., Hokanishi, N., Zaenuddin, A., Iguchi, M., 2019a. A sequence of a plinian eruption preceded by dome destruction at Kelud volcano, Indonesia, on 13 February, 2014, revealed from tephra fallout and pyroclastic density current deposits. *J. Volcanol. Geotherm. Res.* 382, 24–41. <https://doi.org/10.1016/j.jvolgeores.2017.03.002>
- Maeno, F., Nakada, S., Yoshimoto, M., Shimano, T., Hokanishi, N., Zaenuddin, A., Iguchi, M., 2019b. Eruption pattern and a long-term magma discharge rate over the past 100 years at Kelud volcano, Indonesia. *J. Disaster. Res.* 14 (1), 27–39. <https://doi.org/10.20965/jdr.2019.p0027>
- Marsh, B.D., 1998. On the interpretation of crystal size distributions in magmatic systems. *J. Petrol.* 39, 553–599. <https://doi.org/10.1093/petroj/39.4.553>.
- Masotta, M., Pontesilli, A., Mollo, S., Armienti, P., Ubide, T., Nazzari, M., Scarlato, P., 2020. The role of undercooling during clinopyroxene growth in trachybasaltic magmas: insights on magma decompression and cooling at Mt. Etna volcano. *Geochim. Cosmochim. Acta.* 268:258–276. <https://doi.org/10.1016/j.gca.2019.10.009>
- Matsumoto, K., & Geshi, N., 2021. Shallow crystallization of eruptive magma inferred from volcanic ash microtextures: a case study of the 2018 eruption of Shinmoedake volcano, Japan. *Bull Volcanol.* 83(5). <https://doi.org/10.1007/s00445-021-01451-6>
- Morgan, D.J., Jerram, D.A., 2006. On estimating crystal shape for crystal size distribution analysis. *J. Volcanol. Geotherm. Res.* <https://doi.org/10.1016/j.jvolgeores.2005.09.016>
- Morimoto, N., 1989. Nomenclature of pyroxenes. *Mineral. J.* 14(5): 198–221. <https://doi.org/10.2465/minerj.14.198>
- Murch, A.P. & Cole, P.D., 2019. Using microlites to gain insights into ascent conditions of differing styles of volcanism at Soufrière Hills Volcano, *J. Volcanol. Geotherm. Res.* 384, 221–231. <https://doi.org/10.1016/j.jvolgeores.2019.07.022>
- Noguchi, S., Toramaru, A., Nakada, S., 2008. Relation between microlite textures and

- discharge rate for the 1991–1995 eruptions at Unzen, Japan. *J. Volcanol. Geotherm. Res.* 175, 141–155. <https://doi.org/10.1016/j.jvolgeores.2008.03.025>
- Ozawa, T., Kozono, T., 2013. Temporal variation of the Shinmoe-dake crater in the 2011 eruption revealed by spaceborne SAR observations. *Earth Planet Sp.* 65, 5. <https://doi.org/10.5047/eps.2013.05.004>
- Pardo, N., Avellaneda, J.D., Rausch, J., Jaramillo-Vogel, D., Gutiérrez, M., Foubert, A., 2020. Decrypting silicic magma/plug fragmentation at Azufral crater lake, Northern Andes: insights from fine to extremely fine ash morpho-chemistry. *Bull. Volcanol.* 82, 79. <https://doi.org/10.1007/s00445-020-01418-z>
- Popa, R. G., Bachmann, O., Huber, C., 2021. Explosive or effusive style of volcanic eruption determined by magma storage conditions. *Nat. Geosci.* 14(10), 781–786. <https://doi.org/10.1038/s41561-021-00827-9>
- Prambada, O., Arakawa, Y., Ikehata, K., Furukawa, R., Takada, A., Wibowo, H.E., Nakagawa, M., Kartadinata, M.N., 2016. Eruptive history of Sundoro volcano, Central Java, Indonesia since 34 ka. *Bull. Volcanol.* 78, 81–100. <https://doi.org/10.1007/s00445-016-1079-3>
- Preece, K., Barclay, J., Gertisser, R., Herd, R. A., 2013. Textural and micro-petrological variations in the eruptive products of the 2006 dome-forming eruption of Merapi volcano, Indonesia: Implications for sub-surface processes. *J. Volcanol. Geotherm. Res.* 261, 98–120. <https://doi.org/10.1016/j.jvolgeores.2013.02.006>
- Preece, K., Gertisser, R., Barclay, J., Berlo, K., Herd, R. A., Edinburgh Ion Microprobe Facility. 2014. Pre- and syn-eruptive degassing and crystallisation processes of the 2010 and 2006 eruptions of Merapi volcano, Indonesia. *Contrib. Miner. Pet.*, 168(4), 1–25. <https://doi.org/10.1007/s00410-014-1061-z>
- Preece, K., Gertisser, R., Barclay, J., Charbonnier, S.J., Komorowski, J.-C., Herd, R.A., 2016. Transitions between explosive and effusive phases during the cataclysmic 2010 eruption

- of Merapi volcano, Java, Indonesia. *Bull. Volcanol.* 78, 54.  
<https://doi.org/10.1007/s00445-016-1046-z>
- Ruth, D. C. S., & Costa, F., 2021. A petrological and conceptual model of Mayon volcano (Philippines) as an example of an open-vent volcano. *Bull. Volcanol.* 83(10).  
<https://doi.org/10.1007/s00445-021-01486-9>
- Shea, T., Houghton, B. F., Gurioli, L., Cashman, K. V., Hammer, J. E., Hobden, B. J., 2010. Textural studies of vesicles in volcanic rocks: An integrated methodology. *J. Volcanol. Geotherm. Res.* 190(3–4), 271–289. <https://doi.org/10.1016/j.jvolgeores.2009.12.003>
- Shea, T., Gurioli, L., Houghton, B.F., 2012. Transitions between fall phases and pyroclastic density currents during the AD 79 eruption at Vesuvius: building a transient conduit model from the textural and volatile record. *Bull. Volcanol.* 74, 2363–238.  
<https://doi.org/10.1007/s00445-012-0668-z>
- Shea, T., & Hammer, J. E., 2013. Kinetics of cooling- and decompression-induced crystallization in hydrous mafic-intermediate magmas. *J. Volcanol. Geotherm. Res.* 260, 127–145. <https://doi.org/10.1016/j.jvolgeores.2013.04.018>
- Shea, T., 2017. Bubble nucleation in magmas: A dominantly heterogeneous process? *J. Volcanol. Geotherm. Res.* 343, 155–170.  
<https://doi.org/10.1016/j.jvolgeores.2017.06.025>
- Siebert, L., Simkin, T., Kimberly, P., 2011. *Volcanoes of the world*, 3rd edn. University of California Press, Los Angeles, p 551
- Surono, 2007, Pusat Vulkanologi Dan Mitigasi Bencana Geologi, Pos Pengamatan Gunungapi Kelut (Hasil evaluasi tingkat kegiatan G. Kelut): Departemen Energi Dan Sumber Daya Mineral, Republik Indonesia, Badan Geologi, Nomor, 112/GK/X/2007, 30 Oktober 2007. In Indonesian.
- Suzuki, Y., & Fujii, T., 2010. Effect of syneruptive decompression path on shifting intensity in basaltic sub-Plinian eruption: implication of microlites in Yufune-2 scoria from Fuji

- volcano, Japan. *J. Volcanol. Geotherm. Res.* 198, 159–176.  
<https://doi.org/10.1016/j.jvolgeores.2010.08.020>
- Toramaru, A., Noguchi, S., Oyoshihara, S., Tsune, A., 2008. MND (microlite number density) water exsolution rate meter. *J. Volcanol. Geotherm. Res.* 175(1–2), 156–167.  
<https://doi.org/10.1016/j.jvolgeores.2008.03.035>
- Van der Plas, L., Tobi, A.C., 1965. A chart for judging the reliability of point counting results. *Am. J. Sci.* 263, 87–90. <https://doi.org/10.2475/ajs.263.1.87>.
- Wen S., Nekvasil H., 1994. SOLVCALC: an interactive graphics program package for calculating the ternary feldspar solvus and for two-feldspar geothermometry. *Comput. Geosci.* 20, 1025–1040. [https://doi.org/10.1016/0098-3004\(94\)90039-6](https://doi.org/10.1016/0098-3004(94)90039-6)
- Wolf, K.J., Eichelberger, J.C., 1997. Syneruptive mixing, degassing, and crystallization at Redoubt Volcano, eruption of December, 1989 to May 1990. *J. Volcanol. Geotherm. Res.* 75, 19–37. [https://doi.org/10.1016/S0377-0273\(96\)00055-8](https://doi.org/10.1016/S0377-0273(96)00055-8)
- Zellmer, G.F., Sakamoto, N., Matsuda, N., Iizuka, Y., Moebis, A., Yurimoto, H., 2016. On progress and rate of the peritectic reaction  $\text{Fo} + \text{SiO}_2 \rightarrow \text{En}$  in natural andesitic arc magmas. *Geochim. Cosmochim. Acta.* 185:383–393.  
<https://doi.org/10.1016/j.gca.2016.01.005>
- Zellmer, G.F., Sakamoto, N., Matsuda, N., Iizuka, Y., Moebis, A., Yurimoto, H., 2018. Corrigendum to “on progress and rate of the peritectic reaction  $\text{Fo} + \text{SiO}_2 \rightarrow \text{En}$  in natural andesitic arc magmas.” *Geochim. Cosmochim. Acta.* 185:383–393.  
<https://doi.org/10.1016/j.gca.2016.01.005>